Measurement of Liquid Argon Response and Direct Dark Matter Search at Surface with A Liquid Argon Scintillation Detector

液体アルゴン光検出器を用いた
アルゴン応答の測定と
地上実験室における暗黒物質直接探索

March 2021

Masato KIMURA

木村　眞人

Measurement of Liquid Argon Response and Direct Dark Matter Search at Surface with A Liquid Argon Scintillation Detector

液体アルゴン光検出器を用いた
アルゴン応答の測定と
地上実験室における暗黒物質直接探索

March 2021

Waseda University
Graduate School of Advanced Science and Engineering
Department of Pure and Applied Physics
Research on Experimental Particle Physics

Masato KIMURA
木村　眞人

Abstract

Dark matter is a hypothetical matter in the universe which is introduced to coherently explain observations ranging from the scale of galaxies to the whole of the universe. Weakly Interacting Massive Particle, or WIMP, is one of the most promising candidate supported by cosmological and particle physics theories. From an experimental point of view, liquid argon scintillation detector offers several attractive features to detect the WIMP directly. It can in particular be sensitive for low-mass WIMP around 10 GeV/c^2. Systematical and comprehensive understanding of liquid argon response is invariant knowledge to design a detector, interpret observed signals, reduce systematic uncertainty, and claim the discovery.

This dissertation presents measurements of liquid argon scintillation and ionization yields that lead the functional modeling of the liquid argon response. The work comprises two measurements.

One is that for nuclear recoils (that should be induced by WIMP) focusing on both energy- and field-dependencies. This work measures the signal yields for nuclear recoils above 1 kV/cm for the first time using a double-phase time projection chamber. In addition, a response model is constructed with an analogy of that for liquid xenon. We find that observed spectra can be described with five parameters within the model determined by spectra fit with Monte Carlo simulation. It predicts more ionization yield in higher field, which possibly expands the sensitivity for lower-mass WIMP. The other is that for electronic recoils (dominant background in the WIMP search). A single-phase detector with a large optical coverage used in this measurement yields 12.8 ± 0.3 photoelectron/keV for 511.0-keV γ-ray events assuming a photomultiplier tube single photoelectron response modeling with a Gaussian plus an additional exponential term. Notably, this high light collection efficiency enables identification of the 2.8-keV peak of ^{37}Ar. We find up to approximately 25% shift in the scintillation yield across the energy range of 2.8–1275 keV at null electric field. Thomas-Imel box model with its constant parameter $\varsigma = 0.033^{+0.012}_{-0.008}$ is found to explain the result. The result will work to precise evaluation of background contamination after selecting nuclear recoils.

Consequently, the model interpretations of the liquid argon response, as well as the measurement itself of the unseen phase space, is an invaluable input for any WIMP search using any liquid argon detector in both design and analysis phases. The underlying similarity or difference between nuclear- and electronic-recoils are also discussed.

In addition, this dissertation reports a physics run at surface by using the result from property measurement. The run intends to search for the low-mass WIMP under a background-free condition, exploiting a detector based on the best knowledge at this time. An exposure of 0.2 kg · days of a single-phase detector sets an upper limit on WIMP-nucleon cross section of 4×10^{-37} cm^2 for 10 GeV/c^2 WIMP at 90% confidence level. The sensitivity is limited by cosmic-ray induced events. The result suggests that a search for 10 GeV/c^2 WIMP with the cross section of 1.0×10^{-40} cm^2 is achievable with a liquid argon detector at a deep underground laboratory.

Acknowledgments

I am grateful to many people for supporting me throughout my Ph.D life. This work has been accomplished with their huge supports and discussions with them.

Firstly, I would like to thank my supervisor Prof. Kohei Yorita for invaluable guidance and help in this seven years. He also gave me an opportunity to participate in the ANKOK and focus on the research. I have learned a lot about particle physics and further about the way of man (at 30). His words with his passion always stimulated me and accelerated my works. I am grateful to Prof. Masashi Tanaka, who leads the ANKOK group. He has shown me how to do experimental physics, and what is the physicist at the laboratory. Talking with him makes me thinking deeper and deeper and leads to an essence of the research subject. They also provided me chances to do everything related to the experiment; hardware, software, run planning, run coordination, presentation at international conference, publishing scientific paper, and so on. I feel these experience are all very valuable for me to be a physicist. It was my honour to put the right eye of the Daruma. I would like to keep in mind the policy to enjoy research regardless of its situation.

I wish to express my gratitude to Prof. Sachio Komamiya. I am grateful that he politely addressed my research and this dissertation, and gave me both major and minor comments. Lots of advice from him are based on his numerous experience, and these all are helpful for me to improve this dissertation and process the Ph.D examination.

I wish to express my gratitude to Prof. Masakazu Washio. His comments from radiophysics point of view filled an important piece of my thesis. In addition, he kindly lent us a few tons of lead blocks, which was indispensable in this work.

I wish to express my gratitude to Prof. Kentaro Miuchi from Kobe University. I fortunately had several opportunities to discuss with him during my Ph.D course. His insightful comments with his wide knowledge were helpful to advance my research.

My gratitude extends to all the past and present ANKOK members. To Dr. Tatsuki Washimi, the time with him was sometimes fun, sometimes stimulating, and sometimes confusing. We especially tackled to the argon response, and many discussions among that was important for this study. Working with Kazutaka Aoyama is also stimulating, and I respect his patience especially on the hardware. The high light detection efficiency of the detector is achieved by his effort. I would also like to thank Hiroyuki Morohoshi, Ryukichi Ozu, Taichi Nakasone, and Mayu Sakurai. The surface run can be completed owing to their huge efforts in the hot days. I would also like to thank the members working with me in my early days; Shinpei Naka, Yuto Suzuki, Takanori Kikuchi, Yuki Takemura, Tetsuma Yaguchi, and Tomomasa Takeda. I think we all were power-type man.

I wish to thank Dr. Akira Hitachi for valuable comments based on his mastery on noble fluid gas response.

I would also like to express my gratitude to the Underground and Low-Background-Technique community in Japan. There were many opportunities to present my work and discuss it from many points of view. Especially, meeting with young researches was useful and I learned a lot of things. Thank you for the members, Dr. Tomonori Ikeda, Dr. Kiseki Nakamura, and Dr. Atsuhiro Umemoto.

My gratitude goes to the members of the Kohei Yorita Group. Dr. Koji Ebina is so helpful in the development of analysis framework and simulation package. He taught me the computing sometimes kindly and sometimes strictly. Mrs. Atsuko Sakamoto has always helped our research activities as a secretary and warmly encouraged us. It was a great pleasure that I shared a lot of time with the ATLAS members. I would especially like to thank Dr. Tatsumi Nitta, Yoshihiro Shimogama, Takashi Mitani, and Toshiaki Kaji.

Lastly, I would like to give my appreciation to my family. I thank my parents, Naoto and Hiroe, and my brother, Tomohiro, for their moral support for very long time. And I thank my wife Kasumi to be there for supporting me with big patience.

Thank you very much to all concerned with me!

Contents

List of figures

List of tables

Chapter 1

Introduction

Dark matter is a hypothetical non-luminous (dark) mass in the universe which could explain a plethora of astrophysical and cosmological observations ranging from the scale of galaxies to the whole of the universe. The non-luminous means it does not interact electromagnetically. There are other requirements on the nature of dark matter; it must be long-lived at least comparable to the age of the Universe, it must interact very weakly at all with other particles as well as itself, it must not be baryon, and it must be non-relativistic when the Universe clear up. The existence of dark matter is strongly supported by observations, yet all of them rely on gravitational effect and its nature remains one of the most severe puzzle of current physics. The Standard Model (SM) of particle physics beautifully explains phenomena below electroweak scale, however, no SM particle could be dark matter. Therefore, discovering the dark matter and revealing its nature are the clear needle for both cosmological and particle physics.

Among a number of dark matter models, Weakly Interacting Massive Particle or WIMP is one of the promoting candidate which has mass of GeV/c^2 to TeV/c^2 range and interacts with ordinal matter at or below the weak scale. From cosmological point of view, it is attractive to naturally explain current relic density. From particle physics view, it is naturally appeared by introducing an additional symmetry beyond the Standard Model. Significant efforts are made by many groups to experimentally confirm the WIMP model.

Direct WIMP detection experiment aims to detect a tiny and rare signal induced by interaction between target nuclei on Earth and WIMP in the dark matter halo of the Milky Way. Liquid argon (LAr) scintillation detector offers several attractive features for the experiment, such as large signal yields, powerful capability to extract signal against numerous background by use of particle identification (PID) techniques, and availability for large amount of argon with relatively low cost. In this detector, energy deposition inside the liquid argon is primarily converted to scintillation light. The ionization electrons simultaneously emitted from the point drift toward gaseous phase so that they emit electroluminescence light. The scintillation pulse shape, as well as ionization to scintillation ratio, provides PID between nuclear recoils (NR), which comes from WIMP, and electronic recoils (ER), which mainly comes from ^{39}Ar radioactive isotope in argon. The PID capability is so high that several liquid argon experiments have searched for WIMP with mass above a few tens of GeV/c^2 under "background-free" condition.

Concerning the lower mass region, the direct detection becomes more challenging because of small signal yield and lack of understanding about liquid argon response. There are two approaches for the WIMP detection. One is the same as for the high mass WIMP; maximizing the detector sensitivity and seeking NR events. Previous study finds that the maximum sensitivity is achieved by switching off electric field inside the fiducial volume and using only the scintillation signal instead of both scintillation

and ionization signals. Precise measurement of low-energy scintillation response for ER is essential to suppress systematic uncertainty on ER contamination and push down energy threshold. The other approach uses only ionization signal. Owing to the electroluminescence process, the detector is more sensitive to single electron than single photon. Therefore, a search for extra events over the background prediction in the ionization signal spectrum has the sensitivity for the lower-mass WIMP. It is natural to assume that higher electric field results in lower energy threshold by enhancing the ionization yield. Measuring the response under such a high field is need to confirm the assumption.

This dissertation focuses on the direct detection of low-mass WIMP using LAr scintillation detector. Primary target of this study is to test WIMP with mass around 10 GeV/c^2 and WIMP-nucleon cross section around 10^{-41} cm^2, where an indication of WIMP signal have been reported by a direct detection experiment. The dissertation hereafter is organized as follows. Chapter 2 overviews the dark matter evidence and its nature to be satisfied, following the introduction of the Standard Model of particle physics which misses the dark matter candidate. We also introduce WIMP as a promoting candidate. Chapter 3 describes how LAr scintillation detector works as a WIMP search detector. The experimental apparatus and particular detectors used in this study is given in Chapter 4. Then Chapter 5 is the measurement of the LAr response for NR and its parametrization, which is one of the main topic in this dissertation. We present a functional modeling of LAr response under electric fields, along with the experimental setup and analysis procedure. Chapter 6 dedicates the measurement of the ER response, another topic of this dissertation. Detail of the single-phase detector and calibration sources used in this study is shown. This is followed by discussion on the energy dependence of the scintillation yields down to 2.8 keV at null field. We give an interpretation of the result. Based on the measurements in Chapters 5 and 6 and our best knowledge, a physics run is performed, intending to search for WIMP under background-free condition. Chapter 7 gives the measurement and result of this physics run. In Chapter 8, we discuss the result from the physics run and future prospect of the WIMP search using LAr detector. Finally, this dissertation is concluded in Chapter 9.

Chapter 2

Dark matter

The evidence of the existence of dark matter is accumulated over the past century, yet all of them rely on gravitational effect. Recent observation of Cosmic Microwave Background (CMB) shows the universe is roughly 68% dark energy, 27% dark matter, and only 5% ordinary matter. According to numerous studies to unveil the nature of the dark matter, it is likely to consist of particles, yet missing from the Standard Model of particle physics.

There is a number of particle dark matter candidates, of which leading candidate is WIMP or Weakly Interacting Massive Particle. It is amenable to direct detection on a detector through WIMP-nucleon scattering process. A number of experiments are searching for WIMP using a variety of detection techniques. The nature that WIMP are non-relativistic and almost non-collisional requires the detector to be sensitive to low energy rare events (typically less than 100 keV with less than 10^{-3} events/day/kg).

In this chapter we briefly discuss the nature of dark matter, and introduce WIMP as one of the promoting candidate of dark matter.

2.1 The Standard Model of particle physics

To date, the most rigorous theory in the field of elementary particle physics is the quantum field theory, so-called the Standard Model (SM). The SM consists of twelve fermion fields (six quarks and six leptons), and the interactions between them are required to be the local gauge invariance $SU(3) \times SU(2) \times U(1)$. The $SU(3)$ gauge symmetry owes the strong interaction propagated by gluon, while the $SU(2) \times U(1)$ the electroweak interaction by photon and W and Z bosons. A Lagrangian density is symbolically described by

$$\mathcal{L}_{\mathrm{SM}} = -\frac{1}{4} F_{\mu\nu} F^{\mu\nu} + \bar{\psi}(i\gamma^{\mu} D_{\mu}\psi) + y_{ij}\bar{\psi}_i \psi_j \phi + h.c. + |D_{\mu}\phi|^2 + V(\phi) \tag{2.1}$$

where $F^a_{\mu\nu}$ is the field strength ($F^a_{\mu\nu} = \partial_\mu A^a_\nu - \partial_\nu A^a_\mu + g f^{abc} A^b_\mu A^c_\nu$ with gauge field A, the coupling constant of the particular gauge group g and the structure constant of the particular gauge group f^{abc}), ψ and ϕ are the fermion and scalar (Higgs) fields respectively, γ^μ is the matrix representation of the Clifford algebra, D_μ is the covariance derivative ($D_\mu = \partial_\mu - igA^a_\mu T^a$ with the representation matrices T^a), y_{ij} is the Yukawa coupling constant, $V(\phi)$ is the Higgs potential, and $h.c.$ stands for the Hermitian conjugate.

Tables 2.1 and 2.2 summarize the elementary particles of the SM. The $SU(3)$ triplet (color triplet) fermions are called quarks, and singlet fermions are called leptons. Left-handed (right-handed) fermions constitute $SU(2)$ doublets (singlets). The masses of the fermions and bosons are generated by the Higgs mechanism. All of the SM particles have already been observed experimentally.

The SM has successfully proved huge experimental predictions up to around the electroweak scale. However, several phenomena remain unexplained and therefore it is not considered as the complete theory of our universe. One of the most important problem of the SM is that there is no candidate particle of the dark matter. In other words, revealing the nature of dark matter itself allows to unveil the physics beyond the SM.

Table 2.1. A list of the elementary particles of the SM[1]. The columns of J, Q, M, and $SU(3)$ stand for spin, electric charge, mass, and color charge, respectively.

Field	J	Q	M [MeV]	$SU(3)$	Field	J	Q	M [MeV]	$SU(3)$
u	$\frac{1}{2}$	$+\frac{2}{3}$	2.16	3	ν_e	$\frac{1}{2}$	0	$<1.1\times10^{-6\dagger}$	1
d	$\frac{1}{2}$	$-\frac{1}{3}$	4.67	3	e	$\frac{1}{2}$	-1	0.511	1
c	$\frac{1}{2}$	$+\frac{2}{3}$	1.27×10^{3}	3	ν_μ	$\frac{1}{2}$	0	$<0.19^{\dagger}$	1
s	$\frac{1}{2}$	$-\frac{1}{3}$	93	3	μ	$\frac{1}{2}$	-1	105.7	1
t	$\frac{1}{2}$	$+\frac{2}{3}$	172.76×10^{3}	3	ν_τ	$\frac{1}{2}$	0	$<18.2^{\ddagger}$	1
b	$\frac{1}{2}$	$-\frac{1}{3}$	4.18×10^{3}	3	τ	$\frac{1}{2}$	-1	1776.86	1

Field	J	Q	M [MeV]	$SU(3)$	Field	J	Q	M [MeV]	$SU(3)$
γ	1	0	0	1	H^0	0	0	125.10×10^{3}	1
g	1	0	0	8					
$W^{\pm}$	1	±1	80.379×10^{3}	1					
Z	1	0	91.19×10^{3}	1					

† 90% confidence level.

‡ 95% confidence level.

Table 2.2. The hyper charge Y of the SM particles. The subscription L (R) stands for the left-handed (right-handed).

$SU(2)$	Field	Y
2	$\begin{pmatrix} u_L \\ d_L \end{pmatrix}, \begin{pmatrix} c_L \\ s_L \end{pmatrix}, \begin{pmatrix} t_L \\ b_L \end{pmatrix}$	$+\frac{1}{3}$
1	u_R, c_R, t_R	$+\frac{4}{3}$
1	d_R, s_R, b_R	$-\frac{2}{3}$
2	$\begin{pmatrix} \nu_{eL} \\ e_L \end{pmatrix}, \begin{pmatrix} \nu_{\mu L} \\ \mu_L \end{pmatrix}, \begin{pmatrix} \nu_{\tau L} \\ \tau_L \end{pmatrix}$	-1
1	e_R, μ_R, τ_R	-2

2.2 Dark matter evidence

The existence of dark matter in the universe is confirmed by a number of astrophysical and cosmological observations at all scale, from cosmological to single galaxies. Historically, dark matter was introduced by F.Zwicky in the 1930s for the first time[2]. While observing the Coma galaxy cluster, he found that the gravitational mass estimated by velocity dispersion of the objects was surprisingly hundreds times larger than the luminous mass based on the visible objects. In the 1970s, more robust indication of dark mass was came by V.Rubin and K.Ford[3]. They measured the rotation curves of the Andromeda Galaxy via Doppler shift of spectral signature and discovered the flat rotation curve. This could be explained by invisible mass extending beyond the stars and gas clouds. In the years since, numerous experimental observations and theoretical calculations have supported the existence of dark matter, while all relying on gravitational effect.

Galactic scale Measurements of rotation curves of spiral galaxies give an amount of dark matter within the galaxies. Based on Newtonian dynamics, the rotation speed $v(r)$ as a function of galactocentric radius r is given by $v(r) = \sqrt{GM(r)/r}$ where $M(r)$ is the mass contained within the radius. Figure 2.1 shows the measured rotation curve[4]. The curve in the figure is observed to remain constant out to large distance above a few kpc (or "flat curve"), meaning $M(r) \propto r$. This conflicts with the optical observation and Kepler's law which expects almost $v(r) \propto 1/\sqrt{r}$, and implies the existence of nonvisible mass.

Another approach other than relying on the luminous matter uses gravitational lensing effect. Light from a background galaxy is bent as it travels around the foreground galaxy where space-time field is distorted by massive objects and acts as an optical lens. The deflection allows us to evaluate the mass distribution of the foreground objects. Observations of background galaxies with telescopes have found dark matter halo around galaxies[5].

Observation of colliding galaxy clusters via gravitational lensing effect is a direct evidence of dark matter. Figure 2.2 shows an image of the Bullet cluster, on which x-ray emission taken by the x-ray telescope and gravitational potential mapped out with gravitational lensing are overlaid with pink and blue colors, respectively[6]. It finds that most of luminous matter (intracluster plasma) concentrates on the collision region and, controversially, the gravitational mass resides in the outer region. The discrepancy between the luminous intracluster matter, which by far dominates baryonic mass of the cluster and slows down by interactions among the collision, and the total mass distribution, which passes through each other and traces the distribution of galaxies, is a strong evidence of dark matter independent on the Newtonian gravity.

Cosmological scale Interestingly, dark matter introduced in the galactic observations is also required from observations on cosmological scale and evolution of the universe. Fluctuations of CMB is a strong evidence of the existence of dark matter. The CMB light comes to us from the epoch of recombination when the universe is about 380,000 years old and is a nearly (at 10^{-5} level) isotropic black body radiation with 2.726 K. The tiny temperature anisotropies of the CMB are originated from the nonuniformity in

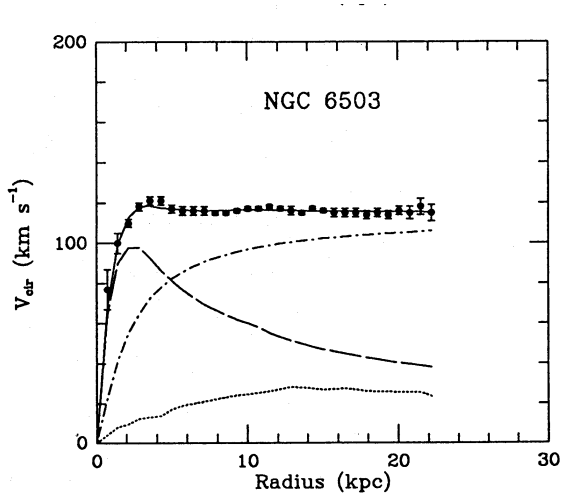

Fig. 2.1. Rotation curve for the galaxy NGC6503 (circular points), showing the need of dark halo (dot-dashed line) in addition to the luminous disk (dashed line) and gas (dot line). The figure is taken from Ref. [4].

Fig. 2.2. Image of the colliding galaxy clusters (the bullet cluster, 1E 0657-56). The pink color represents the x-ray emission from the Chandra X-Ray Observatory, and the blue color represents the mass distribution from the lensing map. The figure is taken from Ref. [7].

the density at that time. The fluctuations in (θ, ϕ) direction $\delta T/T(\theta, \phi)$ are expressed by the so-called angular power spectrum C_l defined as

$$\frac{\delta T}{T}(\theta, \phi) = \sum_{l=0}^{\infty} \sum_{m=-l}^{l} a_{lm} Y_{lm}(\theta, \phi), \tag{2.2}$$

$$C_l \equiv \langle a_{lm} \rangle = \frac{1}{2l+1} \sum_{m=-l}^{l} |a_{lm}|^2, \tag{2.3}$$

where Y_{lm} is the function of spherical harmonics. Figure 2.3 shows the power spectrum observed by the Planck satellite[8]. A particular cosmological model –the Λ-CDM model– explains the spectrum with only six parameters. The model is based on Friedman equation and assumes a flat universe with dark energy. According to the model, Baryon Acoustic Oscillation (BAO) triggered by gravitational potential wells appears in the angular spectrum. The gravitational potential wells is caused by fluctuations of non-baryonic matter density, so the BAO depends on baryon and matter densities. The best fit parameters give baryon density $\Omega_b = 0.049$, cold (i.e. non-relativistic) dark matter density $\Omega_{CDM} = 0.266$, and dark energy density $\Omega_\Lambda = 0.685$.

Galaxies in the universe exhibit a vast foam-like distribution, known as the Large-Scale Structure (LSS), and the formation of this structure needs dark matter. The LSS is originated from the sufficient perturbations in matter density. Perturbations can only grow to create the structure after the recombination epoch, however, that measured from the CMB anisotropy is much smaller than the expectation at this epoch ($\sim 10^{-2}$). A non-baryonic dark matter solves this problem: contrary to the ordinary matter which couples to photons before the recombination, dark matter lets the structure formation start prior to recombination, which becomes a seed of the structure formation. This description is also confirmed by N-body calcula-

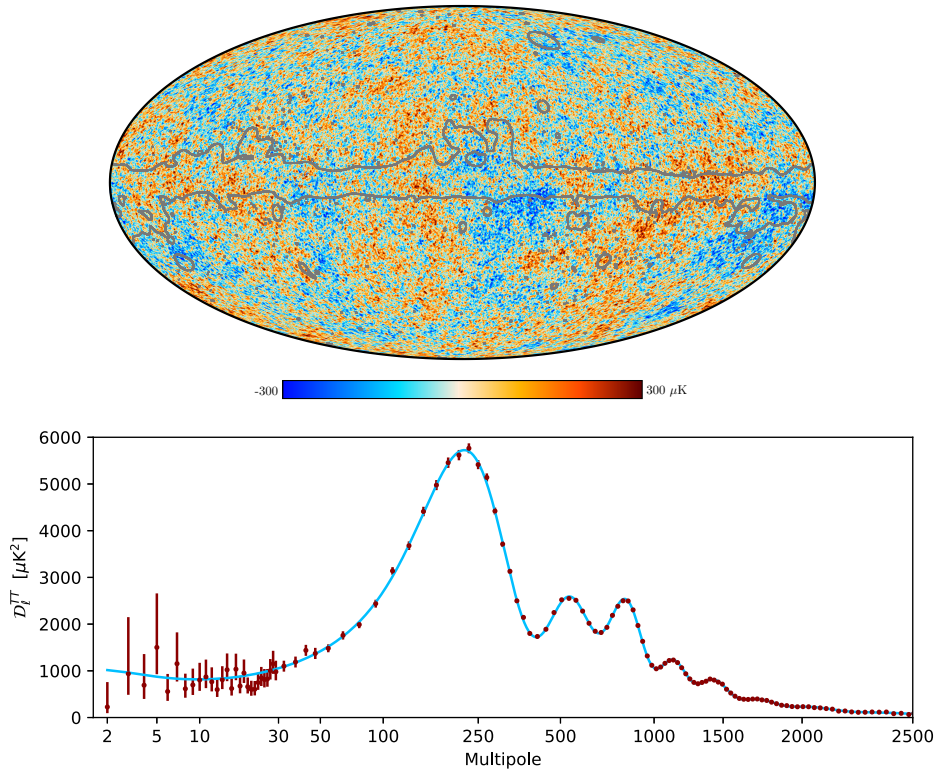

Fig. 2.3. All-sky map of the CMB temperature anisotropies (top) and its angular power spectrum as a function of multipole l (bottom) observed by Planck satellite. The blue line is the best fit model (the Λ-CDM model). Figures are taken from Ref. [9].

tions, as well as observations of far galaxies. The N-body calculation indicates that dark matter should be cold, or the observed structure would not be formed.

2.3 Candidate

2.3.1 Overview

Despite of the significant evidences of the existence of dark matter in the universe, the nature of it remains unknown. Dark matter candidates need to satisfy several criteria to match the observations. They should be electromagnetically neutral and color-singlet; they should interact very weakly at all with ordinal matter and themselves; they should be stable on at least cosmological timescale; and they should be cold (i.e. non-relativistic). There are many proposed candidates such as massive stellar objects, modification of the theory of gravity, and elementary particles. Currently, the particle dark matter is one of the most favorable scenario, as the other candidates have been constrained strongly from various observations. None of the particles in the SM satisfy the criteria, therefore it must be introduced from a theory beyond the SM.

2.3.2 The case for Weakly Interacting Massive Particle

A leading candidate for the particle dark matter is WIMP. It is a hypothetical massive particle typically in GeV/c^2 to TeV/c^2 range and interacts with ordinary matter at or below the weak scale. The most attractive and important feature of WIMP is that it naturally explains the relic density of dark matter in the current universe. We assume WIMP can annihilate to the ordinal SM particle (Fig. 2.5). In the early universe, the temperature is enough high that massive WIMP χ and ordinal SM particles q are in thermal equilibrium ($\chi\chi \rightleftharpoons qq$). The time evolution of the WIMP number density n_χ is governed by the Boltzmann equation,

$$\frac{d}{dt}n_\chi = -3Hn_\chi - \langle\sigma_{ann}v\rangle(n_\chi^2 - n_{\chi,eq}^2), \tag{2.4}$$

where H is the Hubble constant, $\langle\sigma_{ann}v\rangle$ is the thermally averaged annihilation cross section, and $n_{\chi,eq}$ is the co-moving number density in thermal equilibrium. As the universe expands and gets cool, WIMP production ceases because the SM particle no longer has enough energy for WIMP pair-production. WIMP annihilation will also cease because they get too sparse to interact. After this, the number density in a co-moving volume is approximately "freezed-out" until today, as shown in Fig. 2.4. Current WIMP density is numerically calculated from Eq.(2.4) as

$$\Omega_\chi \simeq 0.2\left(\frac{1\text{ pb}\cdot c}{\langle\sigma_{ann}v\rangle}\right). \tag{2.5}$$

Let us consider an electroweak scale particle, roughly $m_\chi \simeq 100$ GeV/c^2 mass and $\alpha \simeq 0.01$ coupling constant. This leads to $\langle\sigma_{ann}v\rangle \sim \alpha^2/m_\chi^2 \sim 1$ pb, and then beautifully agrees with the observed relic density $\Omega_\chi \simeq 0.27$, which is often referred to as "WIMP miracle".

From a field-theoretical point of view, WIMP is particularly attractive because such particle is naturally given by the Supersymmetric model (SUSY). The SUSY introduces an additional symmetry between fermion and boson and generates super-partner particles whose spins are only $1/2$ different from their SM partner. It is one of the most promising theory beyond the SM motivated to solve the hierarchy problem in the SM [1)]. The lightest SUSY particle (LSP) is stable, and in some SUSY parameter space, LSP is neutralino which is a mixture of the superpartner of the electro-neutral bosons. As the neutralino satisfies all the criteria, it is WIMP candidate.

2.3.3 Non-WIMP particle dark matter

Axion is a hypothetical Nambu-Goldstone boson. It is given by spontaneous breaking of a new global $U(1)$ symmetry which is introduced to solve the so-called strong-CP problem of the SM [2)]. Among large parameter space of masses and couplings, axion with mass between 1 μeV and 1 meV is a viable cold dark matter candidate. In some scenario, it can couple to photon via axio-electric effect, which is an analogy of photoelectric effect. It also can couple to two photons, which results to the conversion of

[1)] The hierarchy problem is that the nature has two very different scales, the electroweak scale (10^2 GeV) and the Planck scale (10^{19} GeV).

[2)] The strong-CP problem is that the strong force does not violate CP but the SM does not have any mechanism to conserve the CP and thus need a fine tuning.

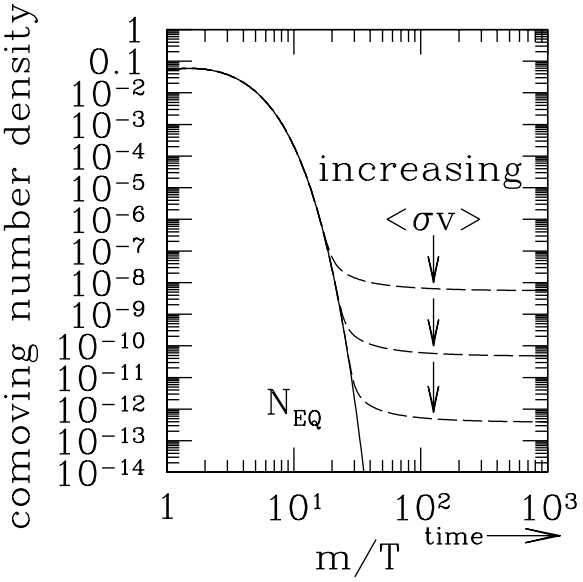

Fig. 2.4. Time evolution of a typical WIMP comoving number density in the early universe. Larger thermally averaged annihilation cross section $\langle \sigma v \rangle$ results in smaller relic density. The figure is taken from Ref. [10].

axion to photon in the presence of magnetic field. There are experiments focusing on dark matter axion (e.g. [11]) and analyses searching for the axion signal in the dataset originally focused on WIMP (e.g. [12, 13]). However, currently no indication have been found and constrains on the parameter space are obtained.

Neutrino is also a viable candidate of dark matter if it has enough mass and moves slow enough to form the LSS. The three kinds of neutrino in the SM, ν_e, ν_μ, and ν_τ, are too hot to be dark matter. However, other neutrino is the candidate if it is given by an extension of the SM to add right-handed chirality one. The new neutrino, often referred to as sterile neutrino, can be produced and interact via mixing with the active neutrinos. It also can decay to the active neutrino and photon. Searches for sterile neutrino and sterile neutrino-induced γ-ray are conducted over the world, however, there are no solid evidence for its existence[14, 15].

2.4 Searches for WIMP dark matter

2.4.1 Overview

One can detect WIMP via three interactions with the SM particle: annihilation, pair production, and scattering. All of them are equivalent in time-space as represented in Fig. 2.5. The annihilation process is used in indirect searches which seeks extra particles in cosmic-ray originated from the process. The pair-production process is what collider experiments uses. They try to create WIMP and detect it by colliding high-energy SM particles. The scattering process is what searched for by direct detection experiments. These three methods are complement to each other, and thus it is important to approach

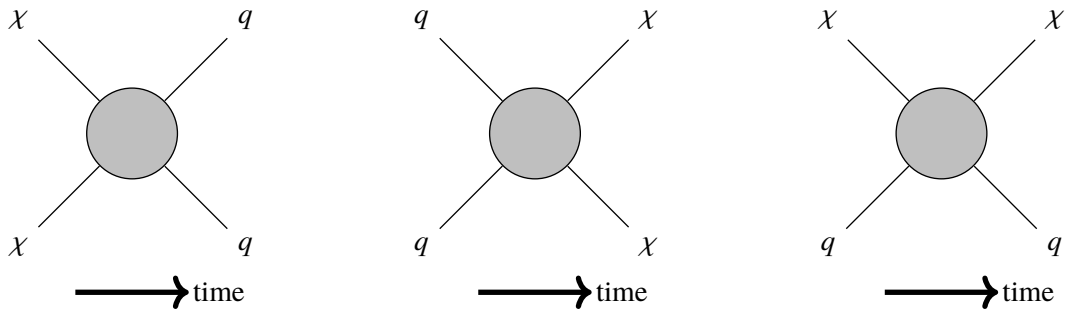

(a) Annihilation. (b) Pair production. (c) Scattering.

Fig. 2.5. Feynman diagrams showing interactions used in (a) indirect, (b) collider, and (c) direct WIMP searches.

WIMP through all the three ways.

Since this dissertation describes a direct detection experiment, we discuss it more detail below.

2.4.2 Direct search

Direct WIMP detection experiment seeks a tiny and rare signal derived from a recoiling nuclei in a detector on Earth. The signal is in the form of light, charge, or heat, and one reconstructs recoiling energy and/or direction from the observables, depending on the detector technology. The interaction between WIMP and nuclei is possibly a simple elastic scattering. Let us consider WIMP with mass $m_\chi = 100$ GeV$/c^2$ and relative velocity of $v = 200$ km/s. The energy of nuclei scattered off by WIMP E_R is then given by

$$E_R = \frac{\mu_\chi^2 v^2 (1 - \cos\theta)}{m_N}, \text{ where } \mu_\chi = \frac{m_\chi m_N}{m_\chi + m_N}. \tag{2.6}$$

where m_N is the target nuclei mass. In case of argon ($m_N \simeq 40$ GeV$/c^2$), for example, $E_R \simeq 20$ keV is obtained.

The WIMP event rate is expected as follows. Dark matter is distributed over the universe, and the Milky Way is also surrounded by dark matter halo. The local dark matter density ρ_0 is approximately 0.3 GeV$/c^2$/cm^3. Let us assume the simple model, so-called Standard Halo Model (SHM), where the dark matter is isotropic and velocity distribution of it is a Maxwellian-Boltzmann distribution with the most probable speed v_0 in the galactic rest frame. The differential recoil rate per unit detector mass, given in units of events/kg/day/keV, is written as

$$\frac{dR}{dE_R} = \frac{N_A}{A_T} n_\chi \int dv v f(v) \frac{d\sigma}{dE_R}(E_R, v), \tag{2.7}$$

where N_A is the Avogadro's number, and A_T is the atomic mass of the target. The $f(v)$ is the dark matter velocity distribution on Earth (on the Solar System) which rotates the Milky Way Galaxy with a velocity

$v_\odot$. If we assume an isotropic scattering cross section, it is then

$$\frac{dR}{dE_R} = \frac{N_A}{A_T}\frac{\sigma(q)\rho_\chi}{2\mu_\chi^2 m_\chi}\int_{v_{min}}^{v_{max}} dv \frac{f(v)}{v} \tag{2.8}$$

where $\sigma(q)$ is the cross section as a function of the nucleus recoil momentum q, $v_{min} = \sqrt{m_N E_R/2\mu_\chi^2}$ is the minimum WIMP velocity to generate the recoil energy E_R, and v_{max} is the maximum velocity constrained by an escape velocity of the SHM. The cross section is split into two parts as

$$\sigma(q) = \sigma_0 F^2(q), \tag{2.9}$$

where σ_0 is the cross section at zero momentum transfer and $F(q)$ is a nuclear form factor. The form factor accounts for an effect from a finite nucleus size and falls down the cross section when the de Broglie wavelength of the momentum transfer is no longer negligible compared to the nuclei size. The cross section has two terms of interactions, spin-independent (SI) and spin-dependent (SD). We only focus on SI interaction here because total nuclear spin of ^{40}Ar is zero. The SI cross section is written as

$$\sigma_0 = \sigma_n \left(Z\frac{f_p}{f_n} + (A-Z)\right)^2 \frac{\mu_\chi^2}{\mu_n^2}, \text{ where } \mu_n = \frac{m_n m_\chi}{m_n + m_\chi}, \tag{2.10}$$

where σ_n is the WIMP-nucleon cross section, f_p and f_n are the WIMP couplings to proton and neutron, respectively, and A and Z are the mass and atomic numbers of the target nuclei. With $f_p = f_n$, which is a typical assumption, the event rate is finally given by

$$\frac{dR}{dE_R} = \frac{N_A}{A_T}\frac{\sigma_n\rho_\chi}{2\mu_\chi^2 m_\chi}A^2\int_{v_{min}}^{v_{max}} dv \frac{f(v)}{v}. \tag{2.11}$$

The values typically used in this community are $v_0 = 220$ km/s, $v_\odot = 230$ km/s, $\rho_\chi = 0.3$ GeV/c^2, and $v_{max} = 544$ km/s. Then total event rate is expressed as[16, 17]

$$R = \frac{361}{m_\chi m_N}\left(\frac{\sigma_n}{1\text{ pb}}\right)\left(\frac{\rho_\chi}{0.3\text{ GeV}/c^2}\right)\left(\frac{v_0}{220\text{ km/s}}\right)\text{ [events/day/kg]}. \tag{2.12}$$

The left panel of Fig. 2.6 shows the differential event rate for several WIMP masses at a cross section of $\sigma_n = 1.0\times10^{-41}$ cm^2 for argon target. The event rate falls quickly as the recoil energy increases, in particular, for low mass ($\lesssim$10 GeV/c^2) WIMP. Thanks to its small atomic number, the spectra for argon targets shows relatively high end point, as demonstrated in right panel of Fig. 2.6. Naively, lower atomic number nuclei target gets more recoiling energy for the low-mass WIMP and thus is sensitive to lower-mass region.

Consequently, key techniques of this experiments are detection capability of the low energy signal and development of ultra-low background event rate.

Experimental methods of the direct search There are three experimental techniques to search for WIMP signal. The simplest and most common way is to search for the nuclear recoils (NR) events

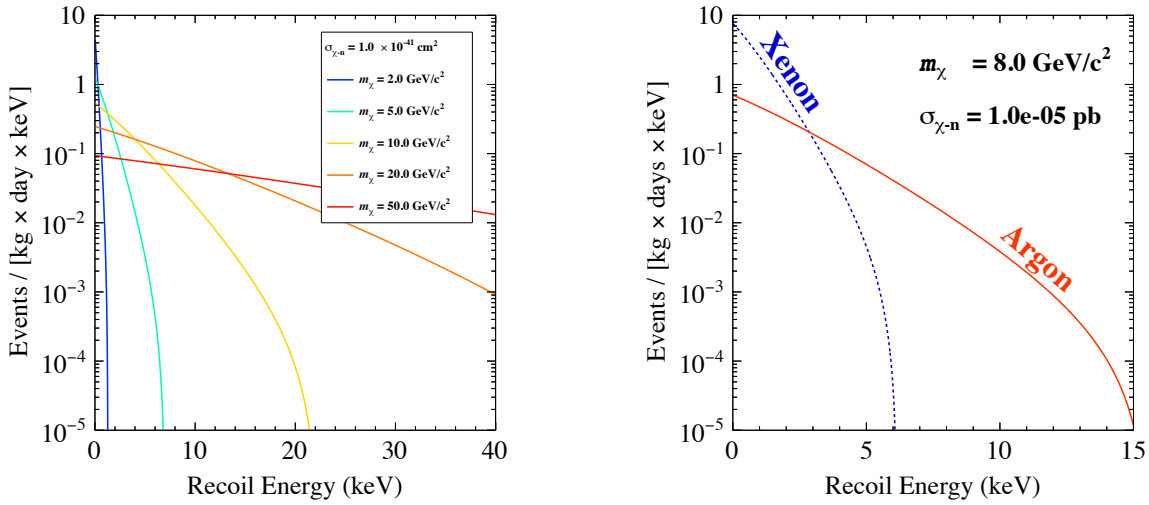

Fig. 2.6. Left: expected recoil energy spectra for several WIMP masses for argon target. Right: the spectra for 8 GeV/c^2 WIMP for argon and xenon targets.

excess over the background prediction. Recoil energy spectrum of the NR signal will support the WIMP detection, as well as constrain the WIMP mass and cross section. Main challenge of these experiments are to very strongly reduce background events, such as NR from ambient fast neutron and electronic recoils (ER) from γ-ray from radioactive isotopes. The other two ways depend on galactic motions. One is to observe annual modulation of dark matter signal statistically. This is based on the fact that the relative velocity of a detector on Earth and dark matter halo in the galaxy modulates annually due to the Earth's revolution. The dark matter signal rate is expected to show peak in June and bottom in December. The other way tries to detect recoiling nuclei direction to confirm the WIMP signal. Since the Solar System goes toward the constellation Cygnus, the "dark matter wind" seems to blow Earth from the Cygnus so that the observed direction of WIMP signal should be biased to the opposite direction of the Cygnus.

2.4.3 Review of direct search experiments

A number of direct WIMP searches have been performed using a variety of target materials and detector technologies. Figure 2.7 shows the current status of direct detection experiments in WIMP mass and WIMP-nucleus cross section plain, assuming dark matter is made of WIMP. Past, current, and future direct detection experiments are summarized in Table 2.3.

Currently, no WIMP signal have yet been observed above a few tens of GeV/c^2. Double-phase xenon detectors, such as XENON, LUX-ZEPLIN, and Panda-X, set the most constraining exclusion limit in this region. The detector consists of liquid phase and gaseous phase, and observes light and charge signals from an interaction occurred in the liquid phase. The detector offers ER background rejection using the light and charge ratio, as well as good self-shielding against external γ-rays. These experiments plan to improve their sensitivity within next two decades to the neutrino floor with an effort to grow up their detector size up to tens of tonne of target mass. Following them is the liquid argon detector, namely

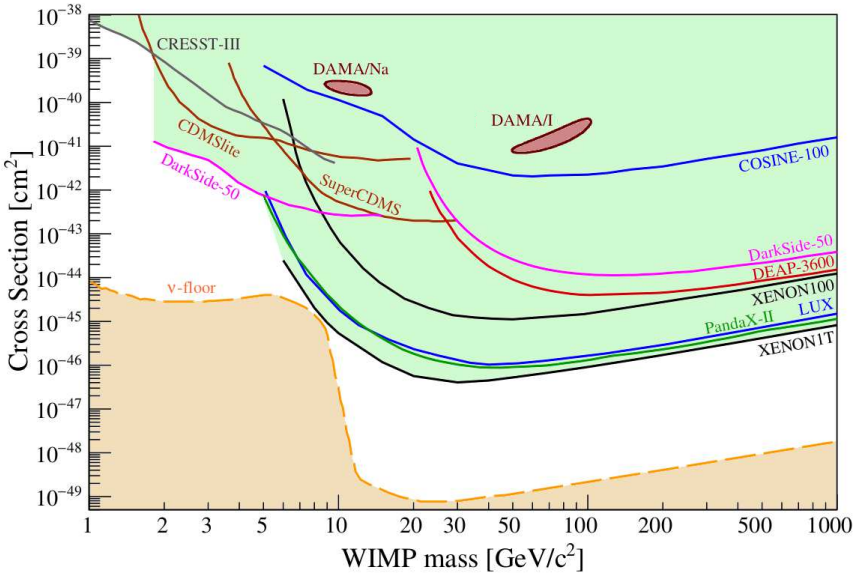

Fig. 2.7. A complication of direct detection experiments on WIMP mass and cross section parameter space. The solid curves are the 90% upper limit from each experiments, and the two contours are the interpretation of DAMA annual modulation signature. The dashed curve represents an approximate limit of the sensitivity of direct detection experiments where irreducible background from solar, atmospheric, and diffuse supernova neutrinos elastic scattering (CEvNS) events will be seen (neutrino floor). Original figure is taken from Ref. [18].

DarkSide and DEAP. It detects light or light and charge signals from an energy deposition in liquid argon. As will be described in the following chapters, ER events are strongly rejected by pulse-shape discrimination (PSD) technique. There are also plans to grow up the detector size up to hundreds of tonne to reach the neutrino-floor.

In the low mass region around 10 GeV/c^2, some tension exist between experimental results. DAMA/LIBRA experiment have claimed the observation of dark matter annual modulation signal. They use high-purity NaI crystal scintillator which does not discriminate NR and ER events, and operate it over more than twenty years. The modulation signal is consistent to the SHM dark matter, and one can interpret it as due to WIMP with mass of about 10 GeV/c^2 and the cross section of 10^{-40} cm^2, as represented with contours in Fig. 2.7. However, none of many other experiments have confirmed such WIMP in spite of their higher sensitivity, as represented with exclusion curves in Fig. 2.7. The DarkSide experiment currently set the most stringent limit in a few GeV/c^2 region by search for a few electron signal excess over the background prediction. In this search, the DarkSide group has achieved enough low threshold by using only charge signal; they analysis both NR and ER events inclusively, in contrast to the searches for the high-mass WIMP which discriminates ER event owing to both scintillation and ionization signals. To confirm or refuse the 10 GeV/c^2 WIMP scenario, it is important to test the signal using variety of experimental methods and target materials at different experimental sites.

As well as the high-mass region, several plans to search for low-mass WIMP around the neutrino-floor have proposed. There are two approaches toward the WIMP detection: one is to measure the energy

spectrum and search for the difference from the background prediction, and the other is to search for single or small number of WIMP-candidate events. Generally, the former approach is more appropriate to exclude the parameter space because it is easier to push down energy threshold and earn detector exposure from an experimental point of view. However, it will face difficulty to claim discovery once they observe an excess, because the WIMP signal is expected to show exponential-like spectrum which can be easily mimicked by other sources. The latter approach is more difficult to expand the exclusion limit, on the other hand, it has more potential to claim the discovery simply because the expected background event rate is so small. Both approaches are important to discover WIMP and identify its nature.

Table 2.3. Summary of past and future direct WIMP detection experiments.

Experiment	Target	Fiducial [kg]	Detection technology	$\sigma_{\chi-n}$ [cm^2]	m_χ [GeV/c^2]	Site	Ref.
Results from past experiments							
XENON1T	Xe	1042	DP-LNG[a]	4.1×10^{-47}	30	LNGS	[19]
PandaX-II	Xe	364	DP-LNG	8.6×10^{-47}	40	CJPL	[20]
LUX	Xe	118	DP-LNG	1.1×10^{-46}	50	SURF	[21]
XMASS	Xe	97	SP-LNG[b]	2.2×10^{-44}	60	Kamioka	[22]
DEAP3600	Ar	2000	SP-LNG	3.9×10^{-45}	100	SNOLAB	[23]
DarkSide-50	Ar	46	DP-LNG	1.14×10^{-44}	100	LNGS	[24]
XENON1T (charge only)	Xe	1042	DP-LNG	3.6×10^{-41}	3	LNGS	[25]
DarkSide-50 (charge only)	Ar	20	DP-LNG	1×10^{-41}	2	LNGS	[26]
CDMSLite	Ge	0.6	Bolometer	2×10^{-40}	2	Soudan	[27]
CRESST-III	O	0.024	Bolometer[c]	1×10^{-39}	2	LNGS	[28]
NEWS-G	Ne	0.3	Gas SPC[d]	1×10^{-38}	2	LSM	[29]
DAMA	NaI	250	Scintillator	-	-	LNGS	[30]
COSINE100	NaI	106	Scintillator	1.14×10^{-40}	10	Y2L	[31, 32]
Future experiments with expected sensitivity							
XENONnT	Xe	4000	DP-LNG	1.4×10^{-48}	50	LNGS	[33]
PandaX-4T	Xe	2800	DP-LNG	6×10^{-48}	40	CJPL	[34]
LZ	Xe	5600	DP-LNG	1.4×10^{-48}	40	SURF	[35]
DarkSide-20k	Ar	20000	DP-LNG	1.2×10^{-47}	1000	LNGS	[36]
DARWIN	Xe	30000	DP-LNG	2.5×10^{-49}	40	(TBD)	[37]
ARGO	Ar	300000	LNG	$\sim 10^{-49}$	1000	SNOLAB	[38]

[a] double-phase liquid noble gas detector.

[b] single-phase liquid noble gas detector.

[c] $CaWO_4$ crystal detector.

[d] Ne + CH_4 gas sphere proportional counter.

CHAPTER 3

Liquid argon scintillation detector

Liquid argon has several features that make it attractive as particle detection medium. Primarily, it works as a highly efficient scintillator: its scintillation and ionization yields are high (approximately 50 photons or electrons per energy deposition of keV), and it is transparent to its own light. Pulse shape of the primary scintillation provides powerful particle identification (PID) capability, which gives an advantage for rare event search such as dark matter observations. The noble liquid medium offers more advantages; it can enclose a large amount of target mass, it can be scaled up with arbitrary detector shape, and it can easily be chemically purified. In addition, since argon is the third most abundant component in the atmosphere, it is cheaply available in large amounts as a byproduct of oxygen production in industry. This benefit leads quick and flexible detector development, construction and operation and a lot of application for experiments other than direct WIMP search.

In this chapter we describe the liquid argon scintillation detector as a detection technique of WIMP. We summarize the physics property of argon, and then explain how the detector works as a particle detector. Operation principles of the single-phase (liquid) type and double-phase (liquid and gaseous) type detectors are discussed. Following this, the PID capability of these detectors and background sources in the dark matter search are discussed. An excellent PID capability of the detector allows us to discriminate the majority of background sources and to perform a background free WIMP search.

3.1 Liquid argon

Liquid argon is a promising detector medium because of its high scintillation and ionization signal yields, fast response, huge PID capability, radiation tolerance, and availability. Physics properties of liquid argon is summarized in Table 3.1. From a technical point of view, operation at relatively low temperature (~90 K) suppresses outgassing from material surface, inhibits the amount of dissolved impurities, and reduces thermal noise of photo-detector, at the expense of relatively small gap of operation temperature (~3 K). LAr-based detectors are widely used in past and future particle physics experiments such as ICARUS (neutrino detector), ATLAS (calorimeter for proton-proton collider), GERDA (veto for $0\nu\beta\beta$ search), DUNE (neutrino and proton decay detector), and GRAMS (γ-ray and anti-matter detector on balloon/satellite).

It is also used in WIMP search such as DarkSide, DEAP, and future huge WIMP search (GADMC).

Why argon is used for WIMP searches? The high signal yields and PID capability of the liquid argon detector satisfy the basic requirement for WIMP search. As shown below, liquid argon detector has

Table 3.1. Physics properties of argon [39].

Atomic number	18
Mass number	39.948
Liquid density	1.399 g/cm^3
Boiling point at 1 atm	87.3 K
Melting point	83.8 K
Concentration in air	9340 ppm
Stable isotope (abundance in air)	^{36}Ar (0.0034), ^{38}Ar (0.0006), ^{40}Ar (0.9960)

capability of searching WIMP signal in zero background condition, which is a crucial requirement for WIMP discovery. In addition, recoil energy of argon nuclei for O(1–10) GeV/c^2-WIMP scattering is relatively high simply because it has small atomic mass. Furthermore, liquid argon detector can confirm the experimental results complementary to other WIMP experiments in both high-mass (with liquid xenon (LXe) detector) and low-mass (with silicon or germanium detectors) regions. Thanks to the fact that large amount of argon is cheaply available, it would be also possible to conduct simultaneous measurement in various experimental sites.

3.2 Interaction of particles in liquid argon

3.2.1 Overview

A particle interacting with liquid argon generates scintillation photon and ionization electron via excitation, ionization, collision, and recombination processes. Figure 3.1 shows the diagram of the conversion process. The energy of the energetic particle is transferred to produce quanta, that is, to raise an electron to a higher energy state or to liberate an electron from the atom, producing an exciton Ar^* and electron-ion pair Ar^+-e^-, respectively. The exciton, either formed by the energy transfer directly or by the recombination process, relaxes producing scintillation photon called primary scintillation or *S1*. When the active volume is subjected to an electric field, a fraction of ionization electrons escapes recombination and drifts along the field. As described in Section 3.2.6, these electrons can be extracted to the gaseous phase above liquid where they produce electroluminescence photon called secondary scintillation or *S2*.

While almost all of the deposit energy from ER is converted to the observable channels, more than half of the deposited energy from NR is consumed to the heat channel which is not detectable in the scintillation detectors[40]. As mentioned before, the energy transfer from WIMP to nucleus in their scattering is tiny, say 100 keV; the recoiled ion is so slow that it can be effectively regarded to remain almost neutral. The nuclear loses its energy by scattering off other nuclei, as illustrated in Fig. 3.2. While the elastic scattering is the dominant process in its path, occasionally the atom leads inelastic scattering to excite or ionize either (or both) of the concerned atoms. Both the scattering and scattered atoms continue to their travels and again cause the elastic or inelastic process. The excitation or ionization is induced only if the recoiling atom has sufficient energy. As a result, a fraction of the initial energy is used to produce measurable quanta (either scintillation photon or ionization electron), while the other

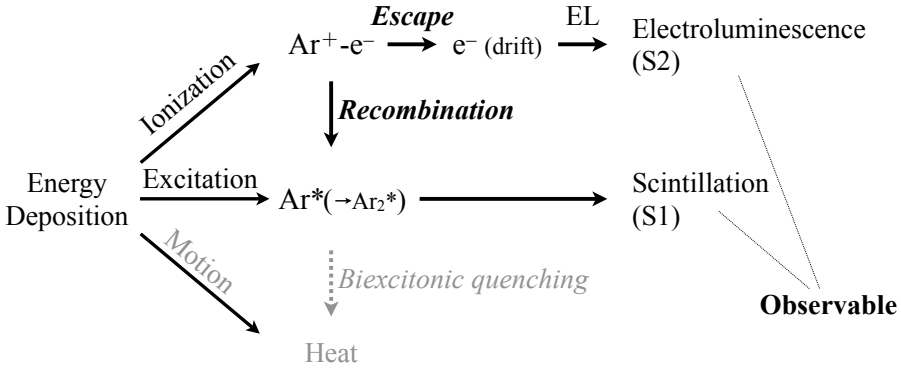

Fig. 3.1. Schematic for the conversion process of energy deposition into observables. Energy deposition is distributed to three channels: ionization, excitation, and atomic motion. The excitations lead to S1, the ionization electrons lead to S2, and the atomic motion is unobservable in LAr scintillation detector. Through the recombination process, a ratio of S1 and S2 changes.

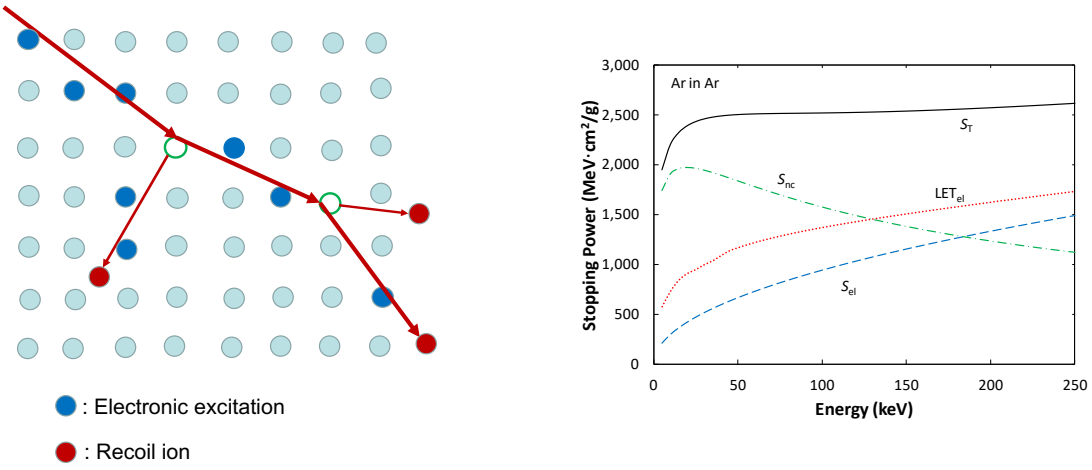

Fig. 3.2. Left: schematic illustration of the collision cascade from the recoiled nuclei travelling the detector medium. The recoiled nuclear losses its energy through elastic or inelastic scattering leaving ionized or excited atoms. Right: calculated stopping power for NR in liquid argon as a function of recoil energy based on Lindhard theory. The lines with S_{nc} and S_{el} represent the stopping power (energy deposition per unit length on the incident particle) given to elastic (electronic) and inelastic (nuclear) processes, respectively, while the S_T is the sum of them. The red line (LET_{el}) represents the electronic linear energy transfer, which gathers contributions from every secondaries and gives the energy used to produce excitation and ionization along the track. The figures are taken from Ref. [41].

to the atomic motion. In addition, since the resulting density of the exciton is so high, conversion of two excitons to only one exciton can be happened by their collisions, which effectively works as further reduction of the observable (biexcitonic quenching).

3.2.2 Energy dissipation

The energy dissipation process starts with an energy deposition of E_{X}, where X is either ER or NR. The average number of total produced quanta N_q, summing excitons N_{ex} and electron-ion pairs N_i, for ER is expressed in the following equation:

$$N_q = N_{ex} + N_i = \frac{E_{\mathrm{ER}}}{W_s}, \tag{3.1}$$

where W_s is the averaged energy expected to produce either scintillation or ionization (so-called effective work function), and a constant value of $W_s = 19.5$ eV[42] is commonly used. Introducing the exciton-to-ion ratio $\alpha \equiv N_{ex}/N_i$, Eq.(3.1) is written as

$$\frac{E_{\mathrm{ER}}}{W_s} = N_i(\alpha_{\mathrm{ER}} + 1). \tag{3.2}$$

Here the subscript ER of α indicates the ratio for electronic recoils. For NR, the energy dissipation is expressed as,

$$N_q = N_{ex} + N_i = \frac{E_{\mathrm{NR}}L}{W_s}, \tag{3.3}$$

and

$$\frac{E_{\mathrm{NR}}L}{W_s} = N_i(\alpha_{\mathrm{NR}} + 1). \tag{3.4}$$

Here, L is an additional factor for NR that accounts for energy loss due to atomic motion. The exciton-to-ion ratio for NR α_{NR} is generally considered to be different to that for ER as discussed below [1)]. The factor L is predicted using Lindhard theory[40] as a function of the dimensionless energy ϵ as follows:

$$\begin{aligned} L &= \frac{kg(\epsilon)}{1 + kg(\epsilon)}, \\ k &= 0.133Z^{2/3}A^{-1/2}, \\ g(\epsilon) &= 3\epsilon^{0.15} + 0.7\epsilon^{0.6} + \epsilon, \\ \epsilon &= 11.5(E_0/\mathrm{keV})Z^{-7/3}, \end{aligned} \tag{3.5}$$

where $Z = 18$ and $A = 40$ are the atomic and mass numbers of argon, respectively. The k and $g(\epsilon)$ are relevant to the rate at which the recoiling nuclei loses its energy by electronic or nuclear stopping powers; the k is proportionality constant between the electronic stopping power and the recoiling nuclei velocity, and the $g(\epsilon)$ is proportional to the quotient between the stopping powers. Note that the particular expression of $g(\epsilon)$ in Eq.(3.5) is an approximation found in Ref. [16].

The ratio α may differs between NR and ER. There are several literature to address it experimentally; for ER, it is measured as 0.21[43], while for NR, it is discussed as 0.6–2.4 depending on NR energy range of 16.9–57.3 keV[44], 0.19[45], 1.0[46], or $1.3\times\exp(-0.60\times F)$ with F in the unit of kV/cm[47]. Complete description of the dependence of α on recoiling particle, as well as its energy and applied electric filed, is still missing. However, the nature of recoiling particle certainly leads different energy loss mechanisms.

[1)] From here on, we will drop the subscript ER or NR in α, always corresponding to that of the energy deposition E_{X}.

A possible picture for higher excitation-to-ionization ratio of NR than ER might be that the recoiled atoms can temporarily form molecular orbitals during the collision process in their path[48, 49]. Ionized electrons in NR track might have very low energy and thus immediately recombine with parent ion (geminate or initial recombination)[50], effectively channeling more energy into excitation. Whatever the physical process behind the parameter, we here parametrize it as an empirical function of the electric field F, similar to the description for liquid xenon in Ref. [51],

$$\alpha = \alpha_0^{\mathrm{X}} \exp(-D_\alpha^{\mathrm{X}} F),\ \mathrm{X} = (\mathrm{NR}, \mathrm{ER}) \tag{3.6}$$

where α_0 and D_α are the free parameters. This parametrization is introduced to explain our measurements[2)].

3.2.3 Electron-ion recombination

A fraction of the ionization electrons recombine with the ions, while the others escape from it and become free (drift or diffused) electrons. The recombination probability depends on the applied field, incident energy, and linear energy transfer (LET, energy deposited from an (initial) ionization particle to the detector material per unit path length along its track), and it is one of the essential parameter to characterize the liquid argon response. An external electric field works to prevent the recombination. Higher field, of course, suppresses more recombination and increases the free electron. LET in liquid has also an impact on the probability, as higher electron-ion density results in higher encounter probability of the electrons and ions.

The recombination is considered to be happened quickly once a pair of electron and ion is close enough so that the drift due to the electric field of the charge careers dominates over that due to the thermal diffusion. This critical distance r_c is called Onsager radius and given by

$$\frac{e^2}{4\pi\epsilon r_c} = k_B T, \tag{3.7}$$

where ϵ is the dielectric constant of the medium, k_B is Boltzmann constant, and $k_B T$ gives the thermal energy of the pair. This process takes place in proportional to the number densities of the careers, $N_\pm$: The recombination rate R is proportional to the number densities of the careers $N_\pm$:

$$R = \kappa N_+ N_-, \tag{3.8}$$

where the subscript $\pm$ stands for positive ion and electron, respectively, and κ is the recombination coefficient.

[2)] While α_0^{NR} and D_α^{NR} are determined in Chapter 5 and α_0^{ER} from literature in Chapter 6, this dissertation does not touch on D_α^{ER} anymore.

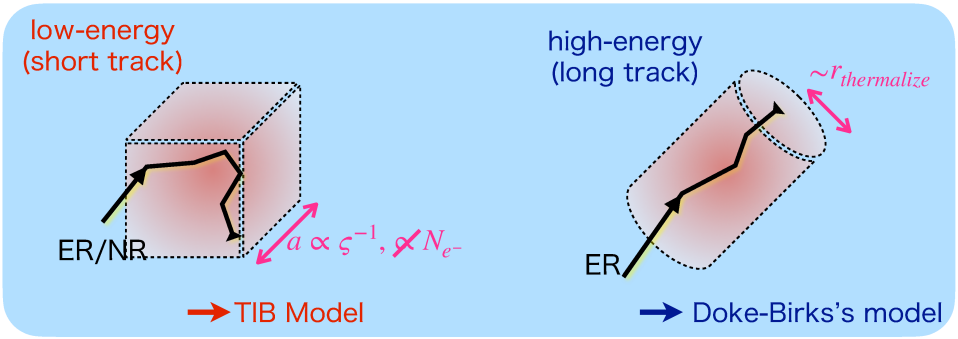

Fig. 3.3. Schematic illustration of an interpretation of the two recombination models with respect to the recoiled particle track length.

Time evolution of the number densities $N_\pm$ described by the model put forth by Jaffé:

$$\frac{\partial N_+}{\partial t} = \mu_+ \boldsymbol{F} \cdot \nabla N_+ + d_+ \nabla^2 N_+ - \kappa N_- N_+, \tag{3.9}$$

$$\frac{\partial N_-}{\partial t} = \mu_- \boldsymbol{F} \cdot \nabla N_- + d_- \nabla^2 N_- - \kappa N_- N_+, \tag{3.10}$$

where $\mu_\pm$ are the mobilities for the two charge carriers, $\boldsymbol{F}$ is the total electric field (i.e., both applied and from diffused carriers), $d_\pm$ are the diffusion constants, and κ is the recombination coefficient. The first terms in the right hand of Eqs.(3.9) and (3.10) represent the drift of careers by the field, the second terms the drift by the diffusion, and the last term recombination process proportional to the number densities of the careers.

Below we consider two approaches to evaluate the overall recombination probability based on Eqs.(3.9) and (3.10); the one is capable of treating relatively short track and the other is of long track.

The case for short track: Thomas-Imel box model

When an ionizing track length is comparable or shorter than the electron thermal distance, the carriers are regarded to spread uniformly within a region with typical size of the thermal distance as shown in the left side of Fig. 3.3. As the total energy deposition increases, the recombination probability increases. It is the case for NR and low energy ER. A good description of the process is given by Thomas-Imel box (TIB) model.

Thomas and Imel simplify the equation as [52]

$$\frac{\partial N_+}{\partial t} = -\kappa N_- N_+, \tag{3.11}$$

$$\frac{\partial N_-}{\partial t} = -v \frac{\partial N_-}{\partial z} - \kappa N_- N_+. \tag{3.12}$$

Here, a constant electric field in the $-z$ direction $\boldsymbol{F} = (0, 0, -F)$ is applied and the drift velocity $\boldsymbol{v} = (0, 0, -v) = \mu_- \boldsymbol{F}$ is assumed. Since the electron diffusion rate in liquid argon is quite small (order of millimeters per meter of drift[53, 54]), corresponding terms in Eq.(3.10) is dropped. In addition, the

positive ion has much smaller mobility and diffusion constant than electron, they treat it as stationary so that the first two terms of Eq.(3.9) are dropped, as represented in Eq.(3.11). Next, the box model boundary condition is applied, where the pairs are assumed to be isolated and the initial distribution of the carriers uniformly populates inside a box with a side length $2a$. This is written as

$$N_{\pm}(t=0) = \begin{cases} \frac{N_0}{8a^3} & |x|,|y|,|z| < a, \\ 0 & otherwise, \end{cases} \tag{3.13}$$

where $N_0 = n_+(t=0) = n_-(t=0) = \int dx^3 N_{\pm}(\boldsymbol{x}, t=0)$ with the total number of the charge carriers $n_{\pm}$. Taking the condition Eq.(3.13) into Eqs.(3.11) and (3.12) and letting $t \to \infty$ finally gives the recombination probability r as

$$r = 1 - \frac{n_-(t=\infty)}{N_0} = 1 - \frac{1}{\xi}\ln(1+\xi), \text{ where} \tag{3.14}$$

$$\xi = \frac{N_0 \kappa}{4a^2 \mu_- F} \equiv N_0 \varsigma. \tag{3.15}$$

Energy dependence of r comes from N_0 in Eq.(3.15) and field dependence from ς through the electron mobility. The recombination law in Eq.(3.14) is called Thomas-Imel box (TIB) model.

An empirical modification[45] of the TIB model provides r as follows:

$$\begin{aligned} r &= 1 - \frac{\ln(1+N_0\varsigma)}{N_0\varsigma}, \\ \varsigma &= \gamma^{\mathrm{X}} F^{-\delta^{\mathrm{X}}}. \end{aligned} \tag{3.16}$$

Here, γ^{X} and δ^{X} (X = (NR, ER)) are free parameters. From Eqs.(3.12) and (3.16), the parameter ς is approximately proportional to the inverse of the electron drift velocity in liquid argon.

TIB model originally intends to describe the recombination process under electric field. By considering finite value of ς, the expression in Eq.(3.16) is extended to null field where electron diffusion may involve with the recombination process, as will be discussed in Section 6.6.

The case for long track: Doke-Birks's model

On the other hand, for a longer track such as high energy ER, the electrons and positive ions are considered to be created along tracks of ionizing particle, as shown in right side of Fig. 3.3. A parameter affecting the recombination process is dE/dx rather than the ionizing particle energy. Since higher energy electron gives lower dE/dx in the energy region of interest, the recombination probability decreases as total energy deposition increases. Doke-Birks's model can be used to express the process.

This model is proposed by Tadayoshi Doke and is another approximation of the Jaffé equation (Eqs.(3.9) and (3.10)) in the absence of electric field. Assuming that electrons and positive ions are formed along

tracks of ionizing particle, both diffusion and drifting of the careers are ignored in the Jaffé model:

$$\frac{\partial N_+}{\partial t} = \frac{\partial N_-}{\partial t} = -\alpha' N_- N_+. \tag{3.17}$$

These careers are considered to be distributed uniformly within a unit length dx along the track,

$$\frac{\partial N_\pm}{\partial t} = -\alpha' N_\pm^2 \tag{3.18}$$

Eq.(3.18) is solved by integrating over the observation time (from 0 to τ),

$$R = S \int_0^\tau -\frac{dN}{dt} dt = \frac{S N_0^2 \alpha' \tau}{1 + N_0 \alpha' \tau}, \tag{3.19}$$

where R is number density of recombined pairs, S the cross section of the electron or ion column, and $N_0 \equiv N_\pm(t = 0)$. Approximating that n_0 is proportional to dE/dx, i.e., $n_0 = K(dE/dx)$, we finally get the recombination probability:

$$r = \frac{R}{N_0} = \frac{SK\alpha'\tau(dE/dx)}{1 + K\alpha'\tau(dE/dx)} = \frac{A(dE/dx)}{1 + B(dE/dx)}. \tag{3.20}$$

From the measurements with heavy-ion beams, a correction term C is added to Eq.(3.20) by Doke:

$$r = \frac{A(dE/dx)}{1 + B(dE/dx)} + C, \quad B = \frac{A}{1 - C}. \tag{3.21}$$

The term C is interpreted as to account for geminate (initial) recombination (one between an electron and its parent ion), while the discussion so far focuses on homogeneous (volume) recombination (one between an electron and an ion other than the parent). The parameters A and C are those experimentally determined. Figure 3.4 shows the relative scintillation yields for various ionizing particles. The solid line represents the Doke-Birks's model whose parameters are determined by relativistic heavy ion and electron tracks. Events with relatively long (typically more than several μm) track are believed to be described by it rather than the TIB model.

In the end of this subsection, we should note that the Onsager model of recombination is not applicable for liquid argon at any LET. The Onsager model assumes that some ionization electrons are thermalized within the Onsager radius and immediately recombine with their parent ion. While the Onsager radius of liquid argon is calculated as roughly 100 nm[55], the thermalization length is calculated as ~1.7 μm[56], meaning that it is not the dominant process. Certainly, it is hard to regard that the recombination process is described only by the Onsager model; if it were, we could not explain any correlation between ionization density and recombination probability seen by numerous measurements.

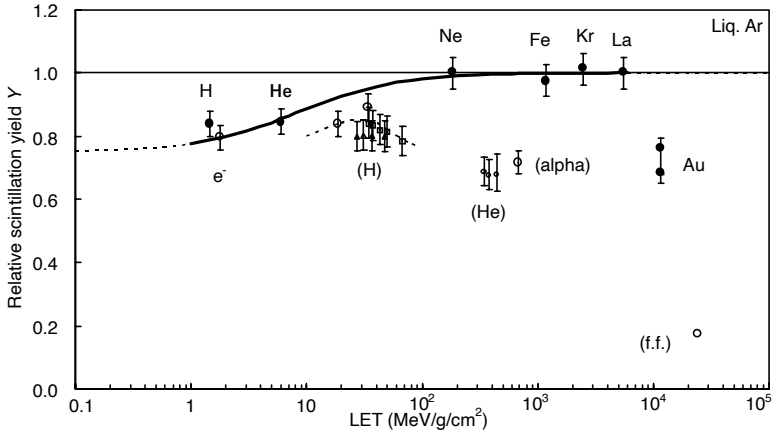

Fig. 3.4. Relative scintillation yield of liquid argon as a function of LET. The circle labeled with e^- at LET = 2 MeV/g/cm^2 is the 1 MeV electron point. Particles given in brackets are non-relativistic. Since the maximum yield is $1/W$ = 51.2 photon/keV, the yield for the electron point corresponds to 41 photon/keV. Also shown is the Doke-Birks's model (black thick line) whose parameters are determined by relativistic heavy ion and electron tracks. The figure is taken from Ref. [42].

3.2.4 Electronic quenching

In addition to the recombination process, within the high density core of NR track, collision between two free excitons can occur:

$$\mathrm{Ar}^* + \mathrm{Ar}^* \rightarrow \mathrm{Ar}^+ + \mathrm{Ar} + \mathrm{e}^-(\text{kinetic energy}). \tag{3.22}$$

This process, called biexcitonic quenching, effectively works as further reduction of the scintillation yield by transitioning two seeds of the photon to one[57]. Consequently, the fraction of NR energy used in the detectable channels is reduced. This effect incorporated by the Mei model [58]. The quenching term f_l is parametrized as

$$f_l = \frac{1}{1 + k_B(\frac{dE}{dx})_{\mathrm{el}}}, \tag{3.23}$$

where k_B is a free parameter. The electronic stopping power $(\frac{dE}{dx})_{\mathrm{el}}$ is presented by Mei *et al.* as a function of the recoil energy E_{NR}, as shown in Fig. 3.5.

3.2.5 Scintillation signal

The primary scintillation signal in liquid argon results from the relaxation of an excimer Ar_2^* as follows. The exciton Ar^* produced directly from the energy transfer is self-trapped in the detector media immediately (within O(ps)) and forms an excimer Ar_2^* of either the singlet state ($^1\Sigma_u^+$) or the triplet state ($^3\Sigma_u^+$)[59]. It then emits single photon when radiatively decaying to ground level. The scintillation light spectrum lies in vacuum ultraviolet (VUV), peaked at 128 nm with approximately 10 nm width, which

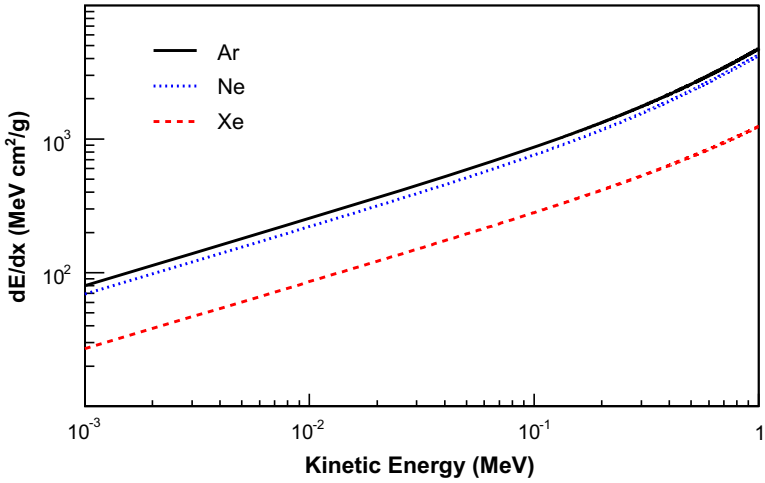

Fig. 3.5. The electronic stopping power $(\frac{dE}{dx})_{\text{el}}$ for argon ion with itself, as well as neon and xenon ions. The figure is taken from Ref. [58].

is independent from the two excimer states. The same applies to an exciton produced from a positive ion Ar^+ at rest through self-trapping and recombination processes. The mechanisms of these two processes are summarized as [53]

$$Ar^* + Ar + Ar \rightarrow Ar_2^* + Ar \qquad \text{excimer formation (self-trapping)} \qquad (3.24)$$

$$Ar_2^* \rightarrow 2Ar + h\nu \qquad \text{de-excitation (VUV emission)} \qquad (3.25)$$

and

$$Ar^+ + Ar + Ar \rightarrow Ar_2^+ + Ar \qquad \text{self-trapping} \qquad (3.26)$$

$$Ar_2^+ + e^- \rightarrow Ar^{**} + Ar \qquad \text{recombination} \qquad (3.27)$$

$$Ar^{**} \rightarrow Ar^* + (\text{heat}) \qquad \text{relaxation} \qquad (3.28)$$

$$Ar^* + Ar + Ar \rightarrow Ar_2^* + Ar \qquad \text{excimer formation} \qquad (3.29)$$

$$Ar_2^* \rightarrow 2Ar + h\nu \qquad \text{de-excitation (VUV emission)} \qquad (3.30)$$

where $h\nu$ stands for the VUV photon.

Since the singlet and triplet states have vast different lifetimes of approximately 7 ns and 1.6 μs, respectively[60], the shape of the scintillation time profile is characterized by the ratio of two states. The VUV photon wavelength and excimer decay lifetimes do not depend on the ionization density, or LET, but the ratio does; this allows for identification of the incident particle in particle detectors. Practical use of this so-called pulse shape discrimination (PSD) technique will be described in Section 3.5.1.

Physics behind the PSD

The difference of the scintillation pulse shape is attributed to elementary process affected by the nature of the incident particle, though it is not yet fully understood why the difference is so large. Let us qualitatively describe the process to explain the large difference in the fraction as a result. LET in liquid argon should affect the probability to generate the triplet state. Followings are the involving processes;

- An excimer generated by direct excitation of the argon atom is likely the singlet. This is explained by the fact that the parent atom is in ground state and has zero spin. Thus the excited electron and the rest of atom (nucleus plus electrons) generally have spins of opposite sign, resulting to form the singlet.
- An excimer generated through ionization process can be both singlet and triplet. It is suffered from either geminate (initial) recombination or homogeneous recombination. The geminate recombination is the one between an electron and its parent ion; hence the singlet state is favored in this case. On the other hand, the spin directions are no longer constrained in the homogeneous recombination. Therefore both single and triplet are possible.
- The exciton-to-ion ratio α can be higher for NR than ER. Consequently, the singlet is more likely to be produced than the triple for NR, and vice versa for ER.
- Generated excimers may change their state via collision processes:

$$^1\Sigma_u^+ + ^1\Sigma_u^+ \rightleftharpoons {}^3\Sigma_u^+ + ^3\Sigma_u^+, \tag{3.31}$$

$$^1\Sigma_u^+ + e^- \rightarrow {}^3\Sigma_u^+ + e^-. \tag{3.32}$$

  This process is expected to be occurred more in lower LET because the thermalized electrons can exist for a long time. As a result, events with low LET such as ER show high percentage of triplet.

All processes above must occur within at least less than 10 ns, since no differences of singlet and triplet decay-time constants are observed between NR and ER. The impact of LET on the process in Eq.(3.32) has not been quantitatively studied.

3.2.6 Extraction of S2 signal

Free electron

Under the appropriate electric field, the ionization electron may escape from recombination process and become free electron. It is then transported along the field with a certain velocity of $O(\mathrm{mm}/\mu\mathrm{s})$. Figure 3.6 shows the drift velocity of electron in liquid argon as a function of the electric field. As described later, the field inside the double-phase argon time projection chamber (TPC) serves to transport them toward liquid surface, where they are accelerated to overcome a potential barrier of a fraction of 1 eV

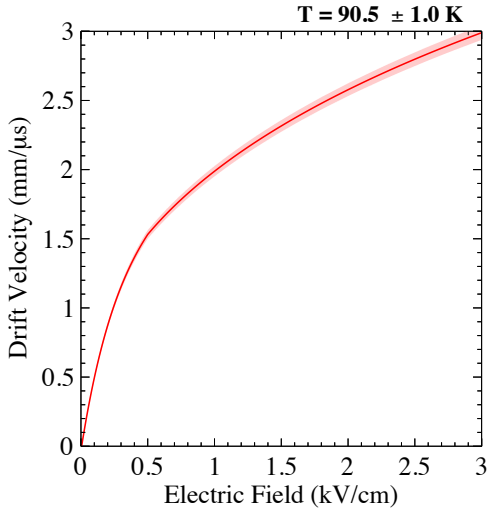

Fig. 3.6. Drift velocity of the free electron in liquid argon of 90.5 ± 1.0 K [61, 62].

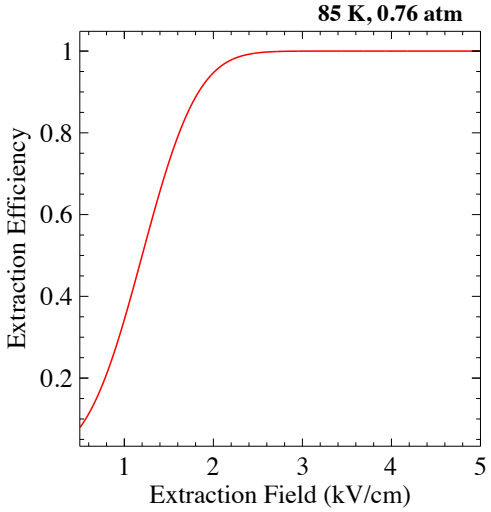

Fig. 3.7. Efficiency of the electron extraction from liquid to gas measured by Ref. [63].

in a stronger electric field to be extracted to the gaseous phase. The extraction efficiency as a function of the applied filed is shown in Fig. 3.7.

The recombination probability of the ionization electron depends on the applied field, incident energy, and LET. Thus, the ratio of the ionization signal to the scintillation signal offers a second method of the particle discrimination. More discussion is also presented in Section 3.5.

Electroluminescence

Once the electron is extracted to the gaseous phase, they are easily accelerated due to the lower density and produces electroluminescence light in their path. The origin of producing light signal is similar to that for the scintillation signal in liquid: the argon atom is excited by the collision with the accelerated electron, forming one of the two states of the excimer and emitting the VUV photon throughout the de-excitation. Unlike the liquid case, relatively small fractions of ultraviolet (UV) and near-infrared (NIR) components are also exists as schematically shown in Fig. 3.8.

The electroluminescence light yield depends on the applied electric field, pressure, and drift path length. The luminescence yield N_{el} per unit drift length x under the electric field F and the number density of the gas ρ is represented as

$$\frac{1}{\rho}\frac{dN_{\mathrm{el}}}{dx}[10^{-17}\mathrm{photon/electron}\cdot\mathrm{cm}^2/\mathrm{atom}] = P_\alpha\frac{F}{\rho} - P_\beta, \tag{3.33}$$

where F/ρ is given in a unit of the reduced electric field Td (10^{-17} V cm^2 atom^{-1}), and P_α and P_β are constant parameters. The measurement in Ref. [64] gives $P_\alpha = 0.081$ and $P_\beta = 0.190$. The electroluminescence yield in a typical detector (luminescence field of a few kV/cm and inner pressure of O(1 atm)) is O(10–100) photon/electron/cm.

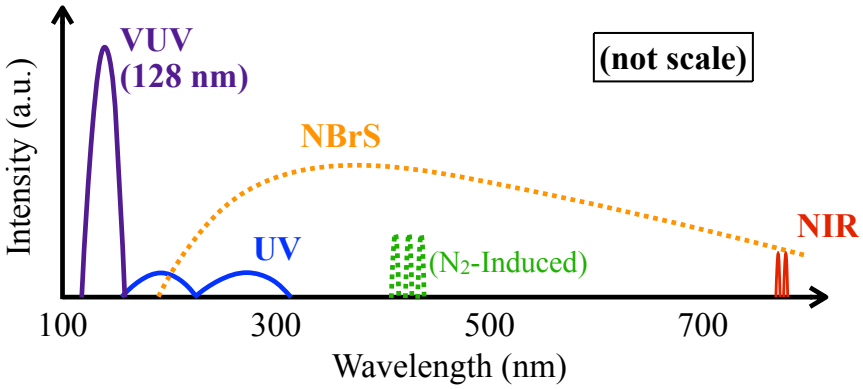

Fig. 3.8. Schematic illustration of the S2 spectrum.

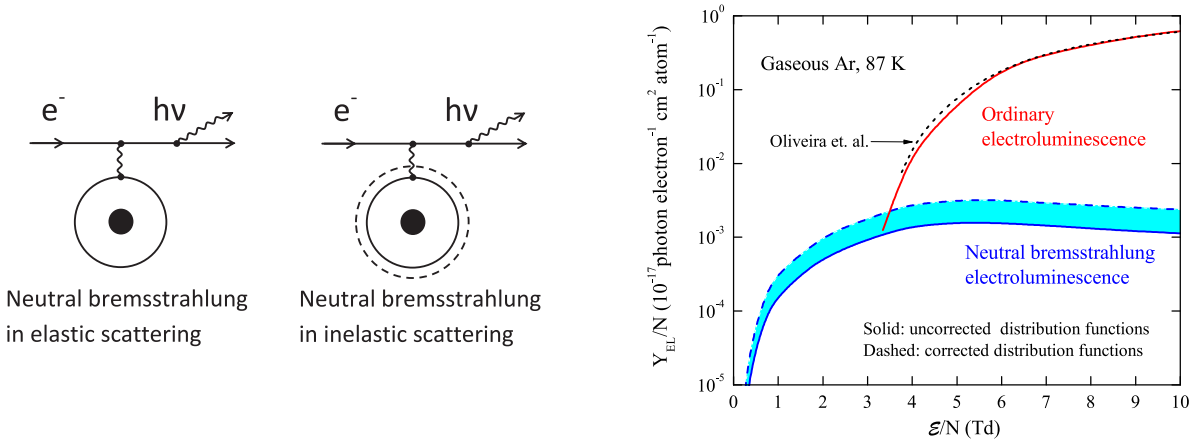

Fig. 3.9. Schematic representation (left) and expected yield (right) of the NBrS. The figures are taken from [65].

In addition to these mechanism, there is another component contributing the light signal in the gaseous phase: neutral Bremsstrahlung (NBrS) [65, 66], which is explained as the Bremsstrahlung of drift electrons at an energy of O(1–10 eV) scattered on neutral atom. The process of the NBrS mechanism and the yield of it is shown in Fig. 3.9. The photon yield from NBrS is calculated as orders of magnitude lower than ordinary luminescence signal. However, under low electric field it could be dominant component of the S2 signal because the field dependencies of the photon yield is much moderate than electroluminescence. It should also be noted that NBrS has a broad emission spectra around visible region.

3.2.7 Total observables yields in liquid argon detector

Summarizing the processes finally gives the expressions of the number of produced scintillation photons $n_{\rm ph}$ and the number of produced ionization electrons n_e. For ER, these are

$$n_{\rm ph} = \frac{E_{\rm ER}}{W_s} \times \left[1 - \left(\frac{1}{1+\alpha}\right)(1-r)\right], \tag{3.34}$$

$$n_e = \frac{E_{\rm ER}}{W_s} \times \left(\frac{1}{1+\alpha}\right)(1-r), \tag{3.35}$$

and for NR,

$$n_{\rm ph} = L \times f_l \times \frac{E_{\rm NR}}{W_s} \times \left[1 - \left(\frac{1}{1+\alpha}\right)(1-r)\right], \tag{3.36}$$

$$n_e = L \times \frac{E_{\rm NR}}{W_s} \times \left(\frac{1}{1+\alpha}\right)(1-r). \tag{3.37}$$

These quantities are related to S1 and S2 as

$$\mathrm{S1} = g_1 n_{\rm ph}, \tag{3.38}$$

$$\mathrm{S2} = g_2 n_e, \tag{3.39}$$

where g_1 is the light collection efficiency (LCE) and g_2 is the average number of detected electroluminescence photons per one drift electron. Both g_1 and g_2 are considered as detector properties and remain constant for NR and ER events.

3.3 WIMP detector : single-phase scintillator and double-phase time projection chamber

Liquid argon scintillation detector observes light signal generated in both liquid and gaseous phases by photo-detectors on the detector end. It is classified into two types of detectors; a single-phase detector and a double-phase detector. Figure 3.10 shows schematics of the detectors, and the observed light signal shapes are illustrated in Fig. 3.11.

In a single-phase detector, scintillation photons generated by an energetic particle are detected (see Section 3.2.5 for detail). As the wavelength lies in VUV region and hence it is technically difficult to be reflected and detected, we usually downshift it by means of wavelength shifter inside the detector. The interacting position is inferred by the signal ratio and the time stamp of the detected photon in each photo-detector.

In a double-phase detector, appropriate electric field is applied in the vertical direction (along with z-axis) so that ionization electrons drift toward the gaseous phase, as described in Section 3.2.6. Higher field is applied near the liquid surface; drifting electrons accelerate around the region and are extracted to the gaseous phase, where secondary light signal (electroluminescence) is generated. Both S1 and S2 photons

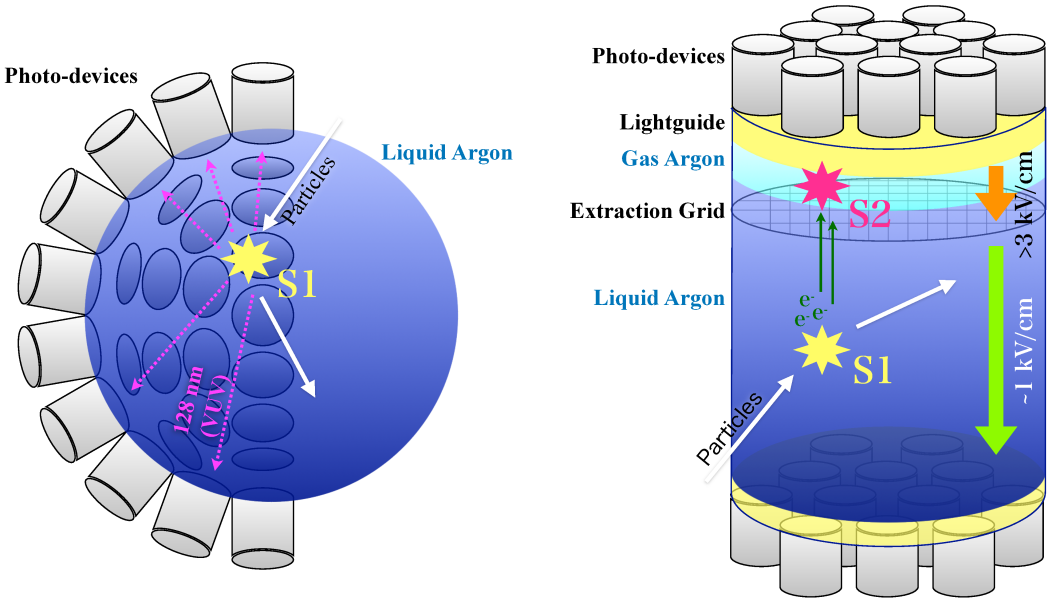

Fig. 3.10. Schematics of the single-phase (left) and double-phase (right) LAr scintillation detectors.

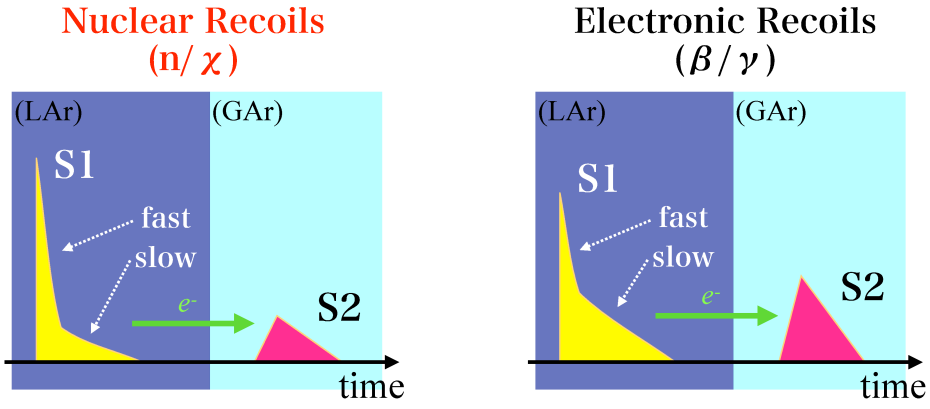

Fig. 3.11. Schematic illustrations of the observed light signals for NR (left) and ER (right).

are detected by photo-detectors usually located at the top and the bottom ends. The double-phase detector works as a TPC, i.e., the z-position of incident particle is reconstructed by time difference between S1 and S2. The horizontal position (in xy-plain) is reconstructed by the distribution of the S2 photons in the top photo-detector array.

In this work, the double-phase detector is used in the NR measurement in Chapter 5 and the single-phase detector is used in the ER measurement in Chapter 6 and the surface run in Chapter 7.

3.4 Energy reconstruction

Deposited energy from the ionizing particle is inferred from the S1 and/or S2 yields. If the detector is operated with nonzero field, the use of the sum of the yields, instead of solely S1 yield, should recover the linear scale as is the case for liquid xenon detector. However, it requires a precise number of S2 photon per drift electron in the particular detector. Therefore, the custom has been to use only S1 yield. A linear scale of the yield works only if the electron-ion recombination probability is energy independent and no energy is transferred to the heat channel, as shown in Fig. 3.1. In fact, this is only the case for ER with the recoil energy typically above 100 keV. This leads a statement that the precise calibration of the liquid argon detector is incredibly essential in the WIMP search experiment which seeks the low-energy rare events.

3.5 Particle identification

Signals acquired with the detector are sensitive to the kind of the recoiled charged particle as a result of processes on generating scintillation photon and ionization electron in Section 3.2. Based on experimental point of view, two kinds of the ratios, the singlet to triplet ratio and the scintillation to ionization ratio, are considered in this section. The former can be extracted by the S1 pulse shape and the latter by the ratio of S1 to S2 photon yield.

3.5.1 S1 pulse shape

As mentioned in Section 3.2.5, two excimer states of argon, $^1\Sigma_u^+$ and $^3\Sigma_u^+$, have lifetimes differing by more than a factor of 200. The ratio can be determined experimentally by computing the percentage of the scintillation yield in time interval after (or before) the fast component sufficiently decaying to the total integral of the yield. We use hereafter in this dissertation a parameter “slow/total” defined as the fraction of light yield detected after 100 ns of the signal so that we can retrieve the PSD ability in a simple way.

For the same recoil energy, NR shows large fraction of singlet to triplet with respect to ER, hence small slow/total. Figure 3.12 shows a comparison of the S1 pulse shape between NR and ER. Clear difference between these waveforms is observed. The PSD power from the waveforms is extremely high. For example, ER leakage of less than 2.7×10^{-8} for 90% NR acceptance in the energy region 44–89 $\mathrm{keV_{ee}}$ has been experimentally measured[67], where $\mathrm{keV_{ee}}$ stands for keV electron equivalent. However, because of the stochastic nature, the power gets weak as the number of detection photon decreases. In addition, the discrepancy of the fraction between NR and ER is found to be smaller in lower energy region, as shown in Fig. 3.13, presumably due to the nature of the LET dependency discussed below. By means of a high detection efficiency of the scintillation photon one can benefit certain PID power in lower energy region.

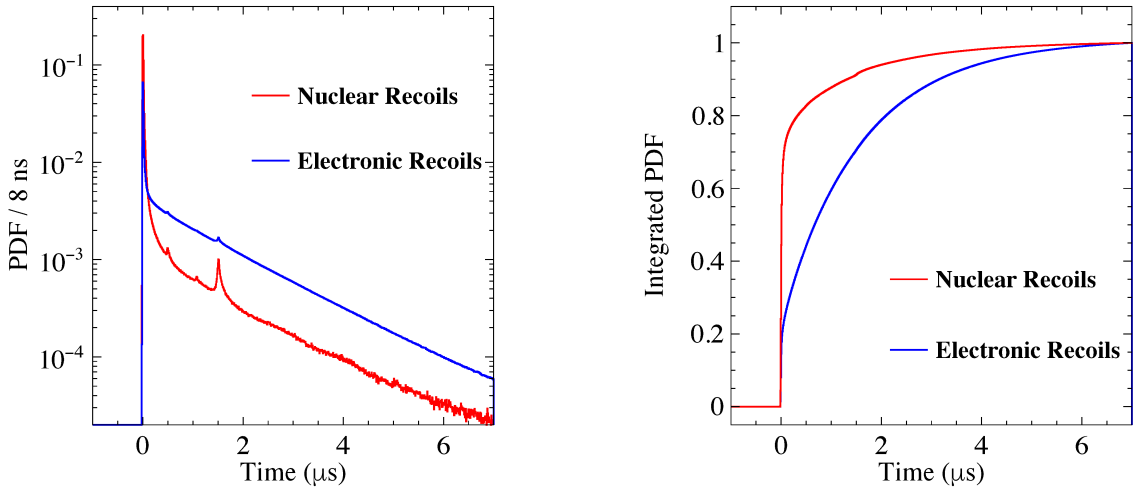

Fig. 3.12. Comparison of the average waveform (left) and its integral (right) between NR and ER measured in the Waseda setup. The peaked structures around 0.5, 1.0, and 1.5 μs is a detector effect (photomultiplier-tube afterpulse, see Appendix A).

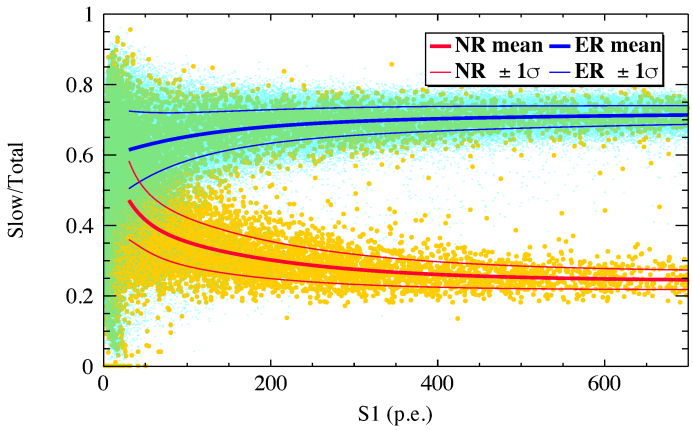

Fig. 3.13. Distributions of ^{252}Cf (both NR and ER) and ^{22}Na (ER) events at null field in S1 versus slow/total plain, where S1 of 50 p.e. corresponds to approximately 5 keV$_{ee}$. The thick and thin lines represent the NR (red) and ER (blue) bands of $\pm 1\sigma$.

3.5.2 S2 to S1 ratio

The ratio of ionization to scintillation is also sensitive to recoiled particle, and a parameter $\log_{10}$(S2/S1) is widely used in practice. The electron-ion recombination probability affects this quantity. As mentioned in Section 3.2.3, the external electric field works to prevent the recombination. Higher field, of course, suppresses more recombination and increases the $\log_{10}$(S2/S1) value. LET in liquid argon also affects the probability, as higher electron-ion density results in higher encounter probability of the electrons and ions. This is the principle of the PID. Figure 3.14 shows the $\log_{10}$(S2/S1) of NR and ER data as

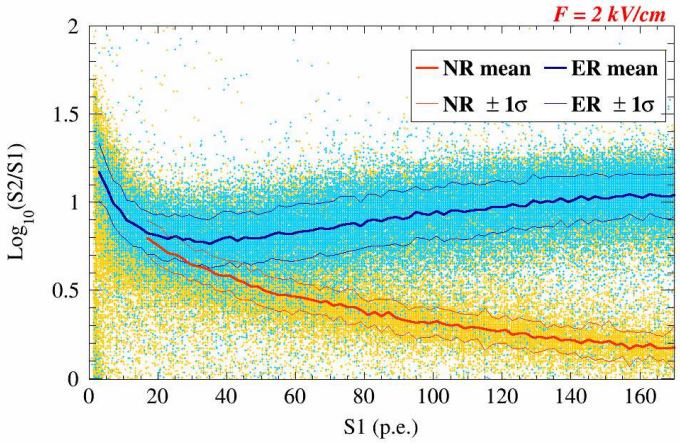

Fig. 3.14. Distributions of ^{252}Cf (both NR and ER) and ^{22}Na (ER) events at $F = 2$ kV/cm in S1 versus $\log_{10}$(S2/S1) plain, where S1 of 15 p.e. corresponds to approximately 5 keV$_{ee}$. The thick and thin lines represent the NR (red) and ER (blue) bands of $\pm 1\sigma$.

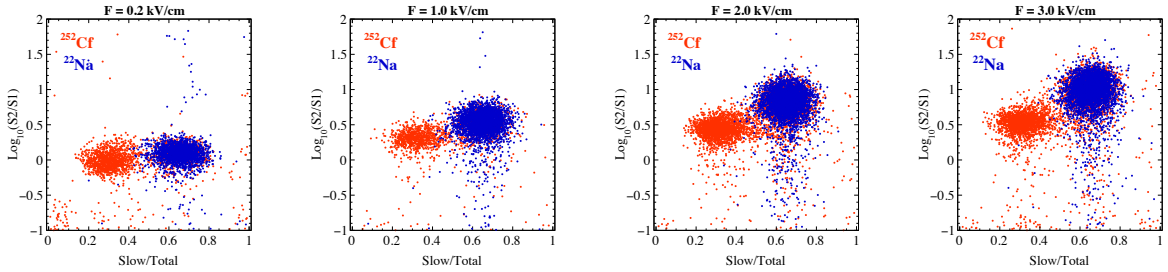

Fig. 3.15. Distributions of ^{252}Cf (both NR and ER) and ^{22}Na (ER) events of approximately 10 keV$_{ee}$ at fields of 0.2, 1.0, 2.0, and 3.0 kV/cm (from left to right) in the PSD parameter versus the ionization to scintillation ratio.

a function of S1 yield. Figure 3.15 shows the field dependencies in the slow/total versus $\log_{10}$(S2/S1) plain, where the mean of $\log_{10}$(S2/S1) increase in both NR and ER.

3.6 Background source in WIMP search

3.6.1 NR background

Single scattering of argon nuclei in the fiducial volume results in NR event indistinguishable from one due to WIMP. It is produced by neutrons and neutrinos.

Fast neutron is the dominant NR source, hence it is the most troublesome background source. The neutron production mechanism involves with radioactivity in detector and ambient materials and cosmic ray interactions.

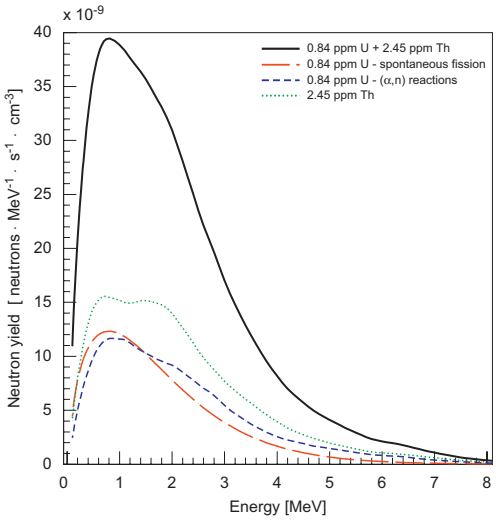

Fig. 3.16. Neutron energy from uranium and thorium in a rock induced by spontaneous fission and (α, n) reaction. The figure is taken from Ref. [69].

Radiogenic neutrons Material containing uranium or thorium emits fast neutrons through spontaneous fission, mainly from ^{238}U. Several α-rays are emitted along their decay chains and also generate fast neutrons through (α, n) reaction with materials. These neutrons come from both inside and outside the detector. The energy is in MeV range so that they easily mimic WIMP's signal.

The neutrons from inside the detector can be suppressed by careful selection of detector material with low radiation level. Reducing radon contamination in liquid argon, which is emanated from material surface is also effective to suppress the background. In fact, as the cross section of (α, n) reaction is higher for lighter nuclei, the radon removal is more important for liquid argon detector compared to liquid xenon detector. The event rate is estimated to be roughly 0.1 events/ppm/day/kg for ^{238}U and ^{232}Th chains, respectively[68], while the contaminations of ^{238}U and ^{232}Th in the liquid argon detector is typically O(1 ppb). This radiogenic neutrons are not the dominant background for a WIMP search at surface because other neutron sources show significantly higher event rate.

The neutrons from ambient materials (such as rock, soil, and concrete surrounding laboratory) are one of the serious background source. Figure 3.16 shows a typical energy spectrum of radiogenic neutron from a rock[69]. The neutron from the ambient materials is the dominant source in deep underground laboratory. In the Kamioka Observatory in Japan located at 2700 m water equivalent (m.w.e.), for instance, the fast neutron flux inside a laboratory is measured to be $3.88 \times 10^{-6}/\mathrm{cm}^2/\mathrm{s}$[70]. Although it is three orders of magnitude lower than that at the surface where the cosmogenic neutrons have huge contribution as will be mentioned below, the WIMP search is limited by this source without taking any measures. The flux and energy spectrum strongly depend on the location and environment of the laboratory. Moderate shielding against the neutrons prevents them from penetrating into the fiducial volume and reduces the background events. In addition, the neutrons can be reduced by removing multiple scattered events. This technique requires a large sensitive volume with respect to the neutron mean free path as well as position resolution to separate the incident points.

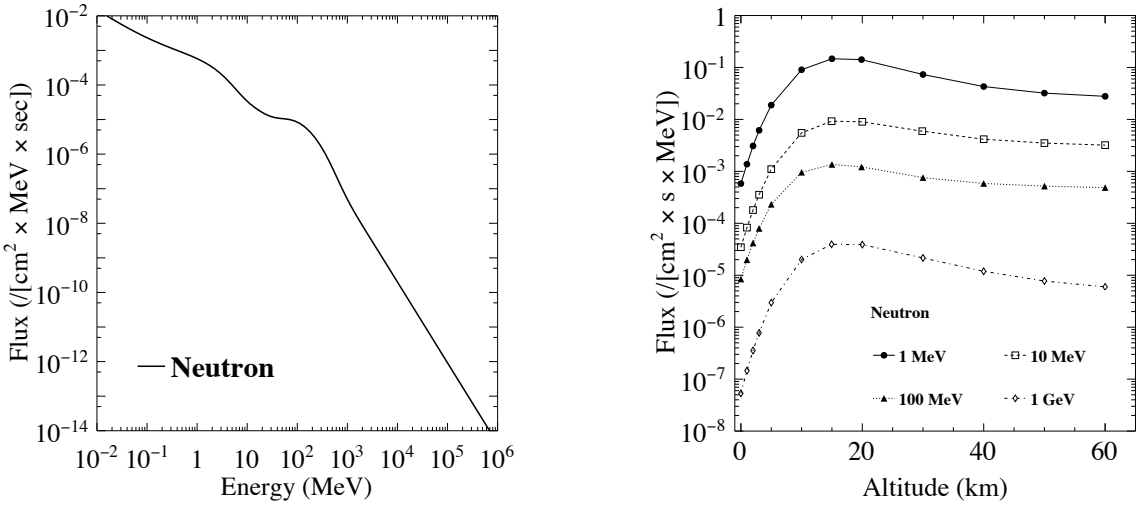

Fig. 3.17. Left: energy spectrum of the ambient neutron at surface calculated using EXPACS. Right: the flux of the neutron as a function of altitude.

Cosmogenic neutrons Cosmic rays interact with any kind of materials and can produce fast neutrons in their path. These interacting materials include air, buildings, shielding materials, detector components, and liquid argon itself.

The neutron flux at surface is predicted by EXPACS[71, 72, 73] and shown in Fig. 3.17 (left) and Appendix C. The neutron is derived from the interaction between primary cosmic-ray and atmosphere. The flux reaches nearly equilibrium at surface as indicated with Fig. 3.17 (right); the flux at shallow depth can roughly be predicted from them. Since the energy of them extends up to TeV, which is very different from the radiogenic neutron, it is hard to moderate them sufficiently with artificial shieldings.

Charged cosmic ray particles, such as muon, electron, proton, and pion, interact with materials and lead to nuclear reaction. It means nuclear spallation, photonuclear process, nuclear capture, hadronic reaction, and so on (see also Section B.1). Fast neutrons are emitted in these processes, and then NR events occur. These events are relatively easily distinguished if we can identify the sign of the incoming cosmic ray by surrounding whole of the detector with an active medium.

The cosmic ray flux in deep underground laboratories is far below than at the surface owing to the overburden rock, as shown in Fig. 3.18[74]. The average energy of cosmic muon in underground, however, is high and therefore the spallation process can be responsible for the NR background. For an experiment at the surface, the cosmogenic neutrons can be the most serious background source due to its high fluence.

Another NR background source is the astrophysical neutrinos resulting coherent elastic neutrino-nucleus scattering (CEvNS). It is an irreducible background for WIMP search because neither shieldings nor single-scattering selection works for reducing these events. The event rate of the SM prediction is so

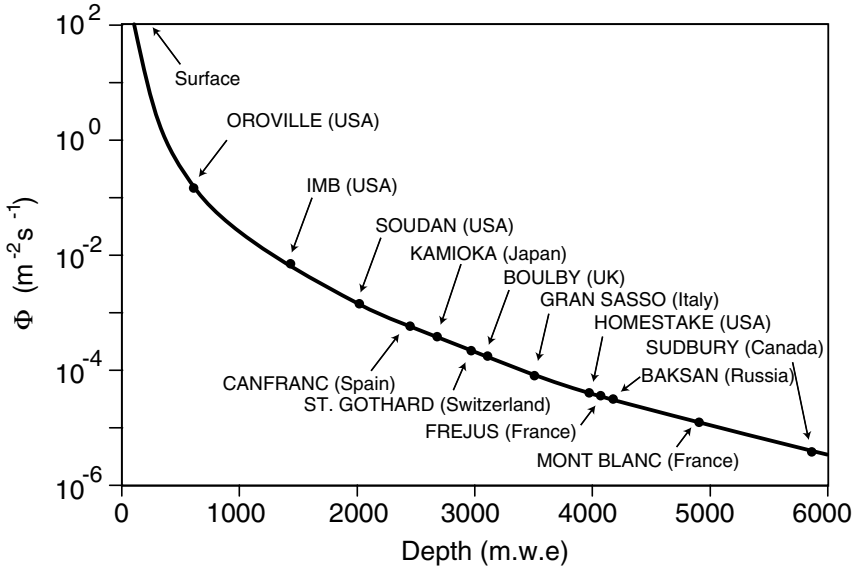

Fig. 3.18. Cosmic-muon flux in various underground laboratories in the world. The figure is taken from Ref. [74].

small that it would be concern for the search for WIMP with its cross section of 10^{-44} cm^2.

3.6.2 ER background

ER events are still one of the most severe background because of the high event rate coming from variety of source, despite the powerful PID capability of the liquid argon detector. Among the ER sources, ^{39}Ar is the unique and main contributor in liquid argon detector.

The radioactive cosmogenic isotope ^{39}Ar exists with a mass fraction of $(8.0 \pm 0.6) \times 10^{-16}$ g/g in atmospheric argon, corresponding to the activity of 1.01 ± 0.08 Bq/kg [75]. It undergoes β-decay with a Q-value of 565 keV, as shown in Fig. 3.19, and has a long half-life of 269 year. Significant efforts are taken to acquire argon with reduced ^{39}Ar by extracting it from deep underground well, and further by depleting it using cryogenic distillation [36]. However, it is still difficult to access the depleted argon. Thus we still need rejecting a number of ^{39}Ar events in PID analysis.

Radioimpurities contaminated in detector materials can contribute to the background budget. These include the β- and γ-rays from their disintegration and Bremsstrahlung x-ray from the β-ray. Cosmogenic γ-ray and ambient γ-ray inside the laboratory can also be the source. Therefore, we are required to carefully select radiation-free materials, design moderate γ-ray shieldings, and tag either incoming particles or multiple scattering with high efficiencies.

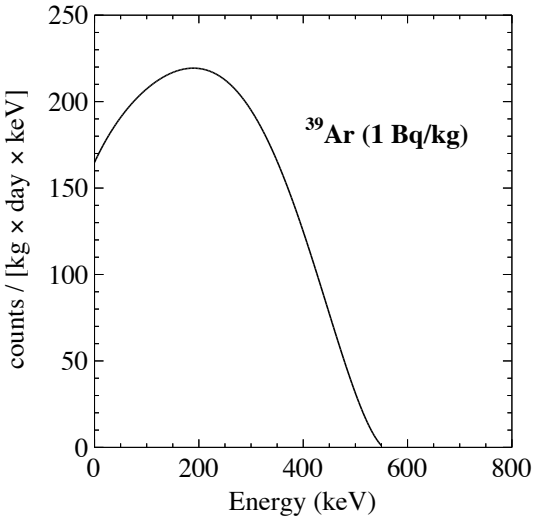

Fig. 3.19. The β-ray energy spectrum of ^{39}Ar.

3.6.3 Detector surface background

The detector surface background is the background of which occurs near detector surface. One of the origin of the background is α-ray emitted on detector surface. Although the radiogenic α-ray has an energy far above the WIMP region of interest (typically a few MeV), it can leave a tiny liquid argon signal mimicking the WIMP one following energy deposition inside the material.

Another origin is electron from ER or β-ray which enters detector surface. In particular, it is troublesome when the surface is coated with a commonly used wavelength shifter, TPB (1,1,4,4-tetraphenyl-1,3-butadiene). When it happens, the TPB on the surface is known to promptly emit photons. Combination of the TPB photon and liquid argon signal from electron results in a signal similar to the NR one. In order to reject this type of background, position resolution near the detector surface is necessary.

3.7 Background component of concern for a surface run

As previously mentioned, fast neutrons induced by cosmic ray are the most severe background component for the search at surface. A part of them is vetoed by detecting the coincidence signal from cosmic-ray particle; however, it is almost impossible to tag and veto all of the incoming particle due to its high event rate and insensitive (“passive”) area of the apparatus. Additionally, precise prediction of the event is difficult from the following reasons.

- The cosmic-ray flux and constitution differ laboratory by laboratory.
- There are nonnegligible uncertainties in the cross section and energy/angular distribution of the nuclear reactions.

- The CPU time required for a Monte Carlo (MC) simulation for the prediction is large.

We should take into account for these facts to perform the surface run (see Chapter 7).

CHAPTER 4

Overview of the liquid argon detector setup at the Waseda - ANKOK experiment

The measurements and the dark matter search presented in this dissertation are all performed at the surface laboratory at Waseda University, as a part of the ANKOK experiment [1)]. The laboratory locates at the lowest floor (semiunderground) of a five-story building in Tokyo, Japan. The building is about 20 m high and made of reinforced concrete. Figure 4.1 is a schematic and picture of the laboratory. Figure 4.2 is a picture of the building and location of the laboratory inside the building.

In this chapter, we describe the experimental apparatus and basic method of waveform analysis.

4.1 Argon handling system

Figure 4.3 shows an overview of the argon handling system. It mainly consists of a stainless-steel cryostat of diameter 50 cm and height 100 cm, in which a scintillation detector sits. The argon filled in the cryostat is cooled by the recirculation system, which extracts hot gas from the cryostat and passes it through the liquefier with a 200 W GM-cryocooler (Sumitomo CH-110). The argon is maintained at a typical pressure of 1.4 atm and at a liquid level that varies by no more than 1 mm throughout the data collection period (typically one or two weeks).

Impurities in the argon (such as water, oxygen, and nitrogen) affect the scintillation properties, resulting in a reduced signal yield [76, 77, 78]. In order to remove adsorbed impurities and outgassing from the detector components, the whole system is pumped to vacuum over about 10 days before the measurement. The pressure of the cryostat reaches below 1.0×10^{-3} Pa. Then commercial liquid argon fills the system via a single path through a liquid filter consisting of a molecular sieve and reduced cooper which removes electronegative impurities. Additional purification is continuously performed by the getters (SAES MicroTorr MC1500-902 and PURERON GP-5) in the recirculation system. The flow rate is typically 30 L/min. Concentrations of these impurities are monitored by the liquid argon signals taken by a calibration source. The nitrogen contamination is evaluated by measuring the decay constant of the S1 waveform, and the electronegative impurities are by measuring the drift electron lifetime via the relationship between S2 yield and drift time. These concentrations are confirmed to be negligible in the following measurement; water and oxygen contaminations of sub-ppb level and nitrogen contamination of sub-ppm level.

[1)] Ankok means “darkness” or “brightness” in Japanese.

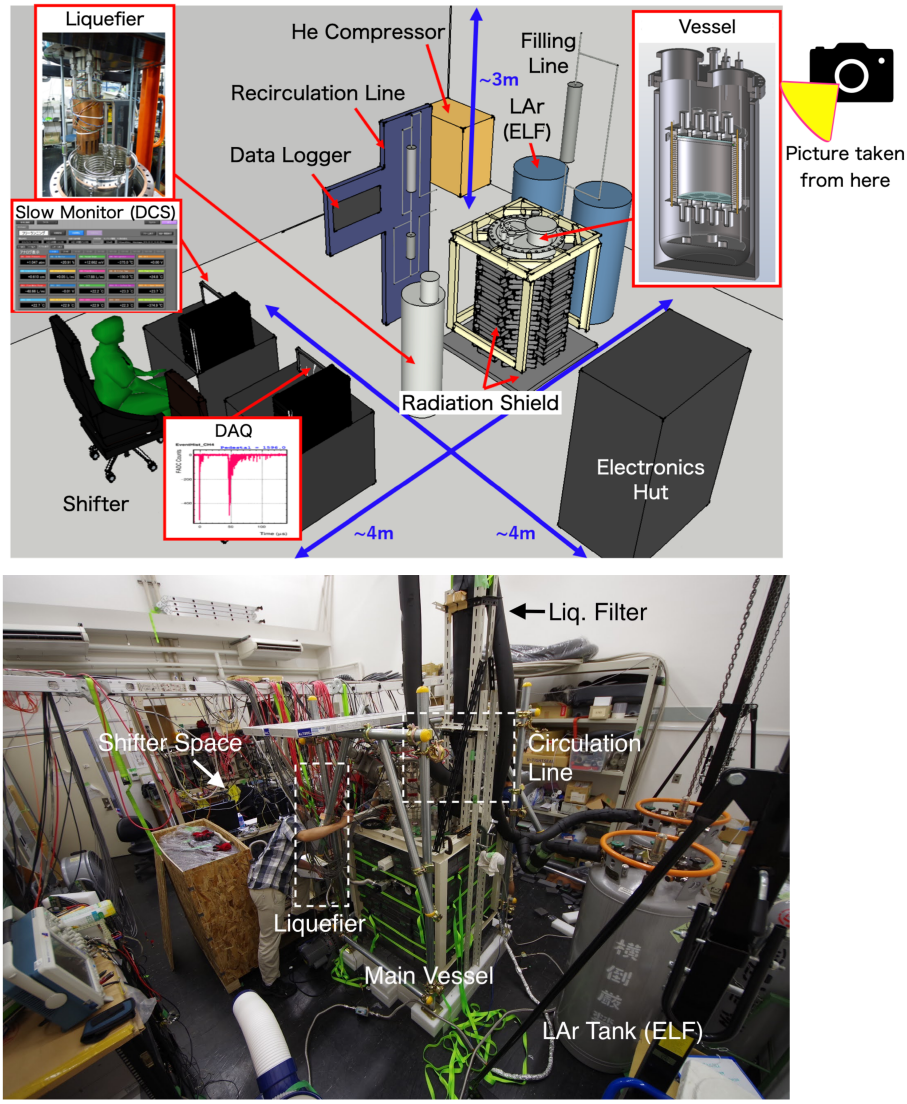

Fig. 4.1. Schematic (top) and picture (bottom) of the laboratory.

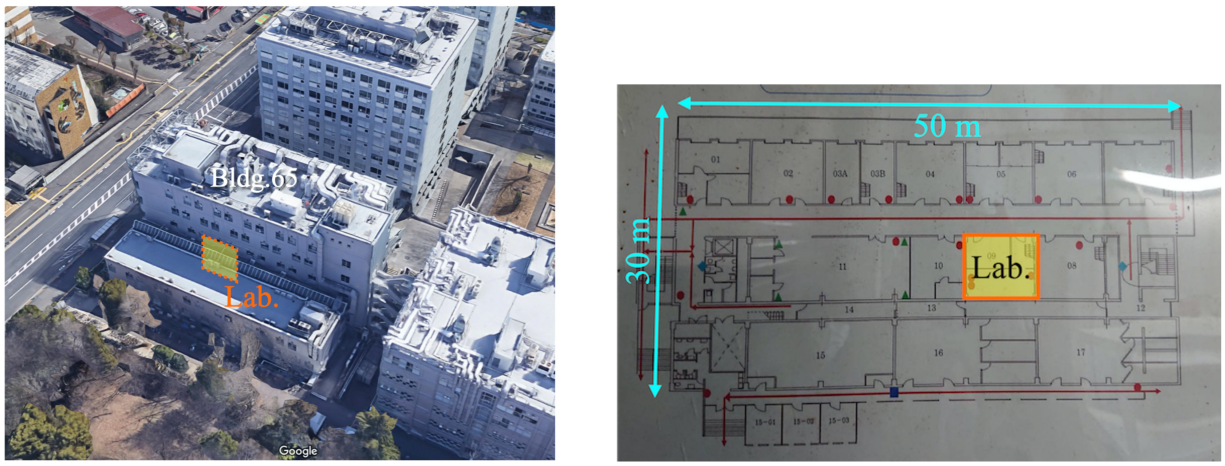

Fig. 4.2. Left: outside view of the building (taken from the Google map). Right: location of the laboratory inside the building.

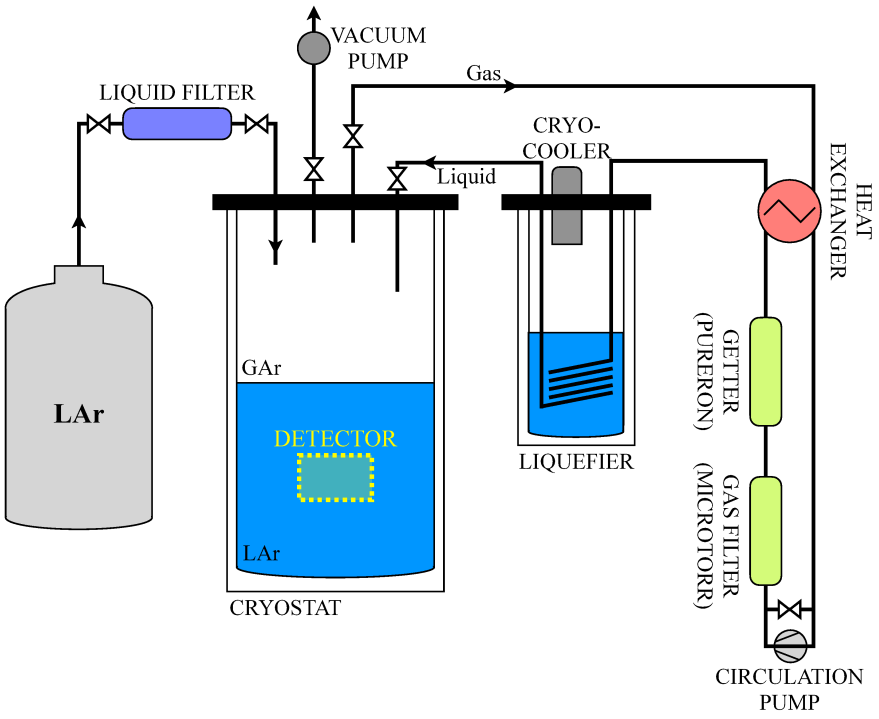

Fig. 4.3. Argon handling system consisting of the filling line (left part of the schematic), the vacuum line (top center), the recirculation line (right), and the main cryostat (center). In the recirculation line, gaseous argon (GAr) extracted from the cryostat is pumped into the getters after passing through a heat exchanger. It then returns to the heat exchanger to be cooled and is condensed in the liquefier. The cryostat containing the detector maintains GAr and LAr in stable cryogenic conditions.

4.2 Detection technology of the light signal

Scintillation signal generated inside a detector is detected by photosensor. As mentioned in Section 3.2, it lies in the VUV and is downshifted to the visible region so that a cryogenic photosensor detects the signal. Detection scheme of the VUV photon is illustrated in Fig. 4.4.

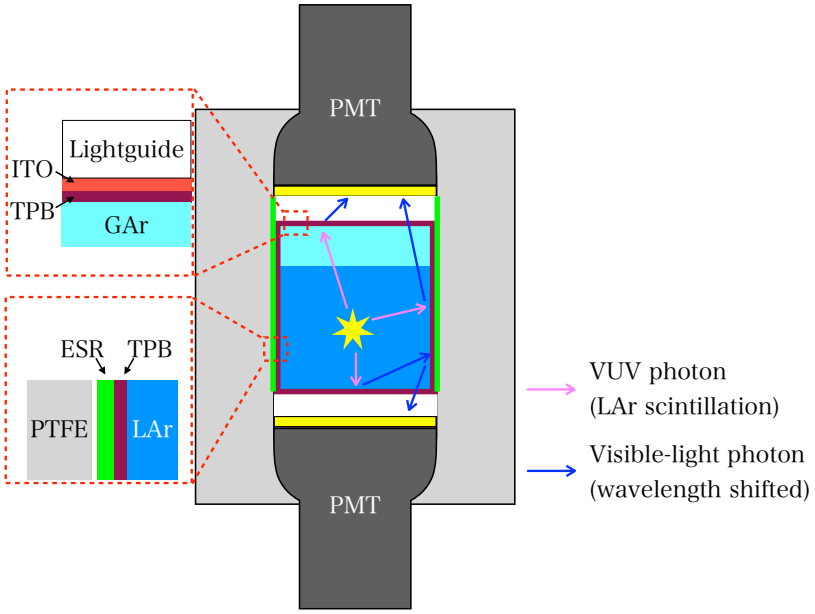

Fig. 4.4. Detection scheme of the LAr scintillation signal in a typical detector made of PTFE bulk. The active volume is surrounded by the reflector (ESR) and the transparent conductive film (indium tin oxide, ITO). The VUV photons are first absorbed by the TPB wavelength shifter on the surface and converted to the visible-light photon. They reaches to the PMT after reflections and refractions to be detected.

PMT A photomultiplier tube (PMT) R11065MOD[2)] produced by Hamamatsu Photonics K.K. [79] is mainly used as the photosensor. It mainly consists of kovar metal and quartz window, with the 3 in. low temperature Bialkali photocathode. Main features of the PMT are low operating temperature (down to liquid argon temperature), low contamination of radioimpurities (< 100 mBq), and high quantum efficiency (QE) for blue light (≥ 30%). Single photon resolution is measured to be approximately 50% at an operation gain of 10^6. No amplifier is used because enough gain can be achieved to observe single photoelectron signal with a negative bias voltage. Basic property of the PMT is measured and summarized in Appendix A.

A PMT R6041-506MOD produced by Hamamatsu Photonics K.K. [80] is also used. It is a compact 2 in. tube and has worse QE and single photon resolution than for R11065. However, this tube requires lower bias voltage than the other one. These properties are suitable for vetoing purpose in outer bath.

[2)] hereafter we refer it simply as R11065

Reflector We use polytetrafluoroethylene (PTFE) as the detector bulk, which has high reflectivity for the visible light. In addition, a multilayer plastic-foil reflector (3M Vikuiti enhanced specular reflector, ESR, of 80-μm thickness) is placed on the fiducial wall because of the following reasons:

- To enhance the reflectivity for the converted visible light. Putting ESR on PTFE wall offers higher reflectance than bare PTFE wall.
- To be used as a base material where the wavelength shifter is vacuum-evaporated as described below. It is easier to uniformly deposit the wavelength shifter on ESR sheet with a controlled condition than to inner surface of a PTFE cylinder.

Wavelength shifter In order to downshift VUV light, we use 1,1,4,4-tetraphenyl-1,3-butadiene (TPB) [81, 82] shown in Fig. 4.5 (left). It absorbs VUV photon and promptly (with a time constant of about 1 ns [83]) re-emits visible photon peaked around 420 nm [84].

The TPB is coated on all surface of materials contacting on the active volume such as lightguide, PMT window, and reflector. These TPB layers are deposited using a vacuum evaporation technique, and their amounts are approximately 30 μg/cm^2 for the lightguide and PMT window and 40 μg/cm^2 for the reflector, corresponding to the deposited-layer thicknesses of $O(1\ \mu\text{m})$ [3)]. These are confirmed by a quartz crystal microbalance sensor and a stylus profiler, as with a procedure similar to that reported in Ref. [85].

Figure 4.5 (right) shows the TPB-coated R11065 PMT. By multiplying the TPB emission spectrum and the R11065 QE, total detection probability for the TPB light with a PMT of QE = 31.03% at 420 nm is calculated as 27.7%, as shown in Fig. 4.6. The PMT QE value is based on the average of that used in this work.

4.3 Data acquisition and trigger

The data acquisition (DAQ) system consists of a 14-bit, 250 MS/s flash analog-to-digital converter (FADC), SIS3316, produced by the Struck Innovative System GmbH. Figure 4.7 shows diagram of the DAQ system. Analog signal from each PMT is directory fed to the FADC through coaxial cable and feedthrough, and it is then digitized and recorded. Binary of the acquired waveform is transferred to a main DAQ PC and further processed.

Trigger decision, such as self trigger and coincidence trigger, is made by the FADC board itself. The board has a trapezoidal finite impulse response (FIR) filter for each FADC channel. The trigger pulse of each channel is armed when the difference between the running sum of the filter and its delayed sum,

[3)] Paper under preparation

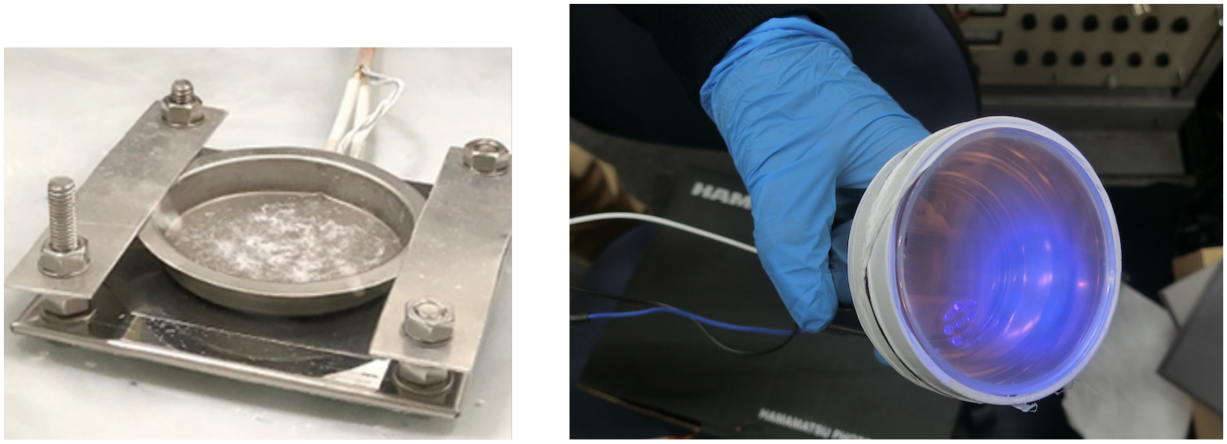

Fig. 4.5. Left: picture of TPB in the crucible used in the vacuum evaporation. Right: picture of the TPB-coated R11065 PMT, illuminated with an ultraviolet light.

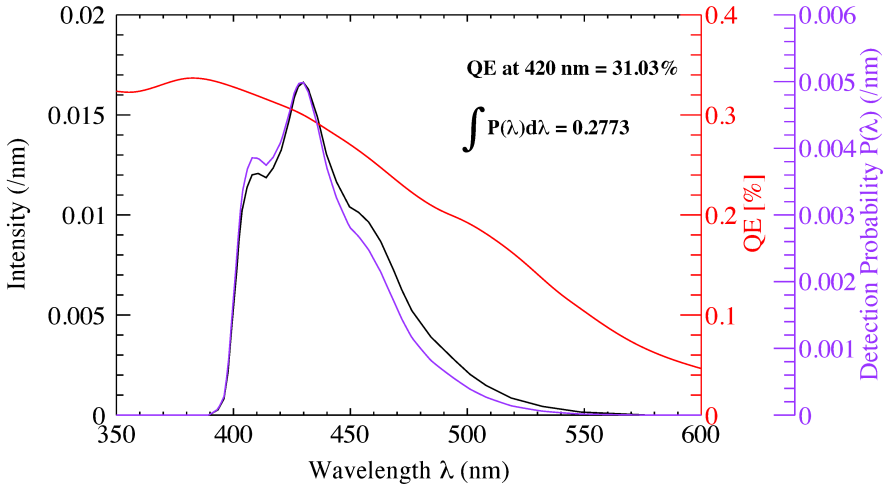

Fig. 4.6. The TPB emission spectrum at LAr temperature from Ref. [84] (black) and the PMT R11065 QE measured by the manufacturer. The total detection probability is calculated by multiplying the emission spectrum and PMT QE and shown in violet line.

called moving average window (MAW), goes above a threshold and falls below the half of its maximum value, as shown in Fig. 4.8.

Once trigger pulses from selected coincidence channel are occurred within 1 μs, an acquisition trigger pulse is generated and is distributed to each FADC board through NIM logic circuit. An inhibition time of typically 100 μs is introduced after each trigger among the circuit to prevent abnormally high trigger rate [4)].

[4)] Otherwise the input rate exceeds the board capacity, and binary can be broken.

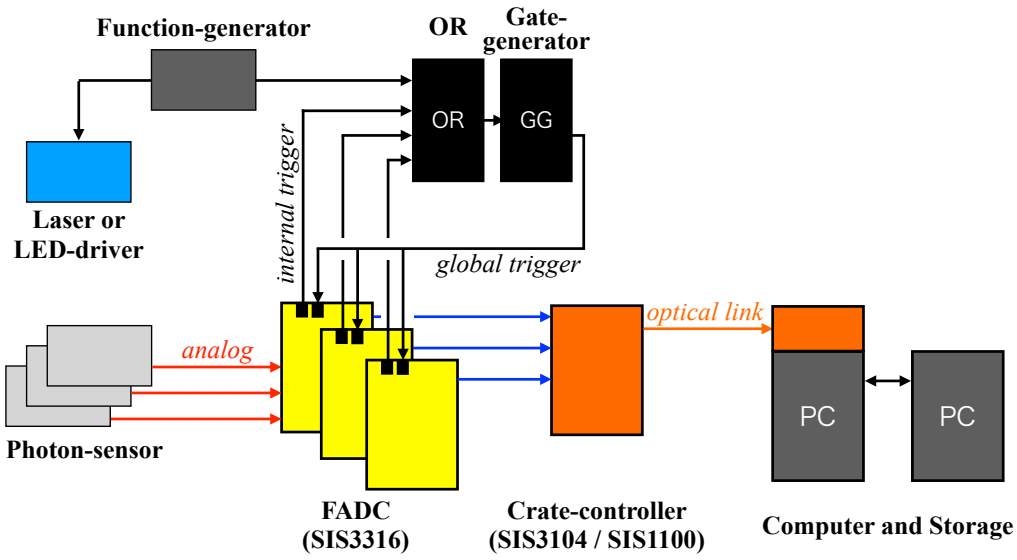

Fig. 4.7. Diagram of the DAQ system based on the SIS3316 FADC. Trigger pulses generated inside each board are once merged in OR then the acquisition trigger is returned to each board. Trigger pulse from function generator is also merged in OR following trigger the laser or LED-driver. The gate generator is implemented to prevent over-triggering.

4.4 Data process

Binary from the FADC board is first converted to ROOT file online and stored in a storage. A photon-counting algorithm is applied offline to the waveform for further analysis. The algorithm takes care of baseline subtraction and charge determination with following steps:

1. For each waveform, calculating the baseline from the pre-trigger window (i.e., negative time window), and subtracting it from the waveform.
2. Identifying the signal detection time (t_0) as the first sampling time above a threshold of 50% peak amplitude
3. For each sample above a software threshold, grouping three neighboring samples (one bin before and two bin after) and making a “clustering” waveform.
4. Determining the detection charge by integrating the waveform in the signal time interval.

Figure 4.9 shows a waveform before and after applying the photon-counting. Since any decoupling condenser does not exists inside the base, little distortion is seen and thus we do not need apply correction.

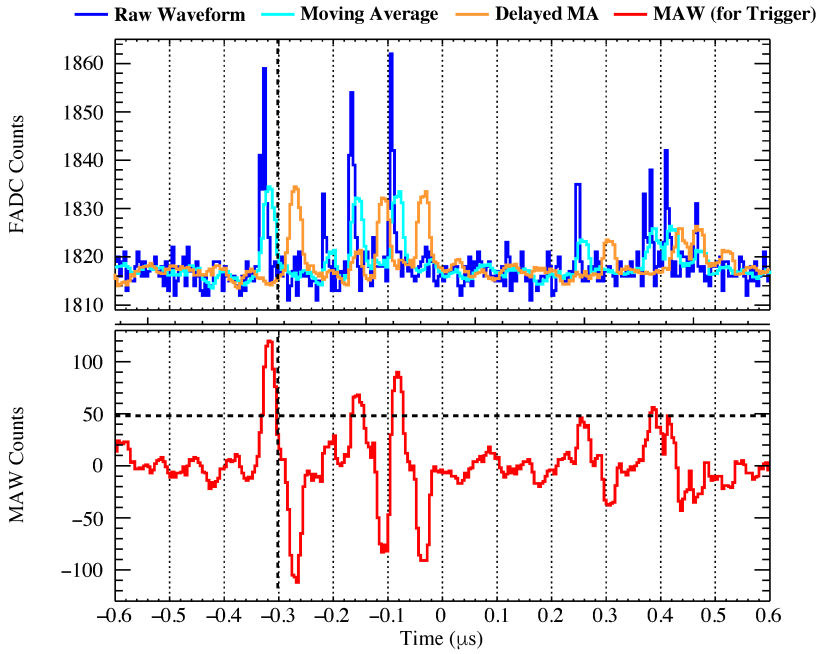

Fig. 4.8. Emulation of the FIR filter inside the FADC board. The MAW waveform, shown in bottom panel, is used for trigger decision. The horizontal dashed line represents a typical 1 p.e. threshold, and the vertical dashed lines represent the trigger timing in this case.

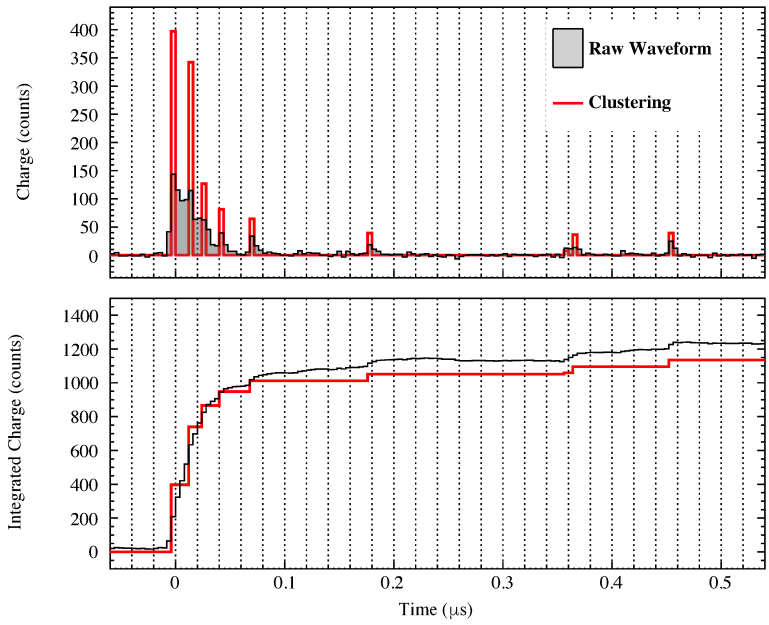

Fig. 4.9. Example of waveform before and after applying the photon-counting algorithm. Both the waveform in FADC sampling bin (top) and integrated charge (bottom) are shown.

4.5 The detectors

Section 4.5.1 describes a double-phase detector used in the measurement presented in Chapter 5, and Section 4.5.2 a single-phase detector used in Chapters 6 and 7. Both detectors share basic design concept and a number of detector parts. The former is characterized by the capability of forming high electric field up to 3 kV/cm, while the latter has light collection efficiency high enough to detect a few keV events.

4.5.1 Double-phase detector capable of forming high electric field

Figure 4.10 shows the double-phase TPC used in this study. It has an active region of diameter of 6.4 cm and height of 10 cm and an extraction region of height of 1 cm. Indium tin oxide (ITO)-coated quartz lightguides cap the regions and serve as anode or cathode. These regions are viewed by two R11065 PMTs on the lightguides. An extraction grid is placed at the top of the active region. The gap between the extraction grid and anode is 1 cm, and the liquid surface is kept centered between them. The inner gas pressure is stably kept at 1.5 atm. These active regions are contained within an approximately 3-cm-thick cylindrical PTFE sleeve. The ESR reflector coated with the TPB wavelength shifter lines the inner surface of the sleeve. The TPB layer also coats the ITO on the lightguides. Copper electrodes are embedded in the PTFE sleeve to maintain field uniformity in the active region. A Cockcroft-Walton (CW) circuit, shown in Fig. 4.11, is mounted in the liquid argon that surrounds the TPC. Each copper electrode, as well as the cathode and the wire grid, are electrically connected to each step of the circuit and supplied static voltage. The use of the CW circuit allows not only to supply stepped voltages to each electrode but also to avoid discharge at feedthrough and/or gaseous phase. An input AC voltage with maximum 0.3 kV_{pp} is introduced, resulting to 30 kV DC at the final step. The potential difference between the wire grid and the anode is 4.5 kV, corresponding to the electric fields of 3.6 and 4.5 kV/cm in liquid and gaseous regions, respectively.

The electric field inside the fiducial region is confirmed through the measurement of electron drift velocity in liquid argon. Figure 4.12 shows an example of drift time distribution at the field of 3.0 kV/cm taken with a γ-ray source. Since the edge (around $t = 39$ μs in this case) corresponds to events happened near the cathode, drift velocity is determined from the edge position. The measured drift velocity is shown in Fig. 4.13, along with a model from ICARUS and Walkowiak [61, 62]. Our data perfectly fit the model prediction curve.

The electron lifetime is measured with a collimated 1.3 MeV γ-ray from a ^{60}Co source. Figure 4.14 (right) shows the distribution of the S2 light yield at the field of 50 V/cm as a function of drift time, where the marker color represents the collimator position. High energy events are selected by the S1 signal cuts as indicated in Fig. 4.14 (left). They are backward scattered γ-rays by the Compton effect. After the selection, relative decrease of S2 yield indicates the electron lifetime τ_e as approximately 1.7 ms [5)]. Since the maximum drift time in the TPC is only 100 μs at 0.2 kV/cm, no corrections for the electron attenuation are applied in the following analysis.

[5)] This corresponds to the electronegative impurities concentration of approximately 2 ppb in oxygen equivalent.

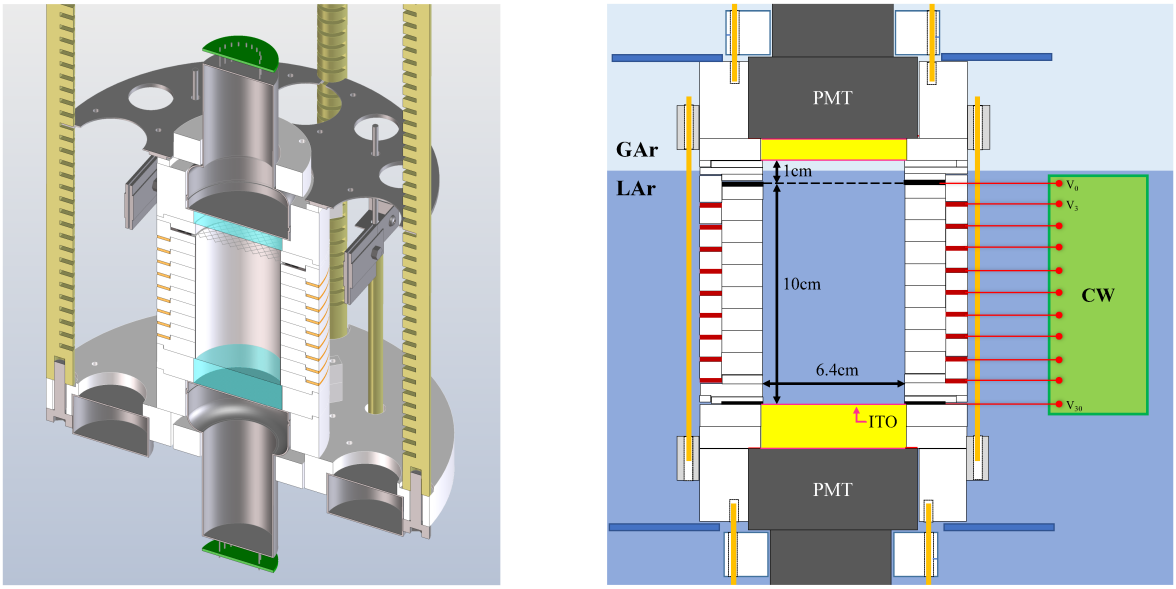

Fig. 4.10. Left: 3D CAD model view of the double-phase TPC used in this study. Right: schematic of the TPC. Each electrode is biased high voltage by corresponding step of the CW circuit.

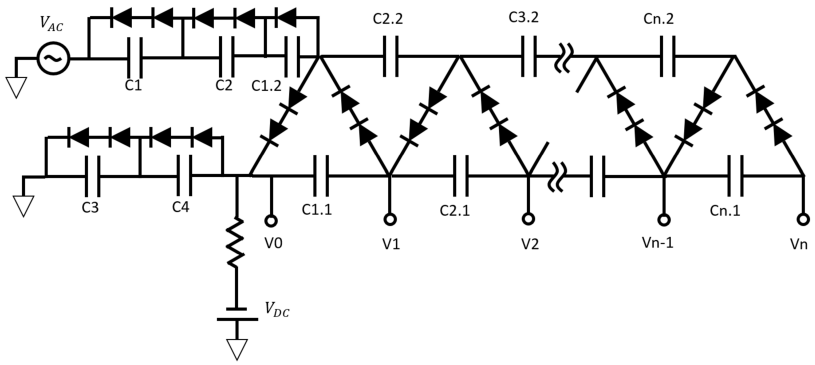

Fig. 4.11. Diagram of the CW circuit. The CW circuit boosts the input AC voltage V_{ac}. A negative voltage of V_{dc} is applied as the offset of the electrostatic potential of each step.

4.5.2 Single-phase detector with high light collection efficiency

The single-phase detector is shown Fig. 4.15, which is designed to minimize the loss of scintillation photons in their path and maximize light collection efficiency (LCE). The cylindrical fiducial volume of the detector has a diameter 6.4 cm and a length 5.0 cm, contained within the PTFE sleeve. Each end of the cylindrical volume is capped by the 3 in. R11065 PMTs whose windows are coated with the TPB. The PMTs are operated with a negative bias voltage of typically -1570 V. The field-shaping rings in the PTFE bulk are biased by the same voltage and ensure electric field inside the fiducial volume less than 1 V/cm so that the measurement under null electric field to be established. It is confirmed by finite element method by Femtet[87], as show in Fig. 4.16.

The whole sleeve is immersed in a liquid argon bath contained in the cryostat. Four 2 in. PMTs

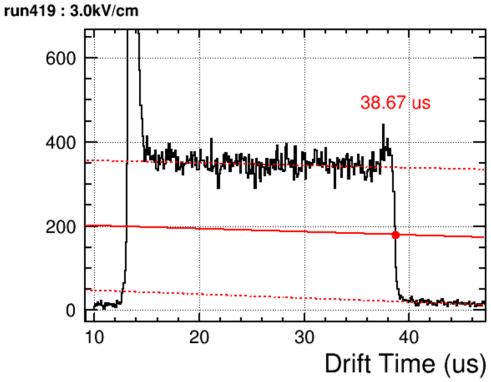

Fig. 4.12. Distribution of the drift time taken with a ^{22}Na source at $F = 3.0$ kV/cm[47]. Distribution excluding the edge region is fit with linear functions (dashed red lines). The solid line is the mean of the two functions, and the drift time corresponding to the cathode edge is determined as the cross point (red marker).

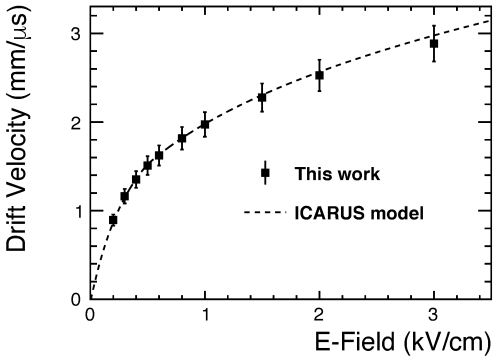

Fig. 4.13. Electron drift velocity measured with ^{22}Na ER events[86]. The dashed line is calculated using the model from ICARUS and Walkowiak[61, 62].

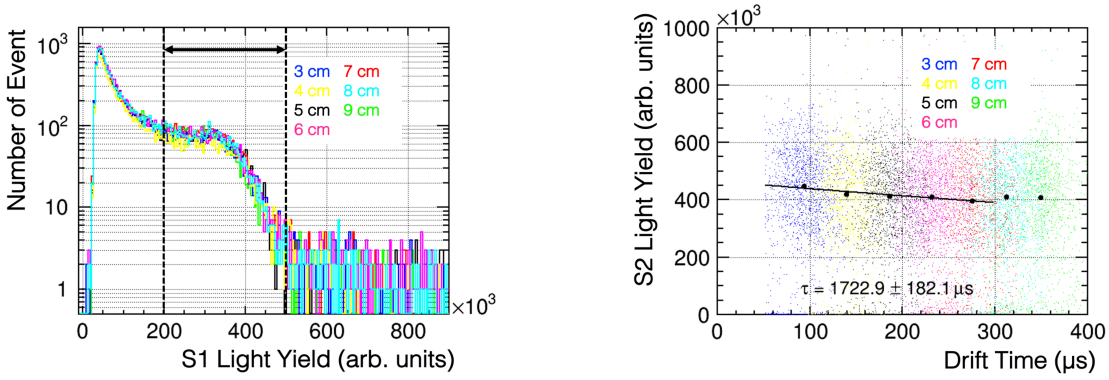

Fig. 4.14. Left: observed S1 spectra for collimated ^{60}Co data taken under $F = 50$ V/cm. The vertical dashed lines and horizontal arrow indicate the Compton-edge selection region. Right: the distribution in drift time versus S2 plain. The black points represent the mean S2 yields for the selected events.

(R6041-506) are implemented to view the liquid argon bath surrounding the fiducial volume, as shown in Fig. 4.17. These PMTs are located 20 cm above the fiducial volume and just below the liquid surface so that additional energy deposition in the outer region is tagged by a coincident scintillation signal. The windows of the outer PMTs are also coated with TPB. Positive voltage of about +800 V is biased, which is high enough to detect at least a few photoelectron signal.

The LCE of the single-phase detector is estimated by a toy MC simulation, based on the following assumption:

- initial point (i.e. interacting point) is distributed uniformly within the fiducial volume,

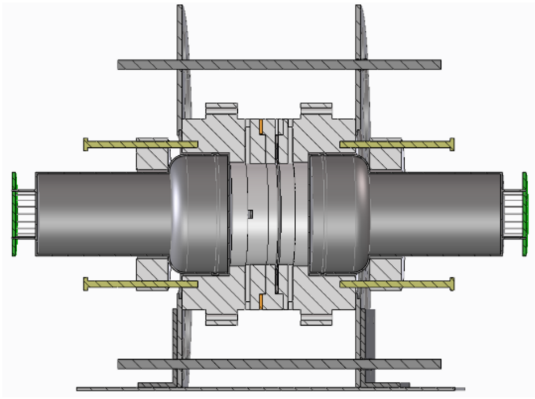

Fig. 4.15. 3D CAD model view of the single-phase scintillation detector.

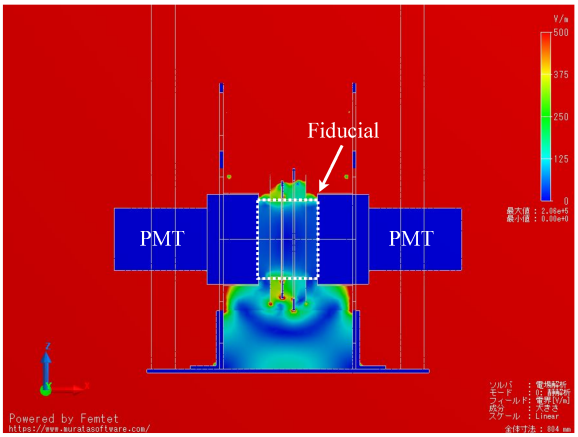

Fig. 4.16. Electric field inside the detector, calculated by finite element method by Femtet.

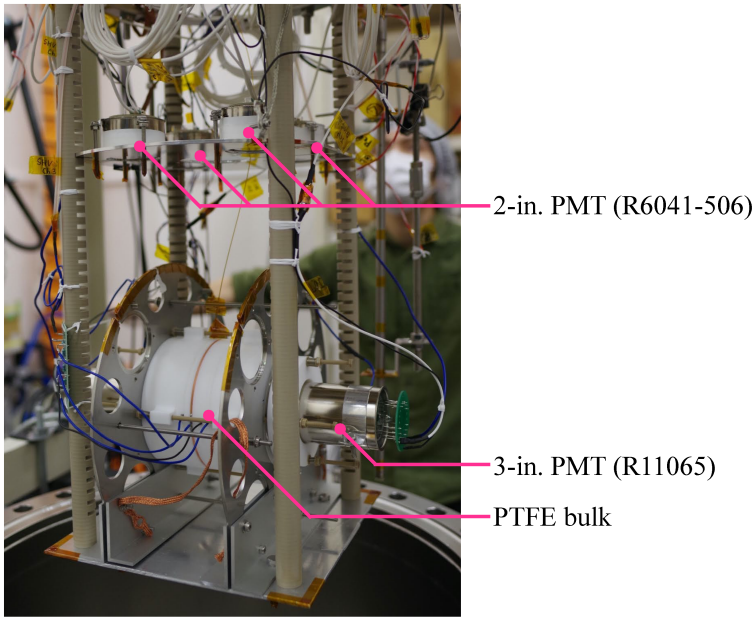

Fig. 4.17. Picture of the single-phase detector and outer-bath PMTs above it.

- visible photon after wavelength shifting emits uniformly,
- the visible photon reaching reflector is diffusely reflected (i.e., the emission angle is weighted by $\cos\theta$).

Figure 4.18 shows the expected number of reflection before reaching the PMT window (left) and photon transportation efficiency as a function of the initial position (center and right). Though the reflectivity is higher than bare reflector (ESR) due to the PTFE wall behind it, we conservatively assume it as the datasheet value (98%) and gets the detection probability as 97%. Position dependency of the LCE is computed to be small (less than 1%), therefore no correction for the interaction point is required.

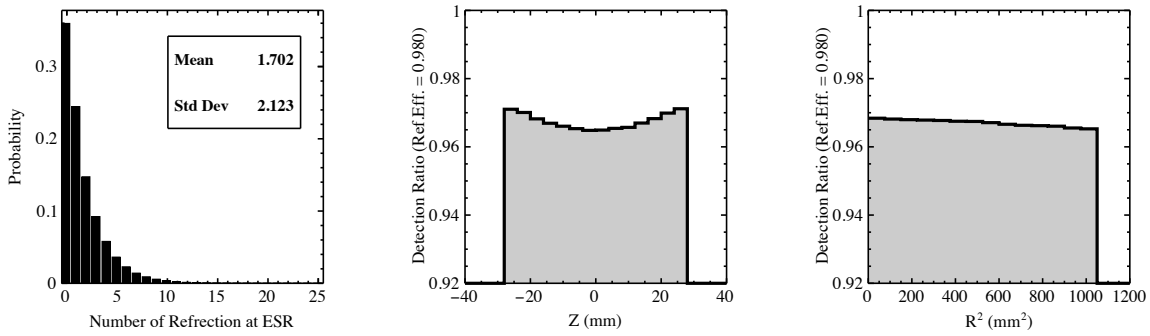

Fig. 4.18. Average number of reflection (left) and the transportation efficiency as a function of the initial position (center and right) computed from the toy MC.

CHAPTER 5

Measurement of the response for nuclear recoils under electric field

In liquid noble gas detectors, it is known that light and charge yields for NR per recoil energy depend on both the energy and applied electric field. The light yield relative to that of ER measured at null field is generally used to represent the dependence and is called "quenching factor" or $\mathscr{L}_{\text{eff}}$. Although it has measured by several groups [88, 89, 44, 90, 91, 46], the properties for electric fields greater than 1 kV/cm have not been explicitly discussed yet.

We present a simultaneous measurement of the light and charge yields resulting from a few tens of keV of NR under electric fields up to 3 kV/cm. The calibration data are taken with ^{252}Cf radioactive neutron source. Observed S1 and S2 spectra are simultaneously fit with spectra derived from Geant4-based MC simulation and a NR model. The NR model with a few parameters allows us to fully predict the light and charge yields at any recoil energy and any electric field between 0 to 3 kV/cm. The result can be used for designing the detector and for the interpretation of experimental data in WIMP dark matter search.

5.1 Measurement overview

5.1.1 Motivation

Precise measurement of liquid argon response on NR is essential to interpret the observables to a signal induced by WIMP. First of all, it determines the recoil energy. The inferred energy of a WIMP candidate event has information about the WIMP's mass. Once the NR signal is observed in a WIMP search, the NR energy spectrum can be compared to the expected spectrum from WIMP recoil, and it will either support or reduce likelihood of the WIMP interpretation. From the point of view of designing an experiment, comprehensive understanding of the response predicts signal yields and maximises the expected sensitivity.

As mentioned in Chapter 3, the response on NR is known to depend both on recoil energy and external electric field. Because of the nature that more than half of the NR energy is consumed by undetectable channel, calibrating the response is difficult, especially in low energy region. Additionally as the NR calibration is performed with elastic scattering of neutrons, it is difficult to explicitly use monoenergetic point, contrary to ER calibration using γ-ray source. Furthermore, little information has been available on the response under high electric field. The ionization yield under high field is especially a subject of

interest because the most sensitive search for a few GeV/c^2 WIMP has been conducted by using only the ionization signal[26].

Although comprehensive and systematical understanding of liquid xenon detector is successfully achieved within the NEST framework, little attempt has been made for liquid argon. A series of the understanding of the liquid xenon response has played an important role for WIMP search in liquid xenon detector. This work intends to establish such kind of a framework for liquid argon by taking an experimental data in wide energy and field ranges so that the sensitivities of current and future liquid argon experiments to be improved.

5.1.2 Procedure

The semi-empirical model accounting for the liquid argon response is already given in Section 3.2. As a reminder, the final expression of the observable quantities is as follows:

$$\mathrm{S1} = g_1 \times L \times f_l \times \frac{E_{\mathrm{NR}}}{W_s} \times \left[1 - \left(\frac{1}{1+\alpha}\right)(1-r)\right], \tag{5.1}$$

$$\mathrm{S2} = g_2 \times L \times \frac{E_{\mathrm{NR}}}{W_s} \times \left(\frac{1}{1+\alpha}\right)(1-r), \tag{5.2}$$

where,

$$f_l = \frac{1}{1 + k_B(\frac{dE}{dx})_{\mathrm{el}}}, \tag{5.3}$$

$$\alpha = \alpha_0^{\mathrm{NR}} \exp(-D_\alpha^{\mathrm{NR}} F), \tag{5.4}$$

$$r = 1 - \frac{\ln(1 + N_i \varsigma)}{N_i \varsigma}, \text{ and} \tag{5.5}$$

$$\varsigma = \gamma^{\mathrm{NR}} F^{-\delta^{\mathrm{NR}}}. \tag{5.6}$$

This work determines the parameters in the model by both S1 and S2 spectra taken under various electric field. The method is as follows.

For NR at a null field, the recombination probability r is expected to be unity; therefore, k_B is the only free parameter to account for the quenching. As applying the electric field, r is expected to decrease, resulting in the suppression of S1 signal and production of more S2 signal. The related parameters of this process are α_0^{NR}, D_α^{NR}, γ^{NR}, and δ^{NR}. In the previous measurements, a value of $\alpha \approx 1$ is suggested to describe the observed data [44, 46]. We interpret this effect such that the value to be approximated at the lower electric field and this constrains α_0^{NR} to 1. As will be shown in Section 5.4, we first determine k_B from the S1 spectrum of the null field data sample, and then D_α^{NR}, γ^{NR}, and δ^{NR} are obtained simultaneously from both S1 and S2 spectra under electric fields ranging from 0.2–3.0 kV/cm.

A 511-keV γ-ray line from a ^{22}Na source is chosen as the reference ER events of the $\mathscr{L}_{\mathrm{eff}}$ in this measurement. The 511-keV line is one of the most suitable point for the reference because several works have commonly presented the observed light yield at this point. The observed S1 light signal ($\mathrm{S1_{Na}}$) by

the energy deposition of $E_{\mathrm{Na}} = 511$ keV from ER at null field is represented as following:

$$\mathrm{S1_{Na}} = g_1 \frac{E_{\mathrm{Na}}}{W_s}\left(1 - \frac{1 - r_{\mathrm{Na}}}{1 + \alpha^{\mathrm{ER}}}\right), \tag{5.7}$$

where r_{Na} is the recombination probability for the ^{22}Na line. From Eqs.(5.1) and (5.7), the scintillation efficiency $\mathscr{L}_{\mathrm{eff}}$ referenced to the 511-keV γ-ray line of a ^{22}Na source is given by

$$\mathscr{L}_{\mathrm{eff}}(E_{\mathrm{NR}}, F) = \frac{(\mathrm{S1}/E_{\mathrm{NR}})}{(\mathrm{S1_{Na}}/E_{\mathrm{Na}})} = \frac{n_{\mathrm{ph}}}{E_{\mathrm{NR}}/W_s}\left(1 - \frac{1 - r_{\mathrm{Na}}}{1 + \alpha^{\mathrm{ER}}}\right). \tag{5.8}$$

Assuming that r_{Na} is unity, it is then

$$\mathscr{L}_{\mathrm{eff}}(E_{\mathrm{NR}}, F) = \frac{n_{\mathrm{ph}}}{E_{\mathrm{NR}}/W_s}. \tag{5.9}$$

5.1.3 Review of the previous measurement

This section reviews measurements of the scintillation and/or ionization yields for NR in the last decade intended to apply to WIMP dark matter and CEvNS searches.

Figure 5.1 shows the $\mathscr{L}_{\mathrm{eff}}$ at null field measured by SCENE [44], MicroCLEAN [89], W.Creus *et al.* [90], and ARIS [46]. All of these measurements expose mono-energy neutron to their detectors and tag the elastically scattered neutron with additional detectors (such as organic scintillator) to kinematically determine the recoil energy. The incident neutrons are generated by either D-D reaction generator (MicroCLEAN and W.Creus *et al.*), proton beam through ^{7}Li$(p,n)^7$Be reaction (SCENE), or ^{7}Li beam through ^{1}H$(^7\mathrm{Li},n)^7$Be reaction. Since the recoil energy is kinematically uniquely determined, this method is capable of model-independent measurement. Main challenge comes from the γ-ray background associated with the neutron sources. Lowering the energy threshold is another challenge because reducing the angle of the tagging detector increases the uncertainty of the recoil angle.

Field dependence of the scintillation yield is measured by SCENE and ARIS. Figure 5.2 shows the $\mathscr{L}_{\mathrm{eff}}$ measured by SCENE experiment at different field strengths. The results are published under electric field up to 1.0 kV/cm for a NR energy range of 7.1–117.8 keV.

The ionization yield is measured by SCENE (under electric field up to 0.5 kV/cm and a NR energy range of 10–57 keV), Bondar *et al.* (up to 2.3 kV/cm and the energy of 80 and 233 keV) [92, 93], and Joshi *et al.* (up to 2.1 kV/cm and 6.7 keV) [45]. Figures 5.3 and 5.4 show the ionization yields of SCENE and Joshi *et al.*, respectively. SCENE measures it with the identical data used in the $\mathscr{L}_{\mathrm{eff}}$ measurement. Joshi *et al.* measures the end point of the S2 spectrum produced by the 70-keV quasimonoenergetic neutron beam. The low energy beam is generated by taking advantage of interference notches of narrow resonance for neutron scattering cross section in iron [94].

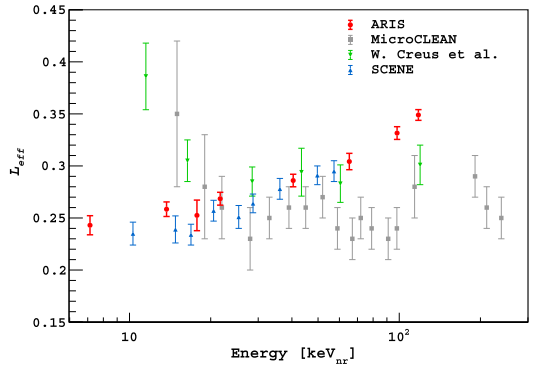

Fig. 5.1. The quenching factor $\mathscr{L}_{\text{eff}}$ at null field in literature[89, 44, 90, 46]. The figure is taken from Ref. [46].

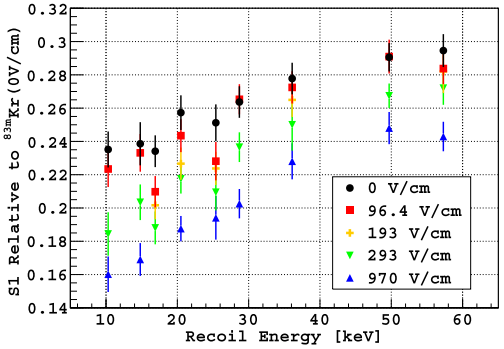

Fig. 5.2. Field dependence of the $\mathscr{L}_{\text{eff}}$ as a function of NR energy measured by SCENE. The figure is taken from Ref. [44].

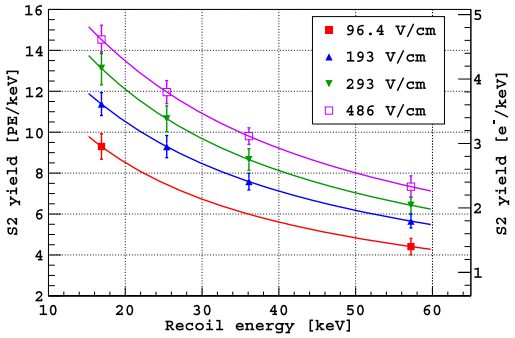

Fig. 5.3. Field dependence of the ionization yield as a function of NR energy measured by SCENE. The figure is taken from Ref. [44].

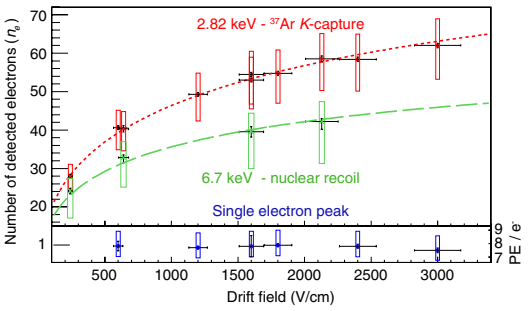

Fig. 5.4. Field dependence of the ionization yield for 6.7 keV NR (green) measured by Joshi *et al.* The figure is taken from Ref. [45].

5.2 Apparatus

5.2.1 Detector and geometry

The measurement is performed with the double-phase TPC using ^{252}Cf neutron source. Figure 5.5 shows a schematic of the geometry where the detector is exposed to fast neutron. The detail of the TPC is described in Section 4.5.1. A ^{252}Cf neutron source with a spontaneous fission rate of approximately 1×10^5 fission/s is placed at a distance of 1.01 ± 0.01 m from the center of the TPC. A NaI(Tl) scintillator (2×2 in.^{2} cylinder) located beside the neutron source provides timing information by detecting associated γ-ray. A lead shield with approximately 10 cm thickness surrounds the vessel to suppress background from ambient γ-rays. Other background arises because of neutrons from the ^{252}Cf source; this background from the ^{252}Cf source reaches the active region via a single or multiple scattering at any part of the materials in the laboratory. Water and polyethylene shields are placed to suppress these scattered neutrons.

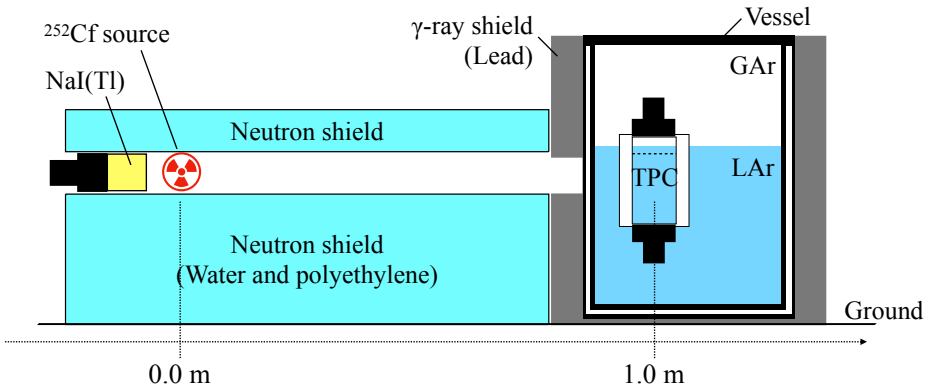

Fig. 5.5. Schematic of the experimental apparatus for the NR measurement.

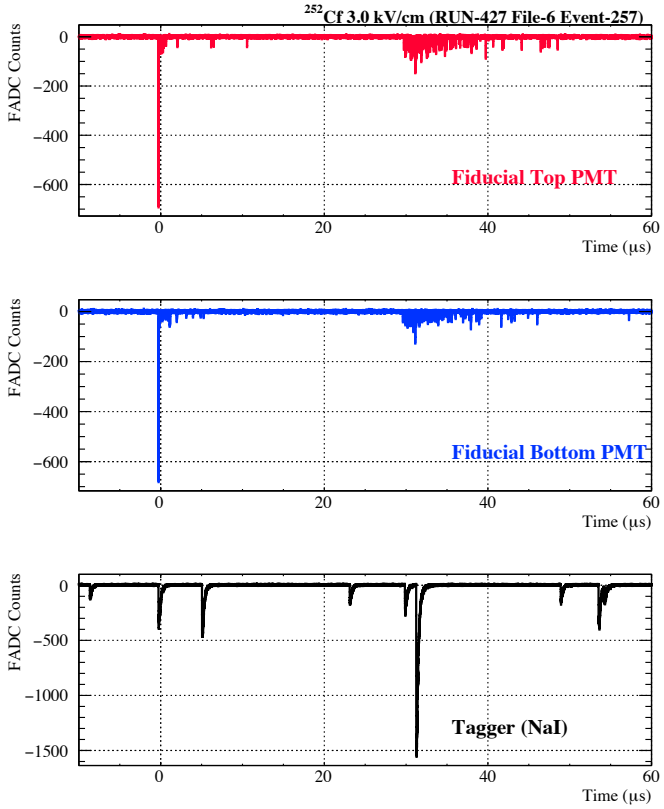

Fig. 5.6. Observed waveforms of a typical NR event taken in this measurement. This event is reconstructed as S1 $\approx$ 120 p.e. and S2 $\approx$ 280 p.e..

The data acquisition is triggered by the coincidence between the TPC PMTs and NaI(Tl) scintillator signals within a 1 μs window. Figure 5.6 is a typical NR event taken at 3.0 kV/cm. The event is triggered by S1 signal at $t = 0$ in coincidence with the NaI(Tl) signal, and corresponding S2 signal appears around $t = 35$ μs.

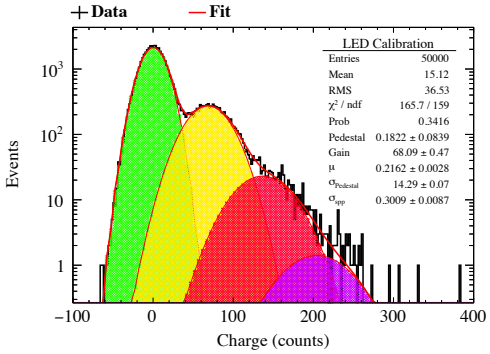

Fig. 5.7. A typical charge distribution of the gain calibration data taken with pulsed LED light. The bias voltage of 1650 V is applied which is the same as the detector operation. The red line represents the fitting function and the other colored lines represent its components.

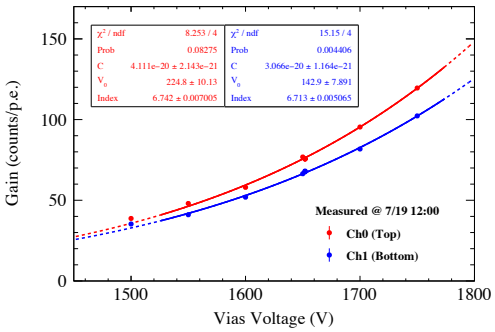

Fig. 5.8. Summary of the PMT gain as a function of the bias voltage.

5.2.2 PMT calibration

The PMT gain is calibrated using a blue light-emitting diode (LED) powered by a pulse generator, and it shows the decline of about 15% over the course of eight days of data taking period. The gain value at the operation voltage (1650 V) is determined by fitting the charge distribution to a model function based on Poisson distribution convoluted by Gaussian function, as shown in Fig. 5.7. As the cross check of the calibration, the gain measurement is performed at the bias voltages 1550 to 1750 V. Figure 5.8 shows the results of the voltage scan. Each point of the gain is fit with an empirical function,

$$G(V) = C \times (V - V_0)^{idx} \tag{5.10}$$

where V is the bias voltage and, C, V_0, and idx are fit parameters. The calibration results performed at beginning and end of the period are shown in Fig. 5.9 (filled stars).

In addition, the PMT gain is independently monitored throughout the data taking period using the liquid argon data, though the monitoring methods do not have enough reliability to determine the absolute value. The single photoelectron waveform is extracted from two time windows of the liquid argon data; pre-trigger region ($[-5\ \mu s, 0\ \mu s]$) and S1-tail region ($[5\ \mu s, 10\ \mu s]$). The photoncounted charge distribution for the two regions are shown in Fig. 5.10. By fitting the single photoelectron peak with Gaussian the PMT gain is evaluated, and the result is shown in Fig. 5.9 (open circles and open squares, respectively). There may be systematic shift in this gain estimation methods, but the time dependency is consistent to the gain correction curve interpolated by the LED calibration. Among the two time windows, the S1-tail region seems to be more sensitive to the absolute value due to the higher signal-to-noise ratio. We apply time-dependent gain correction with a linear function, and assign 5% of uncertainty.

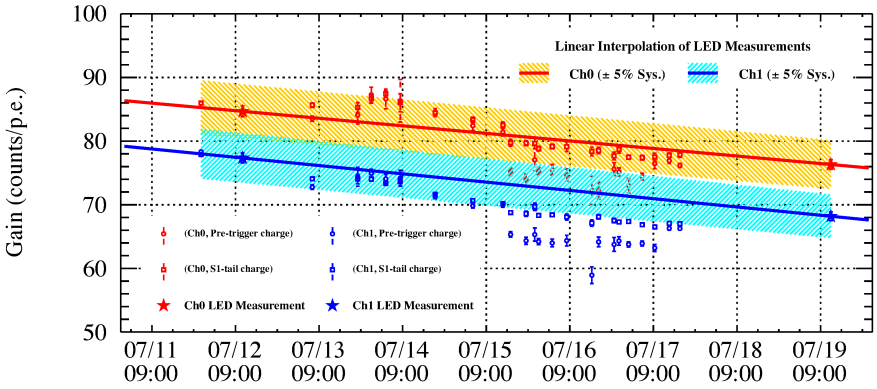

Fig. 5.9. Summary of the time evolution of the PMT gain. The red and blue points are the measured gain for top and bottom PMTs, respectively. Time-dependent linear correction functions are determined from the two LED measurements (star) with 5% uncertainty (shown with band).

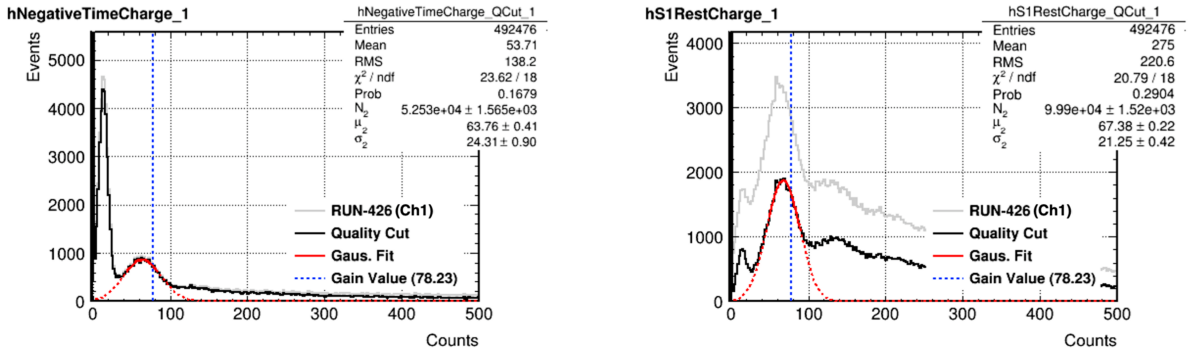

Fig. 5.10. Charge distributions and Gaussian fittings of pre-trigger (left) and S1-tail (right) regions.

5.2.3 Energy Calibration

Energy calibration is performed with 511-keV γ-ray from a ^{22}Na source. The 511-keV γ-ray events are selected by tagging backwards going 511-keV γ-ray with the NaI(Tl) scintillator. Figure 5.11 shows the S1 spectrum of the ^{22}Na data taken at a null field by requiring the time of flight (TOF) between LAr-TPC and NaI(Tl) as nearly 0. We determine the observed S1 signal per ER energy at a null field, $S1_{Na}/E_{Na}$, as 5.9 ± 0.3 p.e./keV$_{ee}$ by fitting 511-keV full-absorption peak with a Gaussian plus exponential function. Assuming that ionization electron-ion pairs in the full-absorption event fully recombine and contribute to the S1 signal, corresponding scintillation LCE g_1 of the detector is calculated as 0.12 ± 0.01.

5.3 Event reconstruction and selection

The energy of the incident neutron from the ^{252}Cf source is reconstructed based on TOF (the time difference between the NaI(Tl) and TPC signals). The arrival time of a pulse is identified as the first

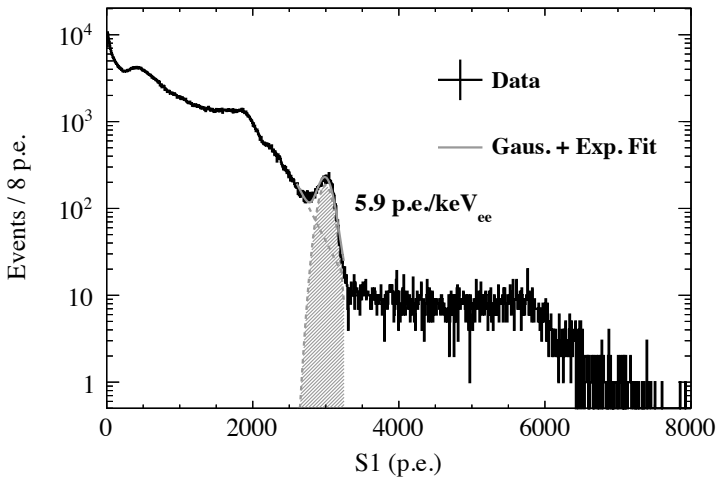

Fig. 5.11. S1 spectrum for the energy calibration at a null field with the ^{22}Na source. Also shown is the Gaussian plus exponential fitting around the 511-keV full-absorption peak.

digitized sample above a threshold of 50% peak amplitude. The S1 is reconstructed as an integrated charge in the time interval between -0.04 and 5.0 μs of the pulse arrival time. The PSD parameter "slow/total" is defined as the fraction of light detected after 0.12 μs of the S1 signal. The S2 is reconstructed as an integrated charge after 10 μs in the data acquisition window.

Events of the data samples are selected by requiring one proper S1 pulse: the event is triggered at proper timing, the event does not have any charge signal before the trigger, and the top-bottom ratio of the event (i.e., the ratio of the observed light yield at the top-side PMT to the bottom-side PMT) is reasonable compared to the majority of the observed signal. For data samples taken under the electric fields, an additional requirement to have only one proper S2 pulse is applied to select single scattered NR events.

Figure 5.12 (left) shows a distribution of the PSD parameter versus the TOF with data taken under the electric field of 3.0 kV/cm, after requiring the observed S1 yield to be greater than 30 p.e. The cluster around (TOF, PSD) = $(0.0, 0.7)$ comes from the ER events by the fission γ-ray, and that around (TOF, PSD) = $(0.05\ \mu\text{s}, 0.25)$ comes from the NR events by the ^{252}Cf fast neutron. Since the fast neutron induces γ-rays within $O(0.1\ \mu\text{s})$ through the interaction with detector components (such as $(n, n'\gamma)$ reaction with ^{19}F in PTFE), there are events around (TOF, PSD) = $(0.05\ \mu\text{s}, 0.7)$ [1)]. Figure 5.12 (right) shows a distribution of the PSD parameter versus observed S1 yield with the same data, after requiring the TOF to be in the range of 43–111 ns, corresponding to an incident neutron energy of 0.41–2.44 MeV. A PSD band cut ($\pm 1\sigma$) is imposed to select NR events and suppress the ER contamination from the induced γ-rays. In addition, $\log_{10}(\text{S2/S1})$ band cut is imposed loosely ($\pm 2\sigma$) to reject events having abnormally large S2 yield, as shown in Fig. 5.13. These rejected events are considered to consist of multiple scattered events, i.e., event in which an incoming neutron is simultaneously scattered within small distance, or event in which an neutron and the associated γ-ray interact at nearby point.

A contribution from accidental coincidence background is estimated from a negative TOF window of

[1)] The γ-rays from this reaction can be used as the calibration sources. See Chapter 6.

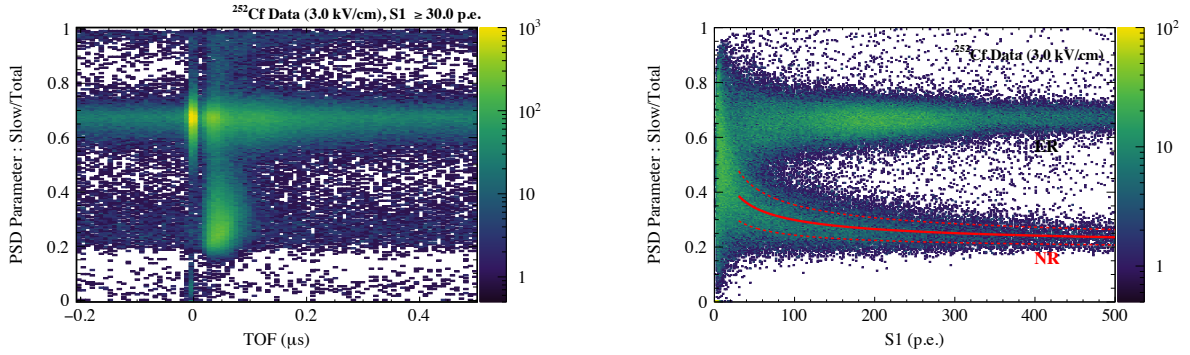

Fig. 5.12. Distribution of TOF versus the PSD parameter slow/total (left, after requiring the observed S1 yield to be greater than 30 p.e.) and the observed S1 yield versus the slow/total (right, after requiring the incident neutron energy as 0.41–2.44 MeV based on TOF) with data taken with the ^{252}Cf neutron source under the electric field of 3.0 kV/cm. Two dashed lines in the right panel correspond to the band for PSD cut ($\pm 1\sigma$).

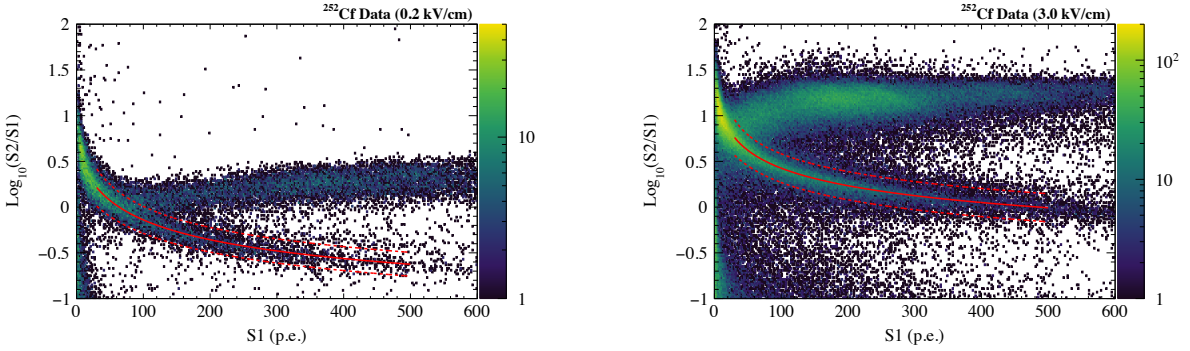

Fig. 5.13. The $\log_{10}$(S2/S1) distributions as a function of S1 yield taken under electric fields of 0.2 (left) and 3.0 kV/cm (right) without the PSD cut . Two dashed lines in each panel correspond to the band for $\log_{10}$(S2/S1) cut ($\pm 2\sigma$).

-0.9 to -0.2 μs. As shown in Fig. 5.14, contribution from the accidental background is estimated as 2–3% in total and about 30% for the longest TOF bin (i.e. lowest neutron energy) used in the following analysis.

The ER contamination is estimated based on the PSD distribution. Figure 5.15 (left) shows the distributions at 3.0 kV/cm after requiring the $\log_{10}$(S2/S1) selection. Assuming that the slow/total distribution is modeled as Gaussian, it is estimated as less than 1% for all bins used in the fitting. The slow/total distribution in the lowest energy range (S1 = [30, 40] p.e.) is shown in Fig. 5.15 (right).

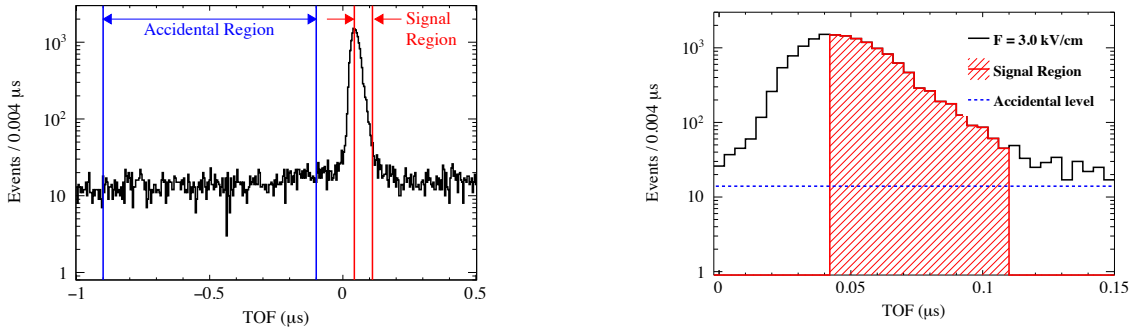

Fig. 5.14. TOF distribution and definition of the signal and accidental regions. The accidental contamination is estimated from TOF = -0.9–-0.1 μs, as shown in the left panel, and the level of the accidental events is represented as the dashed line in the right panel. The data shown is taken at $F = 3.0$ kV/cm.

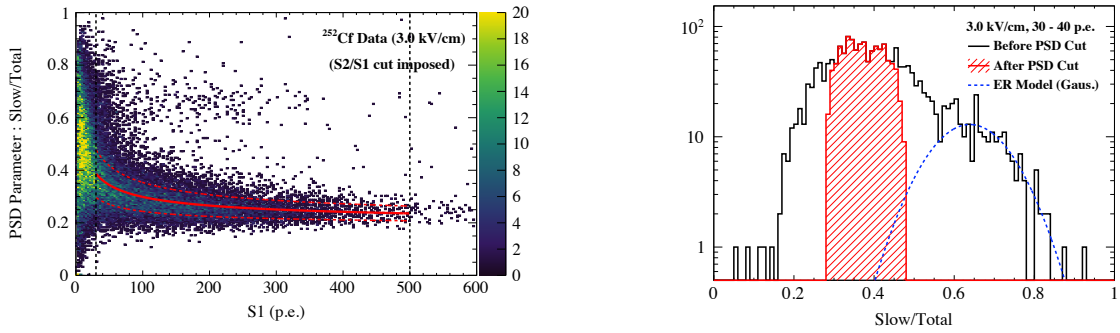

Fig. 5.15. Left: the slow/total distribution as a function of S1 yield taken under electric field of 3.0 kV/cm after requiring the $\log_{10}$(S2/S1) selection. Right: the 1-dimension projection in the the lowest range of S1 = 30–40 p.e.

5.4 Method

5.4.1 Monte Carlo

Energy deposits by the neutrons are simulated in a Geant4-based [95, 96, 97] MC simulation of the experimental apparatus, using a neutron spectrum of ^{252}Cf in Ref. [98] and nuclear data library files G4NDL 4.5 [99, 100, 101] with revised differential cross sections for elastic scattering from Ref. [102]. This revised library solves a problem with the nuclear data library for neutrons in the resolved resonance region and has an effect for the back-scatter edge to be more moderate. This is demonstrated in Fig. 5.16, where NR energy spectra inside a large liquid argon volume from monoenergy neutron beam are compared before and after applying the revision [2)]. We confirmed the validity of the simulation using a comparison of the TOF distribution between data and MC in Fig. 5.17. The resolution of TOF is estimated as 2 ns. The observed events in data at around TOF = 0 mainly consist of low-energy (S1 $\lesssim$ 30 p.e.) events. These events are considered as contamination from ER events and not used in this analysis.

[2)]The revised package is provided by Dr. Alan Robinson from Université de Montréal

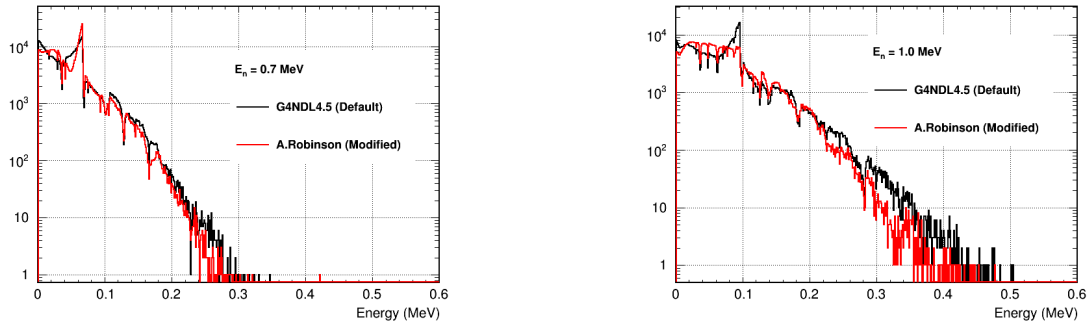

Fig. 5.16. Comparison of the NR energy spectra inside a large LAr volume from 0.7 MeV (left) and 1.0 MeV (right) monoenergy neutron beams before (black line) and after (red) applying the G4NDL modification package.

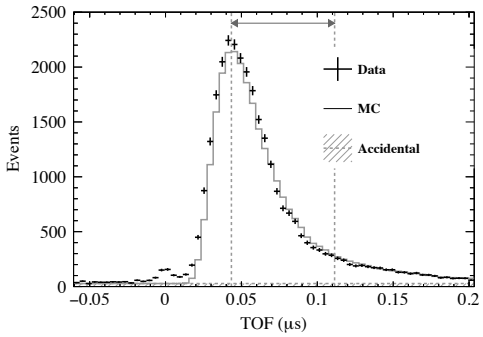

Fig. 5.17. Comparison between data and the MC TOF spectra. The vertical dashed lines and gray arrow represent the TOF range where the simultaneous fit is performed. Contamination from ER events that are not simulated in MC produces the peak around TOF = 0.

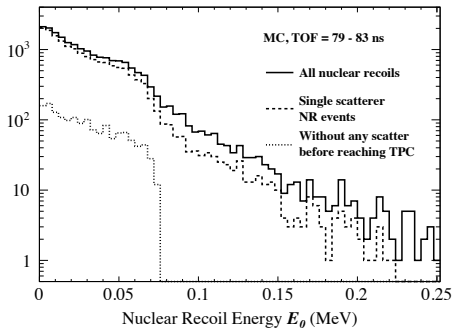

Fig. 5.18. Energy deposition spectra derived from Geant4-based MC simulation. Shown are all NR in the LAr active region (solid line), contributions from single scattered NR events (i.e., neutrons that scattered only once in the active region) (dashed line), and neutrons that reached without any scattering in any part of the apparatus before reaching the active region (dotted line).

Figure 5.18 shows the energy deposition (E_0) distribution from the MC simulation for the TOF range of 79–83 ns, corresponding to a neutron energy of about 0.75 MeV. While the ^{252}Cf source has a continuous neutron spectrum, a backscatter edge would be visible by constraining the TOF. The edge of each TOF bin is useful to resolve degeneracy between the free parameters as described later. The leading contribution is expected from the neutrons that are scattered more than once in any part of the apparatus (such as neutron/gamma shieldings, the vessel, and the liquid argon that surrounds the TPC) before reaching the active region. However, the position of the backscatter edge is not affected, as shown in Fig. 5.18.

5.4.2 Data fitting

The parameters in the NR model are measured by fitting the obtained S1 and S2 spectra of each TOF bin (4 ns interval) with the spectra derived from the MC simulation and the NR model described in Section 5.1.2. The fit is simultaneously performed in the TOF range of 43–111 ns (total 17 TOF bins). The MC spectra of both S1 and S2 are convolved with Gaussian resolution functions of deviations

$$\sigma_{\mathrm{S1}}\ [\mathrm{p.e.}] = \sqrt{(6.32\times10^{-1})\times \mathrm{S1}\ [\mathrm{p.e.}] + 1.10\times10^{-2}\times(\mathrm{S1}\ [\mathrm{p.e.}])^2}, \tag{5.11}$$

$$\sigma_{\mathrm{S2}}\ [\mathrm{p.e.}] = \sqrt{2.73\times10^{-2}\times(\mathrm{S2}\ [\mathrm{p.e.}])^2}, \tag{5.12}$$

where the parameters of S1 and S2 are determined from the null field data and 3.0 kV/cm data, respectively. The fit range for the S1 spectra at null filed is from 50 to 700 p.e. The range for under finite filed are from 30 to 500 p.e. for S1 spectra and 0 to 500 p.e. for S2 spectra. For each MC event, the probability to fall in the ranges are calculated based on the Gaussian resolution functions. Figure 5.19 shows an example of the S1 spectrum and the fitted MC spectrum for a TOF bin of 79–83 ns at a null field. Figure 5.20 shows the spectrum for the entire TOF range of interest with the 17 MC spectra for each TOF bin. The top panels of Fig. 5.21–5.25 show examples of the S1 and S2 spectra and the fitted MC spectra for a TOF bin of 79–83 ns under the electric field from 0.2 to 3.0 kV/cm. Corresponding spectra for the entire TOF range of interest with the respective 17 MC spectra are shown in the bottom panels. The distribution of $\chi^2_i = ((N^{\mathrm{obs}}_i - N^{\mathrm{MC}}_i)/\sqrt{N^{\mathrm{obs}}_i})^2$ of each bin are shown in Fig. 5.26, where N^{obs}_i and N^{MC}_i represent the numbers of observed and predicted events in i-th bin. The total χ^2/ndf[3)] of the fit for null field data (which determines k_B as mentioned before) is 1254/806 = 1.56, and that of the simultaneous fit for field data (which determines D_α, γ, and δ) is 6307/4090 = 1.54. As shown in Fig. 5.26, the fit reasonably explains the data for whole energy and field ranges, although the goodness-of-fit is tiny. The χ^2/ndf distributions of each parameters are shown in Fig. 5.27.

We should note that since the spectra for the entire TOF range of interest have a smooth spectrum shape, as shown in Fig. 5.20 and, for instance, the bottom panel of Fig. 5.25, it is difficult to uniquely resolve the degeneracy between the free parameters by the inclusive shape. However, the backscatter edge of each TOF bin makes it possible to access each parameter. This is because the edges characterize a light and charge yield dependency on the NR energy. While an interpretation of each parameter from physical point of view is introduced in Section 3.2, their impacts on the spectrum shapes can be interpreted as follows. As the parameter k_B is the only parameter accounting for the S1 spectra at null field, it explains the energy dependency of the back-scatter edge in the absence of external field. Field and energy dependencies of the signal yields under electric field are predominantly covered by the parameters from the TIB model, γ^{NR} and δ^{NR}, since they appear in the form of $N_i\gamma^{\mathrm{NR}}F^{-\delta^{\mathrm{NR}}}$. The parameter D^{NR}_α mainly affects the field dependency of the back-scatter edges.

We also note that the fit range of the S2 spectra is constrained to below 500 p.e. as the discrepancy between data and the MC simulation is observed above 500 p.e. This discrepancy is presumably due to the multiple scattered events that survive the event selections mentioned above.

[3)] number degree of freedom

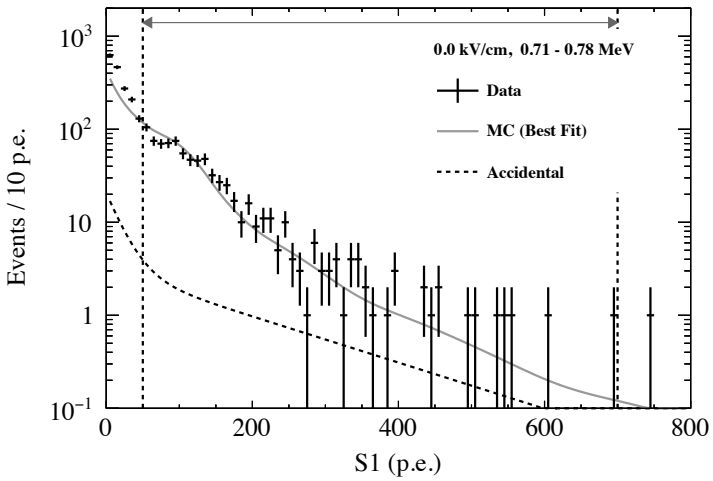

Fig. 5.19. S1 spectrum of the NR data sample taken at a null field and MC-derived spectrum simultaneously fitted to experimental data for TOF in the range of 79–83 ns (corresponding to a neutron energy of about 0.75 MeV). The area indicated by vertical dashed lines and gray arrow represents the fitting range.

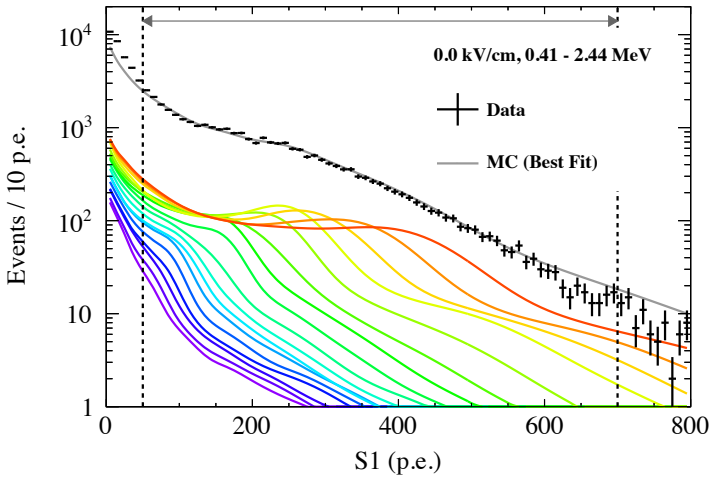

Fig. 5.20. S1 spectrum of the NR data sample taken at a null field (black point) and MC-derived spectrum simultaneously fitted to experimental data (gray line) for the entire TOF range of interest. Also shown are MC-derived spectra (colored lines) representing the contribution of each TOF bin, from 43–47 ns (red, corresponding to a neutron energy of about 0.4 MeV) to 107–111 ns (violet, 2.4 MeV). The area indicated by vertical dashed lines and gray arrow represents the fitting range.

As a demonstration, Fig. 5.28 shows the ^{252}Cf data for all the five values of an electric field with an overlay of the prediction (shown by solid line) in $\log_{10}$(S2/S1) versus the S1 plane. Reasonable agreements of the mean value of the $\log_{10}$(S2/S1) distributions are achieved at all the five electric fields.

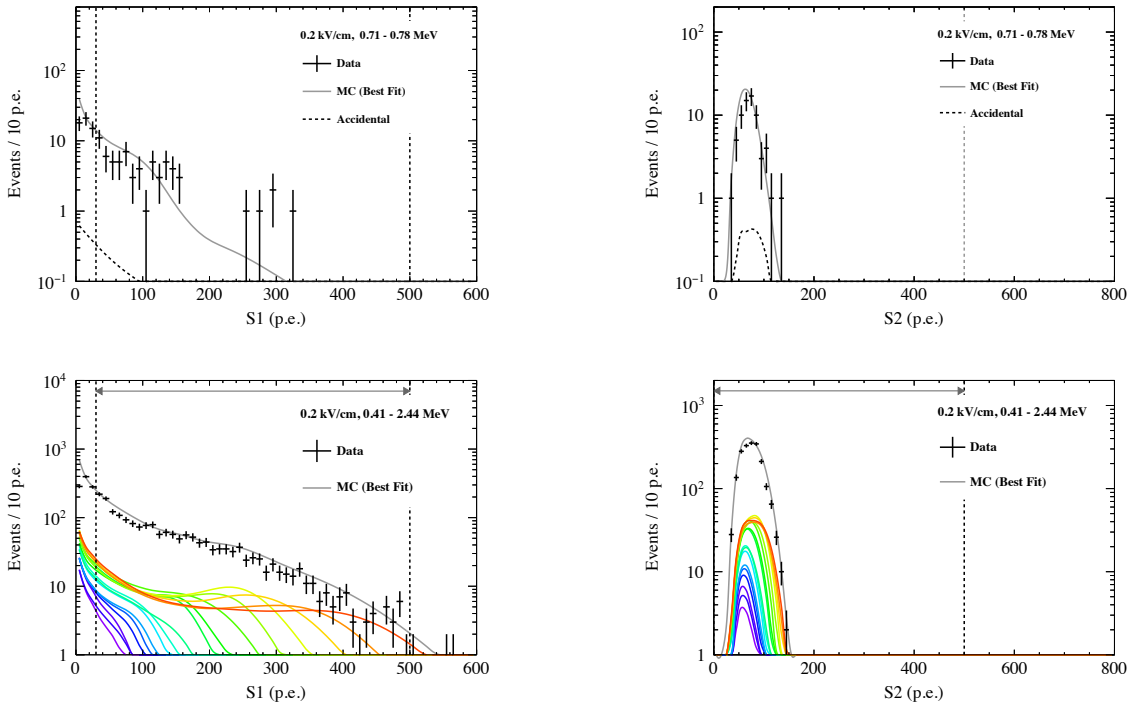

Fig. 5.21. Top: S1 (left) and S2 (right) spectra of the NR data sample taken at the electric field of 0.2 kV/cm and MC-derived spectra simultaneously fitted to experimental data for TOF in the range of 79–83 ns (corresponding to a neutron energy of about 0.75 MeV). The areas indicated by vertical dashed lines and gray arrow represent the fitting range. Bottom: The S1 (left) and S2 (right) spectra for entire TOF range of interest. The figure descriptions are the same as in Fig. 5.20.

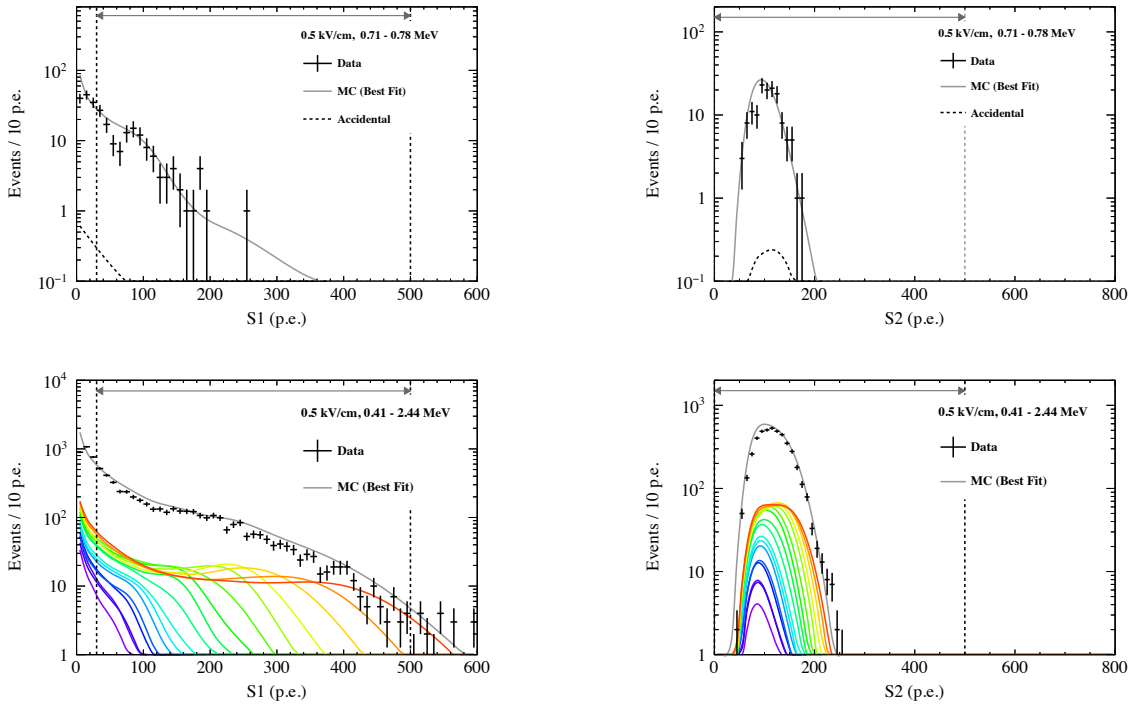

Fig. 5.22. The S1 (left) and S2 (right) spectra taken at the electric field of 0.5 kV/cm and MC-derived spectra simultaneously fitted to experimental data. The figure descriptions are the same as in Fig. 5.21.

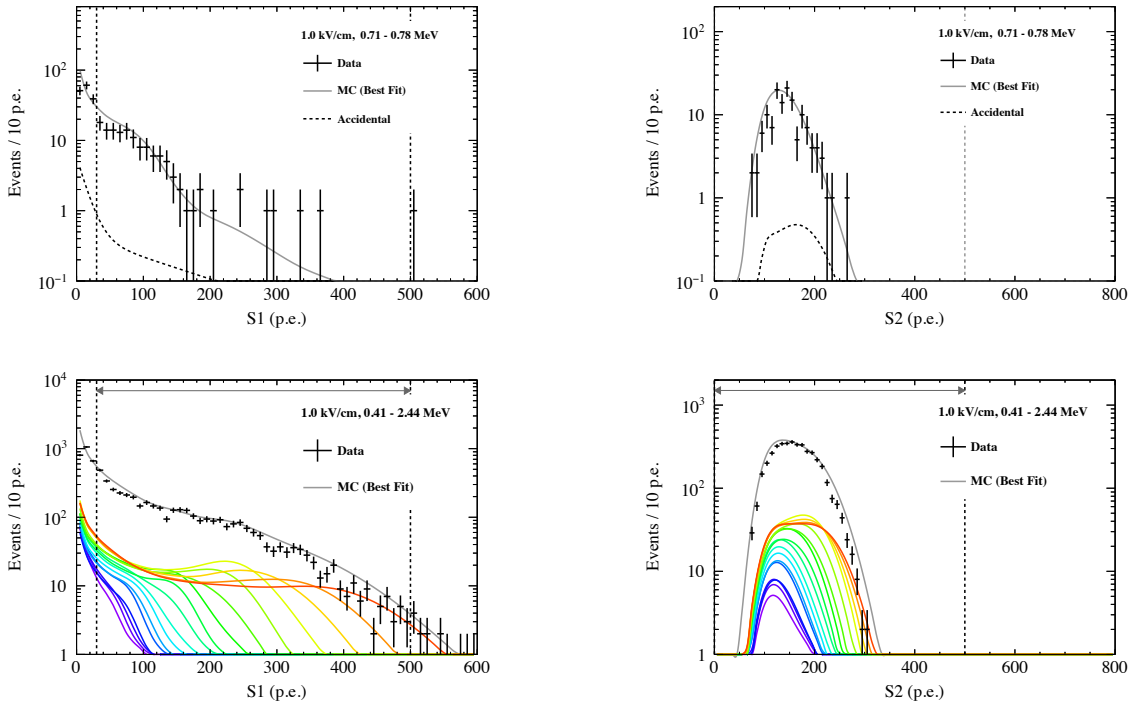

Fig. 5.23. The S1 (left) and S2 (right) spectra taken at the electric field of 1.0 kV/cm and MC-derived spectra simultaneously fitted to experimental data. The figure descriptions are the same as in Fig. 5.21.

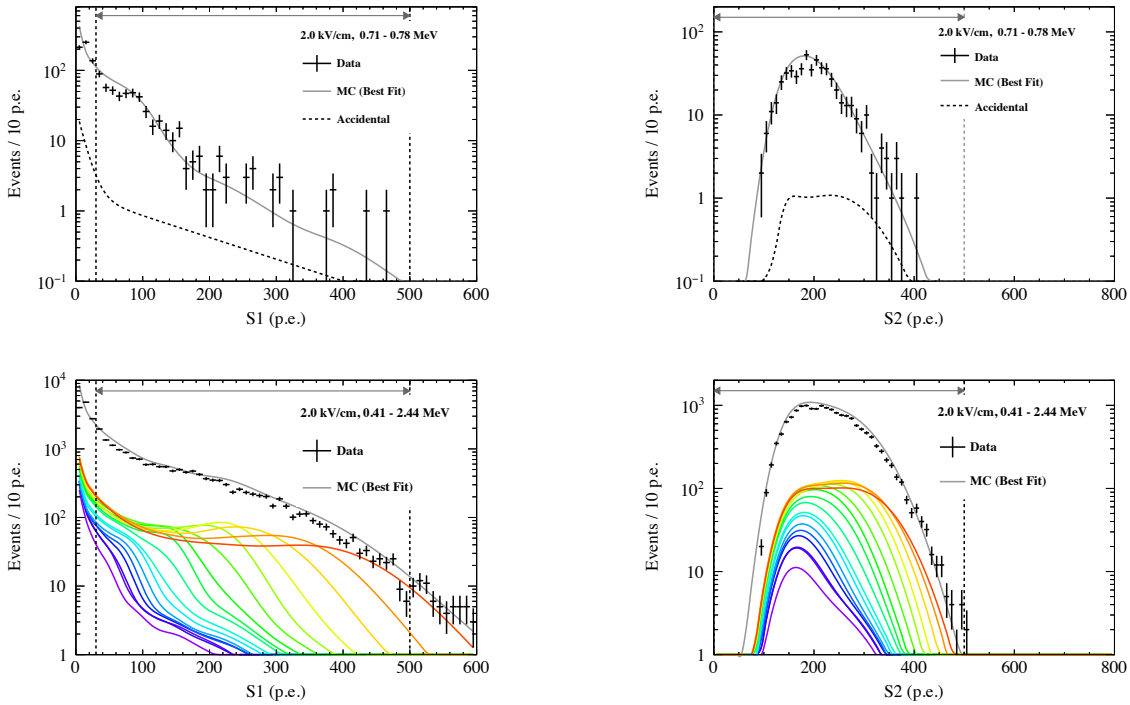

Fig. 5.24. The S1 (left) and S2 (right) spectra taken at the electric field of 2.0 kV/cm and MC-derived spectra simultaneously fitted to experimental data. The figure descriptions are the same as in Fig. 5.21.

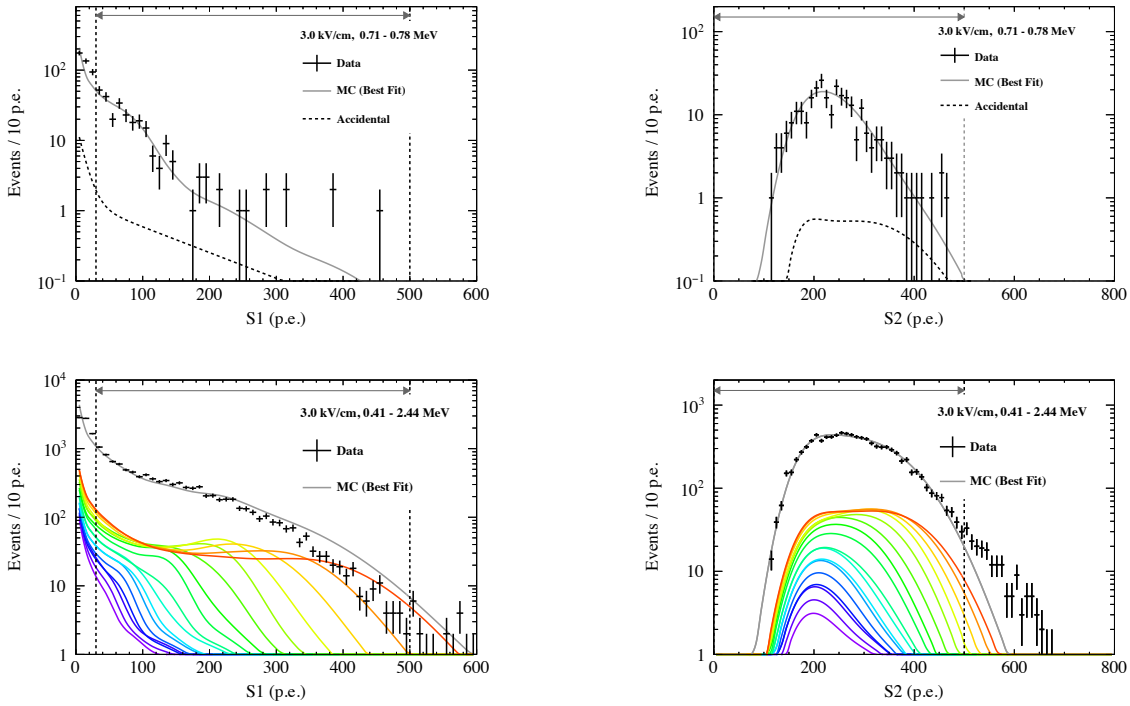

Fig. 5.25. The S1 (left) and S2 (right) spectra taken at the electric field of 3.0 kV/cm and MC-derived spectra simultaneously fitted to experimental data. The figure descriptions are the same as in Fig. 5.21.

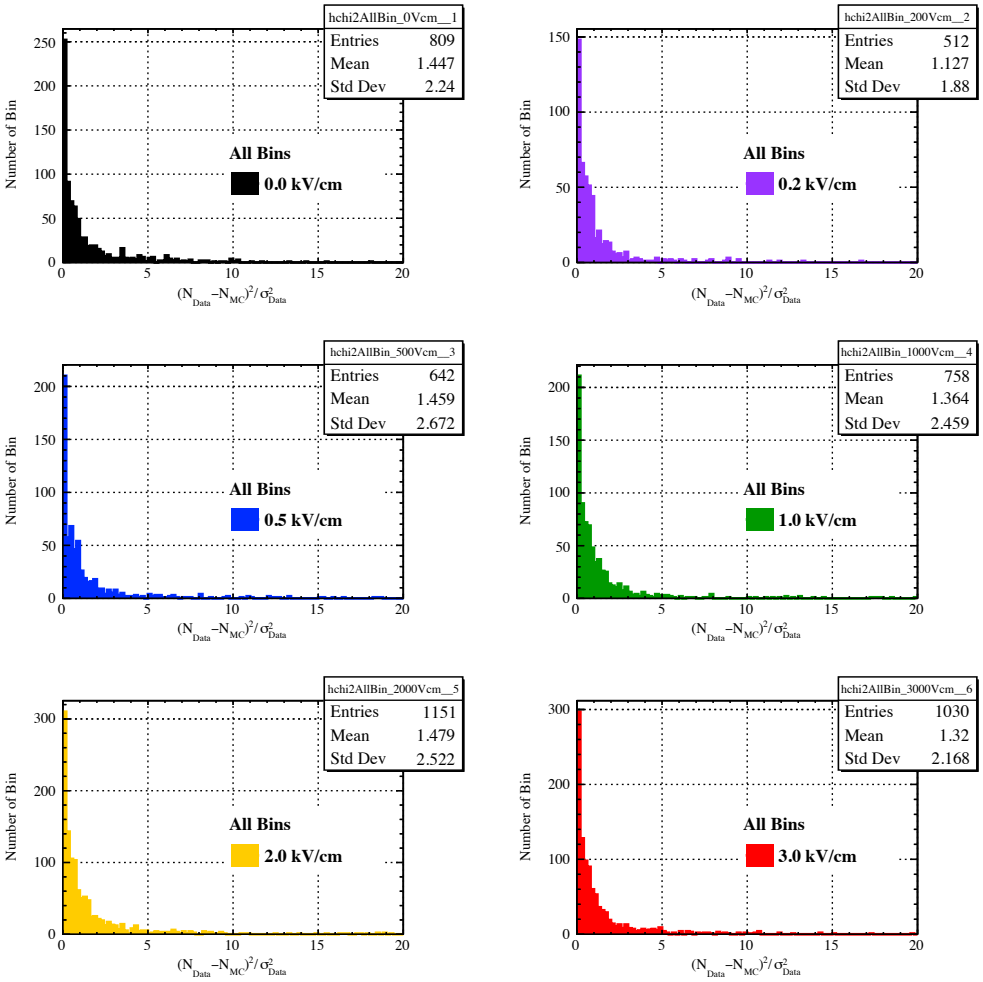

Fig. 5.26. Distributions of χ_i^2 of each bin for each field data.

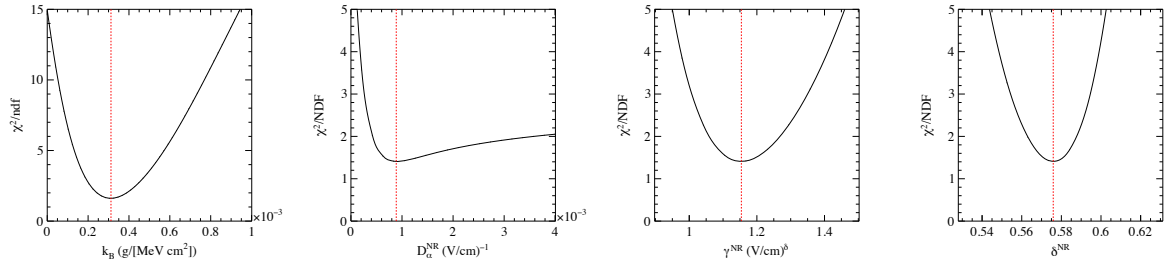

Fig. 5.27. Distributions of χ^2/ndf of each parameter (k_B, D_α^{NR}, γ^{NR}, and δ^{NR} from left to right) in the simultaneous fit. The vertical red dashed lines represent the best-fit values.

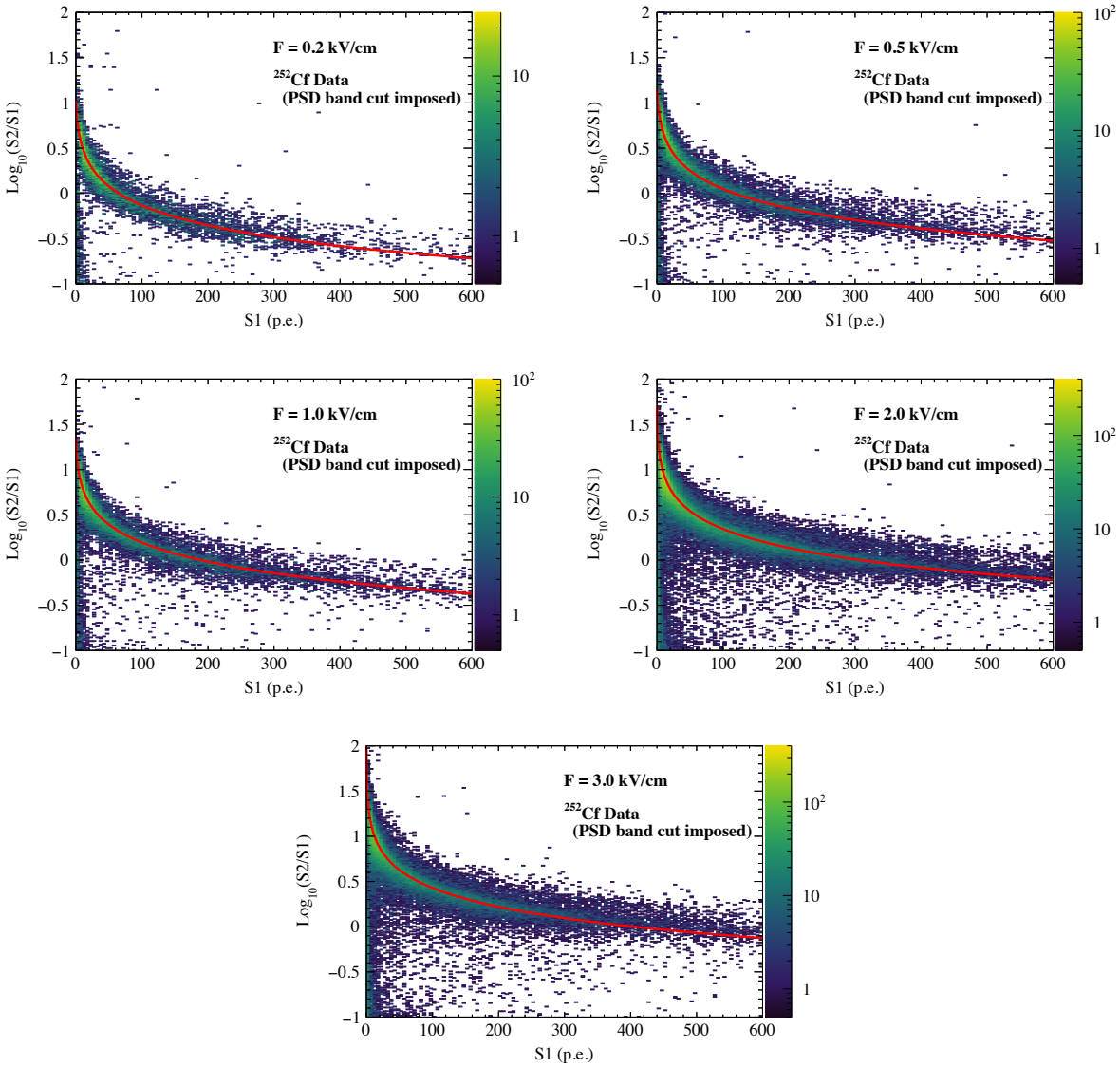

Fig. 5.28. The ^{252}Cf data taken with the electric fields of $0.2, 0.5, 1.0, 2.0$, and 3.0 kV/cm (from left to right and top to bottom) in $\log_{10}(\mathrm{S2/S1})$ versus the S1 plane, overlaid with the prediction from the NR model and the best fit parameters (solid line).

5.5 Result

A set of the best fit parameters is summarized in Table 5.1 and the resulting $\mathscr{L}_{\text{eff}}$ spectrum at each electric field is shown in Fig. 5.29. We constrain the S1 fit range between 30 and 200 keV in order to have sufficient PSD power to extract pure NR events and also to ensure enough statistics for stabilizing the fitting procedure. From the functional modeling, however, the energy range can be extrapolated to both lower and higher energy regions as represented with dashed lines in Fig. 5.29.

Table 5.1. Results from the simultaneous fit of ^{252}Cf data with the MC simulation and the NR model described in Section 5.1.2, together with their statistical uncertainties.

Parameter	Value
k_B [g/(MeV · cm^2)]	$(3.12 \pm 0.05) \times 10^{-4}$
α_0^{NR} (fixed)	1.0
D_α^{NR} [(V/cm)$^{-1}$]	$(8.9^{+0.5}_{-0.4}) \times 10^{-4}$
γ^{NR} [(V/cm)$^{\delta}$]	1.15 ± 0.02
δ^{NR}	$(5.76 \pm 0.03) \times 10^{-1}$

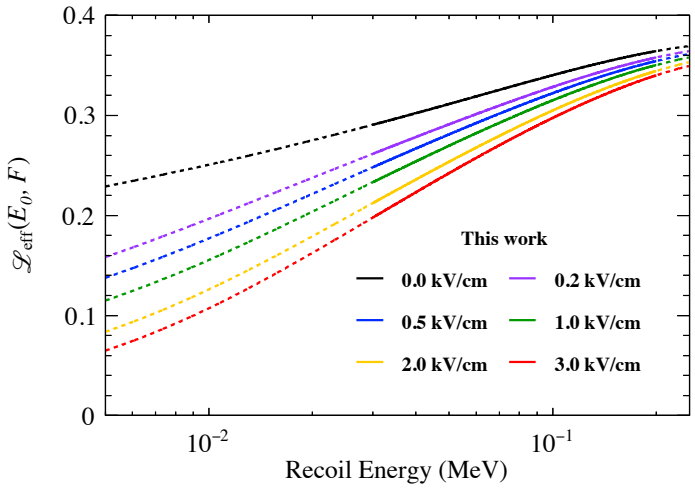

Fig. 5.29. Scintillation efficiencies $\mathscr{L}_{\text{eff}}$ as a function of the NR energy measured in this work. The colored solid lines represent the results from this work, and the corresponding dashed lines are extrapolations.

In this measurement, there are four systematic uncertainties: energy calibration of the detector, the distance from TPC to ^{252}Cf source, the absolute TOF measurement, and the g_2/g_1 ratio, which are considered to be uncorrelated each other. We evaluate the impacts on the fitting parameters by shifting up/down within their uncertainties as shown in Table 5.2. In principle, all the data sets, i.e. all the electric fields data, are affected by these systematic sources in the same way, so we vary each uncertainty for all the data sets in common and reperform all the fitting. It should be noted that uncertainty on energy calibration,

Table 5.2. Sets of fit parameters corresponding to four systematic uncertainty sources (energy calibration of the detector (E-calib.), the distance from TPC to ^{252}Cf source (TOF-arm), TOF time calibration estimated by direct γ-ray events (TOF t_0), and the value of the g_2/g_1 ratio (g_2/g_1)). The units of each parameter are the same as in Table 5.1.

Source		k_B [$\times 10^{-4}$]	D_α^{NR} [$\times 10^{-4}$]	γ^{NR}	δ^{NR} [$\times 10^{-1}$]
E-calib.	+0.3 p.e./keV$_{\mathrm{ee}}$	3.71	9.2	1.15	5.75
	−0.3 p.e./keV$_{\mathrm{ee}}$	2.54	8.9	1.16	5.76
TOF-arm	+1 cm	3.35	8.2	1.16	5.77
	−1 cm	2.90	9.5	1.15	5.75
TOF t_0	+1 ns	3.54	8.9	1.15	5.75
	−1 ns	2.71	8.8	1.15	5.77
g_2/g_1	+20%	N/A	12	0.93	5.78
	−20%	N/A	5.4	1.62	5.86

mainly due to time dependence on the PMT gain and absolute light yield, is partially independent on different data sets, though we treat it as fully correlated to assign conservative error on this measurement. The value k_B is determined by S1 only with null field data; thus, it is not affected by g_2/g_1 uncertainty at all. Statistical uncertainty throughout the measurement is about 10%–20% of the systematic uncertainty. In addition, although we are not aware of any theoretical description of the empirical field dependency of α, the model of Eq.(3.6) seems valid with our data samples and parameterizations.

Since the scintillation response in liquid argon for ER in the range 41.5–511 keV at a null field is constant within 1.6% [46], our result can be subjected to the comparison with other $\mathscr{L}_{\mathrm{eff}}$ measurements using other reference sources (such as ^{83m}Kr [44] or ^{241}Am [46]), a different experimental setup, and analysis method. Figure 5.30 shows the comparison of $\mathscr{L}_{\mathrm{eff}}$ from this work to the previous measurements by other groups [44, 91, 46] for without an electric field (top) and with electric fields (bottom) cases. The colored bands in Fig. 5.30 represent the total uncertainties, evaluated by adding each deviation of $\mathscr{L}_{\mathrm{eff}}$ due to the systematic shift in Table 5.2 in quadrature. Although this work shows systematically higher $\mathscr{L}_{\mathrm{eff}}$ than the other measurements, they are still consistent within their uncertainties. However, possible elements affecting the discrepancy might be listed as follows; (non-)uniformity of LCE for either or both S1 and S2, (non-)uniformity of the electric field, lack of consideration on correlation between scintillation and ionization yields, or incompleteness of functional modeling. We notice, anyway, that more precise data, or simply more results from many measurements, are required to address it more deeply.

5.6 Discussion

5.6.1 Ionization yield

Owing to the functional modeling adopted in this analysis, the ionization yield for NR is derived from the result. Figure 5.31 shows the number of ionization electrons per NR energy for each field. The extrapolation of the result to low energy region shown with dashed lines in Fig. 5.31 indicates that the

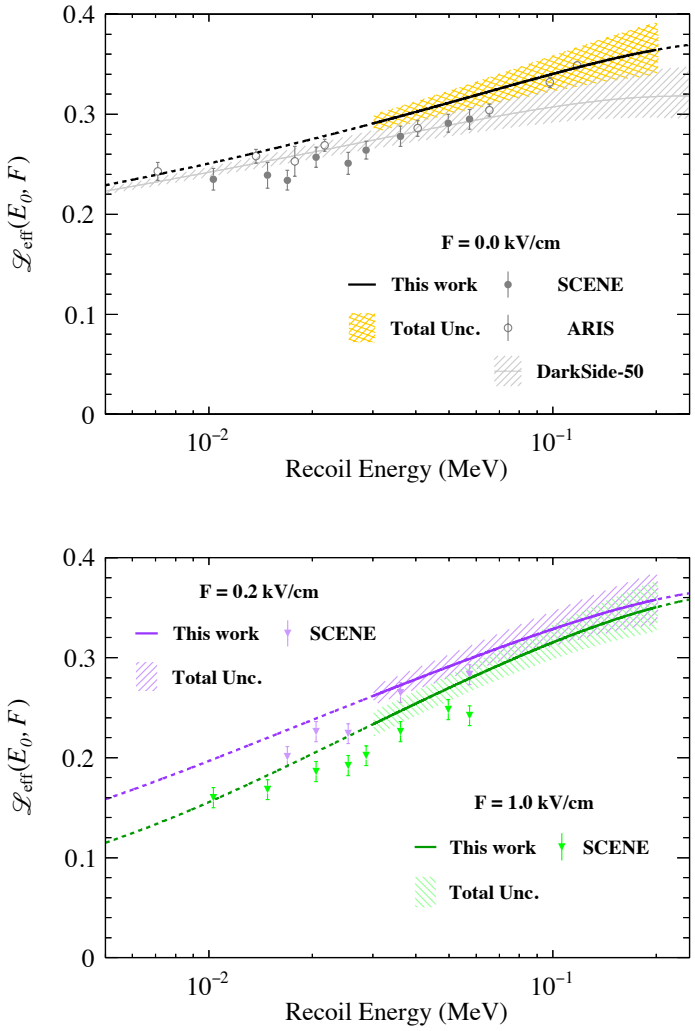

Fig. 5.30. Top: comparison with previous $\mathscr{L}_{\rm eff}$ measurements (SCENE[44], ARIS[46], and DarkSide-50[91]) at a null field. The black solid line is the result from this work (same as in Fig. 5.29), and the orange band represents the total uncertainty on $\mathscr{L}_{\rm eff}$. Bottom: The comparison under electric fields of 0.2 and 1.0 kV/cm. The solid colored lines are the results from this work (same as in Fig. 5.29), and the corresponding bands represent total uncertainty on the $\mathscr{L}_{\rm eff}$, including the uncertainty from the g_2/g_1 ratio.

ionization yield at 3.0 kV/cm is about two times greater than that at 0.2 kV/cm.

The yield at 0.2 kV/cm is compared with that from DarkSide-50 [26] in Fig. 5.32. At NR energy of 30 keV, the yield is consistent for our model and DarkSide-50 results within their uncertainties (1.7 ± 0.3 and $2.2^{+0.5}_{-0.2}$ e^-/keV, respectively). Although the energy threshold of this analysis is 30 keV, we can nevertheless predict the yield for lower NR energy. The prediction from our measurement is systematically lower than the yield from DarkSide-50. This discrepancy is understood as the difference of the assumption of the functional modeling as explained below.

As explained in previous sections, a recoiled nucleus converts their energy in both the electronic excitation

(excitation and ionization) and heat (atomic motion). The latter corresponds to the probability of the elastic scattering of two argon atoms. It is obviously a formidable task to calculate these processes and thus some models are proposed based on different assumption. In this work, the Lindhard theory (Eq.(3.5)) is adopted to represent the nuclear stopping power through whole energy region. This theory is based on an analytical approximation and widely used in liquid argon experiments. On the other hand, the model adopted by DarkSide-50 use a model based on Hartree–Fock methods [49]. These two models differs in the estimation of the screening effect. It is so difficult to measure the effect experimentally that taking dedicated calibration data is necessary, especially focusing on a few keV region.

The result in this work indicates that the ionization yield increases as the field increases, as one naively expects. It is in particular of interest for several-GeV/c^2 mass WIMP search, where only S2 signal is used to identify WIMP-induced event [26]. In this experiment, signal excess of a few keV or below recoil event over the backgrounds is searched. The sensitivity owes to the fact that even one electron signal is detectable in double-phase liquid argon detector. In principle, applying higher field reduces the energy threshold and enhance low-mass WIMP sensitivity because an expected number of ionization electron increases. The functional modeling provides valuable information for future low-mass WIMP search using the S2-only technique.

5.6.2 Prospects

This measurement determines the scintillation and ionization yields by exploiting the functional modeling introduced in Section 5.1.2. This approach has both advantages and disadvantages when compared to the other approach using mono-energy neutron beam and elastically-scattered neutron tagging detector. An important advantage of our approach is that we can interpolate or extrapolate the result to any energy and electric field. In addition, the use of the functional modeling may allow to improve the accuracy in low energy region, because we can extract additional information from higher energy region through the function. The NEST framework[103, 104] for liquid xenon response has been taken this kind of approach and has supported the evolution of the liquid xenon detector significantly. However, we do depend on the modeling and thus may face to some problem arisen from imperfect approximation of the modeling. On the other hand, the other approach measures the signal yields independent from any modeling, though it contains almost irreducible uncertainty in low energy region in principle. Both approach should be performed by many groups and in many detectors to get more precise function and reduce uncertainties. In this context, it is also necessary to pay careful attention on the detector performance such as uniformity of the LCE and electric field. Furthermore, it will be better to use both scintillation and ionization channels considering the correlation between them.

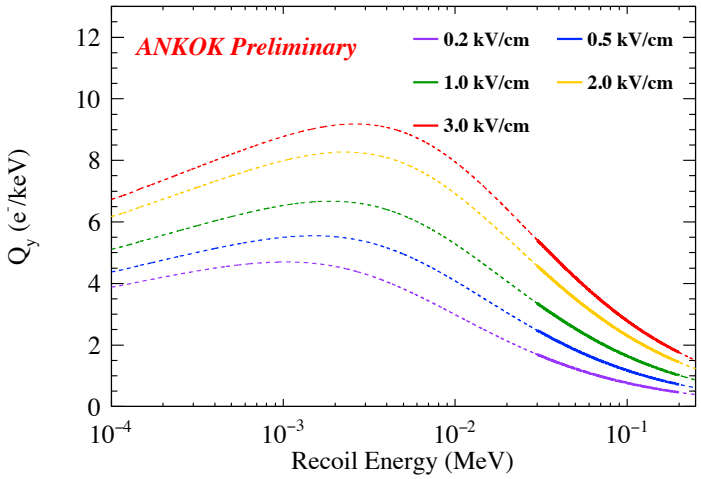

Fig. 5.31. Ionization yield for NR as a function of recoil energy derived from the model function. The colored solid lines represent the energy threshold of this analysis, and the corresponding dashed lines are extrapolations.

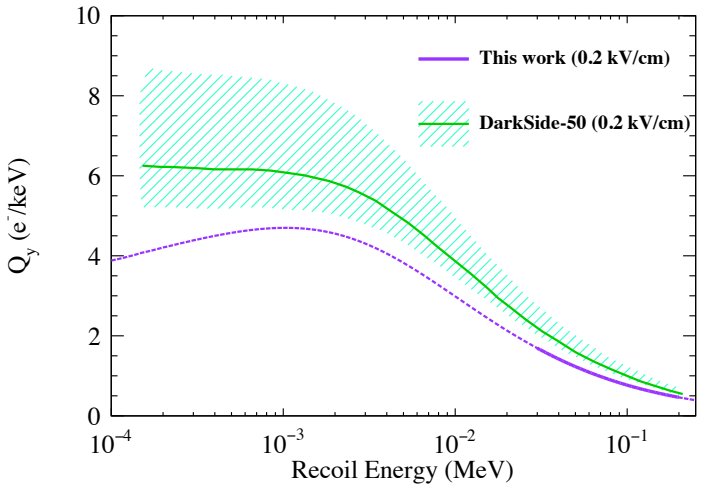

Fig. 5.32. Comparison of the ionization yield at 0.2 kV/cm between the model of this work and result from DarkSide-50.

Chapter 6

Measurement of the response for electronic recoils

The response of liquid noble gas detector on ER depends on both electric field and recoil energy, as is the case for NR shown in Chapter 5. Since the observed signal from typical WIMP recoil energy of 10 keV corresponds to roughly 40 keV electron equivalent energy, the response in O(1–10) keV is of primary interest. Furthermore, that in higher energy region is also important to explain the observed data in context of background expectation.

We measure the liquid argon response to ER ranging from 2.82 to 1274.6 keV using a single-phase detector and variety of calibration sources summarized in Table 6.1. Large optical coverage and optimization of TPB wavelength shifter coating results to the detector light yield of 12.8 ± 0.3 p.e./keV. This high LCE allows to identify 2.82-keV peak of ^{37}Ar, a cosmogenic isotope in atmospheric argon. We also derive the absolute scintillation yield as a function of ER energy, referring a literature value at 1 MeV which is the sole measurement determining it. The result proves approximately 25% shift in the scintillation yield across the energy range.

6.1 Measurement motivation and overview

As mentioned in previous sections, burdensome backgrounds in WIMP search are ER events caused by β-rays from diffused isotopes (such as ^{39}Ar and ^{85}Kr) in liquid argon and γ-rays from radio-impurities in detector components. Despite of the powerful ER rejection of the detector, predicting the measured signal from these background sources is still necessary to estimate its contamination in the signal region of interest. In this context, characterization of the detector response to ER events is crucial for achieving lower energy threshold, suppressing systematic uncertainty related to background contamination, and hence enhancing physics sensitivity of the search. Furthermore, recently the searches for new particles, such as bosonic dark matter and axion-like particle, have been actively performed using the ER events by liquid xenon detectors (e.g. [12, 25, 13]), where its response on energetic particle is well understood [103, 51, 105], while the one for argon is not fully established yet. Therefore the measurement of low energy ER response is essentially important for physics interpretation to extract physics quantity from observed scintillation signal with liquid argon.

The response under null field is considered to be the most fundamental property. In addition, previous studies on PID capability of liquid argon detector[105, 47], combined with the sufficient light yield as described later, insist that single-phase detector is more suitable than double-phase detector with any magnitude of the drift field from the point of view of ER rejection. Thus we herein focus on the

scintillation response at null field, though these kinds of measurement under finite filed is important as well.

In this study the light yields for several energy lines are measured using a variety of calibration sources. Among the points, 2.82-keV line from ^{37}Ar is particularly important where a significant decrease of the light yield is observed. In order to present an essential quantity for liquid argon scintillation detector, the absolute scintillation yield is calculated by referring a literature. Doke *et al.* presents the absolute yield for 1-MeV electron line[42] in Fig. 3.4, and to our knowledge, this is the only point to be referred. We interpret our result in terms of absolute yield by referring and interpolating the Doke's point in 1 MeV.

6.2 Apparatus

Figure 6.1 shows the experimental setup used in this study, and Table 6.1 summarizes the calibration sources. The measurement is performed with the single-phase detector presented in Section 4.5.2. The calibration sources are set on either outside or inside the cryostat. More detail of each source is presented in the following sections. A passive shield against ambient γ-rays surrounds the cryostat, which consists of roughly 2-cm-thick oxygen-free copper and 10-cm-thick lead.

Table 6.1. Summary of the calibration sources and energies used in this measurement.

Energy [keV]	Source	Decay mode	Trigger and selection	Note
2.82	^{37}Ar	e^--capture	Fiducial self, anti-veto coincidence	Diffused isotope
59.54	^{241}Am	α	Coincidence between fiducial and outer-bath	Tagging a coincident α-ray by the outer-bath PMTs
109.8	^{252}Cf	$(n,n'\gamma)$[a]	Coincidence between fiducial and NaI(Tl)	Requiring TOF of neutron with the NaI(Tl)
197.1	^{252}Cf	$(n,n'\gamma)$[a]	Coincidence between fiducial and NaI(Tl)	Requiring TOF of neutron with the NaI(Tl)
356.0	^{133}Ba	e^--capture	Fiducial self	
511.0	^{22}Na	β^+	Coincidence between fiducial and NaI(Tl)	Requiring back-scattered γ-ray with the NaI(Tl)
661.7	^{137}Cs	β^-	Fiducial self	
1274.6	^{22}Na	β^+	Fiducial self	

[a] $(n,n'\gamma)$ reaction between fast neutron from ^{252}Cf and ^{19}F in PTFE.

The signals from two fiducial-viewing PMTs and four outer-bath PMTs are digitized and recorded by the FADC. The length of the digitizer records is set to 25 μs (5 μs before a trigger point and 20 μs after), longer than the lifetime of the slow component of liquid argon scintillation light. The trigger is given by the coincidence, within 1 μs, of the two fiducial PMTs with pulses above a threshold, which is set

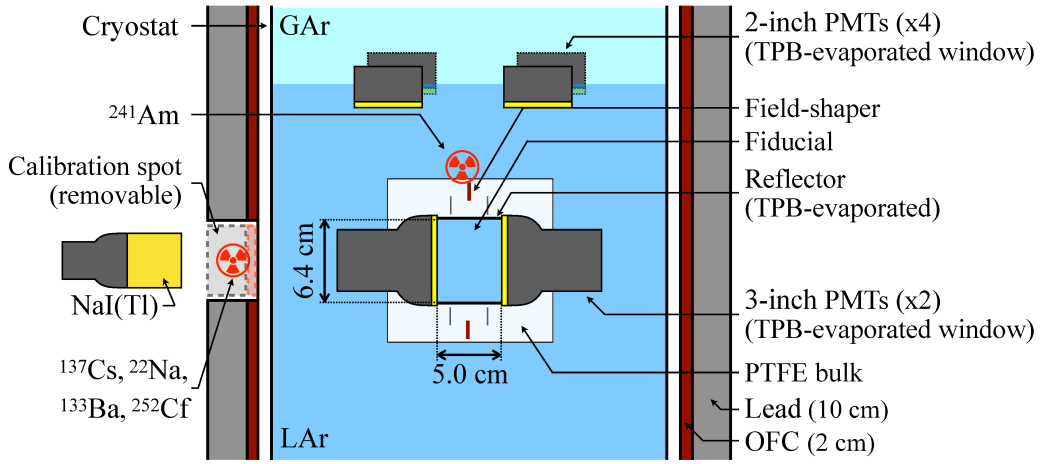

Fig. 6.1. The detector including the PMTs is immersed in LAr. Oxygen-free copper (OFC) of roughly 2 cm thick and lead of 10 cm thick surround the cryostat and act as a passive shield against ambient γ-rays. An ^{241}Am source is installed at the outer surface of the PTFE bulk, and the other sources (^{137}Cs, ^{22}Na, ^{133}Ba, and ^{252}Cf) are placed on the outside surface of the cryostat wall.

just above the baseline noise and below a typical single photoelectron pulse. The coincidence decision is internally made by the FADC board itself. An inhibition time of 100 μs is introduced after each trigger to prevent retriggering of the afterpulse of the PMTs, which mainly occurs after events with far greater energies than the region of interest (e.g., cosmic-ray events). A MC simulation of the liquid argon data sample is generated to evaluate the trigger efficiency. By emulating the internal trigger logic of the FADC board on these MC events, the efficiency is found to be consistent with unity for ER signals larger than 25 p.e., as shown in Fig. 6.21.

6.3 Event analysis

6.3.1 PMT calibration

The gain of the fiducial-viewing PMTs is calibrated using a blue LED powered by a pulse generator. Light pulses from the LED characterized by a width of approximately 20 ns at tenth maximum are injected into the fiducial volume through optical fiber, while the generator simultaneously triggers the DAQ system, and the corresponding waveforms from each PMT are recorded over a window of ± 1 μs. A baseline analog-to-digital converter (ADC) count is determined by the first 0.6 μs of the window, and its subtraction is applied waveform by waveform. The charge response of the PMT is measured by integrating the waveforms within a 48-ns window starting 20 ns prior to the photoelectron pulse arrival time. The gain value is determined by fitting the charge distribution to model functions. In this analysis, two models are considered to describe the PMT response. One expression of the models (gain-model A)

as a function of the integrated charge q is followed to that used in Ref. [106] and referenced therein:

$$\begin{aligned} f(q) &= \sum_n P(n;\lambda) \times f_n(q), \\ f_n(q) &= \rho(q) * \psi_1^{n*}(q), \\ \rho(q) &= G(q; x_0, \sigma_{\text{ped}}), \\ \psi_1(q) &= \frac{p_E}{\tau} \exp(-q/\tau) + (1-p_E) G(q; x_m, \sigma_m) \end{aligned} \tag{6.1}$$

where $P(n;\lambda)$ is a Poisson distribution with mean λ, $G(q; x, \sigma)$ is a Gaussian distribution with mean x and standard division σ, $*$ denotes a convolution, $\psi_1(q)$ is the PMT single photoelectron response, and $\psi_1^{n*}(q)$ is the n-fold convolution of $\psi_1(q)$ with itself. This model consists of two components comprising the PMT response: a simple Gaussian term, which accounts for a photoelectron signal fully amplified by the dynode chain, and an exponential term characterized by a parameter τ, which accounts for underamplified photoelectrons and/or feedback from the dynode photoemission signal. The fraction of the single photoelectron response found to be the underamplified terms is p_E. Another expression (gain-model B) is simpler, consisting of only the Gaussian term; i.e., the fraction p_E in Eq. (6.1) is fixed to 0. This assumes that there is no underamplified or dynode-feedback response in a PMT and that the photoelectron response is perfectly described by Gaussians.

Figure 6.2 shows the charge distribution and fit for a LED calibration run with the gain-model A (which has a nonzero fraction p_E), where 1 count $\cdot$ sample corresponds to an output charge of 9.8×10^{-15} C. The mean charge for a single photoelectron g defined as

$$g = p_E \tau + (1 - p_E) x_m, \tag{6.2}$$

is approximately 2.0×10^6 e^-/p.e. with a bias voltage of -1570 V. The fit with the gain-model B (i.e., simple convolution of Gaussian functions) returns a 12% higher gain value than gain-model A. This difference is nearly consistent with the result reported in Ref. [106]. While we do not have enough data to determine which model is more appropriate to describe the PMT response, the gain-model A is adopted as baseline and the result from the model is used in the later analysis. This calibration is performed every 12 hours during a data collection period lasting seven days, as shown in Fig. 6.3. The overall stabilities of the gain and observed light yield during the period are within less than 0.5% from both the LED measurement and an energy calibration mentioned below.

The nonlinearity of the PMT is studied by a pulsed laser source, and we found that the effect is less than 1% (0.1%) at 1 MeV (below 200 keV) at the operation voltage. The observed light yields are corrected accordingly, and its correction factors are considered as a systematic uncertainty. Detail of the PMT property is described in Appendix A.

6.3.2 Signal analysis and selection criteria

The analysis of the liquid argon scintillation signal is performed following the photon-counting algorithm described in Section 4.4. A set of data quality cuts is applied to remove instrumental effects and event

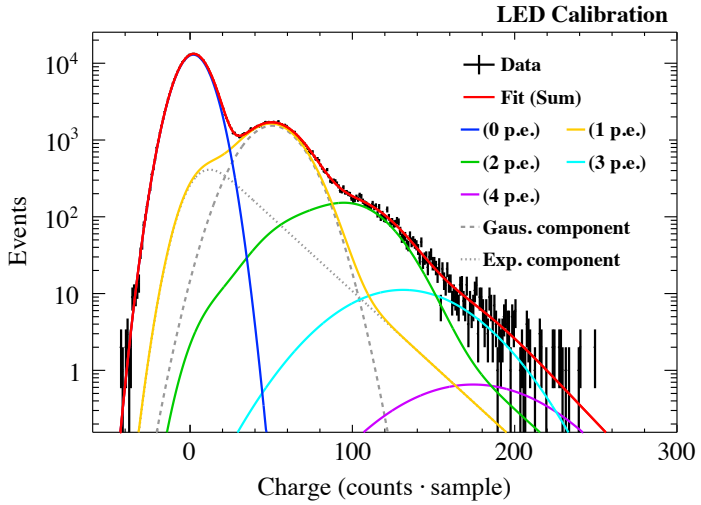

Fig. 6.2. A typical low-light charge distribution of a fiducial-viewing PMT from an LED calibration run. The charge is represented in units of integrated digitizer count (count · samples), where 1 count · sample corresponds to 9.8×10^{-15} C. The solid red line is the model fit as expressed in Eq.(6.1), and the colored lines represent its components. The dashed and dotted lines indicate the Gaussian and exponential terms of the single photoelectron response.

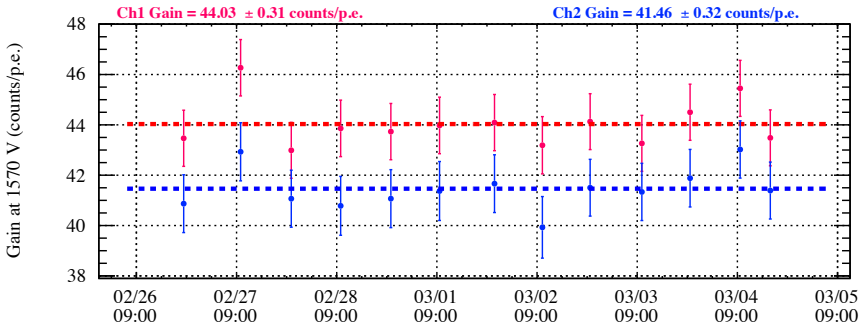

Fig. 6.3. Time evolution of the gain of the two PMTs calibrated with the LED. The error bar of each point includes both statistical and systematical uncertainties.

pileups. The selection criteria are as follows:

1. Software imposes a 10-ms veto after events that contain signals greater than $\approx 2.0 \times 10^4$ ($\approx 5.0 \times 10^3$ p.e.) for datasets taken with a γ-ray source with >100 keV (<100 keV) its energy. This aims to remove the unstable period of the PMT after outputting a large charge signal.

2. The event has a stable baseline noise and no more than 0.7 p.e. pulses in the pretrigger window.

3. The event does not occur near the PMT and is more likely to be a liquid argon scintillation signal than Cherenkov light on the PMT window. The signal asymmetry defined as $A = (N^1_{\text{p.e.}} - N^2_{\text{p.e.}})/(N^1_{\text{p.e.}} + N^2_{\text{p.e.}})$ in which $N^1_{\text{p.e.}}$ and $N^2_{\text{p.e.}}$ are the observed photoelectron signal in each PMT is used to evaluate the interacting position. The cut value is selected to contain approximately 99%

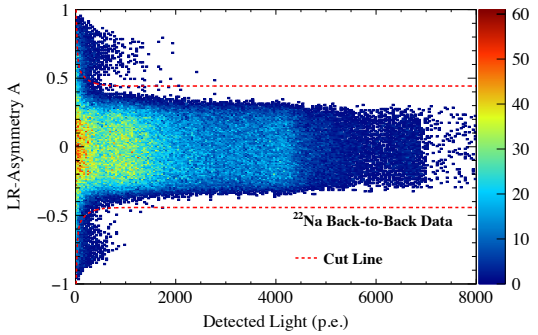

Fig. 6.4. Distribution of the signal asymmetry parameter versus the observed light signal. The data requires the back-to-back tagging described in Section 6.3.3. The red dashed lines are the cut line used in the event selection.

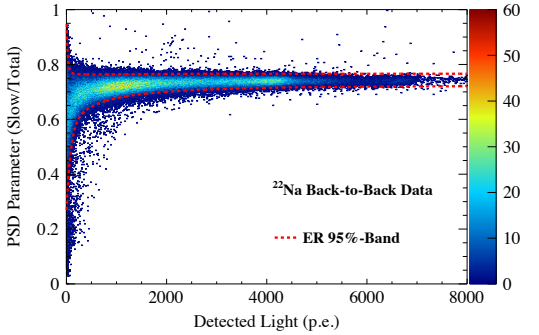

Fig. 6.5. Distribution of the PSD parameter ("slow/total") versus the observed light signal. The data requires the back-to-back tagging described in Section 6.3.3. The red dashed lines correspond to the 95% containing band for ER events.

of the liquid argon signal, as shown in Fig. 6.4.

4. The PSD parameter of the event is consistent with that of the ER. This requirement is particularly important for the ^{252}Cf data because it enhances the γ-ray full-absorption peaks over continuous nuclear recoil spectrum. The band of the parameter used in this cut is determined by ^{22}Na data requiring the coincidence detection of the backwards-traveling 511-keV γ-ray whose details are described in the following section. The selection band contains 95% of ER events, as shown in Fig. 6.5.

6.3.3 Determination of photoelectron per keV with sodium-22 and cesium-137 sources

Determination of the observed light yield, photoelectron per keV of the detector is performed by 511.0-, 661.7-, and 1274.6-keV γ-rays. The γ-ray sources, ^{137}Cs and ^{22}Na, with approximately 1 MBq, respectively, are placed on the outside surface of the cryostat wall to expose the γ-ray to the detector.

Figure 6.6 shows the observed light spectrum obtained with the ^{137}Cs source. The full-absorption peak of the 661.7-keV line of the ^{137}Cs source is fit with a Gaussian with mean μ and width σ. The continuous background components around the peak, mainly coming from the Compton edge and degraded tails, are modeled with error and linear functions and added to the fit function. The fit shown in Fig. 6.6 returns $\chi^2/ndf = 62.5/56$.

The observed light spectra obtained with the ^{22}Na source are shown in Fig. 6.7. In this measurement, an additional NaI(Tl) scintillator (2×2in.^{2} cylinder) is set with the source at opposite sites of the cryostat to tag the backwards-traveling 511.0-keV γ-ray (back-to-back tagging). The distance between the cryostat wall and the source is set to 15 cm, and that between the source and the scintillator to 25 cm. The black and blue spectra in Fig. 6.7 are the observed scintillation spectra before and after requiring the coincidence detection of the 511.0-keV γ-ray signal in the NaI(Tl) scintillator. Since the 1274.6-keV γ-ray is considered to have no angular correlation with back-to-back γ-rays, the corresponding peak appears

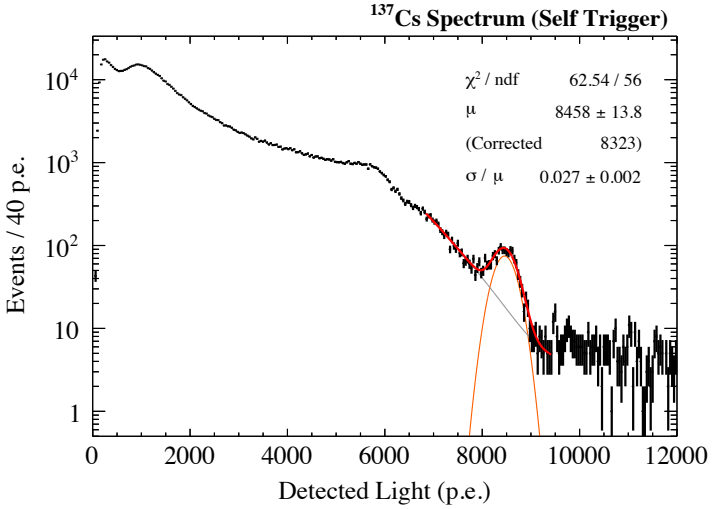

Fig. 6.6. The observed light spectrum from the ^{137}Cs source used for the energy calibration. The red lines represent the fit function for the 661.7 keV peak.

Table 6.2. Fitted γ-ray energy, E_γ, and observed light yields, μ/E_γ, resulting from the full-absorption peak fit. The uncertainties listed in the table are combined with both statistical and systematic uncertainties.

E_γ [keV]	Source	μ/E_γ [p.e./keV]	
		(Gain-model A)	(Gain-model B)
511.0	^{22}Na	12.8 ± 0.3	11.2 ± 0.3
661.7	^{137}Cs	12.6 ± 0.3	11.1 ± 0.3
1274.6	^{22}Na	12.3 ± 0.3	10.8 ± 0.3

only in the former spectrum. Each peak is fit with a Gaussian plus background model function consisting of error and linear functions. Values of $\chi^2/ndf = 72.6/72$ and $\chi^2/ndf = 96.5/48$ are returned from the fits for 1274.6- and 511.0-keV peaks, respectively.

These observed photoelectron signals contain extra charge from PMT afterpulses and systematic effect from the photon-counting algorithm. A correction for these effects is thus applied to reconstruct the observed light signal per ER energy. This correction is based on an independent study of the PMT response as well as a MC simulation of the liquid argon signal. It is relatively small, approximately 1% for the ^{137}Cs line and less than 3% for the whole energy region of interest of this analysis, where the amount of afterpulse is estimated as 2%–4% of the photoelectron signal, and the algorithm can systematically slightly underestimate the charge signal. The observed light yields after the corrections are summarized in Table 6.2 with uncertainties. The uncertainty includes the estimation of PMT afterpulses, systematic error in the corrections, and stability of the detector.

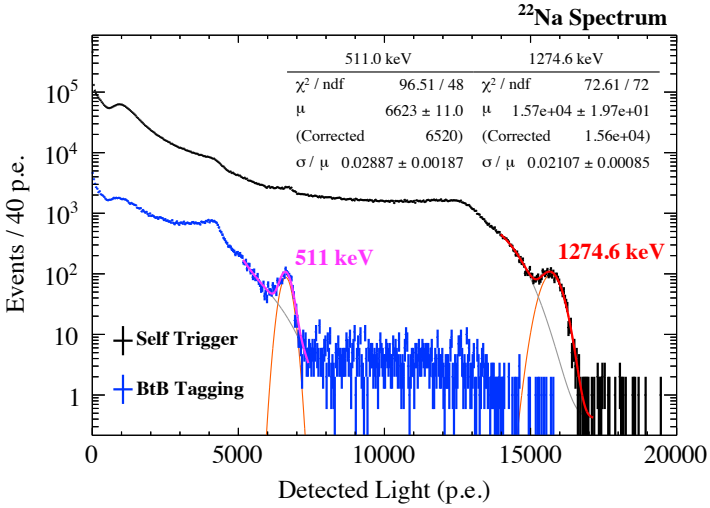

Fig. 6.7. The observed light spectra from the ^{22}Na source, before and after requiring back-to-back coincidence (BtB tagging). The red and magenta lines represent the fit function for the 1274.6 keV peak in self-trigger data and the 511 keV peak in back-to-back data, respectively.

6.4 Measurement

6.4.1 Barium-133 source

The detector is exposed to 356.0-keV γ-ray using a ^{133}Ba radioactive source with approximately 1 MBq. The spectrum obtained with a ^{133}Ba source is shown in Fig. 6.8. The peak around 4700 p.e. corresponds to the γ-ray line and fitted with a Gaussian. An exponential function is added to the fit function to model the overall background components; the main background sources are due to the degraded γ-ray tail and the γ-ray spectra of the other two lines of the ^{133}Ba source around the peak energy that have relatively high intensity (those at 383.9 keV with a branching ratio of 8.9% and 302.9 keV with 18.3%, as compared with that at 356.0 keV with 62.1%) . The resulting fit function is overlaid in Fig. 6.8.

6.4.2 Californium-252 source exploiting γ-rays through $(n, n'\gamma)$ reaction with fluorine-19

Measurements for the 109.8- and 197.1-keV quasimonoenergetic lines are performed using γ-rays emitted from the $(n, n'\gamma)$ reaction with ^{19}F [107]. As an external fast neutron source, a ^{252}Cf source with a spontaneous fission rate of approximately 1×10^5 fission/s is used. The use of this reaction allows to calibrate a few hundred of keV region with an external source regardless of the presence of surrounding liquid argon volume. The distance between the center of the fiducial volume and the source is set to 90 cm. The NaI(Tl) scintillator is placed beside the source to detect associated γ-rays from the spontaneous fission and to provide timing information. Fast neutrons from ^{252}Cf generate $(n, n'\gamma)$ reaction with ^{19}F in the PTFE bulk, producing quasimonoenergetic γ-rays. Although the intensities of each quasimonoenergetic line depend upon their incident neutron energy, 109.8- and 197.1-keV lines are major channels for the range of neutron energy from ^{252}Cf as shown in Fig. 6.9, where the energy distribution is calculated by

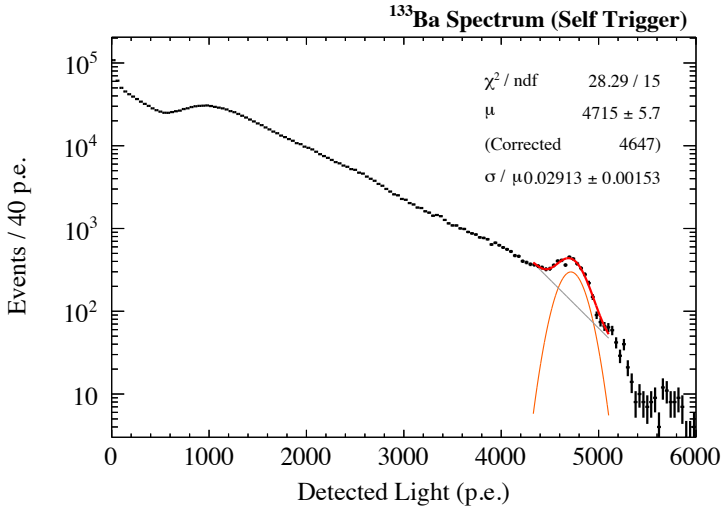

Fig. 6.8. The observed light spectrum from the ^{133}Ba source. The red line represents the fit function.

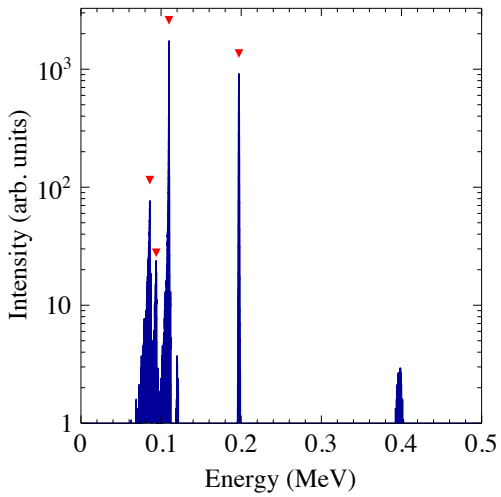

Fig. 6.9. The γ-ray energy spectrum from $(n,n'\gamma)$ reaction in ^{19}F induced by ^{252}Cf fast neutron based on PHITS [108]. The red markers indicate the energies of 85.9, 93.9, 109.8, and 197.1 keV based on a peak-finding algorithm.

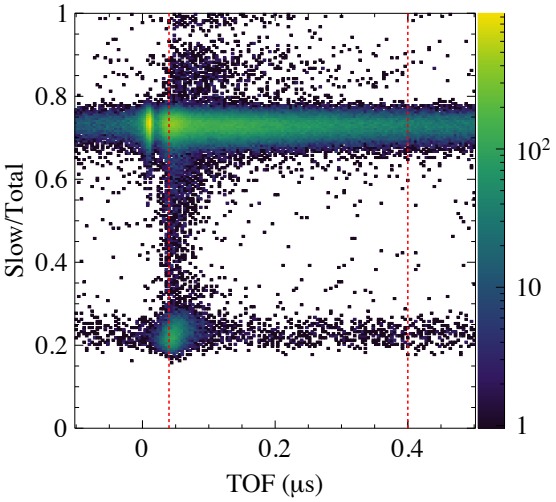

Fig. 6.10. Distribution of the PSD parameter versus the TOF in a detected light yield range between 1000 and 4000 p.e. The red dashed lines represent the selected region.

PHITS package[108]. The deexcitation mean life of the 197.1 keV (109.8 keV) state is 0.1 μs (less than 0.01 μs)[109]. Time differences between the NaI(Tl) and fiducial signals (TOF) are used to remove γ-ray events that come directly from the fission, as shown in Fig. 6.10. Figure 6.11 shows the spectrum and fitting results for corresponding peaks. Each peak is fit by a Gaussian plus exponential function.

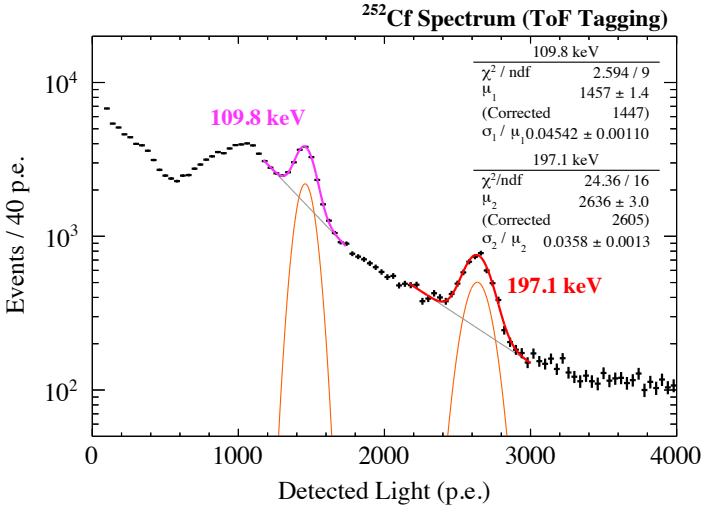

Fig. 6.11. The observed light spectrum from the ^{252}Cf source after requiring the TOF to be consistent with fast neutrons. The magenta and red lines represent the fit functions for 109.8- and 197.1-keV peaks, respectively.

6.4.3 Americium-241 source

To expose the detector to 59.5-keV γ-rays, an ^{241}Am source of approximately 40 Bq is used. The radioactive source is deposited on a 100-μm-thick platinum foil installed at the outer surface of the PTFE bulk, as shown in Fig. 6.12. It decays into an excited level of ^{237}Np via α-ray transition, and subsequent deexcitation of the ^{237}Np emits γ-rays with a major line of 59.5 keV. The half life of the excited state is 68.1 ns. The scintillation signal from the α-ray from the primary disintegration is detected by the outer-bath PMTs, allowing the γ-ray interaction to be proved in the fiducial volume. Since the α-ray energy is sufficiently high and regarded as NR in liquid argon detector, the α-ray signal is easily selected by both the detected light yield and PSD parameter as shown in Fig. 6.14. The time difference between the fiducial- and outer-bath light signals, shown in Fig. 6.15, proves the ^{241}Am tagging method, where the half life is consistent to the literature value. Figure 6.16 shows the observed light spectrum after requiring the detection of the α-ray signals in the outer region. Because of the relatively low energy of the γ-ray from ^{241}Am and the passive components between the source and the fiducial volume, the spectrum does not exhibit a clear full-absorption peak. The tail of the peak comes from γ-rays that reach the fiducial volume via single or multiple scattering from any materials in their path.

The detector response to a 59.5-keV γ-ray is evaluated via MC simulation of the experimental setup based on the Geant4 toolkit. The MC simulation takes into account the detector geometry and composition inside the liquid argon bath, as well as the radioisotope mounting structure. It proceeds by generating γ-rays from ^{241}Am with a random momentum direction and calculating the energy deposition in the fiducial volume. The observed spectrum is fitted by converting the energy deposition to the observed light yield with a constant scintillation yield, constant LCE, and Gaussian resolution. The best fit spectrum is also shown in Figure 6.16; although the fit is performed only around the 59.5-keV peak (700–900 p.e.), reasonable agreement between the data and MC is found down to around 400 p.e.

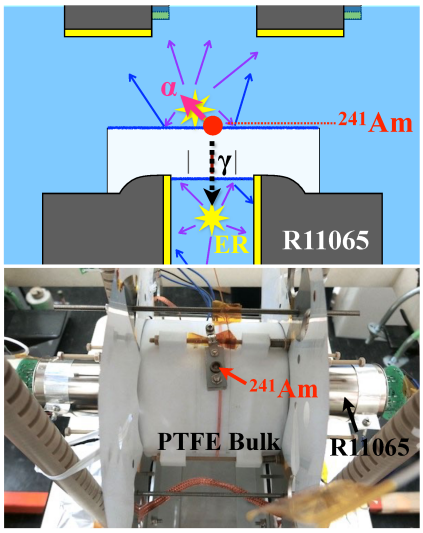

Fig. 6.12. Schematic of the ^{241}Am source and detection process (top) and its picture (bottom).

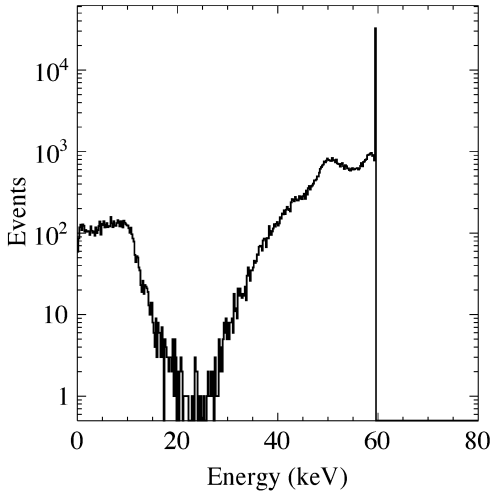

Fig. 6.13. Simulated energy spectrum in the fiducial volume from the ^{241}Am γ-ray.

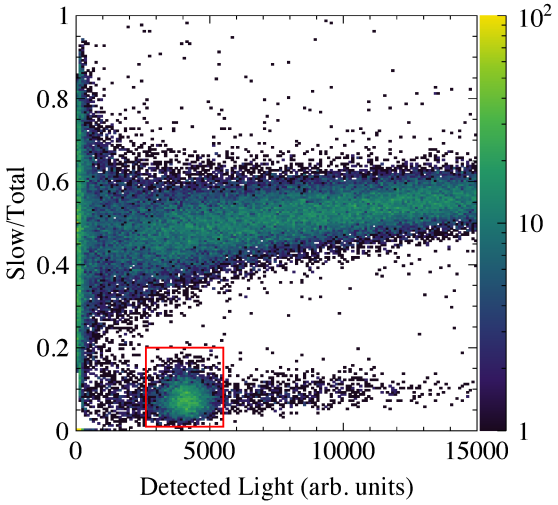

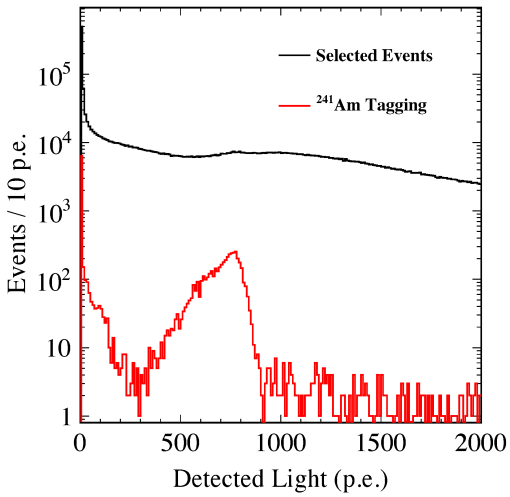

Fig. 6.14. Left: distribution of the observed signal by outer-bath PMTs in the detected-light versus PSD plain. The ^{241}Am region is defined to select the α-ray tagging signal. Right: observed spectrum in fiducial before and after requiring the α-ray signal inside the red box.

6.4.4 Argon-37 source

Measurement for ER of a few keV is performed using ^{37}Ar, which is the second most abundant radioactive isotope in atmospheric argon, comprising an abundance of $\approx 1.3\times10^{-20}$[110], corresponding to the activity of several tens of mBq/kg. It decays via electron capture to the ground state of ^{37}Cl with a half-life of 35 days, producing x-rays and Auger electrons with a total energy release of 2.82 keV (for K-shell capture),

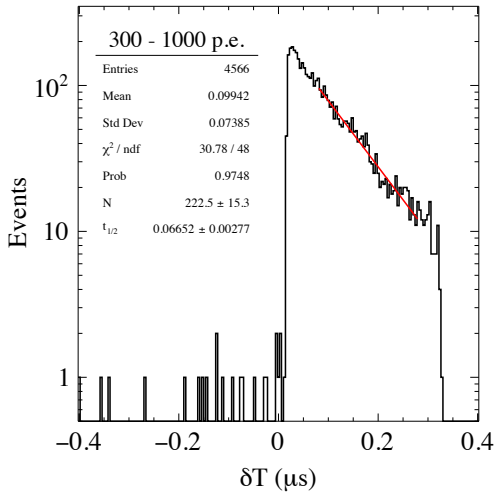

Fig. 6.15. Time difference between the fiducial and outer-bath signals of the ^{241}Am-tagged events.

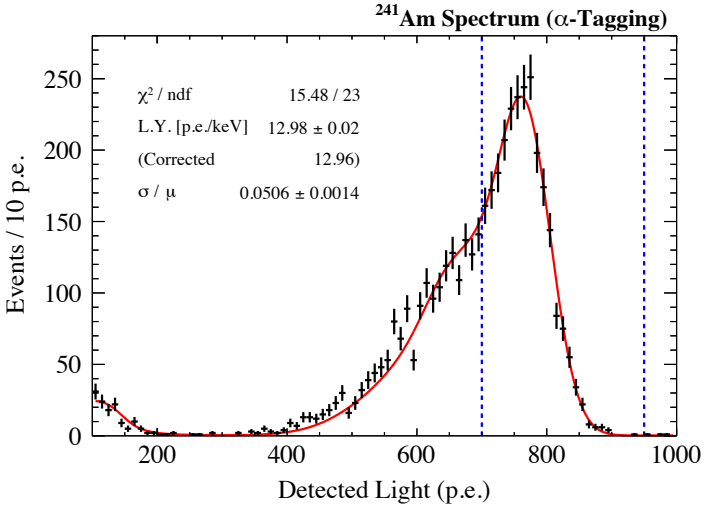

Fig. 6.16. The observed light spectrum from the ^{241}Am source by requiring α-ray detection by the veto PMTs, along with the MC fit spectrum (red line). The blue dashed vertical lines represent the fitting range.

0.27 keV (for L-shell capture), or 0.02 keV (for M-shell capture), as summarized in Table 6.3[111, 112]. The production of ^{37}Ar is mainly due to cosmogenic activation of atmospheric argon[110], such as

$$\begin{aligned} &^{40}\mathrm{Ar}(\mathrm{n},4\mathrm{n})^{37}\mathrm{Ar} && \text{interaction with fast (} > 20 \text{ MeV) neutron,} \\ &^{36}\mathrm{Ar}(\mathrm{n},\gamma)^{37}\mathrm{Ar} && \text{thermal neutron absorption,} \\ &^{40}\mathrm{Ar}(\gamma,3\mathrm{n})^{37}\mathrm{Ar} && \text{interaction with } O(10) \text{ MeV} \gamma\text{−ray.} \end{aligned} \tag{6.3}$$

Table 6.3. Decay mode, branching ratio (BR), and produced radiations in the decay of ^{37}Ar [111, 112].

Decay mode	BR (%)	Energy (keV)	
		Auger electrons	x-ray
K	81.3 (3)	2.82	0.0
	2.76 (7)	0.20	2.62 (K_{α_1})
	5.46 (14)	0.20	2.62 (K_{α_2})
(sum)	90.21 (24)	2.82 (total energy release)	
L	8.72 (20)	0.27	0.0
M	1.06 (7)	0.02	0.0

Therefore, it is expected to reach equilibrium and the decay rate of ^{37}Ar in the detector is expected to be constant from the argon filling time to the end of measurement.

The data used in this measurement come from approximately 27 hours of detector operation without any external sources [1)]. The events taken during the campaign are mainly induced by external radiation such as ambient γ-ray and cosmic-ray induced particle. It is crucial for the identification of the low-energy event to enhance the signal (^{37}Ar) to noise (background) ratio. In addition to the event selections of Section 6.3.2, as partly shown in Figs. 6.17 and 6.18, we tightly require anti-coincidence between the fiducial and any of the four outer-bath PMTs. The cut value is set as in Fig. 6.19 so that events associated with multiple scattering or cosmic-ray are vetoed. Figure 6.20 shows the observed light spectra sequentially imposed the selections.

Resulting light spectrum for this measurement is shown in Fig. 6.21. The peak around 25 p.e. is attributed to the energy release of 2.82 keV from ^{37}Ar. No structures corresponding to the L- or M-shell capture could be seen, probably due to the large amount of random coincidence background and the lack of photostatistics. The spectrum with ^{37}Ar is fitted with the sum of the Gaussian, exponential, and constant terms that describe the signal and low energy background model. The goodness of fit for the peak is $\chi^2/ndf = 82.21/84$.

We have performed several checks to investigate the peak in the context of the ^{37}Ar interpretation. The ^{37}Ar decay rate returned by the fit is approximately 25 mBq/kg, which is compatible with literature values[110, 113, 26]. The ^{37}Ar candidates are distributed uniformly through the observation time, as partly shown in Fig. 6.22. Neither the trigger turn-on nor the PSD band cut affect the overall conclusion; slight shifts of the fitting result before and after these correction/selection are considered as systematic uncertainties. Sequential changes of the cut value for the anti-coincidence selection allows to check the presence of unexpected analytical bias. The signal to noise ratio of the peak looks to be elevated as the cut value tightens, as one naively expects. Replacing the empirical background modeling with alternative functions, such as third-order polynomial or first-order polynomial with a minimum allowable value, does not change the conclusion. Consequently, it is reasonable that the peak corresponds to the 2.82 keV energy release from ^{37}Ar.

[1)] except the ^{241}Am source sitting inside the LAr volume

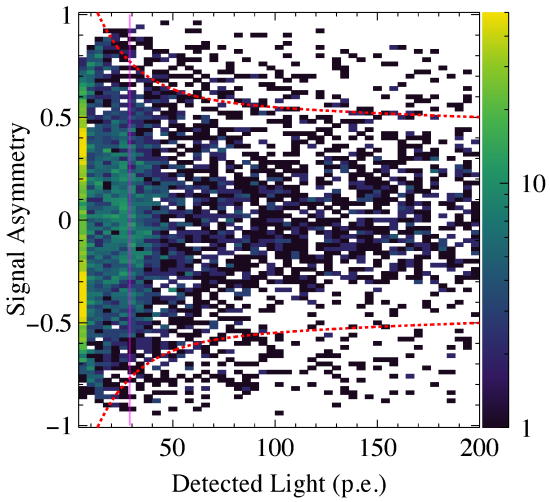

Fig. 6.17. Distribution of the signal asymmetry $((N^1_{\text{p.e.}} - N^2_{\text{p.e.}})/(N^1_{\text{p.e.}} + N^2_{\text{p.e.}}))$ as a function of the total signal yield $(N^1_{\text{p.e.}} + N^2_{\text{p.e.}})$. Events inside the red dashed lines are selected. The vertical magenta line corresponds to the ^{37}Ar peak.

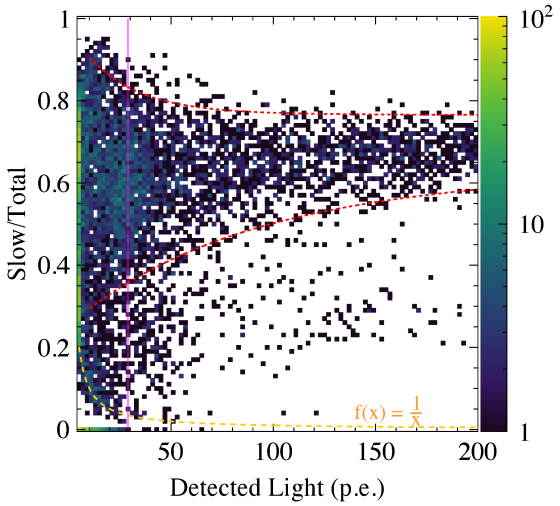

Fig. 6.18. Distribution of the PSD parameter versus the observed light signal. The orange dashed curve corresponds to events that have only 1 p.e. slow component, for reference. Events inside the red dashed lines are selected. The vertical magenta line corresponds to the ^{37}Ar peak.

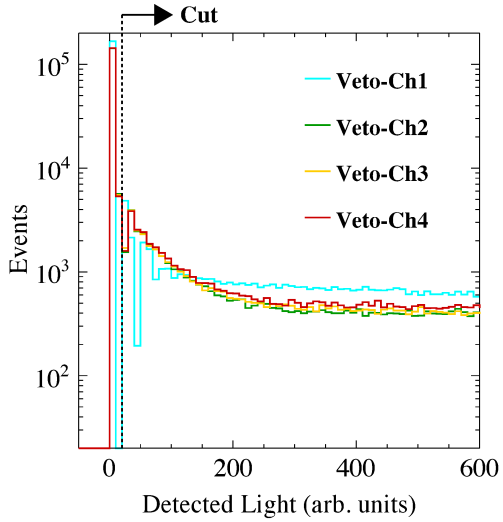

Fig. 6.19. Scintillation spectra of the four outer-bath PMTs. The dashed black line represent the cut value.

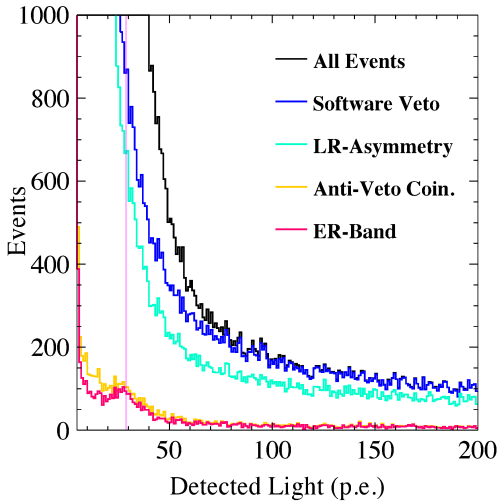

Fig. 6.20. Scintillation spectra of the ^{37}Ar dataset at each step of event selections. The vertical magenta line corresponds to the ^{37}Ar peak.

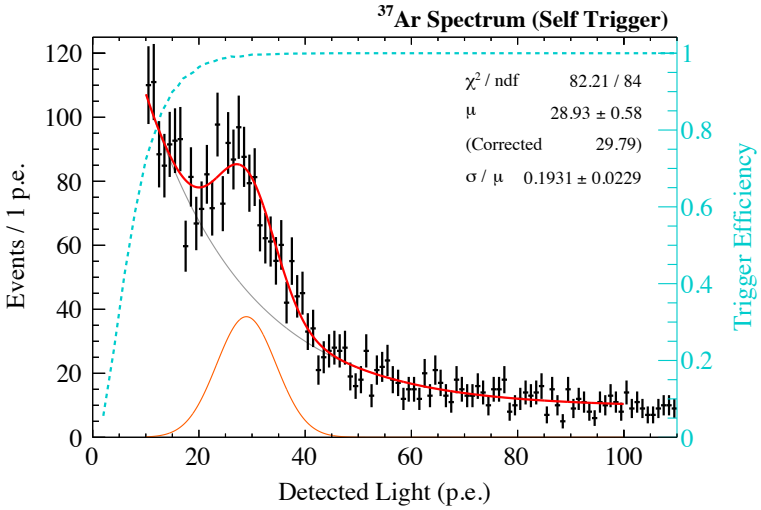

Fig. 6.21. The ^{37}Ar spectrum obtained by requiring anti-coincidence with the outer bath PMTs for the no external source data. The cyan dashed line represents the estimated trigger efficiency and the data is corrected based on this curve.

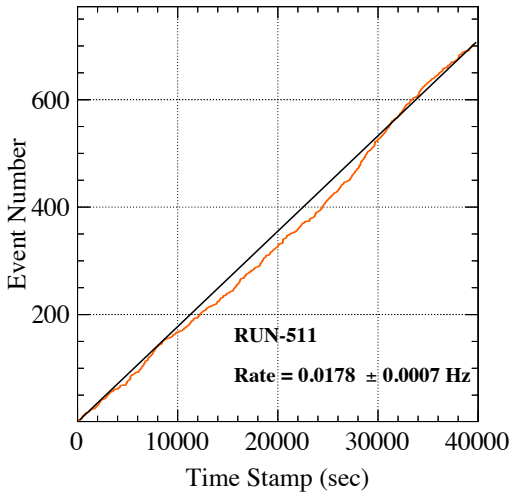

Fig. 6.22. Observed time of the ^{37}Ar peak event in a period of approximately 40000 s. Each colored point represent the observed time of ^{37}Ar-candidate event and black line represent the average through the period.

6.5 Result

The upper panel of Fig. 6.23 summarizes the mean values of the number of detected photoelectron divided by corresponding incident energies, measured by the set of radioactive sources described in the previous section. Nonlinear response on the scintillation yield is seen, which peaks around 200 keV. This trend can be attributed to the energy dependence of the ionization electron-ion recombination probability.

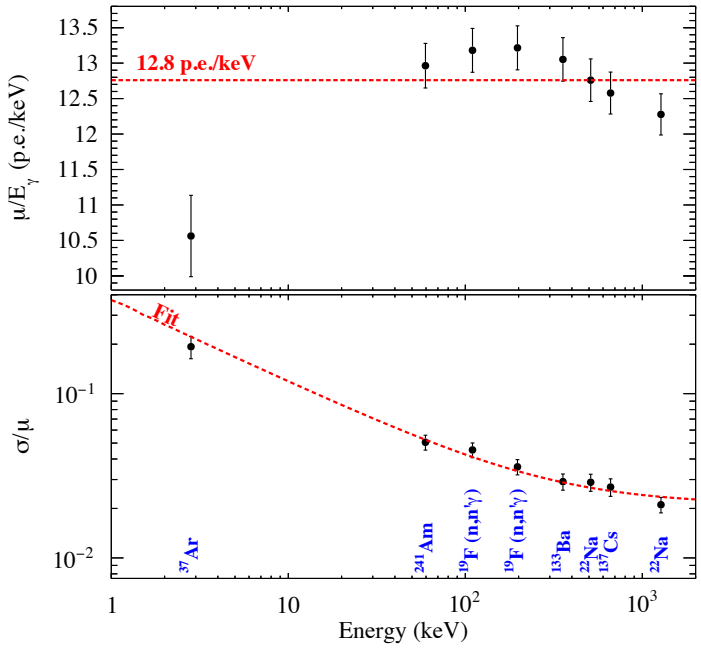

Fig. 6.23. Top: observed light yields obtained by the fitting analysis for each calibration line, divided by corresponding incident energy. The red dashed line represents the energy calibration using 511.0 keV full-absorption peak. Bottom: energy resolution of the detector measured with full-absorption peaks. The red dashed line represents the fit function with stochastic and constant terms (see text).

The TIB model[52] and the Doke-Birks' model[114] can presumably explain the data, as is the case for the liquid xenon scintillation detector[103]. For the higher energy range, the Doke-Birks's model is generally applied to deal with longer-range tracks and to predict the decrease of the probability as the track energy increases (or dE/dx decreases). On the other hand, for the lower energy range, typically less than $O(10\,\mathrm{keV})$, it is known that the TIB model is suitable for modeling the data because it is based on the low energy recoiled track whose range is comparable to or shorter than the mean ionization electron-ion thermalization distance. The TIB model predicts the increase of the probability as the track energy increase (or number of ionization electron-ion pair increase). Further study for quantitative evaluation and modeling of the liquid argon response will be discussed in Section 6.6.

The energy resolution of the detector is also characterized based on the full-absorption peaks and is shown in the lower panel of Fig. 6.23. The set of points is fit to the function

$$\frac{\sigma}{\mu} = \sqrt{\frac{\sigma_s^2}{E_\gamma} + \sigma_c^2}, \tag{6.4}$$

where σ_s accounts for stochastic fluctuation and σ_c accounts for the variance of the mean value of monoenergy deposition. The values are found to be $\sigma_s = 0.37 \pm 0.03$ and $\sigma_c = 0.021 \pm 0.002$, respectively.

Several sources are expected to degrade the energy resolution. The contribution of each source is

Table 6.4. Observed coefficients and estimated contributions of the stochastic (S) and constant (C) terms of the energy resolution. Although the origin of the constant term is not quantitatively estimated, almost all of which is believed to come from the geometrical effect.

Type	Source	Coefficient (α)
S ($\frac{\sigma}{\mu} = \frac{\alpha}{\sqrt{E_\gamma}}$)	Data	0.37 ± 0.03
	Photostatistics	≈0.3
	Multiple scattering	<0.1
	PMT gain and afterpulse	≲0.2
	Photoncounting algorithm	≈0.0
	TPB wavelength shift	0.0–0.1
C ($\frac{\sigma}{\mu} = \alpha$)	Data	0.021 ± 0.002
	Geometrical effect	(≈0.02)

examined and listed in Table 6.4. Convoluting the stochastic terms ($\sigma_s/\sqrt{E_\gamma}$) listed in Table 6.4 explains approximately 90% of the stochastic term observed in the data. The rest of the term possibly comes from fluctuations in the ionization electron-ion recombination process; detecting the charge yield would be necessary to fully address it. The constant term (σ_c) is believed to mainly consist of the geometrical effect.

The result is subjected to several systematic uncertainty sources which stem from both the detector response and the analysis procedure, as listed in Table 6.5. The former is the linearity of the PMT gain and its afterpulse, explored by the PMT response study using both liquid argon data and a property measurement of the PMT after the liquid argon detector operation, and the time stability of the detector complex, monitored by the regular calibrations throughout the data collection period. The latter mainly comes from the photon-counting algorithm part and the related correction of the analysis. We assign the size of the correction as the uncertainty. Relatively small uncertainty is attributed to the fit of the full-absorption peak, which is estimated by refitting the peak with a simple Gaussian function. The trigger efficiency is an additional uncertainty source for the ^{37}Ar line analysis. We refit the peak without the correction, and assign the corresponding uncertainty as the variation between these results.

The uncertainty of the energy resolution is considered as typically 10% in total, mainly from the fitting modeling.

6.6 TIB model interpretation and absolute yield on scintillation response

The absolute scintillation yield, the number of photons generated by an incident particle n_{ph} per unit energy deposition photon/keV is a more essential quantity for the liquid argon scintillation detector than the observed light signal per incident energy, p.e./keV. As mentioned in Section 6.1, the yield for recoiled electron is measured by Doke *et al.* as 41 ± 2 photon/keV using a 1-MeV electron source[42].

On the other hand, the 511-keV full-absorption point is the most suitable energy for the comparison between the previous measurements since several works[115, 106, 46, 116] have commonly presented the observed light yield at this point. As the scintillation yield of a γ-ray full-absorption event is affected

Table 6.5. Summary of the systematic uncertainty sources for the observed light yields (in unit of p.e.) for each full-absorption peak and energy resolution.

Systematic	Scintillation yields		Energy resolution	
	Dataset	Fraction	Dataset	Fraction
PMT afterpulse	All	2.0%		
PMT gain non-linearity	All	<1.0%		
Time stability of the detector	All	0.5%		
Photoncounting algorithm	All	1.0%		
Function modeling	^{241}Am	0.8%	all	10%
	Others	0.5%		
Trigger efficiency	^{37}Ar	4.5%		
	Others	0		

by the energy dependence of that for recoiled electrons because of multiple scattering, we perform a Geant4 MC simulation to evaluate it. Figure 6.24 shows the average number of the interaction points. It indicates that 511-keV full-absorption events contain about three interaction points on average; however, a discrepancy between the yield for the 511-keV γ-ray and that for the β-ray is found to be less than 2% when assuming the Doke-Birks's model (gray line in Fig. 6.25) [42]. Therefore, we determine the absolute scintillation yield by using the 511-keV point and referring the Doke's measurement.

Figure 6.25 shows the scintillation yield obtained in this analysis, where the uncertainty includes the uncertainties from the measurement and in the referenced literature. As mentioned in the previous section, the energy dependence of the yield is attributed to the ionization electron-ion recombination probability. For a lower energy event, the TIB model presumably predicts the response;

$$\begin{aligned} n_{\mathrm{ph}} &= \frac{E_{\mathrm{ER}}}{W_s}(N_{ex} + rN_i) = \frac{E_{\mathrm{ER}}}{W_s}\frac{1+r}{1+\alpha}, \\ r &= 1 - \frac{1}{N_i\varsigma}\ln(1 + N_i\varsigma). \end{aligned} \tag{6.5}$$

Considering the facts that the number of the interaction point of the ^{37}Ar events can be approximated to be one due to its low energy deposition and decay mode mainly consisting of Auger electrons[111], and that the TIB model is fully applied for liquid xenon at corresponding energy where the electron track length is smaller than the thermalization distance of the ionization electron[103, 56], we determine the parameter ς from the ^{37}Ar data. It is calculated as $\varsigma = 0.033^{+0.012}_{-0.008}$ and represented with the red band in Fig. 6.25. Further studies, such as additional measurements around 10 keV and discussion on the stitching between the TIB model and Doke-Birks's model, should be performed in future work. This result also would be practically essential input for tuning the response model implemented, for instance, in the NEST package[117].

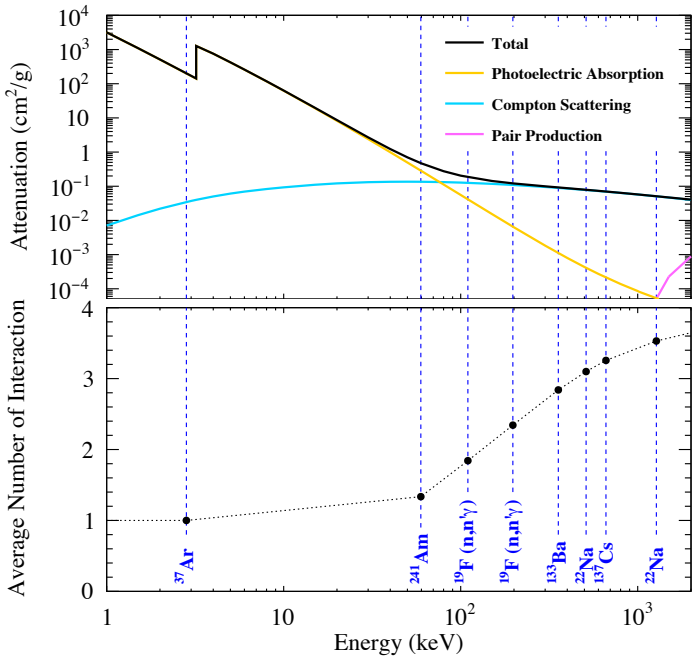

Fig. 6.24. Top: the γ-ray cross sections for argon provided by XCOM[118]. Bottom: average number of interaction points for the full-absorption peaks calculated by the Geant4 MC simulation.

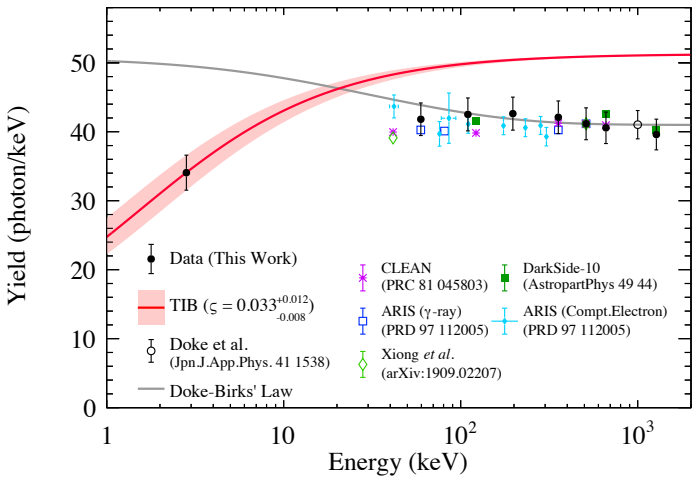

Fig. 6.25. Measured scintillation yield as a function of the incident energy E_γ (black solid circle). The absolute yield is determined by referring the measurement by Doke *et al.* (black open circle)[42]. The TIB model function with a parameter found by the 2.82 keV point is shown with its uncertainty (red band). The results from other experiments, CLEAN (violet star point)[115], DarkSide-10 (green filled square)[106], ARIS (blue open square and blue filled rhombus)[46], and Xiong *et al.* (green open rhombus)[116] are also shown where each yield is normalized at 511 keV referring the Doke-Birks' model (gray solid line)[42].

6.7 Future prospects

6.7.1 Independent measurement of the absolute yield

In the previous section, the absolute scintillation yield is determined by referring the literature values. Although this method works well as mentioned above, it is worth considering an independent measurement will allow direct comparison of the quantity and provide non-correlated and complementary quantity.

Determination of the scintillation yield requires absolute values of the wavelength shifting efficiency from VUV to visible light, LCE of the detector, and PMT QE. Among these, the PMT QE is calculated by the wavelength shifter (TPB) emission spectrum and the manufacturer datasheet as approximately 28% (Fig. 4.6). The LCE of the detector is estimated as 97% under some assumptions, as described in Section 4.5.2. Position dependency of the LCE is also computed to be small (less than 1%) by the same estimation, therefore no correction for the interaction point is required. Finally, we need the TPB wavelength shifting efficiency. However, there is a discussion on the value (ranging from ~0.4 to ~1.2[119, 120]) and we have no idea which value is more appropriate in our configuration. Thus, we can conclude that the primary work to determine the absolute yield is to measure the shifting efficiency.

To our knowledge, it can be claimed that the measurement in this work do not show inconsistency with the Doke's measurement when assuming the 100% efficiency.

6.7.2 Possible calibration sources for a few tens of keV region

One or more calibration points around 10 keV are required so that the energy dependency of the scintillation yield is determined more precisely. There are several promising candidates. Unfortunately these sources cannot be used in this measurement because of several constrains; however, additional measurement would reveal the low-energy response on liquid argon scintillation yields and reduce the uncertainty.

Another γ-ray from Americium-241 In addition to the 59.5 keV γ-ray from ^{241}Am presented in Section 6.4.3, it emits another γ-ray of 26.3 keV. Although the branching ratio of 26.3 keV line is smaller than that of the 59.5 keV line (2.4% and 35.7%, respectively), the emission of these lines is competing process and thus the single 26.3 keV peak should be detectable. Corresponding peak is not detected because platinum foil and PTFE bulk exist between the source and fiducial volume. However, it would be possible by, for example, turning over the ^{241}Am-deposited foil and using lower-Z material instead of PTFE. The α-ray-tagging method demonstrated in this work allows to see the peak with good signal-to-noise ratio.

Metastable krypton-83 One of the commonly used calibration source in noble liquid detector is $^{83}\mathrm{Kr}^{m}$. It has a half life of 1.83 hour and subsequently decays via internal transition with a emission of 32.1- and 9.4-keV conversion electrons. The half life between the first and second electron emissions is 157 ns.

The $^{83}Kr^{m}$, produced as a decay product of ^{83}Rb, is introduced into whole liquid argon volume and used as a diffused source.

The use in calibrating the liquid argon detector is not straightforward because of the short time between two emission electrons. One of the approach is to deal the two electrons as independent events and analytically separate using waveform analysis technique, as demonstrated in Ref. [121]. Another approach is more model-dependent technique. As the $^{83}Kr^{m}$ energy is in the region where TIB model and Doke-Birks's model compete, one expects different total (41.5 keV) yields with a different assumption. For example, if the total yield is lower than Doke-Birks's model prediction, the TIB model can be valid at least at 9.4 keV. To that end, the $^{83}Kr^{m}$ is effective for the calibration when used with other energy points and model interpretation [2)].

Compton electron tagging Single-scattered Compton electron can be used in the calibration by tagging the scattered γ-ray with additional detectors. Tagging 511 keV γ-ray at scatter angle of 20 degree, for example, one expects a peak from the Compton electron at 30 keV. Main challenge of this measurement arises from trade-off between the angular resolution and signal event rate. To achieve a calibration with small uncertainty, one is required a high-intensity γ-ray source, a tiny fiducial volume, a tiny tagging detector, and small amount of detector materials.

Characteristic x-ray The use of characteristic x-ray from detector component is more challenging but promoting method. As the low-energy x-ray immediately absorbed by materials, the source must be in touch with the fiducial. Replacing the PTFE bulk with copper is a choice for this purpose. By irradiating the fiducial with γ-ray, the 9.0 keV x-ray from copper is induced and would provide a calibration point. Tagging energy deposition in the outer bath region, the signal-to-noise ratio of the peak would be enhanced. As the mean free path of 9.0 keV x-ray in liquid argon is $O(100\ \mu\text{m})$, careful analysis for the surface event should be attended.

[2)] In case of using the source such as $^{83}Kr^{m}$, the laboratory must satisfy the rule about an unsealed radioactive source

Chapter 7

Direct dark matter search at surface

A search for WIMP is performed with the single-phase detector at surface laboratory with an exposure of 0.2 kg · days. The detector is surrounded by shieldings such as liquid argon, oxygen-free copper (OFC), lead, and polyethylene so that the low background condition to be achieved. The high LCE of the detector allows to reduce the energy threshold down to 6 keV, combined with the understandings of the liquid argon response presented in the previous chapters. Even after selecting NR events by PSD, a number of events have been found to remain. Regarding all of the remaining events as the signal, we exclude WIMP with mass of 10 GeV/c^2 at 4×10^{-37} cm^2.

7.1 Apparatus

7.1.1 Detector design

Intending to search for WIMP with a "background-free" condition, the high light yield single-phase detector is chosen in this experiment. Based on previous studies [47], sensitivity for the low-mass WIMP with PID technique is maximized at null field rather than under any magnitude of electric fields. This is because the ER rejection with the combination of the S2/S1 ratio and the S1 pulse shape is less efficient than solely with the pulse shape at null-field. The scintillation yield decreases as the field strength increases, and thus the PSD power decreases instead of an increase of the S2/S1 discrimination capability. However, the S2/S1 ratio has insufficient power to recover the PSD. As shown in Fig. 7.1, the strength of the field does not matter at least up to 3.0 kV/cm. Therefore the best path in this search is to use a single-phase detector and maximize the LCE.

The ultimate target WIMP-nucleus cross section of the ANKOK experiment is $\sim 10^{-41}$ cm^2. It should be achieved by an exposure of several tens of kg × days, and so the detector is required to have order of 1 kg fiducial volume. The single-phase detector matches this requirement.

7.1.2 Scintillation detector

As mentioned before, the detector is the one presented in Section 4.5.2 and used in Chapter 6, containing 0.224 kg of the active volume. Following improvements are made to suppress background events:

- It sits on a 1 cm thick oxygen-free copper plate instead of a thin aluminum one.

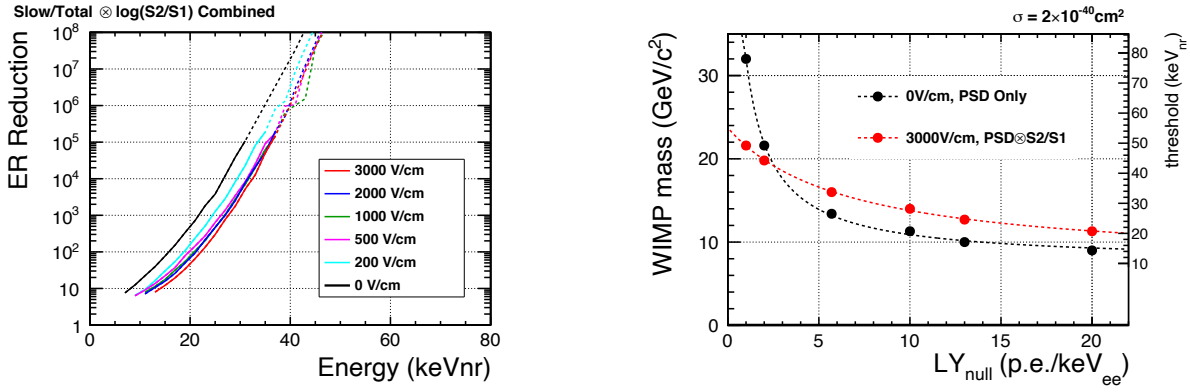

Fig. 7.1. Left: ER rejection power with a combination of PSD and $\log_{10}(S2/S1)$ at various fields as a function of NR energy. Right: expected sensitivity under an assumption of ^{39}Ar background. The black point is based on ER rejection with PSD at null field and the red point is with PSD and $\log_{10}(S2/S1)$ combination at 3.0 kV/cm. The figures are taken from Ref. [47].

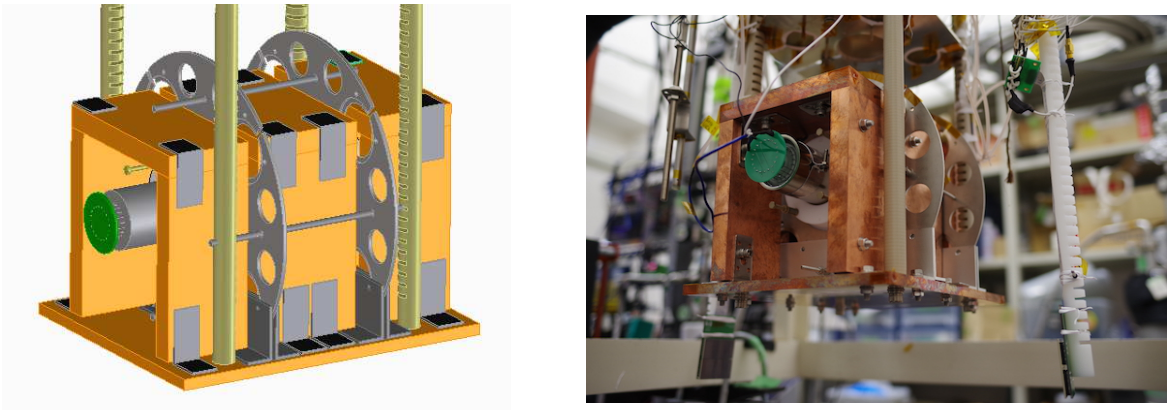

Fig. 7.2. Schematic view (left) and picture (right) of the detector.

- An oxygen-free copper plate with 2-cm-thickness surrounds the detector and serves as the passive shield against γ-ray.
- All surface of the detector components are ultrasonically cleaned in ethanol.
- It is immersed in a deeper liquid argon bath.

Schematic and picture of the detector are shown in Fig. 7.2.

7.1.3 Liquid argon in the vessel

Figure 7.3 shows a diagram of the apparatus inside the vessel. The vessel is filled with approximately 60-cm-high liquid argon. The scintillation detector is set nearly center of liquid argon bath. Liquid surface is continuously monitored by a liquid-level meter and platinum-register thermometers.

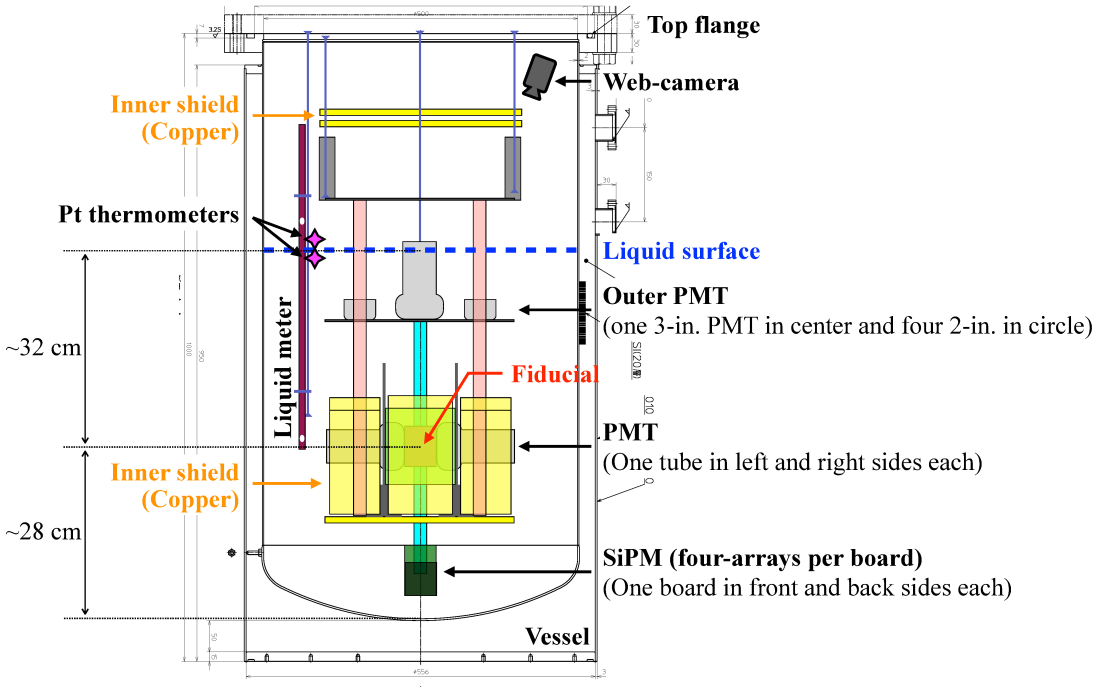

Fig. 7.3. Diagram of the experimental apparatus.

As mentioned in Section 4.5.2, the liquid argon bath works as active shielding against backgrounds and is shown by the four 2 in. PMTs. In order to enhance the vetoing efficiency, one 3 in. PMT (R11065) and two silicon photomultiplier (SiPM) modules (four 2.4×2.4 cm^2 SiPM arrays in each) are additionally implemented as shown in Fig. 7.3. The PMT locates between the four PMTs and the SiPM modules locate below the fiducial volume. The SiPM array (Hamamatsu S13361) consists of sixteen through silicon via (TSV) Multi-Pixel Photon Counter (MPPC) which is sensitive to visible light. The SiPM module consists of a custom board which gangs four SiPM arrays[1)]. The windows of all five PMTs and two SiPM modules are coated with the TPB. In addition, a TPB-coated ESR reflector is put on the outer surface of the inner copper shield to enhance LCE of the outer region. Figure 7.4 is a picture of the whole apparatus. Figure 7.5 is an inside view of the LAr-filling apparatus seen by a webcamera.

7.1.4 Passive shielding

The vessel is surrounded by shieldings against γ-ray and neutron from ambience. From inside to outside, approximately 2-cm-thick oxygen-free copper, 10-cm-thick lead, and 20-cm-thick polyethylene are placed as schematically shown in Fig. 7.6.

Lead acts as the shields against γ- and β-rays. Total amount of the lead is about 5 ton. The lead has a radioactive isotope ^{210}Pb with half life of 22.3 y, and its daughter ^{210}Bi decays via β-ray transition with the Q-value of 1163 keV. It can result in Bremsstrahlung x-ray as shown in Fig. 7.7. As lead is not sufficient for its own radiations, oxygen-free copper is placed between lead and vessel.

[1)] Paper under preparation

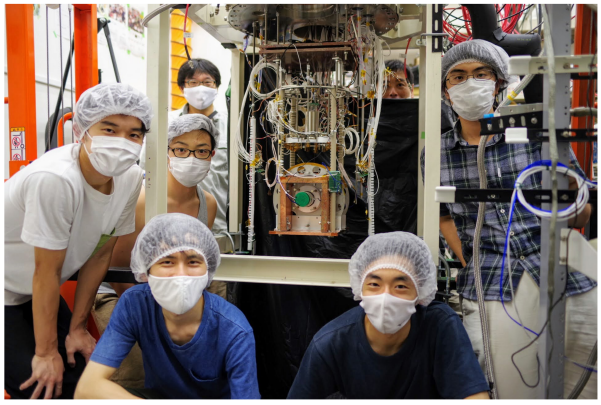

Fig. 7.4. Picture of the apparatus.

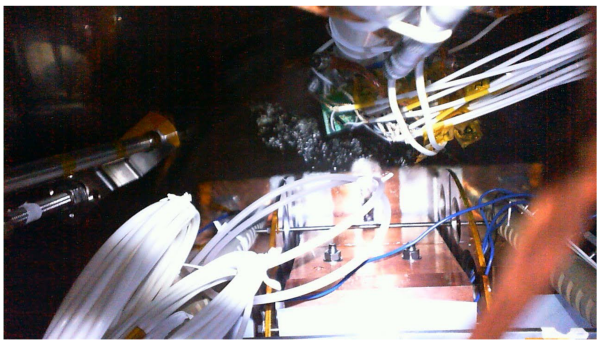

Fig. 7.5. Picture of the inside the vessel during the LAr filling taken by a webcamera. The OFC shield surrounding the detector and the top of SiPM board are seen. Liquid surface is found just above the bottom OFC plate.

Polyethylene acts as the shields against ambient neutron. Molded polyethylene is placed on top and bottom of the vessel, and polyethylene pellet is placed on the side. A PHITS-based MC simulation expects that ambient neutron below 20 MeV is shielded by less than 1/10.

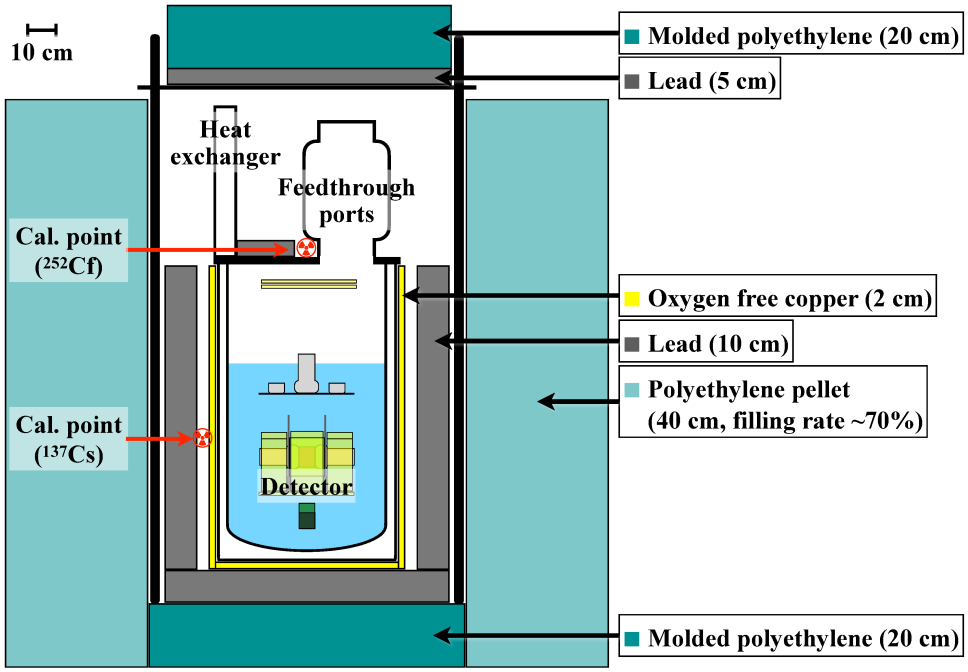

Fig. 7.6. Schematic view of the passive shieldings surrounding the vessel. Also shown are the calibration points where ^{252}Cf or ^{137}Cs sources are placed in the calibration run.

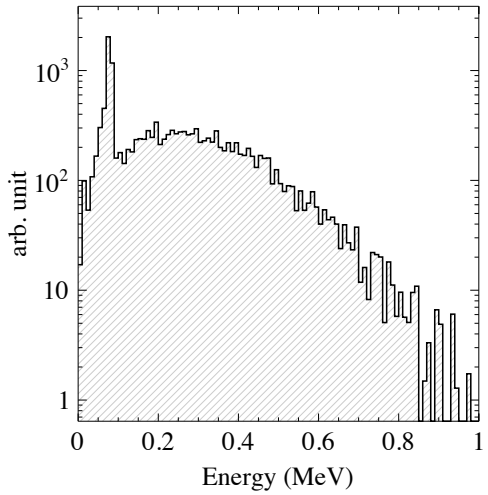

Fig. 7.7. Relative intensity of x-ray from ^{210}Pb and its daughter calculated using PHITS simulation.

7.2 Calibration

7.2.1 PMT calibration

The gain of the fiducial-viewing PMTs is calibrated as with the same method described in Section 6.3.1. Currently, a nanosecond pulsed laser (Thorlabs NPL45B) is used instead of the blue LED due to its operationality. Its center wavelength is 450 nm and pulse width is ~10 ns. Typical charge distribution and fit is shown in Fig. 7.8. This calibration is performed every 12 hours during the experiment, as shown in Fig. 7.9, and overall stabilities of the gain and light yield are 0.5%. It is almost same as that in the measurement described in Chapter 6.

7.2.2 Energy calibration

Energy calibration of the detector is performed with the 109.8- and 197.1-keV quasimonoenergetic lines produced by $(n,n'\gamma)$ reaction with ^{19}F. The ^{252}Cf fast neutron source is placed on the top flange so that the neutron reaches the PTFE bulk and induces the γ-rays. Figure 7.10 (left) shows the scintillation spectrum and fitting results. The light yield is determined as 13.2 ± 0.3 p.e./keV. It is consistent with the previous measurement in Chapter 6. Periodical measurement ensures the stability of the detector within 0.5% as shown in Fig. 7.11.

Additional calibration with the ^{137}Cs source is also performed. Because of the passive shieldings, it is impossible to beam the γ-ray toward the fiducial center. Therefore, this calibration is performed with the events near the PMT window (i.e. events that have relatively large left-right-asymmetry value) by putting the source on a narrow gap between the vessel and lead. Figure 7.10 (right) shows the spectrum obtained by setting the source along with the PMT side. It returns 12.3 ± 0.3 p.e./keV. This value is also consistent to the expectation when considering the energy dependency of the scintillation yield.

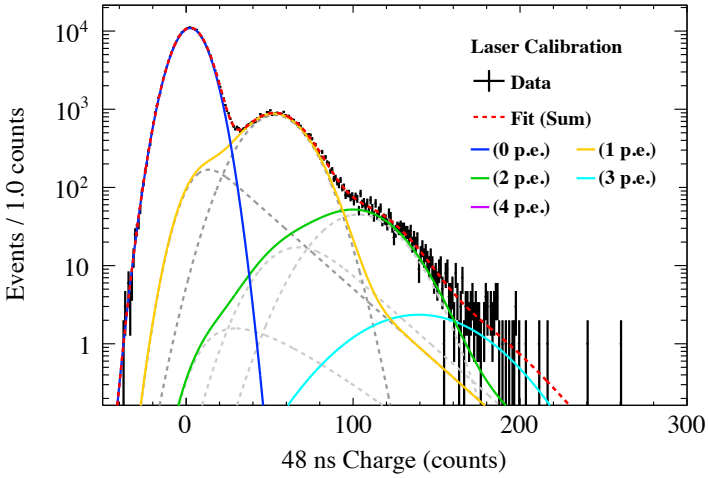

Fig. 7.8. A typical charge distribution in the laser calibration. The PMT gain is evaluated by the fit with Gaussian plus exponential model (gain-model A) described in Section 6.3.1.

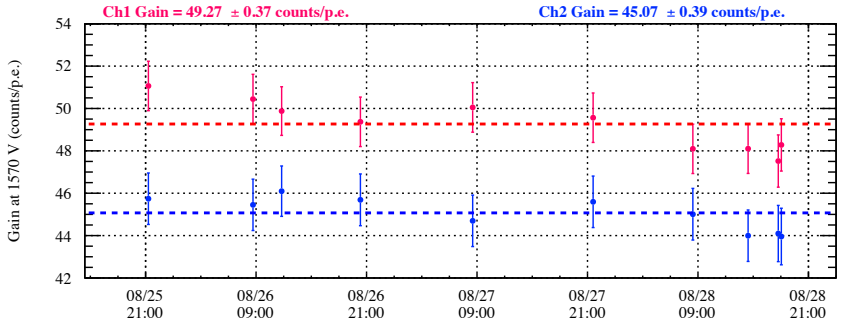

Fig. 7.9. Time evolution of the gain of the two PMTs calibrated with the nanosecond pulsed laser.

Recoil energy of each event in the WIMP search run is reconstructed using the results presented in Chapter 5 and Chapter 6 for NR and ER event, respectively. Figure 7.12 shows the resulting relationship between the observed scintillation yield and the reconstructed energies.

7.2.3 PSD parameter

Both NR and ER bands of the PSD parameter are evaluated to define signal region and estimate background leakage. The ^{137}Cs and ^{252}Cf datasets, used in the energy calibration in the previous section, are also used. The analysis procedure is basically common to that in Section 6.3. For the ^{252}Cf data, we operate the NaI(Tl) scintillator near the source to get the TOF information.

The mean μ and deviation σ of the slow/total distribution are evaluated for both NR and ER events by the ^{137}Cs and ^{252}Cf data, respectively. The distribution in each energy window is empirically modeled

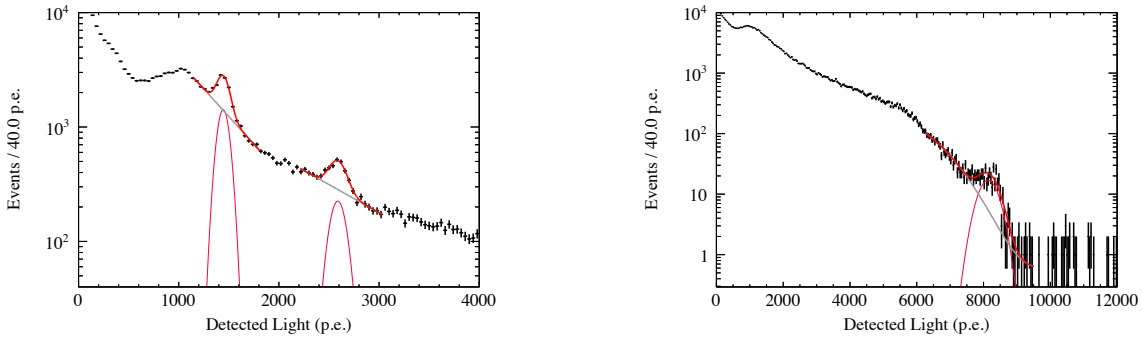

Fig. 7.10. Energy calibration of the detector using the 109.8- and 197.1-keV quasimonoenergetic lines in the ^{252}Cf data (left) and 661.7 keV line in ^{137}Cs data (right).

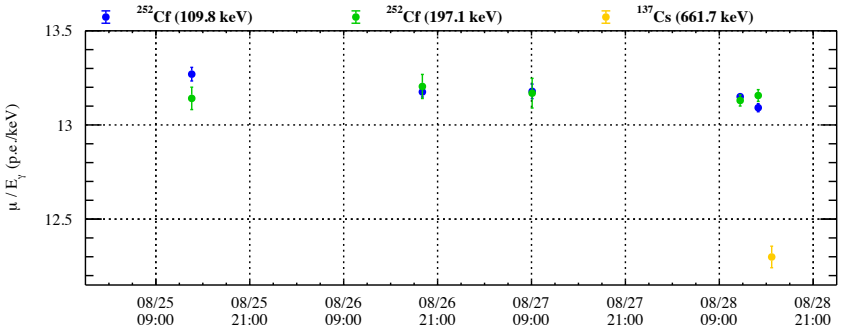

Fig. 7.11. Time evolution of the light yield calibrated with the ^{252}Cf and ^{137}Cs sources.

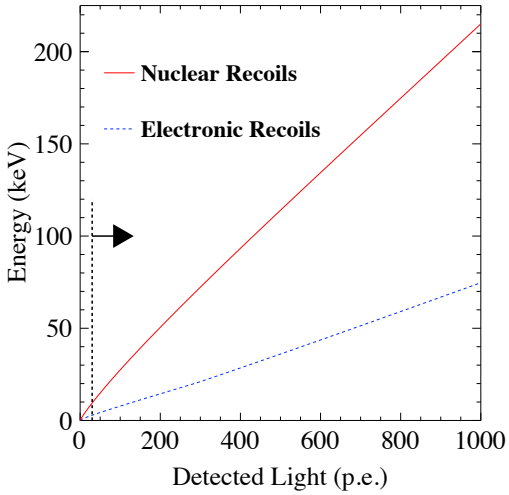

Fig. 7.12. Relationship between the observed scintillation yield and reconstructed energies for NR and ER in this detector. The vertical dashed line and the arrow represent the energy threshold of the WIMP search analysis.

with beta distribution:

$$f(x;\alpha,\beta) = \frac{x^{\alpha-1}(1-x)^{\beta-1}}{B(\alpha,\beta)}, \tag{7.1}$$

$$B(\alpha,\beta) = \int_0^1 x^{\alpha-1}(1-x)^{\beta-1}dx, \text{ where} \tag{7.2}$$

$$\alpha = \frac{\mu^2(1-\mu)}{\sigma^2} - \mu, \tag{7.3}$$

$$\beta = (\frac{1}{\mu} - 1)\alpha. \tag{7.4}$$

First, the ER band is evaluated by the ^{137}Cs data. Figure 7.13 shows the slow/total distribution and the fit with the model of the energy ranges from 28–32 p.e. to 92–96 p.e. Then, the NR band is evaluated by the ^{252}Cf data. Since the ^{252}Cf data contains not only NR events but also ER, a simple sum of two beta distributions is used for the fit. The ER band parameterization is constrained from the ^{137}Cs data fit. Figure 7.14 shows the distribution and the fit with the sum of ER and NR models. Resulting NR and ER bands are shown in Fig. 7.15.

7.3 Measurement

7.3.1 Measurement overview

The experiment was started on August 24th 2020 and halted in 28th. The WIMP search data presented here was taken in two periods, as summarized in Table 7.1. These periods are taken under the same condition except the trigger inhibition time, within which time a new trigger pulse is prevented in hardware to remain the DAQ system within its capacity (see Section 4.3). The trigger logic is also the same as that described in Section 6.2; it is fired by a coincidence, within 1 μs, of the two fiducial PMTs with pulses above the threshold below single-photon pulse. Figure 7.16 shows the trigger rate of the WIMP search run. The mean trigger rate is 2.8 Hz (4.8 Hz) for the first (second) period and is stable within about 10%.

Then the data analysis is performed following the photon-counting technique.

Table 7.1. Summary of WIMP search data used in this analysis.

#	Start	End	Real time	Trigger inhibition
1	Aug. 25th 21:20	Aug. 26th 08:28	11h 8m	1 ms
2	Aug. 27th 09:15	Aug. 27th 19:46	10h 51m	100 μs

7.3.2 Livetime

The trigger inhibition time of 1 ms or 100 μs, which ensures stable data taking, has to be taken into account for the livetime calculation. We should also take into account the software 10 ms veto imposed

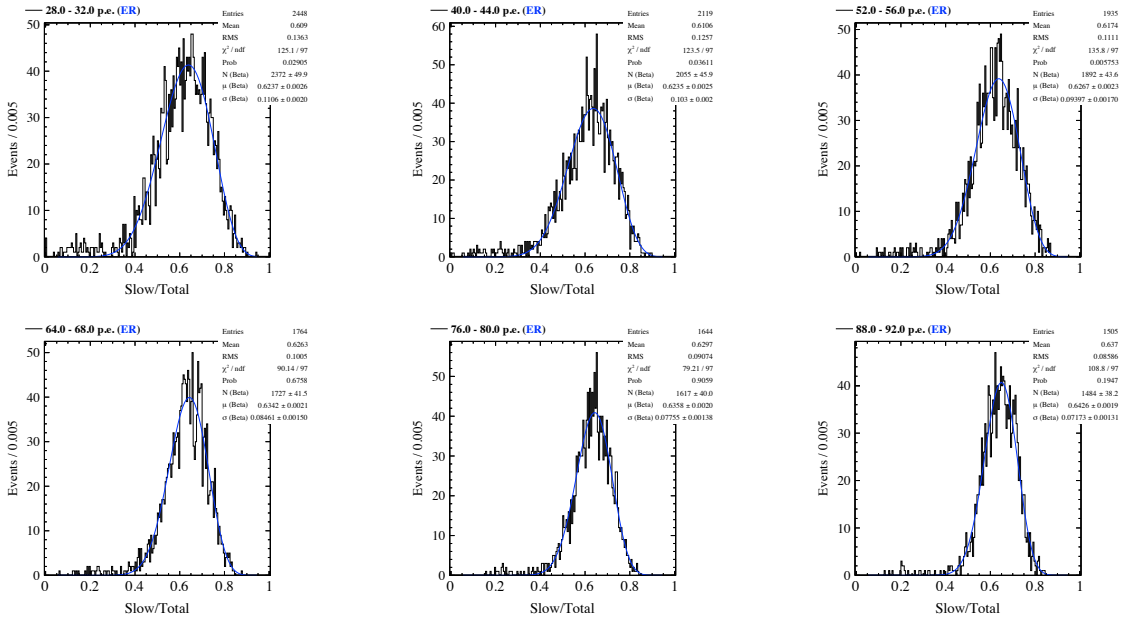

Fig. 7.13. Distributions of the PSD parameter slow/total of ER event in photoelectron bins of 28–32 p.e., 40–44 p.e., 52–56 p.e., 68–72 p.e., 80–84 p.e. and 92–96 p.e. (from left to right and top to down). The blue lines represent the fit with the beta distribution. The data are taken with the ^{137}Cs source.

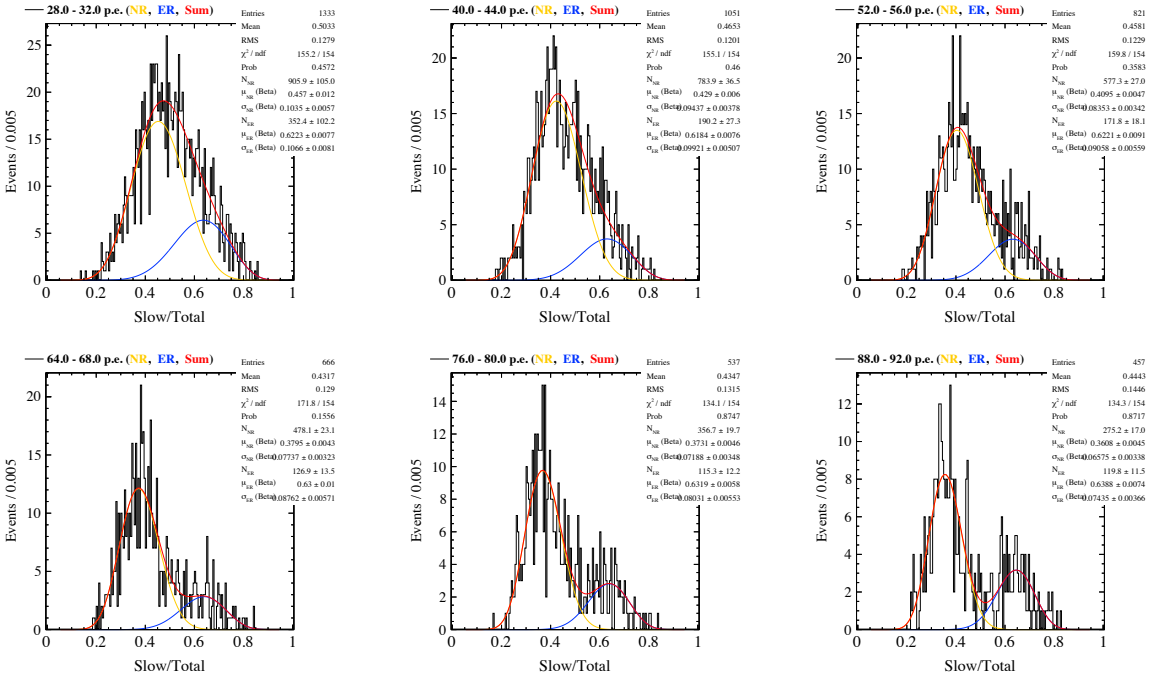

Fig. 7.14. Distributions of the PSD parameter slow/total of both NR and ER events in the photoelectron bins. The red lines represent the fit with two beta distributions consists of NR and ER components shown with orange and blue lines respectively. The data are taken with the ^{252}Cf source.

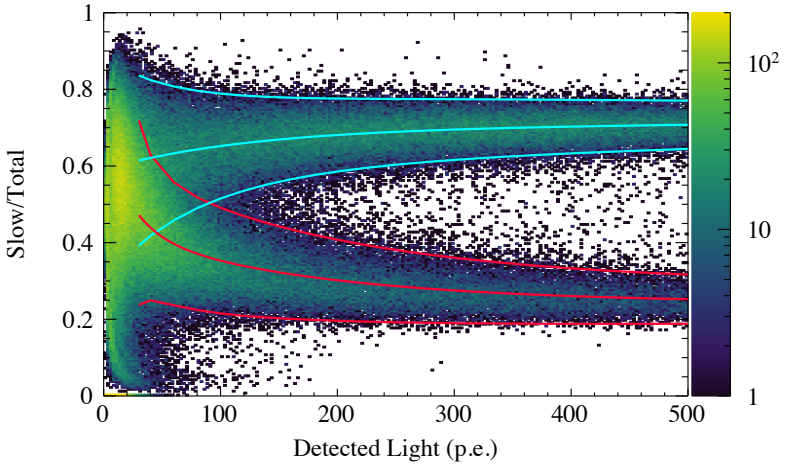

Fig. 7.15. The NR and ER bands of PSD parameter slow/total as a function of observed light signal. The bands represent the $\mu \pm 2\sigma$ regions that are determined from the ^{137}Cs and ^{252}Cf data, and the scattered data shown is the ^{252}Cf data.

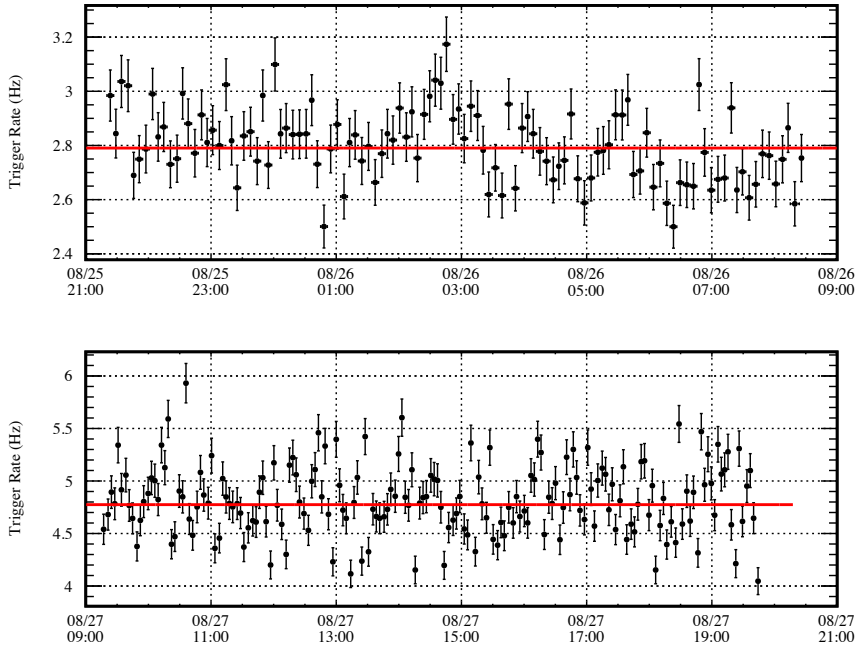

Fig. 7.16. Trigger rate during the WIMP search for the first (top) and second (bottom) periods. The error bar represents the uncertainty from Poisson fluctuation. The red lines represent the average in each period. Difference between these two periods is due to contiguous trigger from PMT afterpulses after detecting large light signal.

after huge energy deposition in the fiducial volume, as mentioned in Section 6.3.2. Consequently, the livetime in this search is evaluated to be 0.88 days. It corresponds to 98% of the real time.

7.3.3 Event selection

A set of event selection is defined and applied.

1. The event is triggered in proper timing and charge, the event has a stable baseline noise, and the event has no more than 0.7 p.e. pulses in the pretrigger window. These requirements reject the events during unstable period and ensure that we can find candidate WIMP events in proper condition.

2. The event does not occur near the PMT and is more likely to be a liquid argon scintillation signal. The signal asymmetry in the two fiducial PMTs is used to estimate it, as mentioned in Section 6.3.2. This selection suppress events with the Cherenkov light on the PMT window or energy deposition within the TPB on the window surface.

3. The event does not have any pileup. Two quantities are used to evaluate it: the photoelectron-weighted time-average of the signal waveform and stray light yield, that is, the charge yield just after the signal-integration window.

4. The event satisfies anti-coincidence with any of the outer-bath photo-detectors.

A number of β-ray events, from ^{39}Ar, allows to validate these selections, because all conditions above should also be satisfied by the diffused β-ray events. Figure 7.17 shows the energy spectrum of the ER events in each step. Assuming the ^{39}Ar activity as 1.0 Bq/kg, overall efficiency of the selection criteria is estimated as nearly 100%. Corresponding systematic uncertainty is discussed in the following section.

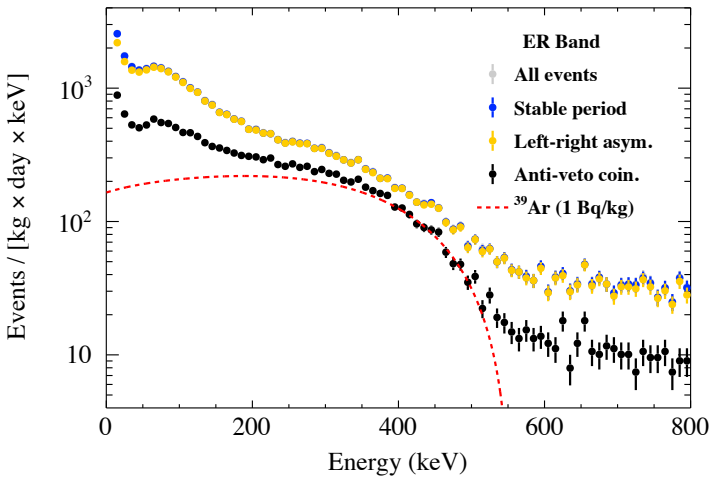

Fig. 7.17. Energy spectra of the ER events observed in the WIMP run, where event selections are sequentially imposed. The red dashed line represents the contribution from ^{39}Ar with 1.0 Bq/kg.

7.3.4 Signal region definition

The detector has, in principle, a capability to detect low-energy NR signal from WIMP. However, unfortunately, this search is not expected to claim the discovery of any WIMP events because the sensitivity of the detector is far less than that of existing exclusion limits from other underground experiments. Therefore, we do not perform any "blind" strategy. The signal region is determined to maximize the sensitivity based on the observed PSD bands and ER background spectrum.

The ER background is directory evaluated from the physics run data. The number of ER event in each photoelectron bin is measured by fitting the PSD distribution, and ER spectrum is obtained as shown in Fig. 7.18. The spectrum is modeled with an empirical function as represented with the red line in Fig. 7.18. Main sources of these events are ^{37}Ar diffused isotope, cosmic-ray induced γ-ray, and x- and γ-rays from radioimpurities inside the detector components. More discussions will be presented in Chapter 8.

Following procedure is performed for each WIMP mass to determine the selection cut based on PSD.

1. Set a common energy threshold as 30 p.e.
2. For a given WIMP mass, compute the differential event rate for a WIMP-nucleon cross section of 1×10^{-37} cm^2 as described in Section 2.4.3.
3. For each photoelectron bin, obtain a slow/total cut value where a value $N_S/\sqrt{N_S + N_B}$ is maximized (N_S : expected number of WIMP event, and N_B : observed number of ER events).
4. Scan the slow/total value and determine signal box.

Figure 7.19 shows the signal regions for several WIMP masses. The region is at least within $\pm 2\sigma$ of the NR band to reject unphysical events. Selection efficiency of the PSD cut is shown in Fig. 7.20 for each mass point.

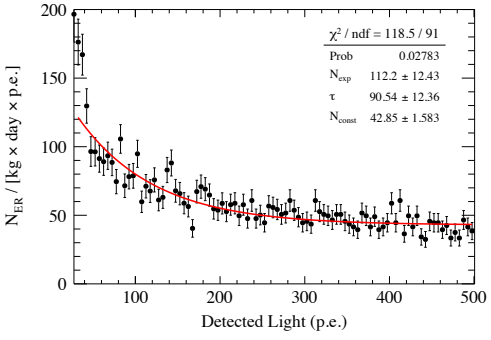

Fig. 7.18. ER spectrum evaluated by the same data used in the WIMP search. The red line is an empirical model function.

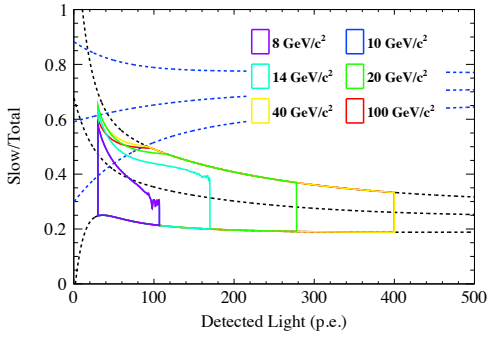

Fig. 7.19. Signal regions of each WIMP masses defined to maximize the sensitivity.

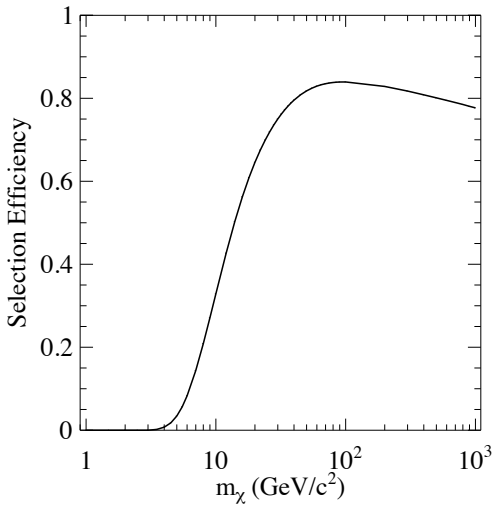

Fig. 7.20. Selection efficiency of the PSD box cut defined in Fig. 7.19. Note that this efficiency contains only the PSD cut.

7.3.5 Systematic uncertainty

Six sources are considered as potential systematic uncertainties in this search; the energy calibration of the detector, the NR response model ($\mathscr{L}_{\rm eff}$, used to reconstruct recoil energy), the PSD parameter calibration, the ER background function, the event selections, and the total exposure of the detector. The dominant contribution is expected to come from the $\mathscr{L}_{\rm eff}$ value of 10%. Uncertainty on the energy calibration (~3%) can be included in the $\mathscr{L}_{\rm eff}$ uncertainty. The other terms are found to have little impact compared to it.

The systematics can change the final result up to approximately ±30%. Primary, more precise measurement of the NR response than ever performed is required to reduce the uncertainty. As the $\mathscr{L}_{\rm eff}$ value is based on the scintillation yield for 511-keV γ-ray, energy calibration at this particular point would also reduce the uncertainty.

The center value of the following result is based on the best-knowledge of the $\mathscr{L}_{\rm eff}$ and other values, and the uncertainty band from the $\mathscr{L}_{\rm eff}$ uncertainty is also presented.

7.4 Result

Figure 7.21 shows the distribution of the events survived all of the event selections, and Fig. 7.22 shows the energy spectrum for NR events fallen in the core NR-band ($\mu \pm 2\sigma$). Applying the signal box defined in Section 7.3.4 and counting up the event falling inside the box, 90% confidence level (C.L.) upper limit of WIMP-nucleon cross section for each WIMP mass is calculated. Figure 7.23 shows the 90% C.L. exclusion curve obtained in from this analysis. For WIMP mass of 10 GeV/c^2 (8 GeV/c^2), the cross section of 4×10^{-37} cm^2 (3×10^{-36} cm^2) is excluded. Obviously, the sensitivity is limited by the

NR events. Discussions on the background source and improving the sensitivity are presented in the following chapter.

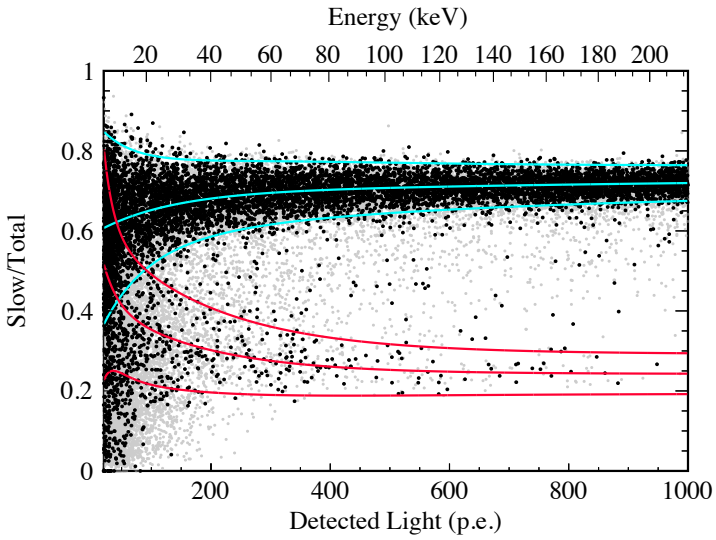

Fig. 7.21. Distribution of the events surviving all event selections (black point) in the detected light versus slow/total plain. The gray point represents the event surviving all selections but anti-veto coincidence. Also shown are the mean and 2σ bands for ER and NR, respectively.

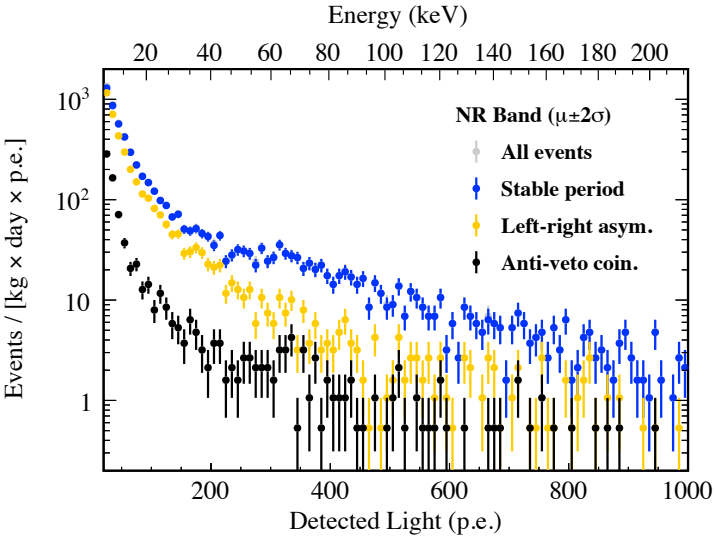

Fig. 7.22. NR energy spectrum from the events within $\mu \pm 2\sigma$ of the NR band, derived from the physics run.

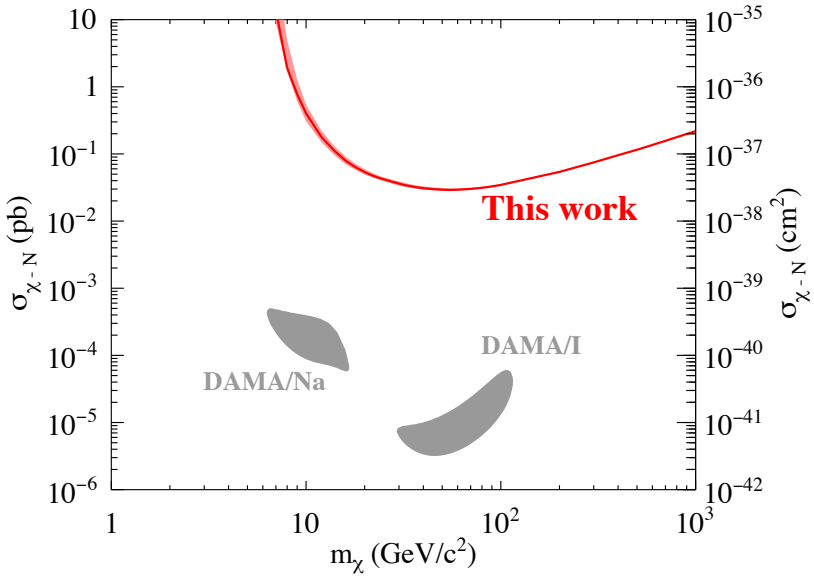

Fig. 7.23. WIMP-nucleon cross section 90% C.L. upper limit derived from this search (red line). The band represents the systematic uncertainty. The gray contours represent the indication from DAMA annual modulation observation.

CHAPTER 8

Discussion

This chapter discusses on several terms that limit the direct search performed in Chapter 7. In that experiment, systematic uncertainty on the liquid argon response can affect the sensitivity with a more or less magnitude. We push forward the attempt on comprehensive understanding of the liquid argon response based on the results from Chapters 5 and 6. Discussion the background event in the search is also presented, which limits the sensitivity more significantly. In particular, NR background has fairly contribution to the background budget. With a MC simulation and additional data taking with an organic liquid scintillator (LS) setup, the most severe source is suggested as cosmic-ray related fast neutron. Based on these discussions, we predict the sensitivity for the direct detection experiment once we upgrade the detector and laboratory environment appropriately.

8.1 The response model

8.1.1 Reduction of the uncertainty of the surface run

As mentioned before, the scintillation and ionization yields of liquid argon are essential quantities to interpret the observed signal. Among them, the yields for NR is the most essential one. Although some measurements are performed on the NR response as shown in Section 5.1.3, there is still lack of comprehensive understandings when compared to liquid xenon.

In liquid xenon detector, the NEST framework[103, 104] works very effective to predict the signal yields and reduce systematic uncertainties. It is achieved by a number of measurements of the liquid xenon property, as well as huge efforts on a simulation study (e.g. Ref. [50]), as shown in Fig. 8.1. Part of the difficulty for liquid argon comes from its scintillation wavelength; the need of wavelength shift makes it difficult to directly compare independent measurements and compare experimental result with model prediction. The use of VUV-sensitive photodetector (such as VUV-MPPC[122] or cryogenic PMT with magnesium-fluoride window[123]) may relax the problem. Nevertheless, it is necessary to perform many measurements and cross-checking by different sources, detector conditions, and groups.

Besides these simulation-related efforts, it is important to perform the liquid argon property measurement with the same calibration sources with the WIMP search run. Usually, the detector used in the property measurement differs to one used in WIMP search. It is more difficult to calibrate NR response in the WIMP search detector than ER. One of the effective and realistic avenue to reduce the uncertainty is to calibrate the WIMP detector with the same ER source used in an independent NR calibration measurement. The uncertainty of the surface run, for instance, can be reduced if we calibrate the detector with the ^{22}Na

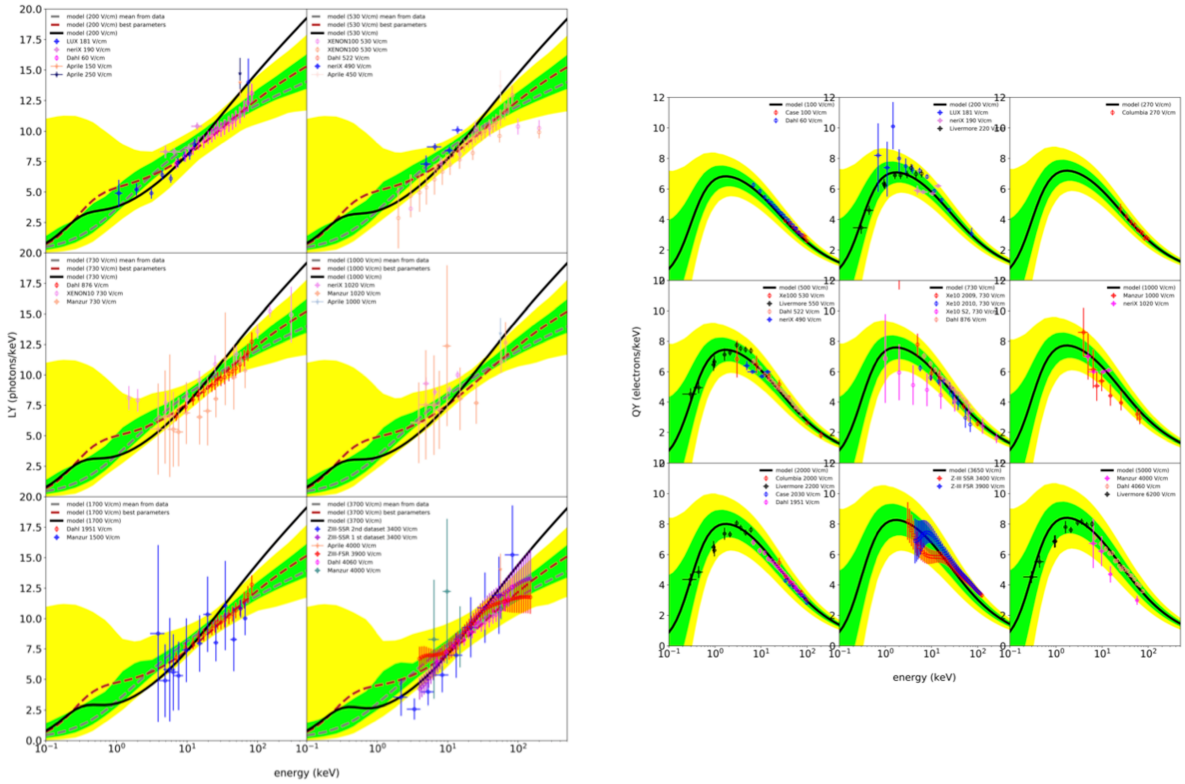

Fig. 8.1. The NEST prediction of the scintillation (left) and ionization (right) yields of LXe for NR at various electric fields, compared to world data. The figure is taken from Ref. [104]

.

source during the WIMP search campaign. It is more suitable to use ^{37}Ar as the reference point, since its energy locates at the WIMP region of interest (ROI).

As for ER, one can expect that the response of liquid argon is simpler than that for liquid xenon. Thanks to the low binding energy of the atomic electron and smaller shell structure, interaction of γ-ray with argon should be more "point-like" than that of xenon (Fig. 8.2). This indicates that liquid argon detector has a potential to reconstruct low ER energy with relatively small uncertainty. The detection of ^{37}Ar point presented here will be an unique method for further understandings.

8.1.2 Unification of NR and ER

Discussions in Chapters 5 and 6 imply that the low-energy liquid argon response is described by the same phenomenological model (the TIB model) for both NR and ER. The parameter independently obtained by the measurements is in the same order; the ς for the ER at null field (0.033) corresponds to that for the NR at ~0.5 kV/cm. It is also in the same order with that of liquid xenon.

This parameter originally depends on the "box" size where the ionization electron-ion pairs are distributed. It may improve the understanding of the liquid argon response by combine a track simulation with an appropriate cut length. It is also important to measure the field dependence of the parameter for ER, though it is left for future work.

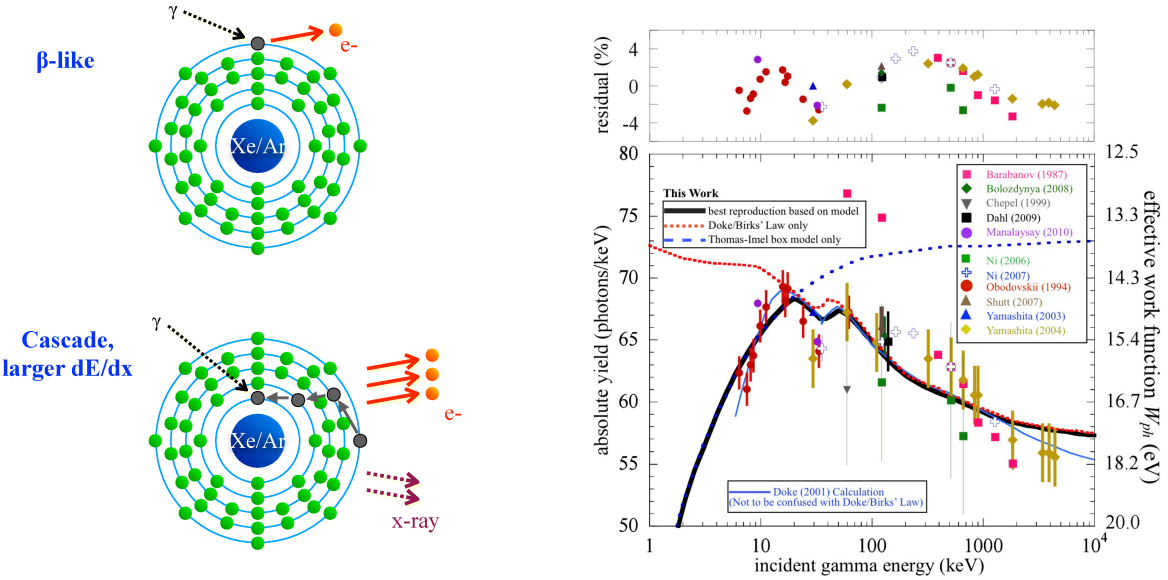

Fig. 8.2. Left: schematic illustration of the interaction between γ-ray and argon or xenon nuclei. While the left case emits one electron from the outermost shell, the right case emits a cascade of Auger-electrons and characteristic x-ray. Right: the scintillation yield for LXe as a function of the incident γ-ray energy. The dip around 30 keV come from a resonance at the K-edge for production of low-energy Auger electrons. The figure is taken from Ref. [103].

Furthermore, modeling both NR and ER comprehensively is an input for future experiments of both single-phase and double-phase. For instance, the scintillation to ionization ratio shows a characteristic trend as shown in Fig. 3.14. Quantitative evaluation of that in very low energy region can offer another way to search for low-mass WIMP.

8.2 Background source of the surface run

The direct search performed in Chapter 7 is obviously background limited. The potential background source is categorized into three types; that involves with the detector materials, involves with the environmental materials, and involves with cosmic-rays. Before that we will discuss on each impact on the WIMP search run separately in the following subsections, we first overview the several dominant contributions. Figure 8.3 illustrates the origins of these backgrounds.

As the search is performed at surface, cosmic-ray accounts for part of the remaining ER background; energy deposition of cosmic-ray at passive shielding materials, for example, leads relatively low energy ER following the emission of secondary γ-ray. In addition, we have performed material screening of the detector components, and the ER background is found to partly come from the uranium and thorium in PMT-base (Section 8.2.1). It is expected to produce comparable low-energy event rate to ^{39}Ar. This background could be significantly suppressed by using appropriate material such as radiopure epoxy.

Another ER source is the γ-ray from outside the vessel. In this case, it is important to enhance the LCE of the outer-bath so that multi-Compton γ-ray from both inside and outside liquid argon is tagged and vetoed (Section 8.2.2).

As for the NR background, cosmogenic fast neutron is the origin (Section 8.2.3). We again categorize the neutrons in two types. One is that originating from an interaction between cosmic-ray charged particle and materials around detector such as lead. The other is that having high enough energy ($\geq$10 MeV) to pass through the shieldings and interacting with the liquid argon directly. To evaluate the contribution from these origins, we perform a Geant4 MC simulation with an independent measurement in Appendix B. Prediction from the MC simulation reasonably agrees with the observed data, as shown in Fig. 8.10.

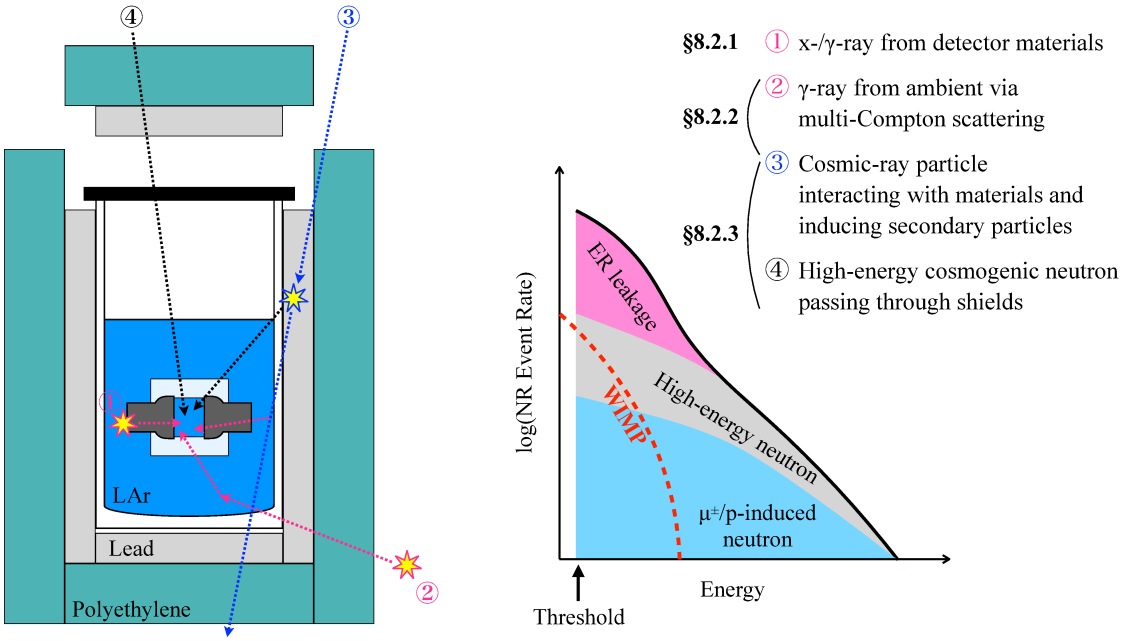

Fig. 8.3. Schematic illustrations of the main background origins (left) and contributions of them for the NR energy spectrum (right). Corresponding section number for each origin is also represented.

8.2.1 Background from detector materials

Radioimpurities in detector components induce both ER and NR events. It is one of the origin of the low-energy ER events. Material screening with inductively coupled plasma mass spectrometry (ICP-MS) [1)] is performed for detector components. Table 8.1 summarizes the uranium and thorium contamination of the materials around the fiducial. It reveals that fiber reinforced plastics (FRP) plate used in the PMT base and SiPM ganging board contains large amount of radioimpurities. Indeed, the PMT base is expected to induce huge low-energy ER events because x- and γ-rays from it easily penetrate to the fiducial throughout the PMT whose inside is vacuumed. The FRP-induced ER event rate is naively estimated based on the solid angle from the PMT-base to the fiducial volume as to be $O(10^4)$ events/day.

[1)] supported by the Material Characterization Central Laboratory at Waseda University.

The NR events from materials are considered to be negligible compared to other neutron source.

Table 8.1. Uranium and thorium contamination in the materials used near the fiducial volume.

Sample	Component	Mass	Quantity	^{238}U [ppm]	^{232}Th [ppm]	Ref.
PMT-base	FRP	~6 g	2	2.48	12.8	ICP-MS
PMT R11065	Kovar etc.	-	2	~20 mBq/PMT	~3 mBq/PMT	[124][a]
PTFE	C_2F_4	~1.8 kg	-	< 0.005	< 0.005	[125][b]
TPB	$C_{28}H_{22}$	~10 mg	-	< 0.005	< 0.01	ICP-MS
ESR	Polyester	~1.2 g	-	< 0.005	< 0.01	ICP-MS
OFC-shield	Cu	~30 kg	-	< 0.005	< 0.01	ICP-MS

[a] Measured by the manufacturer (Hamamatsu Photonics K.K.).

[b] Typical value.

8.2.2 Background from radiogenic isotope in environment

Neutron

As mentioned before, uranium and thorium series inside ambient materials cause fast neutron via spontaneous fission and (α, n) reaction. The neutron energy from these processes are not more than 10 MeV. The polyethylene surrounding the detector reduces it as more than $1/10$. In addition, the flux of the radiogenic neutron is orders of magnitude smaller than cosmic-ray neutron flux in general. Therefore, it is reasonable to neglect the contribution from this source.

γ-ray

The ambient materials also emit γ-rays up to 2.6 MeV, and it is one of the main ER background source. Since the fiducial volume of the detector is small, forward Compton scattering of the γ-ray originates low-energy ER events. The γ-ray flux in the laboratory is measured as summarized in Table 8.2. The lead and copper shields suppress these γ-ray in factor $1/100$. However, it still causes the ER with an event rate comparable to ^{39}Ar as shown in Fig. 8.4. More suppression of the background could be achieved by following approaches.

- Put lead and copper shields on the top side. As shown in Fig. 7.6, the shielding capability against γ-ray in current configuration is much weaker for the top direction than other directions because of several geometrical constrains.
- Improve light detection efficiency of the outer-bath region so that small energy deposition in the outer-bath can be detected. There should also be large nonuniformity in current apparatus due to the amount of the outer-bath photodetector.

Table 8.2. Summary of the γ-ray flux independently measured in the laboratory.

Series	Fluence [1/cm^2/s]	Components
^{232}Th (upper stream)	0.6	γ-rays from ^{228}Ac and ^{224}Ra
^{232}Th (lower stream)	0.5	γ-rays from ^{212}Pb , ^{212}Bi, and ^{208}Tl
^{238}U (lower stream)	1.0	γ-rays from ^{214}Pb and ^{214}Bi
^{40}K	0.6	

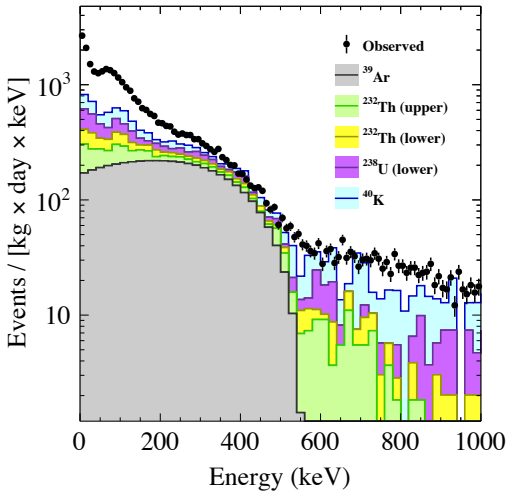

Fig. 8.4. Observed ER spectrum (black point) and the radiogenic γ-rays induced ER spectra expected by PHITS simulation (colored filled histogram). The gray histogram represents ^{39}Ar of 1 Bq/kg.

8.2.3 Background from cosmic-ray induced reactions

Figure 8.5 shows the cosmic-rays flux predicted by EXPACS. As the energy of the neutron from the atmosphere reaches more than 1 GeV, the neutron can directly reach the fiducial volume and produce NR, despite the passive shieldings against radiations. In addition, a number of energetic particles exist inside the liquid argon volume because the shieldings do not have capability of rejecting the interaction of the cosmic-rays with themselves. In particular, the secondary fast neutron is the most problematic source. It is the production of processes such as muon-capture or spallation. Lead shielding is the main origin because these neutron production processes are known to more likely to occur with higher atomic-number (high-Z) materials (see Appendix B in detail). Cosmic rays also produce ER events via secondary γ-rays, whose event rate is expected to be almost same as that from ambient γ-ray.

We evaluate the contribution of cosmic-ray particles to the NR background in the WIMP search using a MC simulation. Firstly, NR energy spectrum is subjected to discuss. The black point in Fig. 8.7 shows the NR spectrum without requiring the anti-coincidence with the outer-bath PMTs. This means that the spectrum depends on neither LCE of the outer bath nor the timing resolution of them.

The MC simulation is based on the Geant4 toolkit and is performed for the liquid argon setup including

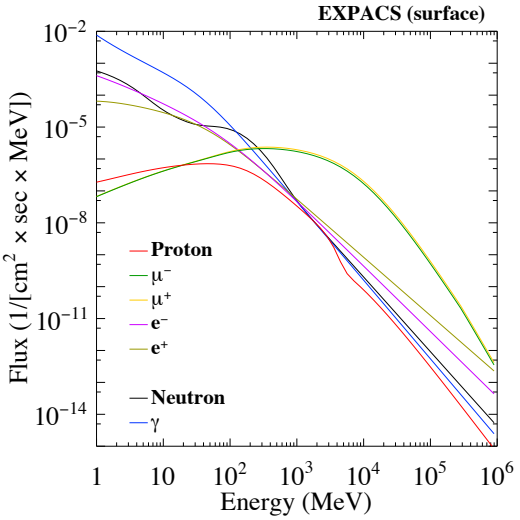

Fig. 8.5. Cosmic-rays flux at surface calculated by EXPACS.

the liquid argon volume, detector components, and passive shieldings. Precise flux of each cosmic-ray particle at the particular laboratory is poorly known; this is because it should be strongly affected by geometrical condition, and it is almost impossible to implement the whole effect to a simulation (we may be required to perform huge simulation such as whole the building). Therefore, in this study, initial spectrum shape of each cosmic-ray is assumed to that of EXPACS, while the absolute fluence is empirically independently determined from a measurement using a liquid scintillator detector. Detail of this independent measurement also appears in Appendix B, and the resulting fluences are summarized in Table 8.3. This measurement cannot "directly" distinguish negative and positive muons though, each fluence is determined by exploiting the negative-muon capture process under the assumption of EXPACS spectrum shape. For the neutron generated outside the detector apparatus, on the other hand, the liquid scintillator measurement lacks the sensitivity to measure it. We herein assume the ratio of the atmospheric neutron fluence of EXPACS to that in the laboratory is identical between the neutron and μ^-. Discussion on these assumptions will be addressed later.

The MC simulation is firstly validated in energy range above the ROI for the WIMP search. Figure 8.6 shows the comparison between data and MC for high-energy ER events such as minimum ionization particle (MIP). The data herein is taken by changing the PMT gain to $<1/20$ of the default one to avoid PMT saturation. The MIP event rate (ER energy of >10 MeV) is measured as to be 0.22 ± 0.01 Hz, which is consistent to the MC prediction. As shown in Fig. 8.7 (right), the MC simulation also explains nearly

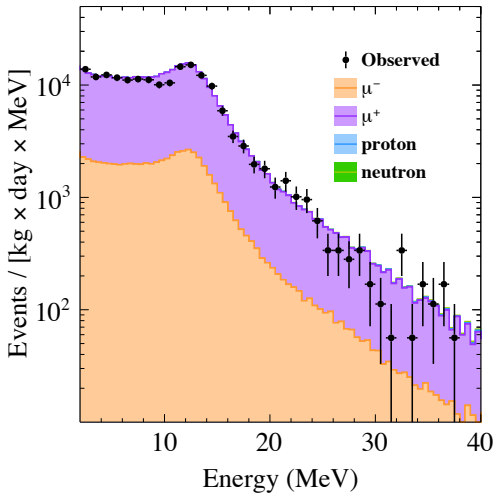

Fig. 8.6. Comparisons between data and MC for high-energy ER event.

all of the observed NR events above 300 p.e. (corresponding to the NR energy of about 60 keV).

Table 8.3. Input flux of each cosmic-ray particle in the MC simulation, determined from the liquid scintillator measurement in Appendix B.

Particle	Energy range [MeV]	Fluence [1/cm^2/s]	Ratio to EXPACS
$\mu^{-\dagger}$	1.0×10^1–1.0×10^6	1.6×10^{-3}	0.19
$\mu^{+\dagger}$	1.0×10^1–1.0×10^6	8.0×10^{-3}	0.81
proton	1.0×10^1–1.0×10^6	7.7×10^{-5}	0.33
neutron	1.5–1.0×10^6	5.3×10^{-4}	0.16

† The μ^- and μ^+ fluences are effectively determined to account for muon-capture (induced only by μ^-) and muon-spallation (induced by both μ^- and μ^+ with the same magnitude) events in the LS measurement. Therefore, these values may not be the true fluences but rather be the effective parameters working with the EXPACS prediction.

The simulated spectrum may be used to be subtracted from the observed data as known NR source. Since the outer-bath region is not designed to uniformly collect the scintillation signal, it is difficult to convert the energy deposition to the observed photoelectron signal and to estimate the detection efficiency. Therefore, an assumption is applied that any energy deposition in the top-half of the outer-bath region is tagged and rejected by the anti-veto requirement. This assumption on the MC simulation is conservative for the NR background subtraction. Validation of this rough assumption is performed with ER event; Fig. 8.8 (left) shows the comparison of the ER energy spectrum between data and MC for ER events that have the outer-bath coincident signal, and Fig. 8.8 (left) shows the comparison of the time difference between fiducial and outer-bath signals δT. These events mainly consist of the cosmic-ray shower events. It shows the consistency between data and MC within ~10%, so it is reasonable to consider that the

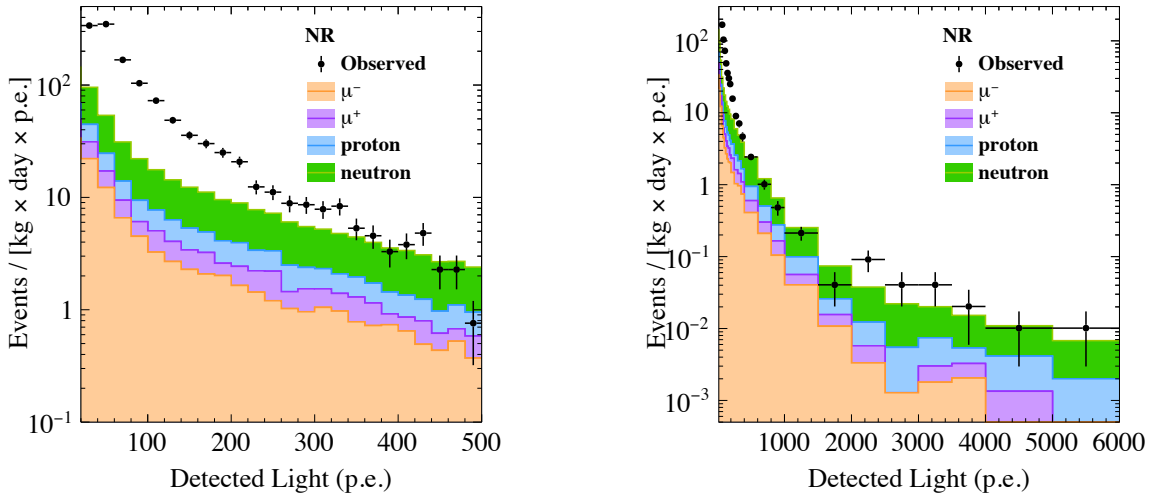

Fig. 8.7. Comparisons between data and MC for the WIMP search dataset, before requiring the anti-veto coincidence.

assumption on the anti-veto requiring is valid within $O(10\%)$.

The time difference for the NR events is also compared between data and MC to check the validity of the MC simulation together with the assumptions. Figure 8.9 shows the time difference for NR events with >300 p.e. Delayed neutrons from the muon capture are observed as to be predicted by the MC simulation.

Figure 8.10 shows the comparison of the NR spectrum after requiring the anti-veto coincidence. Assuming that no additional systematical uncertainties are appeared, the WIMP search result presented in Chapter 7 is expected to extend by roughly 50%, as represented with the blue dashed line in Fig. 8.11.

Lastly, we address the assumption on the muon and cosmogenic neutron fluxes. As for the muon, while we assume the initial energy spectrum shapes to that of EXPACS, overburden materials inside the building could bias it toward the high energy. The negative-muon capture process occurs more likely for lower energy range. Since the expected fluence is determined from the negative-muon capture rate in the liquid scintillator measurement, the bias on the energy spectra would result in negative and positive muons for larger and smaller fluences than the measured values, respectively. However, we believe it does not change the total muon-induced neutron yields significantly, because the neutron yield is the product of the input muon spectrum and negative-muon capture rate and the flucences are determined to account for the liquid scintillator measurement. For neutron, we assume that ratio of the fluence of EXPACS to that in the laboratory is identical between the neutron and μ^-. Despite the very simple assumption, it seems to relatively valid, considering the consistency between data and MC in the high-energy region. The discrepancy in low-energy region, as shown in Fig. 8.7 (left), may be qualitatively explained as follows; the high energy neutron likely associates other particles by creating hadronic shower during its path inside the building, and the secondary particles may occur ER simultaneously with the primary NR. Decrease of the PSD power for lower energy event may let these events survive the NR selection applied to the real data.

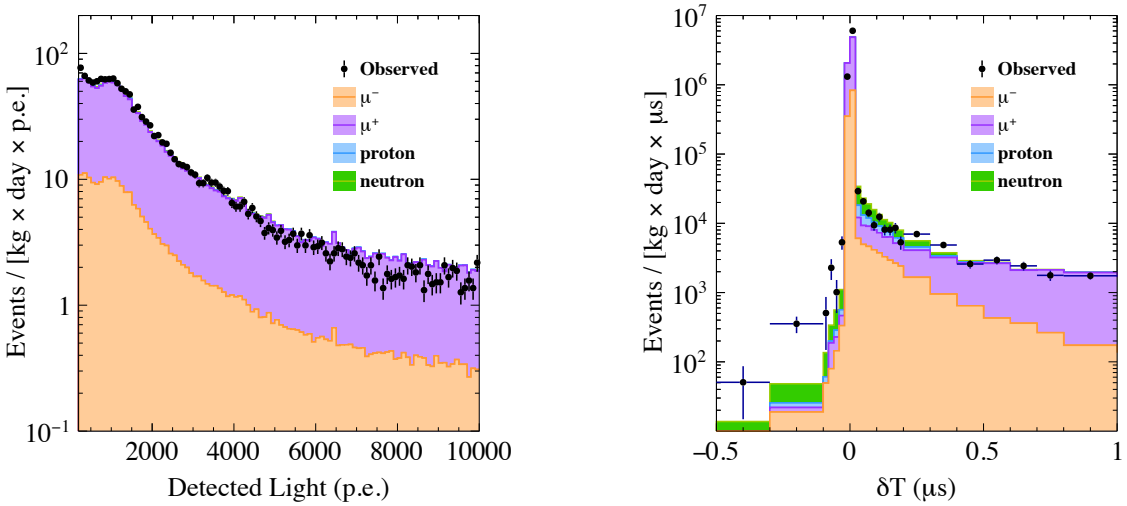

Fig. 8.8. Comparison of the ER energy spectrum (left) and the time difference δT (right) between data and MC for the ER event in WIMP search dataset. These events are required coincident signal in the outer-bath.

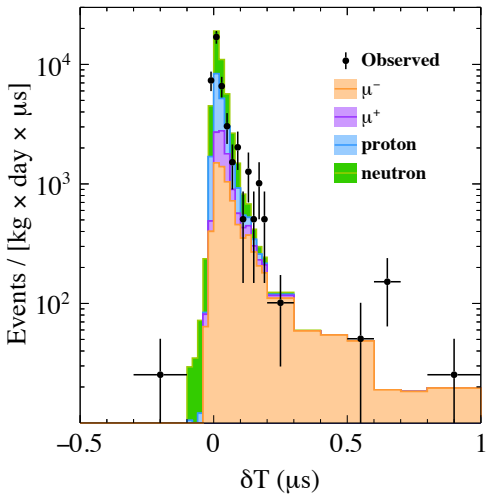

Fig. 8.9. Comparison of the time difference δT between data and MC for the WIMP search dataset for NR events above 300 p.e.

8.3 Outlook and expected sensitivities of future experiment

The NR background is found to originate from cosmic-rays such as muon, proton, and neutron. The easiest way for reducing the NR background is to optimize the passive shieldings. By putting the lead shield outside of the polyethylene, the NR event rate is expected to be roughly half of the observed rate. However, the rest of cosmogenic neutron is too fast to moderate by a realistic laboratory apparatus.

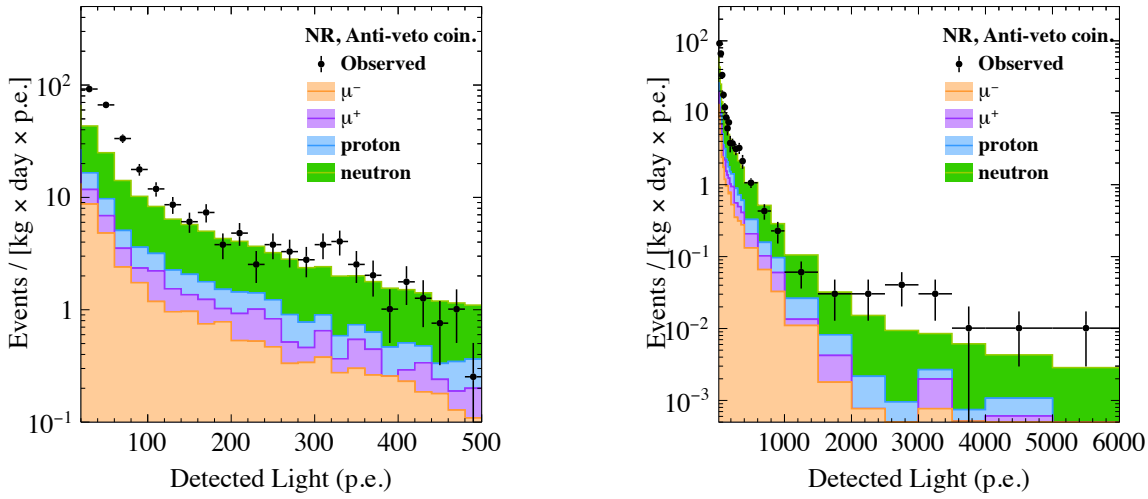

Fig. 8.10. Comparisons of the distributions of the NR events between data and MC for the WIMP search dataset, after requiring the anti-veto coincidence. See text for the assumption on the MC spectrum.

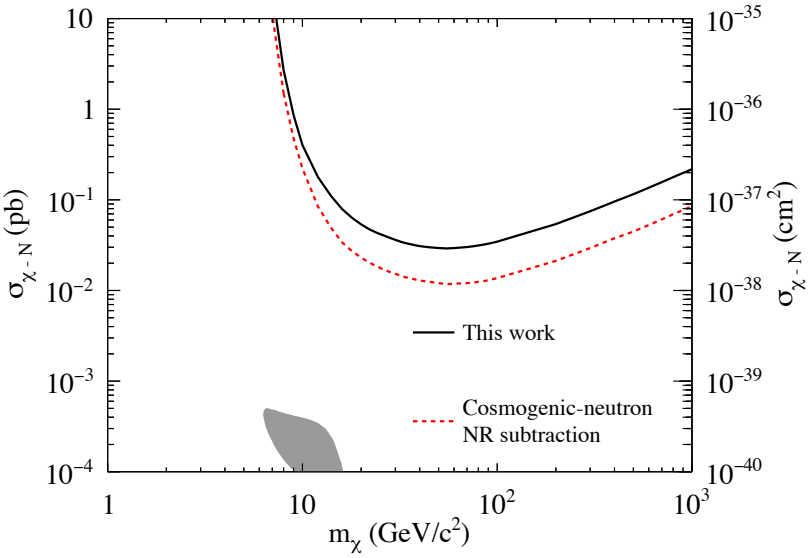

Fig. 8.11. Expected WIMP-nucleon cross section 90% C.L. upper limits by subtracting the cosmic-ray induced NR events (red dashed line). The black solid line is the same as in Fig. 7.23

.

They can be significantly suppressed in an underground laboratory, as described in Section 3.6 (five orders of magnitude lower for the muon and three orders for the neutron). This means that these flux is so low that the NR background is regarded as to be zero for the corresponding exposure of the search. The expected sensitivity is estimated by pseudo experiment, assuming the null NR background hypothesis and the observed ER background rate. The result is shown in Fig. 8.12 with the red line.

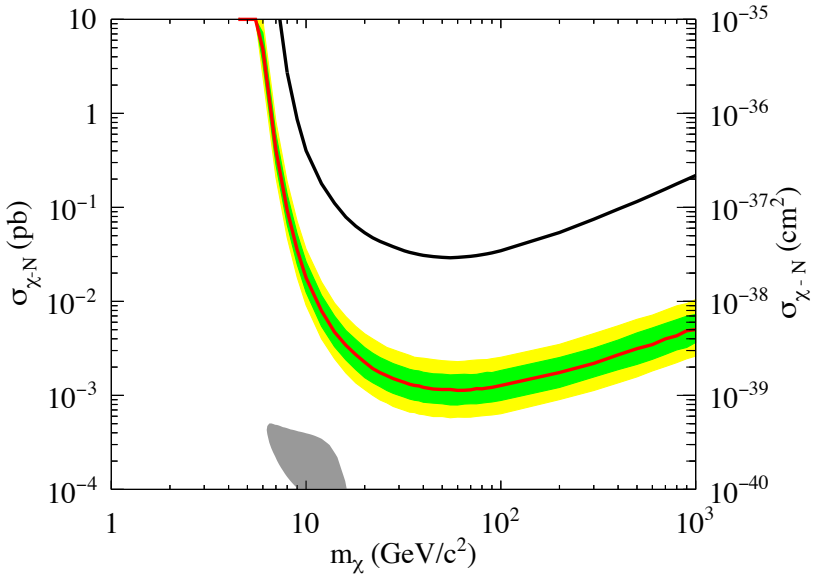

Fig. 8.12. Expected WIMP-nucleon cross section 90% C.L. upper limits assuming null NR background (red line). The black solid line is the same as in Fig. 7.23.

With the null-NR background assumption, an detector exposure of 250 days is sensitive to the WIMP with mass of 10 GeV/c^2 and the cross section of 1.0×10^{-39} cm^2. An improvement can be realized by suppressing the ER background rate. The background rate is expected to be down to that comparable to ^{39}Ar rate by careful selection of detector components and improvement of anti-veto coincidence efficiency. The red dot line (blue dot-dashed line) in Fig. 8.13 shows the expected sensitivity when ER background source is only ^{39}Ar (that observed in the search). It would reach the cross section of 1.0×10^{-40} cm^2.

Furthermore, the use of the depleted-argon (underground argon, UAr)[36] will drastically improve the sensitivity. The ^{39}Ar abundance in the UAr is depleted by 1400 ± 200, and will be further, with respect to the normal argon (atmospheric argon, AAr)[126]. As shown in the brown dot-dot-dashed line in Fig. 8.13, WIMP with mass of 10 GeV/c^2 and cross section of 1.0×10^{-41} cm^2 is expected to be searched for by combination of the high-LCE single-phase detector, deep underground laboratory, sufficient exposure time, and the UAr which has $1/1400$ of ^{39}Ar of the AAr.

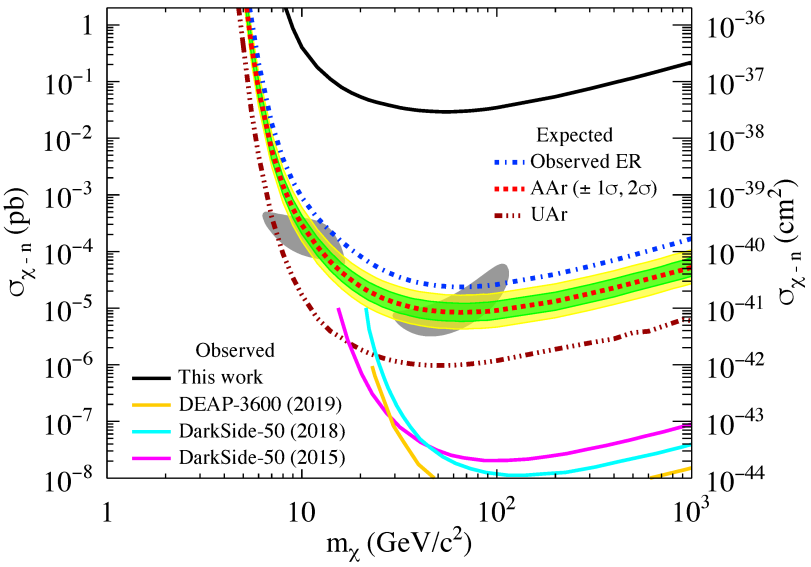

Fig. 8.13. Expected WIMP-nucleon cross section 90% C.L. upper limits assuming null NR background. The blue, red, and brown dashed lines assume ER background source as the observed rate, only ^{39}Ar in AAr, and only ^{39}Ar in UAr. Exposure time is set to 250 days. Also shown are the published 90% upper limits by DEAP-3600 (orange) [23], DarkSide-50 latest result (cyan) [24] and DarkSide-50 first result (magenta) [127].

Chapter 9

Conclusion

The existence of dark matter is strongly suggested by cosmological and astrophysical observations, yet its nature remains unknown. WIMP is one of the most favored scenario supported by theoretical models. Liquid argon scintillation detector offers several attractive features for the direct detection of WIMP in dark matter halo of the Milky Way Galaxy.

Systematical understanding of liquid argon response is important to design a detector, interpret observed signals, and reduce systematic uncertainty for the direct detection experiment, in particular, searching for low mass WIMP. The responses for NR and ER are measured in Chapters 5 and 6, respectively.

The NR measurement focuses on the response under electric field. The double-phase detector observes both S1 and S2 signals from NR above 1 kV/cm for the first time. With the MC simulation and the parametrization model describing the response, the scintillation and ionization yields are experimentally determined in the NR energy range of 30–200 keV and field range of 0–3 kV/cm within systematic uncertainty. The model allows us to fully predict the signal yields at any recoil energy and any electric field up to 3 kV/cm. As these quantities are essential to convert the observables (S1 and/or S2) to the recoil energy by WIMP-argon scattering, the comprehensive parameterization of liquid argon property makes use of interpretation between the experimental data and physics process. It also can contribute to assess systematic uncertainty on low energy region. In addition, the model offers information about the yields in unprecedented energy and field regions of below a few keVand above kV/cm; it is strongly involved with the $\sim$1 GeV/c^2 WIMP search which relies solely on the S2 signal.

The measurement of the scintillation yield for ER is performed only at the null-field but between a wide energy range. It is down to 2.8 keV from ^{37}Ar source; this is the first measurement of the ER response below typical energy threshold of WIMP search of about 10 keV$_{ee}$ at null field. Measurement with a variety of calibration sources confirms that the scintillation yield decreases in the low energy (below a few tens of keV) region. It is interpreted by analogy with the LXe scintillation response, where the ionization electron-ion recombination probability is attributed to the energy dependence of the yield. By referring the previous measurement of the scintillation yield at 1 MeV, the TIB model parameter ς is calculated by the 2.8 keV point as $\varsigma = 0.033^{+0.012}_{-0.008}$. In the low-mass WIMP search, such a low-energy ER events are the most severe sources disturbing the lower energy threshold, hence, reducing WIMP sensitivity. The result from this measurement makes use of the precise estimation of background contamination in the low energy region and suppression of the uncertainty.

Based on these measurements, a WIMP search is conducted by a single-phase high-LCE detector at surface, as presented in Chapter 7. The exposure of 0.20 kg $\cdot$ days gives upper limit on the WIMP-nucleon cross section of 4×10^{-37} cm^2 for WIMP with mass of 10 GeV/c^2. The sensitivity is found to be limited

by fast neutrons from cosmic-rays. The MC simulation expects that these backgrounds will be reduced by tagging the incoming cosmic-rays and requiring anti-coincidence with them. Further reduction will be achieved by performing the search at deep underground laboratory where the cosmic-rays flux is several orders of magnitude lower than at surface. Data taking with the improved detector at proper site could reach the sensitivity for the 10 GeV/c^2 WIMP down to 1.0×10^{-40} cm^2 under background-free condition.

In conclusion, the low energy liquid argon response is measured and interpreted systematically. For the first time, the NR response is studied under high electric field and the ER response is down to a few keV. The modeling of the liquid argon response, as well as the measurement itself, will be the foundation of the comprehensive liquid argon response parametrization. Certainly, the description presented herein will support any low-mass WIMP search experiment using liquid argon detector in both designing and analyzing phases by assessing WIMP and background signals. The surface run demonstrates it partly, as well as the high potential of liquid argon detector for the low-mass WIMP discovery.

Appendix A

PMT R11065MOD property

This chapter describes detail of a course of property measurement of the PMT Hamamatsu R11065MOD.

A.1 Basic property

Table A.1 summarizes the PMT used in this measurement. Also shown are the datasheet value provided by the manufacturer.

Figure A.1 shows the design of the divider circuit. It is designed to be operated with negative bias voltage.

Table A.1. Summary of the R11065MOD PMTs used in this study.

#	Purchased	Gain at 1500 V	QE	Position at the detectors	
				double-phase	single-phase
BA0176	Oct.2015	4.759×10^6	31.23%	Gas-phase	Ch1
BA0177	Oct.2015	4.270×10^6	30.82%	Liquid-phase	Ch2

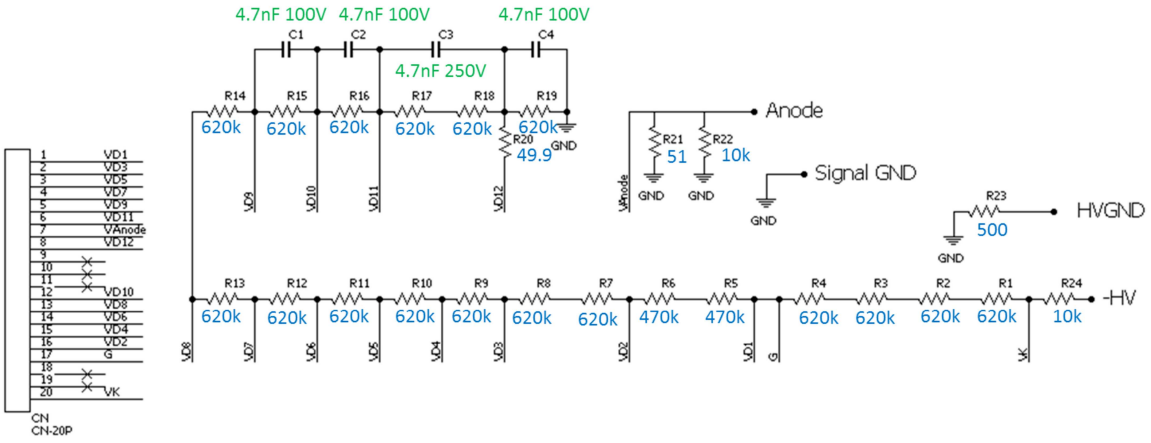

Fig. A.1. Design of the divider circuit.

A.2 Gain

Electron multiplication within a PMT is a stochastic process, and an output charge for a photoelectron at the PMT anode is commonly described with a simple Gaussian distribution. This is a good approximation when all the incoming photoelectrons are multiplied by the dynode chain by the optimal trajectory. This approach often leads to a biased estimation, however, due to incomplete multiplication coming from a variety of sub-optimal trajectories[128, 129, 130]. These include a photon passing through the photocathode and inducing photoelectric effect at the first dynode and a photoelectron inelastically backscattered without any multiplication at the first dynode. Ignoring these effects may lead an underestimation of the incoming photoelectron signal.

We performed a measurement to confirm the existence of the underamprified signal in the particular PMT. Figure A.2 shows the experimental setup at room temperature. The PMT in a black box is illuminated by the nanosecond pulsed blue laser through optical fiber. The intensity is adjusted by optical filters between the laser and the fiber. Data are taken with two configurations; one is that taken with a small laser output ($\mu \ll 1$, where μ is the average number of photoelectron per laser output), and the other is taken by switching off the laser. The charge output of each event is integrated around the laser timing. Figure A.3 shows the comparison of the charge distributions between them. They are normalized using the pedestal (0 p.e.) peak. The subtraction between them, shown with the orange line, corresponds to the PMT response for 1 p.e. input. There is a fraction of unnatural component with a normal Gaussian one.

We approximate the underamprified component by an exponential function as described in Section 6.3 and Ref. [106].

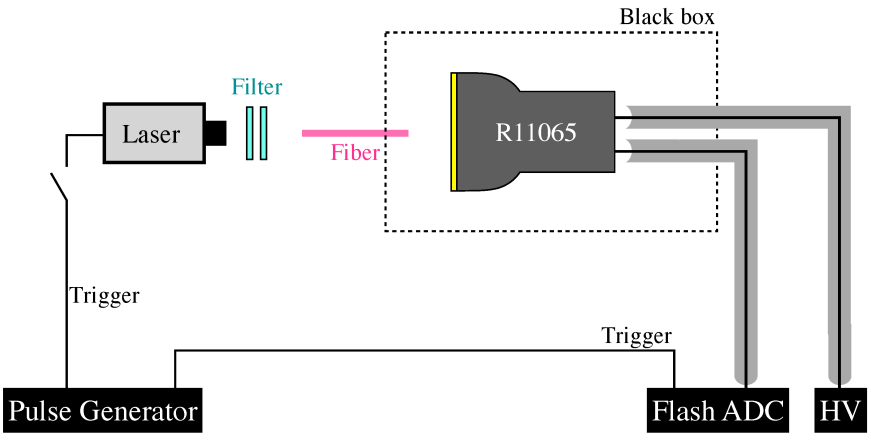

Fig. A.2. Schematic illustration of the setup to measure the PMT gain and afterpulse.

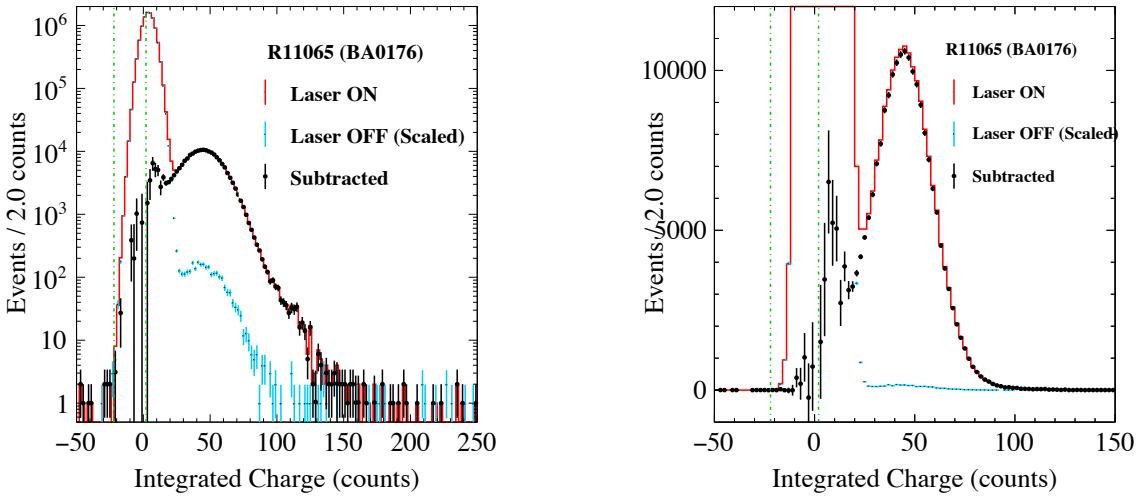

Fig. A.3. Single photoelectron charge distribution (black) obtained by the small-intensity laser data (red) and the blinded data (blue). The vertical green dot-dashed lines represent the pedestal region used to scale the two datasets.

A.3 Afterpulse

The PMT occasionally outputs extra noise pulses following a normal photoelectron signal, called afterpulse. Residual-gas molecule inside the PMT can be ionized by a photoelectron drifting from photocathode to the first dynode, and then it drifts to the photocathode and generate the afterpulse of typically a few photoelectrons.

The delay time of the afterpulse is calculated by the ion mass and electric potential inside the PMT. The ion travel time T is expressed as

$$T = \int_{s_0}^{0} \frac{ds}{v} = \sqrt{\frac{m}{2q}} \int_{s_0}^{0} \frac{ds}{\sqrt{V(s_0) - V(s)}}, \tag{A.1}$$

where s_0 is the ionized position, m and q are the mass and charge of the drifting ion, v is its velocity, and $V(s)$ is the electric potential as a function of position s (photocathode locates at 0). For the R11065, a quadratic potential is known to be a good approximation[131, 132]:

$$V(s) = V_0 \left(\frac{s}{L}\right)^2, \tag{A.2}$$

where L is the position of the focusing grid. From Eqs.(A.1) and (A.2),

$$T = \sqrt{\frac{m}{sq}} \frac{L}{\sqrt{V_0}} \arcsin\left(\frac{s}{s_0}\right)\Big|_{s=s_0}^{s=0} = \frac{\pi}{4} \sqrt{\frac{2m}{qV_0}} L. \tag{A.3}$$

The travel time is independent from the ionization position between the photocathode and the first dynode.

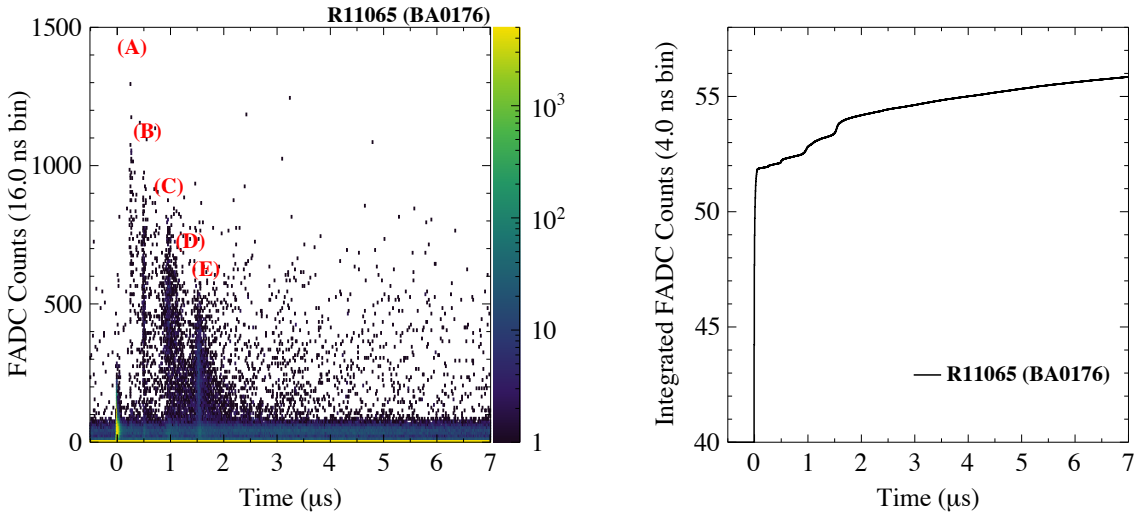

Fig. A.4. Observed charge amplitude (left) and integrated charge (right) as a function of time. The input laser signal appears at $t = 0$. Following are the afterpulses from (A): H^+, (B): He^+, (C): CH_4^+, (D): Ne^+, and (E): Ar^+, respectively. Continuous component is also shown, as clearly seen after the peak (E).

The afterpulse is evaluated with the same setup described in Section A.2. The intensity of the PMT illuminating laser is adjusted to relatively high (a few photoelectrons per pulse) for this purpose. Figure A.4 shows the observed charge amplitude as a function of time. Four peaks exist after the output of the laser signal (around $t \approx 0.3$ μs). Based on their time and electric field inside the PMT, the origins of these peaks are found to be H^+, He^+, CH_4^+, Ne^+, and Ar^+. In addition to these peaks, there is a continuous pulse consisting of single photoelectron amplitude and lasting over ~3 μs, as shown in Fig. A.4 (left).

At liquid argon temperature, contributions from H^+ and CH_4^+ are likely negligible because these molecules frozen out to the metal surface of the PMT[132]. We assess the contribution of the rest three origins as 2–4% of the initial photoelectron signal. It is the product of the probability for occurring the afterpulse and the mean number of the emitted photoelectron per one positive ion feedback.

A.4 Proportionality

There are several possible sources affecting the linearity of the PMT output when it receives a high intense or high repetition rate light signals. Some effects result in saturation of the charge output (underlinearity), while the others results in overproportionally with the input charge (overlinearity).

A.4.1 Nonlinearity from photocathode current saturation

Since the photocathode can provide only limited photoelectron current at once, the output current may deviate from the ideal linearity for too large light input. The photocathode of R11065 is the special bialkali photocathode (Bialkali-LT), which is identical to that of R11410, a PMT developed for LXe experiments.

The cathode characteristic is measured in Ref. [133], and it is linear to within 1% at −150 °C (25 °C) up to 0.05 nA (100 nA). By extrapolating the measurement, we find it does not matter in the liquid argon experiments in this dissertation.

A.4.2 Nonlinearity from dynode chain

The output anode current may show both underproportionality and overproportionality for too large or too frequent light input. Two factors are considered to involve with this deviation;

- Space charge effect. When large number of photoelectrons are multiplied at once, space charge density at the last dynode becomes too high to multiply and correct the all current flow, leading

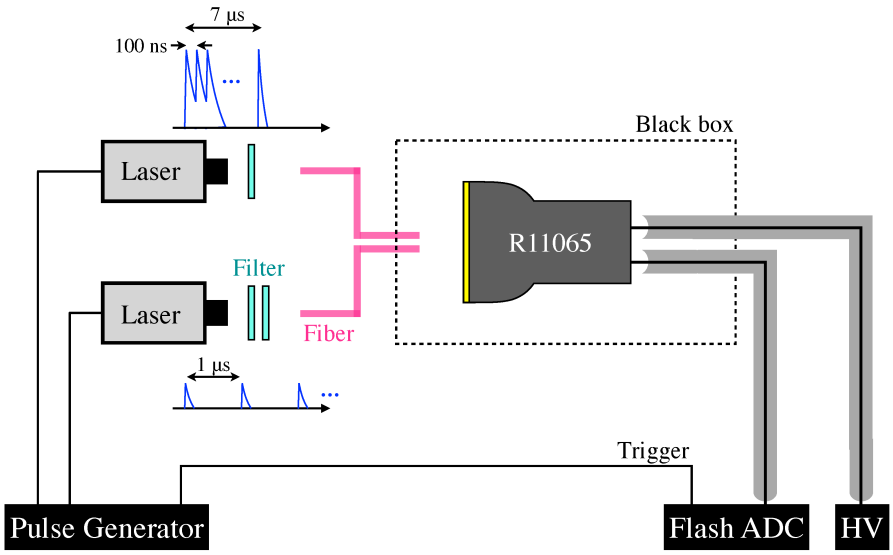

Fig. A.5. Schematic illustration of the setup to measure the non-linearity.

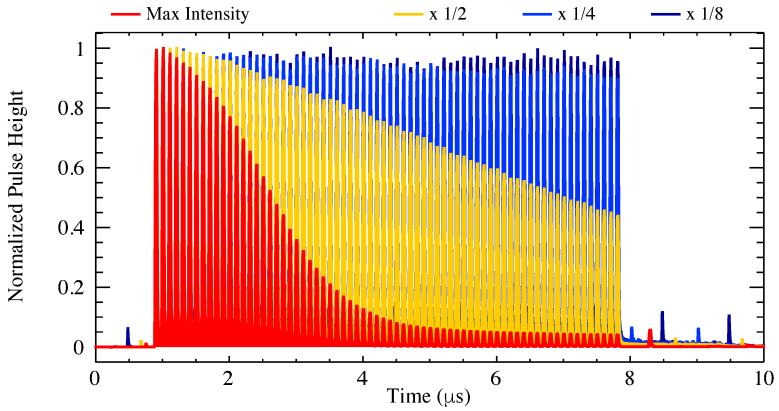

Fig. A.6. Examples of the observed signal waveforms from the laser pulses with different intensities, where each waveform is normalized to their pulse heights.

the saturation of anode output. This effect depends on the PMT structure and potential difference between each dynode.

- Change in each dynode voltage from the divider circuit. The divider circuit may not provide enough charge for dynodes or may not apply correct potential difference if the input signal is too large pulse or too high rate. While the former leads a reduction of output current, the latter can lead both underlinearity and overlinearity by changing the field distribution. These impacts are affected by capacitors and resistances on the circuit.

We evaluate overall impact of the nonlinearity on the liquid argon scintillation signal by performing a dedicated PMT test. Figure A.5 shows the experimental setup, which uses two pulsed laser source. One of the laser emits a relatively strong light signal with 100 ns interval lasting 7 μs, while the other emits a small signal in every 1 μs continuously. The intensity of each laser light is adjusted by the optical filters. The PMT is operated as the same way as in the liquid argon experiment.

Several kind of datasets are acquired by changing the light intensities. Figure A.6 shows the typical observed signals with different laser intensities, where the output pulse heights decreases as the laser intensity increases. We find the PMT response for the discrete pulse input is characterised by two constants τ_1 and τ_2 as

$$\delta Q(t = t_i) = \sum_{j=0}^{j=i-1} Q_{\mathrm{in}}^{j}\Big(p\exp(-\frac{j\Delta t}{\tau_1}) + (1-p)\exp(-\frac{j\Delta t}{\tau_2})\Big), \tag{A.4}$$

where Q_{in}^{i} is the ideal charge output for the i-th input pulse, Δt is the time interval between each input pulse, and p represents the fraction between two recovering terms. The dynode voltage is usually kept stable within certain range by the capacitor in the divider circuit, and $\delta Q(t)$ is interpreted as the deviation of the capacitor charge from the stable state. In this measurement $Q_{\mathrm{in}} - i$ is regarded as constant. Figure A.7 shows the ratio of the output i-th pulse to the first one as a function of δQ. Also shown are the other datasets taken with different pulse intensities or intervals. The parameters are estimated as $\tau_1 \approx 2.1$ μs, $\tau_2 \approx 75$ μs, and $p \approx 0.87$.

Based on this measurement, impact on the liquid argon signal is assessed. The non-linearity is found to be less than 1% (0.1%) for 1 MeV (below 200 keV) liquid argon scintillation signal, as shown in Fig. A.8.

No overlinearity is found to affect the analysis in this dissertation.

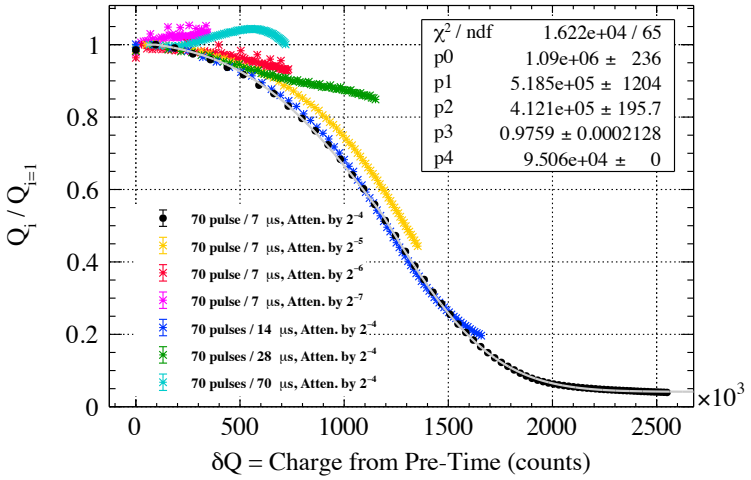

Fig. A.7. The measured ratio of the i-th pulse output charge to the first one as a function of the parameter δQ. The data is approximated by an error function.

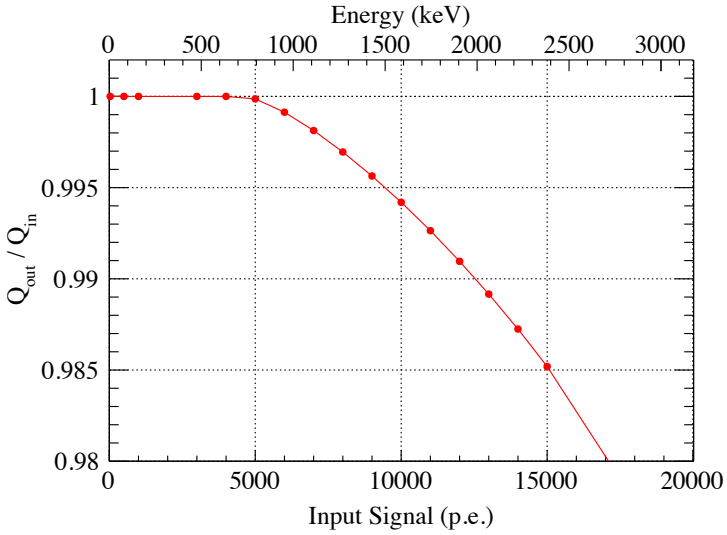

Fig. A.8. Evaluated impact of the output nonlinearity of the PMT as a function of LAr scintillation signal. The top axis represents the corresponding energy assuming the result in Chapter 6.

Appendix B

Cosmogenic neutron background

Cosmic-ray particles induce secondary radiations such as fast neutron and γ-ray following the interaction with materials. In particular, as discussed in Chapter 8, the secondary fast neutron is expected to be one of the significant background source in the surface run in Chapter 7. In order to confirm the origin and estimate its impact qualitatively, a dedicated measurement is performed with a liquid scintillator (LS) detector.

B.1 Process

Cosmic-ray at surface consists of muon, electron, neutron, proton, and pion with their energy up to several TeV, as shown in Fig. 8.5. They originate fast neutrons via interactions with experimental and ambient materials. Several production processes are shown in Fig. B.1. These interactions are more likely to occur with high-Z materials, that is, for example, lead.

B.2 Measurement of cosmic-ray induced fast neutron with an organic liquid scintillator

B.2.1 Setup and measurement

Figure B.2 shows an overview of this measurement. The LS is Saint-Gobain BC501A which offers good PSD ability between NR and ER. The detector ($2 \times 2\text{in.}^2$ cylinder) is surrounded by 10-cm-thick lead and thin plastic scintillator (PS) modules. The PS modules (two in top and two in side) provide timing information about cosmic-ray interaction.

B.2.2 Result and discussion

Figure B.3 shows the observed NR spectra taken with and without the surrounding lead. The detector observes significant NR events that likely come from the cosmic-ray interactions with lead. Indeed, as shown in Fig. B.4, a decay constant of $\tau = 85 \pm 13$ ns is appeared in the time difference between the LS and the PS, which is consistent to the literature value of negative-muon capture in lead (74.8 ± 0.4 ns)[134].

A Geant4 MC simulation, using a provided physics list package QGSP_BIC_HP, is performed for the LS setup to estimate the NR background. In this MC, we consider negative muon, positive muon, and

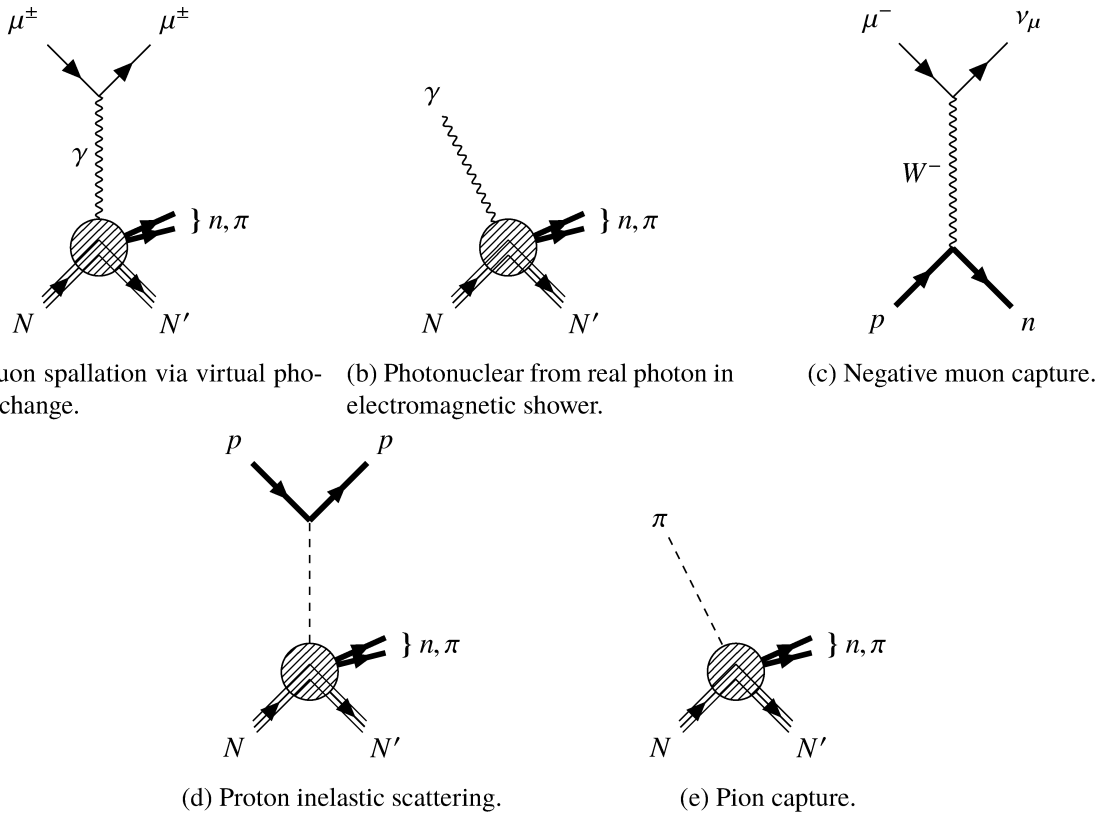

(a) Muon spallation via virtual photon exchange.

(b) Photonuclear from real photon in electromagnetic shower.

(c) Negative muon capture.

(d) Proton inelastic scattering.

(e) Pion capture.

Fig. B.1. Neutron production processes.

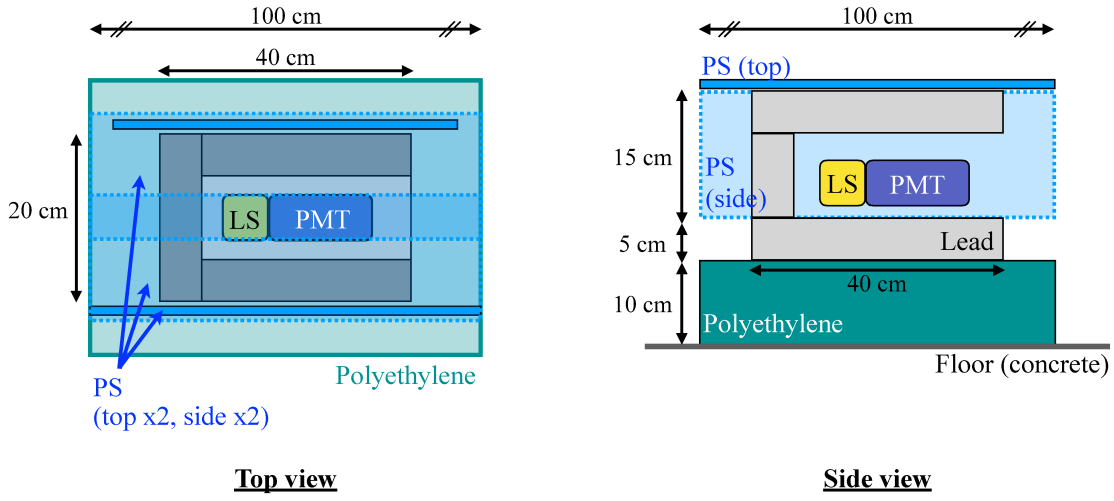

Fig. B.2. Schematic view of the setup of the LS measurement. Whole setup is built on a polyethylene to reduce neutrons from the floor.

proton as primary cosmic-rays and simulate them from just above the setup. The precise energy spectra and fluences of each cosmic-ray particles at the particular laboratory are poorly known. Therefore, the

cosmic-ray spectra are assumed to be that of EXPACS, and the absolute fluences are determined with the data. Figure B.5 shows the comparison between the data and MC. Three variables are used to determine the scale factor between EXPACS and data for each particle; visible energy for the MIP event (which is derived from minimum-ionizing particle passing through the LS detector), visible energy for the NR event, and the time difference between LS and PS for the NR event. The best-fit scale factor is summarized in Table B.1. The fit is effectively constrained by the number of MIP event and the number of muon-capture event. Consequently, as mentioned in Section 8.2.3, these scale factors may not correspond to the "true" muons fluences, but rather effective parameters working with the input flux from EXPACS. We should note that cosmogenic neutron (i.e. fast neutron generated outside the detector setup) is neglected here because it leaves neither MIP signal nor coincidence signal in the PS modules.

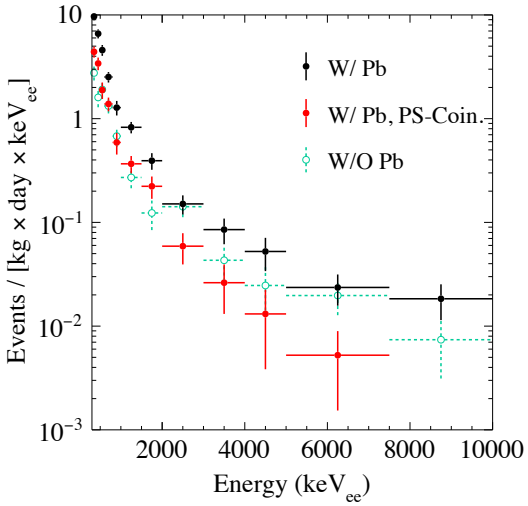

Fig. B.3. NR energy spectra observed in the LS setup. The blue and black spectra come from data taken with lead, where the latter is required the coincident cosmic-ray signal in the PS. The cyan spectrum comes from data without lead.

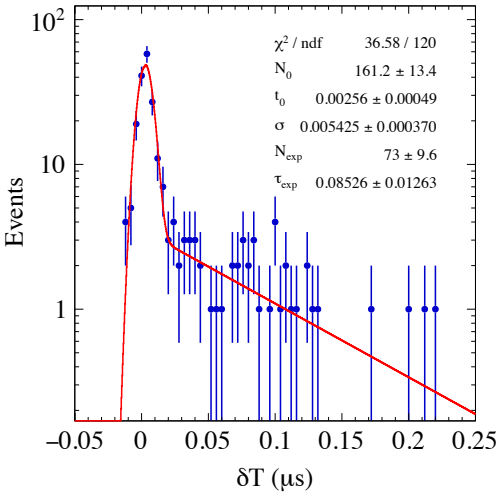

Fig. B.4. Time difference between the LS and the PS for the NR events in data taken with lead, fit with Gaussian plus exponential function.

Table B.1. Best-fit scale factors for cosmic-ray particles between EXPACS and LS data. The uncertainty is statistical only.

Particle	Scale factor
μ^-	0.164 ± 0.001
μ^+	0.799 ± 0.003
proton	0.333 ± 0.001

B.3 Expected event rate on the liquid argon detector

Event rate of the cosmic-ray induced NR in the liquid argon detector is evaluated with the Geant4-based MC simulation. Such event contributes the indistinguishable background of the WIMP search run. The MC simulation setup is basically the same as that for the LS one, but here the cosmogenic neutron is also taken into account. Figure B.6 shows the simulated NR energy spectra and the time difference between fiducial and outer-bath signals δT.

Figures B.7 and B.8 show the detector materials where the fast neutron inducing the NR events originates. The lead shield surrounding the vessel is clearly the main origin of the fast neutron for all the incoming particles except neutron. There are also other origins such as interactions between muon and copper, muon and argon, and proton and polyethylene. The lifetimes of the muon-capture in copper and argon are 160 and 570 ns, respectively[134, 135]. Effective approaches against these background are to place

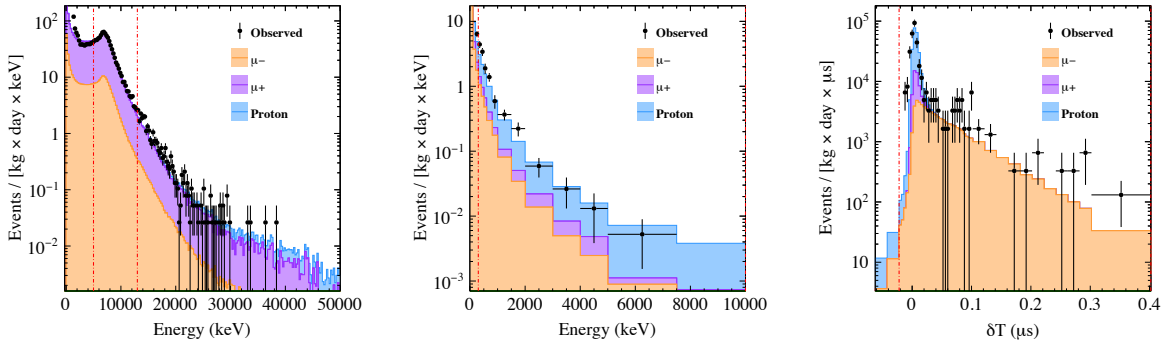

Fig. B.5. Comparisons between data and MC for the LS setup in ER energy spectrum (left), NR energy spectrum after requiring a coincident comic-ray signal in PS (center), and time difference between the LS and the PS (right).

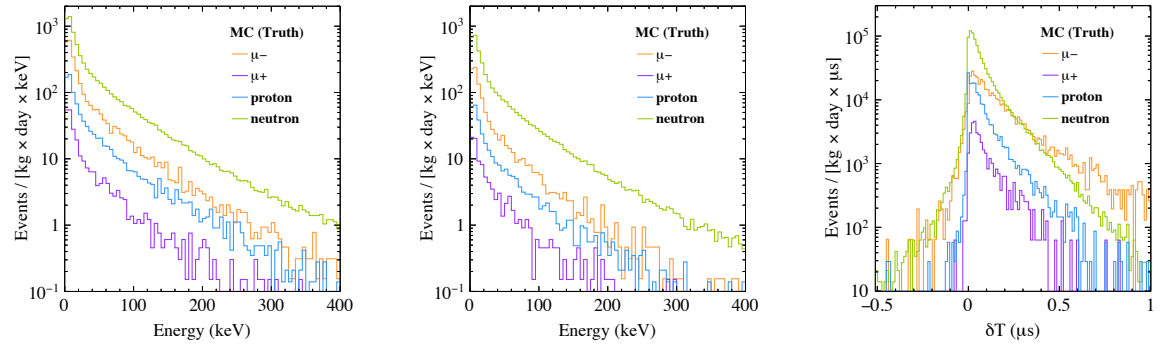

Fig. B.6. Predictions from the MC simulation for the LAr setup of (left:) the NR energy spectra from each cosmic-ray particle, before requiring the anti-veto coincidence, (center:) the spectra after requiring the anti-veto coincidence, and (right:) time difference δT for the NR events above the energy threshold of 30 p.e. Note that these spectra assume the initial EXPACS fluences and do not use the scale factor in Table B.1.

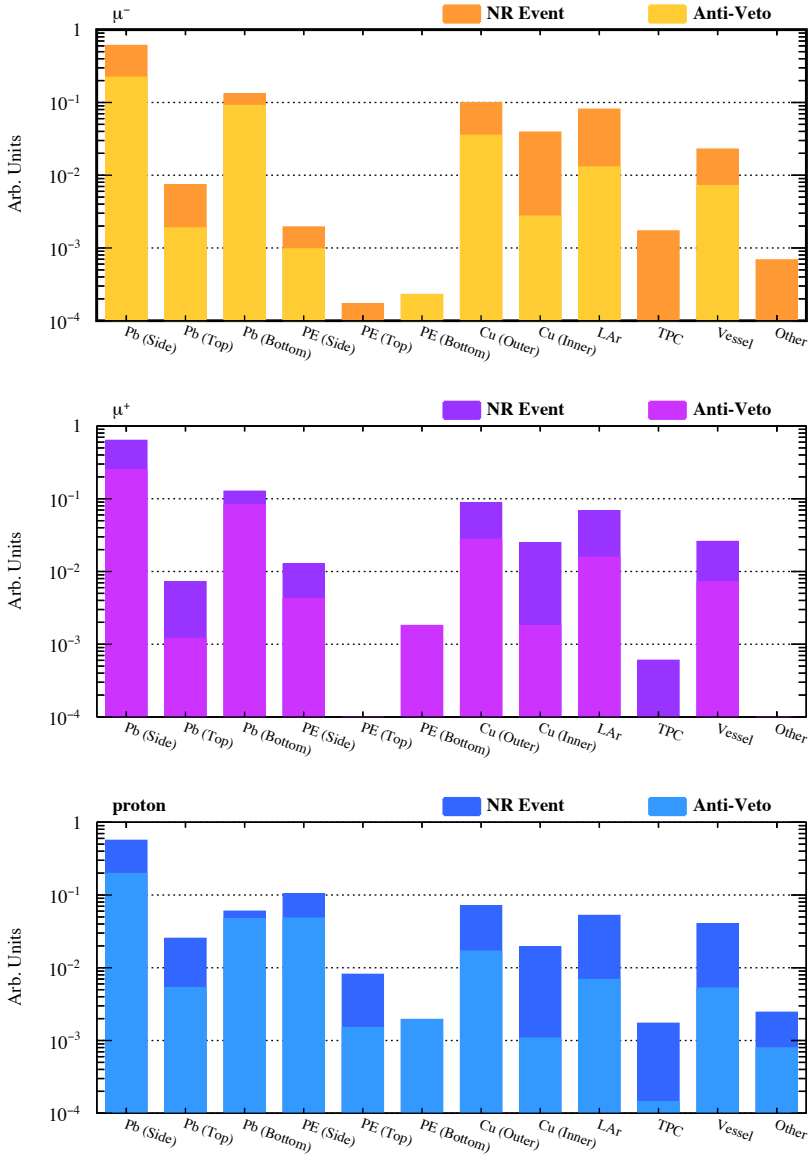

Fig. B.7. Relative intensities of detector materials where the fast neutron originates for μ^- (top), μ^+ (middle), and proton (bottom). For each incoming particle, two histograms corresponds to before and after the anti-veto coincidence.

sufficient neutron shield inside the lead and copper shieldings, to tag incoming particle and gate off several micro seconds after it, and to go underground facility. For the neutron, a large fraction of NR events come directly from the primary neutron, while several per cent of them are suggested to come from secondary neutron from the interaction with lead. Performing the experiment in an underground facility is the only realistic way to be overburdened by sufficient materials against neutrons.

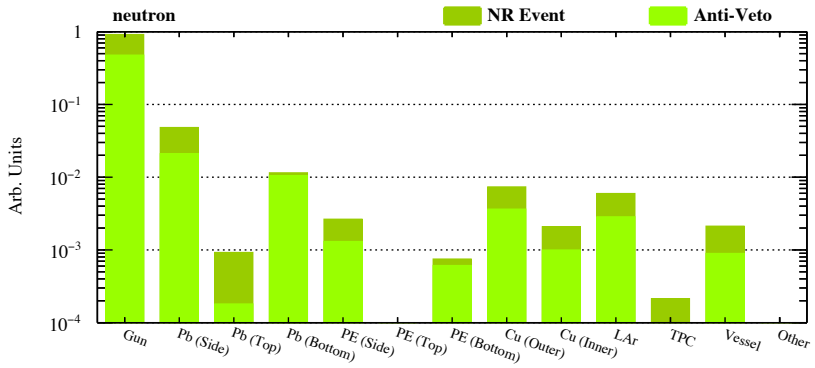

Fig. B.8. Relative intensities of detector materials where the fast neutron originates for the cosmogenic neutron. The figure descriptions are the same as in Fig. B.7.

Appendix C

Cosmic ray flux

Figure C.1 to C.8 show the flux of each cosmic ray particle in various altitude. These are calculated from EXPACS with input parameters summarized in Table C.1.

Table C.1. EXPACS input parameters.

Parameter	Value
EXPACS Version	4.09
Location	Lat. 38 degree, Long. 142 degree
Time	Sep.28th,2020
Surrounding environment	Ground

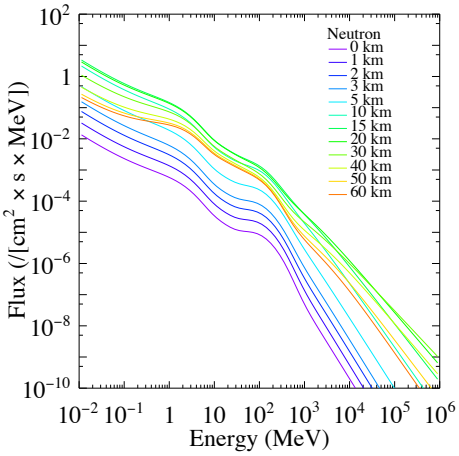

Fig. C.1. Flux of the cosmic ray neutron.

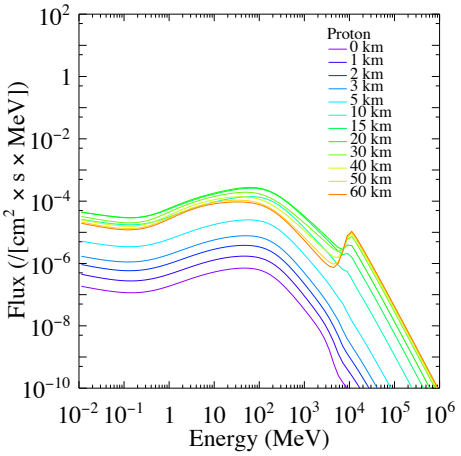

Fig. C.2. Flux of the cosmic ray proton.

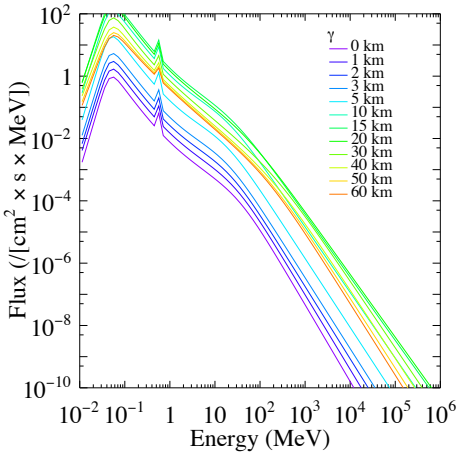

Fig. C.3. Flux of the cosmic ray photon.

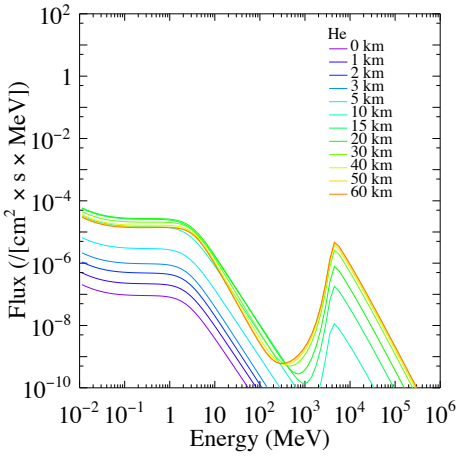

Fig. C.4. Flux of the cosmic ray helium-nuclei.

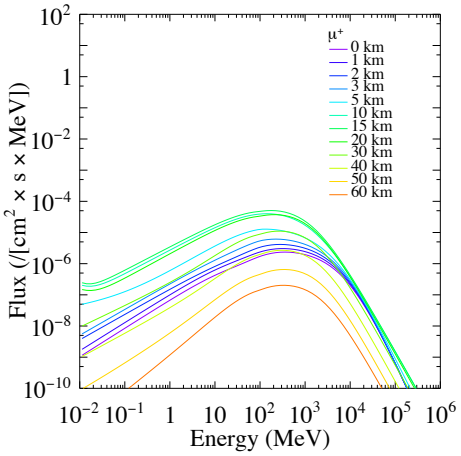

Fig. C.5. Flux of the cosmic ray negative muon.

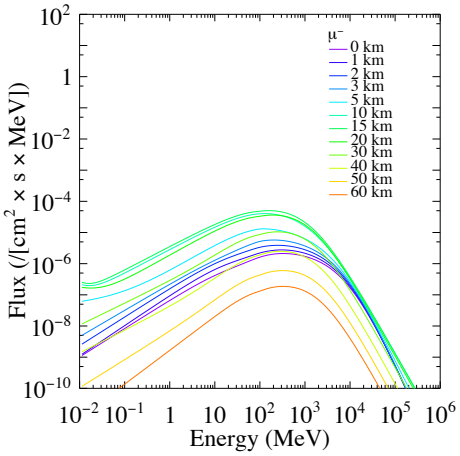

Fig. C.6. Flux of the cosmic ray positive muon.

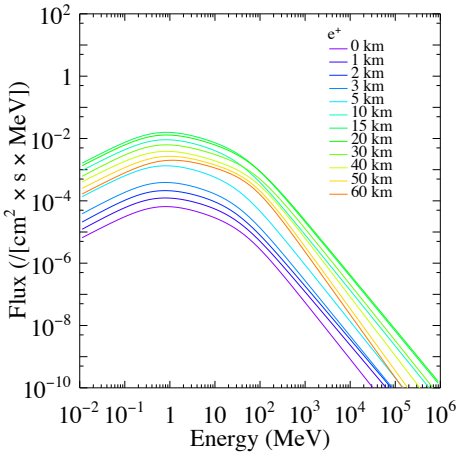

Fig. C.7. Flux of the cosmic ray electron.

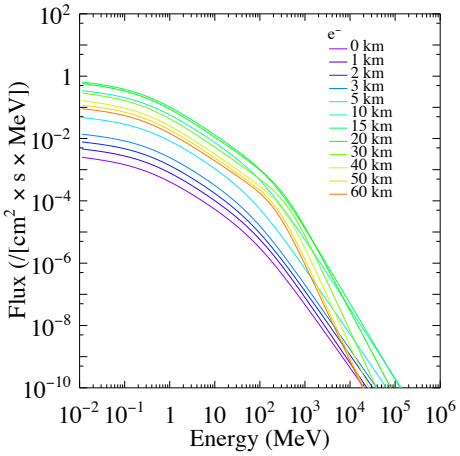

Fig. C.8. Flux of the cosmic ray positron.

Bibliography

[1] P. Zyla *et al.* (Particle Data Group Collaboration), Review of Particle Physics, PTEP **2020**, 083C01 (2020).

[2] F. Zwicky, Die Rotverschiebung von extragalaktischen Nebeln, Helv. Phys. Acta **6**, 110–127 (1933).

[3] V. C. Rubin and J. Ford, W.Kent, Rotation of the Andromeda Nebula from a Spectroscopic Survey of Emission Regions, Astrophys. J. **159**, 379–403 (1970).

[4] K. G. Begeman, A. H. Broeils, and R. H. Sanders, Extended rotation curves of spiral galaxies: dark haloes and modified dynamics, Monthly Notices of the Royal Astronomical Society **249**, 523–537 (1991).

[5] A. Refregier, Weak gravitational lensing by large scale structure, Ann. Rev. Astron. Astrophys. **41**, 645–668 (2003).

[6] D. Clowe, M. Bradac, A. H. Gonzalez, M. Markevitch, S. W. Randall, C. Jones, and D. Zaritsky, A direct empirical proof of the existence of dark matter, Astrophys. J. Lett. **648**, L109–L113 (2006).

[7] NASA Chandra X-ray Obsarvatory, Image credit: X-ray: NASA/CXC/CfA/M.Markevitch et al.; Optical: NASA/STScI; Magellan/U.Arizona/D.Clowe et al.; Lensing Map: NASA/STScI; ESO WFI; Magellan/U.Arizona/D.Clowe et al., the image is available online at https://chandra.harvard.edu/photo/2006/1e0657/.

[8] N. Aghanim *et al.* (Planck Collaboration), Planck 2018 results. I. Overview and the cosmological legacy of Planck, Astron. Astrophys. **641**, A1 (2020).

[9] ESA and the Planck Collaboration, Planck 2018 results, the images are available online at https://www.cosmos.esa.int/web/planck/picture-gallery.

[10] P. Gondolo, Non-baryonic dark matter, NATO Sci. Ser. II **187**, 279–333 (2005).

[11] T. Braine *et al.* (ADMX Collaboration), Extended Search for the Invisible Axion with the Axion Dark Matter Experiment, Phys. Rev. Lett. **124**, 101303 (2020).

[12] D. Akerib *et al.* (LUX Collaboration), First Searches for Axions and Axionlike Particles with the LUX Experiment, Phys. Rev. Lett. **118**, 261301 (2017).

[13] E. Aprile *et al.* (XENON Collaboration), Excess electronic recoil events in XENON1T, Phys. Rev. D **102**, 072004 (2020).

[14] A. Aguilar-Arevalo *et al.* (LSND Collaboration), Evidence for neutrino oscillations from the observation of $\bar{\nu}_e$ appearance in a $\bar{\nu}_\mu$ beam, Phys. Rev. D **64**, 112007 (2001).

[15] M. Drewes *et al.*, A White Paper on keV Sterile Neutrino Dark Matter, JCAP **01**, 025 (2017).

[16] J. Lewin and P. Smith, Review of mathematics, numerical factors, and corrections for dark matter experiments based on elastic nuclear recoil, Astropart. Phys. **6**, 87–112 (1996).

[17] K. Miuchi and K. Hamaguchi, Toward the direct detection of the dark matter in the universe, Butsuri **75**, 68–76 (2020), *in Japanese*.

[18] M. Schumann, Direct Detection of WIMP Dark Matter: Concepts and Status, J. Phys. G **46**, 103003 (2019).

[19] E. Aprile *et al.* (XENON Collaboration), Dark Matter Search Results from a One Ton-Year Exposure of XENON1T, Phys. Rev. Lett. **121**, 111302 (2018).

[20] X. Cui *et al.* (PandaX-II Collaboration), Dark Matter Results From 54-Ton-Day Exposure of PandaX-II Experiment, Phys. Rev. Lett. **119**, 181302 (2017).

[21] D. Akerib *et al.* (LUX Collaboration), Results from a search for dark matter in the complete LUX exposure, Phys. Rev. Lett. **118**, 021303 (2017).

[22] K. Abe *et al.* (XMASS Collaboration), A direct dark matter search in XMASS-I, Phys. Lett. B **789**, 45–53 (2019).

[23] R. Ajaj *et al.* (DEAP Collaboration), Search for dark matter with a 231-day exposure of liquid argon using DEAP-3600 at SNOLAB, Phys. Rev. D **100**, 022004 (2019).

[24] P. Agnes *et al.* (DarkSide Collaboration), DarkSide-50 532-day Dark Matter Search with Low-Radioactivity Argon, Phys. Rev. D **98**, 102006 (2018).

[25] E. Aprile *et al.* (XENON Collaboration), Light Dark Matter Search with Ionization Signals in XENON1T, Phys. Rev. Lett. **123**, 251801 (2019).

[26] P. Agnes *et al.* (DarkSide Collaboration), Low-Mass Dark Matter Search with the DarkSide-50 Experiment, Phys. Rev. Lett. **121**, 081307 (2018).

[27] R. Agnese *et al.* (SuperCDMS Collaboration), Search for Low-Mass Dark Matter with CDMSlite Using a Profile Likelihood Fit, Phys. Rev. D **99**, 062001 (2019).

[28] A. Abdelhameed *et al.* (CRESST Collaboration), First results from the CRESST-III low-mass dark matter program, Phys. Rev. D **100**, 102002 (2019).

[29] Q. Arnaud *et al.* (NEWS-G Collaboration), First results from the NEWS-G direct dark matter search experiment at the LSM, Astropart. Phys. **97**, 54–62 (2018).

[30] R. Bernabei *et al.*, First model independent results from DAMA/LIBRA-phase2, Nucl. Phys. Atom. Energy **19**, 307–325 (2018).

[31] G. Adhikari *et al.*, An experiment to search for dark-matter interactions using sodium iodide detectors, Nature **564**, 83–86 (2018), [Erratum: Nature 566, E2 (2019)].

[32] G. Adhikari *et al.* (COSINE-100 Collaboration), Search for a Dark Matter-Induced Annual Modulation Signal in NaI(Tl) with the COSINE-100 Experiment, Phys. Rev. Lett. **123**, 031302 (2019).

[33] E. Aprile *et al.* (XENON Collaboration), Projected WIMP sensitivity of the XENONnT dark matter experiment, JCAP **11**, 031 (2020).

[34] H. Zhang *et al.* (PandaX Collaboration), Dark matter direct search sensitivity of the PandaX-4T experiment, Sci. China Phys. Mech. Astron. **62**, 31011 (2019).

[35] D. Akerib *et al.* (LUX-ZEPLIN Collaboration), Projected WIMP sensitivity of the LUX-ZEPLIN dark matter experiment, Phys. Rev. D **101**, 052002 (2020).

[36] C. Aalseth *et al.*, DarkSide-20k: A 20 tonne two-phase LAr TPC for direct dark matter detection at LNGS, Eur. Phys. J. Plus **133**, 131 (2018).

[37] J. Aalbers *et al.* (DARWIN Collaboration), DARWIN: towards the ultimate dark matter detector, JCAP **11**, 017 (2016).

[38] A. Caminata (GADMC Collaboration), DarkSide-50 Results and the Future Liquid Argon Dark Matter Program, PoS **EPS-HEP2019**, 077 (2020).

[39] E. Aprile, A. Bolotnikov, A. Bolozdynya, and T. Doke, *Noble Gas Detectors* (Wiley-VCH, 2006) pp. 1–345.

[40] J. Lindhard, V. Nielsen, M. Scharff, and P. Thomsen, Integral equations governing radiation effects, Mat. Fys. Medd. Dan. Vid. Selsk **33**, 1–42 (1963).

[41] A. Hitachi, N. Kizaki, and N. Hasebe, Scintillation yield for slow recoil ions in liquid argon for dark matter searches, in *XeSAT2018* (2018).

[42] T. Doke, A. Hitachi, J. Kikuchi, K. Masuda, H. Okada, and E. Shibamura, Absolute Scintillation Yields in Liquid Argon and Xenon for Various Particles, Jap. J. Appl. Phys. **41**, 1538–1545 (2002).

[43] M. Miyajima, T. Takahashi, S. Konno, T. Hamada, S. Kubota, H. Shibamura, and T. Doke, Average energy expended per ion pair in liquid argon, Phys. Rev. A **9**, 1438–1443 (1974).

[44] H. Cao *et al.* (SCENE Collaboration), Measurement of Scintillation and Ionization Yield and Scintillation Pulse Shape from Nuclear Recoils in Liquid Argon, Phys. Rev. D **91**, 092007 (2015).

[45] T. Joshi *et al.*, First measurement of the ionization yield of nuclear recoils in liquid argon, Phys. Rev. Lett. **112**, 171303 (2014).

[46] P. Agnes *et al.*, Measurement of the liquid argon energy response to nuclear and electronic recoils, Phys. Rev. D **97**, 112005 (2018).

[47] T. Washimi, Study of Electron Recoil Background Rejection in Double Phase Argon Detector for the WIMP Dark Matter Search, Ph.D. thesis, Waseda U. (2018), *in Japanese*.

[48] U. Fano and W. Lichten, Interpretation of Ar+-Ar Collisions at 50 KeV, Phys. Rev. Lett. **14**, 627–629 (1965).

[49] F. Bezrukov, F. Kahlhoefer, M. Lindner, F. Kahlhoefer, and M. Lindner, Interplay between scintillation and ionization in liquid xenon Dark Matter searches, Astropart. Phys. **35**, 119–127 (2011).

[50] C. E. Dahl, The physics of background discrimination in liquid xenon, and first results from Xenon10 in the hunt for WIMP dark matter, Ph.D. thesis, Princeton U. (2009).

[51] B. Lenardo, K. Kazkaz, A. Manalaysay, J. Mock, M. Szydagis, and M. Tripathi, A Global Analysis of Light and Charge Yields in Liquid Xenon, IEEE Trans. Nucl. Sci. **62**, 3387–3396 (2015).

[52] J. Thomas and D. Imel, Recombination of electron-ion pairs in liquid argon and liquid xenon, Phys. Rev. A **36**, 614–616 (1987).

[53] T. Doke, Fundamental Properties of Liquid Argon, Krypton and Xenon as Radiation Detector Media, Portugal. Phys. **12**, 9–48 (1981).

[54] P. Agnes *et al.* (DarkSide Collaboration), Electroluminescence pulse shape and electron diffusion in liquid argon measured in a dual-phase TPC, Nucl. Instrum. Meth. A **904**, 23–34 (2018).

[55] S. Kubota, M. Hishida, M. Suzuki, and J.-z. Ruan(Gen), Dynamical behavior of free electrons in the recombination process in liquid argon, krypton, and xenon, Phys. Rev. B **20**, 3486 (1979).

[56] A. Mozumder, Free-ion yield in liquid argon at low-let, Chemical Physics Letters **238**, 143 – 148 (1995).

[57] A. Hitachi, Properties of liquid xenon scintillation for dark matter searches, Astropart. Phys. **24**, 247–256 (2005).

[58] D.-M. Mei, Z.-B. Yin, L. Stonehill, and A. Hime, A Model of Nuclear Recoil Scintillation Efficiency in Noble Liquids, Astropart. Phys. **30**, 12–17 (2008).

[59] A. Hitachi, T. Doke, and A. Mozumder, Luminescence quenching in liquid argon under charged-particle impact: Relative scintillation yield at different linear energy transfers, Phys. Rev. B **46**, 11463 (1992).

[60] A. Hitachi, T. Takahashi, N. Funayama, K. Masuda, J. Kikuchi, and T. Doke, Effect of ionization density on the time dependence of luminescence from liquid argon and xenon, Phys. Rev. B **27**, 5279–5285 (1983).

[61] S. Amoruso *et al.*, Analysis of the liquid argon purity in the ICARUS T600 TPC, Nucl. Instrum. Meth. A **516**, 68–79 (2004).

[62] W. Walkowiak, Drift velocity of free electrons in liquid argon, Nucl. Instrum. Meth. A **449**, 288–294 (2000).

[63] A. Bondar, A. Buzulutskov, A. Grebenuk, D. Pavlyuchenko, R. Snopkov, and Y. Tikhonov, Two-phase argon and xenon avalanche detectors based on gas electron multipliers, Nucl. Instrum. Meth. A **556**, 273–280 (2006).

[64] C. Monteiro, J. Lopes, J. Veloso, and J. dos Santos, Secondary scintillation yield in pure argon, Phys. Lett. B **668**, 167–170 (2008).

[65] A. Buzulutskov, E. Shemyakina, A. Bondar, A. Dolgov, E. Frolov, V. Nosov, V. Oleynikov, L. Shekhtman, and A. Sokolov, Revealing neutral bremsstrahlung in two-phase argon electroluminescence, Astropart. Phys. **103**, 29–40 (2018).

[66] A. Bondar, A. Buzulutskov, A. Dolgov, E. Frolov, V. Nosov, V. Oleynikov, E. Shemyakina, and A. Sokolov, Neutral bremsstrahlung in two-phase argon electroluminescence: further studies and possible applications, Nucl. Instrum. Meth. A **958**, 162432 (2020).

[67] P.-A. Amaudruz *et al.* (DEAP Collaboration), Measurement of the scintillation time spectra and pulse-shape discrimination of low-energy β and nuclear recoils in liquid argon with DEAP-1, Astropart. Phys. **85**, 1–23 (2016).

[68] D.-M. Mei, C. Zhang, and A. Hime, Evaluation of (alpha,n) Induced Neutrons as a Background for Dark Matter Experiments, Nucl. Instrum. Meth. A **606**, 651–660 (2009).

[69] V. Tomasello, V. Kudryavtsev, and M. Robinson, Calculation of neutron background for underground experiments, Nucl. Instrum. Meth. A **595**, 431–438 (2008).

[70] K. Mizukoshi *et al.*, Measurement of ambient neutrons in an underground laboratory at the Kamioka Observatory, PTEP **2018**, 123C01 (2018).

[71] T.Sato, EXPACS: Excel-based program for calculating atmospheric cosmic-ray spectrum, http://phits.jaea.go.jp/expacs/.

[72] T. Sato, Analytical model for estimating the zenith angle dependence of terrestrial cosmic ray fluxes, PLOS ONE **11**, 1–22 (2016).

[73] T. Sato, Analytical model for estimating terrestrial cosmic ray fluxes nearly anytime and anywhere in the world: Extension of parma/expacs, PLOS ONE **10**, 1–33 (2015).

[74] J. Carmona *et al.*, Neutron background at the Canfranc Underground Laboratory and its contribution to the IGEX-DM dark matter experiment, Astropart. Phys. **21**, 523–533 (2004).

[75] P. Benetti *et al.* (WARP Collaboration), Measurement of the specific activity of Ar-39 in natural argon, Nucl. Instrum. Meth. A **574**, 83–88 (2007).

[76] R. Acciarri *et al.* (WArP Collaboration), Oxygen contamination in liquid Argon: Combined effects on ionization electron charge and scintillation light, JINST **5**, P05003 (2010).

[77] R. Acciarri *et al.* (WArP Collaboration), Effects of Nitrogen contamination in liquid Argon, JINST **5**, P06003 (2010).

[78] B. Jones, T. Alexander, H. Back, G. Collin, J. Conrad, A. Greene, T. Katori, S. Pordes, and M. Toups, The Effects of Dissolved Methane upon Liquid Argon Scintillation Light, JINST **8**, P12015 (2013).

[79] Hamamatsu Photonics K.K., R11065 data sheets, (2009).

[80] Hamamatsu Photonics K.K., R6041-506mod data sheets, (2012).

[81] W. Burton and B. Powell, Fluorescence of Tetraphenyl-Butadiene in the Vacuum Ultraviolet, Appl. Opt. **12**, 87–89 (1973).

[82] G. Porter and M. R. Topp, Nanosecond flash photolysis, Proceedings of the Royal Society of London. A. Mathematical and Physical Sciences **315**, 163–184 (1970).

[83] S. Hanagodimath, B. Siddlingeshwar, J. Thipperudrappa, and S. K. B. Hadimani, Fluorescence-quenching studies and temperature dependence of fluorescence quantum yield, decay time and intersystem crossing activation energy of TPB, Journal of Luminescence **129**, 335 – 339 (2009).

[84] R. Francini *et al.*, VUV-Vis optical characterization of Tetraphenyl-butadiene films on glass and specular reflector substrates from room to liquid Argon temperature, JINST **8**, P09006 (2013).

[85] B. Broerman *et al.*, Application of the TPB Wavelength Shifter to the DEAP-3600 Spherical Acrylic Vessel Inner Surface, JINST **12**, P04017 (2017).

[86] T. Washimi, M. Kimura, M. Tanaka, and K. Yorita, Scintillation and ionization ratio of liquid argon for electronic and nuclear recoils at drift-fields up to 3 kV/cm, Nucl. Instrum. Meth. **A910**, 22–25 (2018).

[87] Murata Software Co. Ltd., CAE software femtet, https://www.muratasoftware.com.

[88] R. Brunetti *et al.* (WARP Collaboration), Warp liquid argon detector for dark matter survey, New Astron. Rev. **49**, 265–269 (2005).

[89] D. Gastler, E. Kearns, A. Hime, L. Stonehill, S. Seibert, J. Klein, W. Lippincott, D. McKinsey, and J. Nikkel, Measurement of scintillation efficiency for nuclear recoils in liquid argon, Phys. Rev. C **85**, 065811 (2012).

[90] W. Creus, Y. Allkofer, C. Amsler, A. Ferella, J. Rochet, L. Scotto-Lavina, and M. Walter, Scintillation efficiency of liquid argon in low energy neutron-argon scattering, JINST **10**, P08002 (2015).

[91] P. Agnes *et al.* (DarkSide Collaboration), Simulation of argon response and light detection in the DarkSide-50 dual phase TPC, JINST **12**, P10015 (2017).

[92] A. Bondar, A. Buzulutskov, A. Dolgov, E. Grishnyaev, S. Polosatkin, L. Shekhtman, E. Shemyakina, and A. Sokolov, Measurement of the ionization yield of nuclear recoils in liquid argon at 80 and 233 keV, EPL **108**, 12001 (2014).

[93] A. Bondar, A. Buzulutskov, A. Dolgov, E. Grishnyaev, V. Nosov, V. Oleynikov, S. Polosatkin, L. Shekhtman, E. Shemyakina, and A. Sokolov, Measurement of the ionization yield of nuclear recoils in liquid argon using a two-phase detector with electroluminescence gap, JINST **12**, C05010 (2017).

[94] T. Joshi, S. Sangiorgio, V. Mozin, E. Norman, P. Sorensen, M. Foxe, G. Bench, and A. Bernstein, Design and demonstration of a quasi-monoenergetic neutron source, Nucl. Instrum. Meth. B **333**, 6–11 (2014).

[95] S. Agostinelli *et al.* (GEANT4 Collaboration), GEANT4–a simulation toolkit, Nucl. Instrum. Meth. A **506**, 250–303 (2003).

[96] J. Allison *et al.*, Geant4 developments and applications, IEEE Trans. Nucl. Sci. **53**, 270 (2006).

[97] J. Allison *et al.*, Recent developments in Geant4, Nucl. Instrum. Meth. A **835**, 186–225 (2016).

[98] J. W. Boldeman, B. E. Clancy, and D. Culley, Measurements of the Prompt Fission Neutron Spectrum from the Spontaneous Fission of ^{252}Cf, Nuclear Science and Engineering **93**, 181–192 (1986).

[99] E. Mendoza, D. Cano-Ott, T. Koi, and C. Guerrero, New Standard Evaluated Neutron Cross Section Libraries for the GEANT4 Code and First Verification, IEEE Transactions on Nuclear Science **61**, 2357–2364 (2014).

[100] E. Mendoza, D. Cano-Ott, C. Guerrero, and R. Capote, New evaluated neutron cross section libraries for the Geant4 code, Tech. Rep. INDC(NDS)-0612 (International Atomic Energy Agency, 2012).

[101] E. Mendoza and Cano-Ott, Update of the Evaluated Neutron Cross Section Libraries for the Geant4 Code, Tech. Rep. INDC(NDS)-0758 (International Atomic Energy Agency, 2018).

[102] A. E. Robinson, New libraries for simulating neutron scattering in dark matter detector calibrations, Phys. Rev. C **89**, 032801 (2014).

[103] M. Szydagis, N. Barry, K. Kazkaz, J. Mock, D. Stolp, M. Sweany, M. Tripathi, S. Uvarov, N. Walsh, and M. Woods, NEST: A Comprehensive Model for Scintillation Yield in Liquid Xenon, JINST **6**, P10002 (2011).

[104] Matthew Szydagis and Greg Rischbieter (NEST Collaboration), A comprehensive, exhaustive, complete analysis of world lxe nr data with a final model, Analysis Reports (2019), available at http://nest.physics.ucdavis.edu.

[105] M. Szydagis, J. Balajthy, J. Brodsky, J. Cutter, J. Huang, E. Kozlova, B. Lenardo, A. Manalaysay, D. McKinsey, M. Mooney, and et al., Noble Element Simulation Technique v2.0, (2018), 10.5281/zenodo.1314669.

[106] T. Alexander *et al.* (DarkSide Collaboration), Light Yield in DarkSide-10: A Prototype Two-Phase Argon TPC for Dark Matter Searches, Astropart. Phys. **49**, 44–51 (2013).

[107] V. Rogers, Inelastic neutron scattering in F-19, Phys. Rev. C **9**, 527–530 (1974).

[108] T. Sato, Y. Iwamoto, S. Hashimoto, T. Ogawa, T. Furuta, S. ichiro Abe, T. Kai, P.-E. Tsai, N. Matsuda, H. Iwase, N. Shigyo, L. Sihver, and K. Niita, Features of particle and heavy ion transport code system (phits) version 3.02, Journal of Nuclear Science and Technology **55**, 684–690 (2018).

[109] C. M. P. Johnson, G. A. Jones, W. R. Phillips, and D. H. Wilkinson, A study of the levels in ^{19}F following the β-decay of ^{19}O, Proceedings of the Royal Society of London. Series A, Mathematical and Physical Sciences **252**, 1–15 (1959).

[110] R. Saldanha, H. Back, R. Tsang, T. Alexander, S. Elliott, S. Ferrara, E. Mace, C. Overman, and M. Zalavadia, Cosmogenic production of ^{39}Ar and ^{37}Ar in argon, Phys. Rev. C **100**, 024608 (2019).

[111] B. Cleveland, T. Daily, J. Davis, Raymond, J. R. Distel, K. Lande, C. Lee, P. S. Wildenhain, and J. Ullman, Measurement of the solar electron neutrino flux with the Homestake chlorine detector, Astrophys. J. **496**, 505–526 (1998).

[112] M.-M. Bé, V. Chisté, C. Dulieu, X. Mougeot, V. Chechev, F. Kondev, A. Nichols, X. Huang, and B. Wang, *Table of Radionuclides*, Monographie BIPM-5, Vol. 7 (Bureau International des Poids et Mesures, Pavillon de Breteuil, F-92310 Sèvres, France, 2013).

[113] R. Purtschert, M. Kalinowski, P. Bourgouin, E. Wieslander, X. Blanchard, R. Riedmann, L. Raghoo, J. Kusmierczyk-Michulec, A. Gheddou, and C. S. adn Yutaka Tomita, Ar-37, be-7, and xe-133 in the atmosphere, in *CTBT Science and Technology 2017 Conference (CTBT, Vienna, 2017)* (2017) sec. T1.3-O2.

[114] T. Doke, H. Crawford, A. Hitachi, J. Kikuchi, P. Lindstrom, K. Masuda, E. Shibamura, and T. Takahashi, Let Dependence of Scintillation Yields in Liquid Argon, Nucl. Instrum. Meth. A **269**, 291–296 (1988).

[115] W. Lippincott, S. Cahn, D. Gastler, L. Kastens, E. Kearns, D. McKinsey, and J. Nikkel, Calibration of liquid argon and neon detectors with ^{83}Kr^{m}, Phys. Rev. C **81**, 045803 (2010).

[116] W.-X. Xiong, M.-Y. Guan, C.-G. Yang, P. Zhang, J.-C. Liu, C. Guo, Y.-T. Wei, Y.-Y. Gan, Q. Zhao, and J.-J. Li, Calibration of liquid argon detector with ^{83m}Kr and ^{22}Na in different drift field, *preprint* arXiv:1909.02207 (2019).

[117] NEST Noble Element Simulation Technique, http://nest.physics.ucdavis.edu.

[118] M.J. Berger, J.H. Hubbell, S.M. Seltzer, J. Chang, J.S. Coursey, R. Sukumar, D.S. Zucker, and K. Olsen, XCOM: Photon cross sections database, (2010).

[119] V. M. Gehman, S. R. Seibert, K. Rielage, A. Hime, Y. Sun, D. M. Mei, J. Maassen, and D. Moore, Fluorescence Efficiency and Visible Re-emission Spectrum of Tetraphenyl Butadiene Films at Extreme Ultraviolet Wavelengths, Nucl. Instrum. Meth. A **654**, 116–121 (2011).

[120] C. Benson, G. Orebi Gann, and V. Gehman, Measurements of the intrinsic quantum efficiency and absorption length of tetraphenyl butadiene thin films in the vacuum ultraviolet regime, Eur. Phys. J. C **78**, 329 (2018).

[121] D. Akimov *et al.* (COHERENT Collaboration), Development of a ^{83m}Kr source for the calibration of the CENNS-10 Liquid Argon Detector, *preprint* arXiv:2010.11258 (2020).

[122] T. Igarashi, M. Tanaka, T. Washimi, and K. Yorita, Performance of VUV-sensitive MPPC for Liquid Argon Scintillation Light, Nucl. Instrum. Meth. A **833**, 239–244 (2016).

[123] C. Ransom, Studies of a pmt with magnesium fluoride window for direct detection of liquid argon scintillation light, in *Joint SPS and OePG meeting 2017* (2017).

[124] Y. Hotta, Latest developments in pmts for low temperature operation, in *UCLA Dark Matter 2014* (2014).

[125] radiopurity.org, https://www.radiopurity.org.

[126] P. Agnes *et al.* (DarkSide Collaboration), Separating ^{39}Ar from ^{40}Ar by cryogenic distillation with Aria for dark matter searches, *preprint* arXiv:2101.08686 (2021).

[127] P. Agnes *et al.* (DarkSide Collaboration), Results From the First Use of Low Radioactivity Argon in a Dark Matter Search, Phys. Rev. D **93**, 081101 (2016), [Addendum: Phys.Rev.D 95, 069901 (2017)].

[128] R. Dossi, A. Ianni, G. Ranucci, and O. Y. Smirnov, Methods for precise photoelectron counting with photomultipliers, Nucl. Instrum. Meth. A **451**, 623–637 (2000).

[129] J. T. M. de Haas and P. Dorenbos, Methods for accurate measurement of the response of photomultiplier tubes and intensity of light pulses, IEEE Transactions on Nuclear Science **58**, 1290–1296 (2011).

[130] R. Saldanha, L. Grandi, Y. Guardincerri, and T. Wester, Model Independent Approach to the Single Photoelectron Calibration of Photomultiplier Tubes, Nucl. Instrum. Meth. A **863**, 35–46 (2017).

[131] K. J. Ma *et al.*, Time and Amplitude of Afterpulse Measured with a Large Size Photomultiplier Tube, Nucl. Instrum. Meth. A **629**, 93–100 (2011).

[132] P. Barrow *et al.*, Qualification Tests of the R11410-21 Photomultiplier Tubes for the XENON1T Detector, JINST **12**, P01024 (2017).

[133] K. Lung *et al.*, Characterization of the Hamamatsu R11410-10 3-Inch Photomultiplier Tube for Liquid Xenon Dark Matter Direct Detection Experiments, Nucl. Instrum. Meth. A **696**, 32–39 (2012).

[134] D. Measday, The nuclear physics of muon capture, Phys. Rept. **354**, 243–409 (2001).

[135] T. Mamedov, V. Grebinnik, K. Gritsai, V. Duginov, V. Zhukov, V. Ol ' shevskii, and A. Stoikov, Total rates of nuclear capture of negative muons in the isotopes ^{132}Xe and ^{40}Ar, Jetp Lett. **69**, 192–195 (1999).

List of publications

Publications

1. T.Washimi, M.Kimura, M.Tanaka, and K.Yorita, Scintillation and ionization ratio of liquid argon for electronic and nuclear recoils at drift-fields up to 3 kV/cm, Nuclear Instruments and Methods in Physics Research Section A **910**, 22-25 (2018).
2. M.Kimura, M.Tanaka, K.Yorita, and T.Washimi, Measurement of the scintillation efficiency for nuclear recoils in liquid argon under electric fields up to 3 kV/cm", Physical Review D **100**, 032002 (2019).
3. M.Kimura, K.Aoyama, M.Tanaka, and K.Yorita, Liquid argon scintillation response to electronic recoils between 2.8–1275 keV in a high light yield single-phase detector, Physical Review D **102**, 092008 (2020).

Conference Proceedings

1. M. Kimura, K.Yorita, and M.Tanaka, Status and prospect of the ANKOK project: Low mass WIMP dark matter search using double phase argon detector, Journal of Physics: Conference Series **1342**, XV International Conference on Topics in Astroparticle and Underground Physics (TAUP2017), 012069 (2020).
2. M.Kimura, Measurement of liquid argon scintillation and ionization response on nuclear recoils under electric fields up to 3 kV/cm, Journal of Physics: Conference Series **1468**, 16th International Conference on Topics in Astroparticle and Underground Physics (TAUP2019), 012055 (2020).
3. M.Kimura, M.Tanaka, K.Yorita, and T.Washimi, Measurement of liquid argon scintillation and ionization response on nuclear recoils under electric fields up to 3 kV/cm, Journal of Instrumentation **15**, Light Detection in Noble Elements 2019 (LIDINE 2019), C03042 (2020).
4. M.Kimura, K.Aoyama, T.Takeda, M.Tanaka, and K.Yorita, Measurements of argon-scintillation and -electroluminescence properties for low mass WIMP dark matter search, Journal of Instrumentation **15**, The International Conference Instrumentation for Colliding Beam Physics (INSTR2020), C08012 (2020).

Talks at Conference

1. M. Kimura, K.Yorita, and M.Tanaka, Status and prospect of the ANKOK project: Low mass WIMP dark matter search using double phase argon detector, XV International Conference on Topics in Astroparticle and Underground Physics (TAUP2017), July 24-28 2017, Sudbury, Ontario, Canada.
2. M.Kimura, M.Tanaka, K.Yorita, and T.Washimi, Measurement of liquid argon scintillation and ionization response on nuclear recoils under electric fields up to 3 kV/cm, Light Detection in Noble Elements 2019 (LIDINE 2019), August 28-30 2019, Manchester, United Kingdom.
3. M.Kimura, K.Aoyama, T.Takeda, M.Tanaka, and K.Yorita, Measurements of argon-scintillation and -electroluminescence properties for low mass WIMP dark matter search, International Conference on Instrumentation for Colliding Beam Physics (INSTR20), February 24-28 2020, Novosibirsk, Russian Federation.

Poster Presentations

1. M.Kimura, Measurement of the Scintillation Efficiency for Nuclear Recoils in Double-Phase Argon Detector for Low Mass WIMP Search, Revealing the history of the universe with underground particle and nuclear research 2019 (UGND2019), March 7-9 2019, Sendai, Japan.
2. M.Kimura, Measurement of liquid argon scintillation and ionization response on nuclear recoils under electric fields up to 3 kV/cm, 16th International Conference on Topics in Astroparticle and Underground Physics (TAUP 2019), September 9-13 2019, Toyama, Japan

Seminar

1. M.Kimura, Measurement of Liquid Argon Response and Direct Dark Matter Search at Surface with A Liquid Argon Scintillation Detector, J-PARC Particle and Nuclear Physics Seminar, October 20 2020.